

Aus dem Max-Planck-Institut für Polymerforschung in Mainz

Colloidal Concepts towards Latent-Reactive Thermosetting Polymers

Dissertation

Zur Erlangung des Grades

„Doktor der Naturwissenschaften“

im Promotionsfach Chemie

am Fachbereich Chemie, Pharmazie und Geowissenschaften

der Johannes Gutenberg-Universität Mainz

Ann-Christin Bijlard

geboren in Siegen

Mainz, 2016

Die vorliegende Arbeit wurde in der Zeit von Januar 2013 bis Februar 2016 am Max-Planck-Institut für Polymerforschung im Arbeitskreis von [REDACTED] angefertigt.
Die Arbeit wurde in Kooperation mit der Henkel AG & Co. KGaA in Düsseldorf durchgeführt.

Dekan: [REDACTED]

1. Gutachter: [REDACTED]

2. Gutachter: [REDACTED]

Tag der mündlichen Prüfung: 22.03.2016

Table of Contents

1	Motivation.....	1
2	Theoretical Background.....	3
2.1	Colloidal Systems	3
2.1.1	Emulsions	3
2.1.2	Stability	4
2.2	Surfactants	7
2.2.1	Non-Ionic Surfactants	8
2.2.2	Functional Surfactants.....	9
2.3	Preparation of Nanoparticles by (Mini)Emulsion Polymerization	11
2.3.1	Chain-Growth Polymerization in (Mini)Emulsions.....	11
2.3.2	Step-Growth Polymerizations in Miniemulsions	14
2.4	Thermosetting Polymers.....	15
2.4.1	Epoxy-Amine Thermosets.....	15
2.4.2	Thermosets and Miniemulsion Polymerization.....	20
2.5	Film Formation	21
2.6	Reaction Latency in Colloidal Systems.....	23
2.6.1	Latent Catalysis	24
2.6.2	Latency Triggered by Film Formation.....	25
2.6.3	Latency in Self-Healing Films	26
3	Preparation and Characterization Techniques	28
3.1	Dynamic Light Scattering (DLS)	28
3.2	Imaging Techniques	29
3.2.1	Scanning Electron Microscopy (SEM)	29
3.2.2	Transmission Electron Microscopy (TEM).....	29
3.2.3	Confocal and Dual Color-STED Microscopy (DC-STED).....	30
3.3	Thermal Methods.....	30
3.3.1	Thermogravimetric Analysis (TGA).....	30

3.3.2	Differential Scanning Calorimetry (DSC).....	31
3.3.3	Isothermal Titration Calorimetry (ITC)	31
3.4	Mechanical Properties	32
3.4.1	Oscillatory Rheology.....	32
3.5	Electrospinning.....	35
4	Results and Discussion	36
4.1	Reaction Latency by Triggered Catalysis.....	36
4.1.1	Motivation	37
4.1.2	Nanocapsule Synthesis	39
4.1.3	Morphology.....	41
4.1.4	Thermal Properties	43
4.1.5	Thermolatent Catalysis.....	45
4.1.5.1	Rheology	45
4.1.5.2	FT-IR/NIR Analysis	51
4.1.5.3	Composite-Morphology	53
4.1.6	Conclusion.....	55
4.2	Reaction Latency in “pseudo” 1K Systems.....	56
4.2.1	Motivation	56
4.2.2	P1K-Thermosets.....	58
4.2.2.1	Hydrophobic Polyamines	58
4.2.2.2	P1K-Systems	60
4.2.2.3	Properties.....	61
4.2.3	Cross-Linkable Surfactants*	67
4.2.3.1	Motivation	68
4.2.3.2	Properties.....	70
4.2.3.3	Colloidal Stability.....	74
4.2.3.4	Interfacial Stabilization	75
4.2.3.5	Reactivity.....	77
4.2.3.6	Conclusion.....	78
4.2.4	Colloidal Latency in the P1K.....	79
4.2.4.1	Colloidal Stability.....	80

4.2.4.2	Film Formation.....	85
4.2.4.3	Turbidity Measurements.....	92
4.2.4.4	Fluorescence Characterization.....	94
4.2.4.5	Conclusion.....	98
4.3	Reaction Latency in Nanofibers**	99
4.3.1	Motivation	100
4.3.2	Nanofiber Synthesis	101
4.3.3	Morphology and Distribution of Compartments	102
4.3.3.1	External Morphology as studied by SEM.....	102
4.3.3.2	Internal Morphology as studied by (DC-STED)	103
4.3.3.3	TEM and Simulations.....	106
4.3.4	Reactivity	108
4.3.5	Self-Healing	111
4.3.6	Conclusion.....	115
5	Experimental Part.....	116
5.1	Experimental Details for Chapter 4.1	116
5.1.1	Materials.....	116
5.1.2	Synthesis of the Nanocapsules containing a PU-Catalyst.....	116
5.1.3	Catalytic Cure of PU-Composites	117
5.1.4	Characterization Methods	118
5.1.4.1	Dynamic Light Scattering.....	118
5.1.4.2	Electron Microscopy	118
5.1.4.3	Thermal Analysis.....	118
5.1.4.4	X-Ray Fluorescence Spectroscopy.....	118
5.1.4.5	NIR-Coupled Oscillatory Rheology	118
5.1.4.6	Dynamic Mechanical Analysis.....	119
5.2	Experimental Details for Chapter 4.2	120
5.2.1	Materials and Purification	120
5.2.2	Preparation of the PIK-Thermosets	120
5.2.3	Characterization Methods	120
5.2.3.1	Epoxy Titration.....	120
5.2.3.2	Amine Titration	120

5.2.3.3	Thermal Analysis.....	121
5.2.3.4	Oscillatory Rheology.....	121
5.3	Experimental Details for Chapter 4.2.3	122
5.3.1	Materials.....	122
5.3.2	Synthesis of the Epoxy Surfactants	122
5.3.3	Non-Reactive Epoxy Surfactants	122
5.3.4	Preparation of Amine Miniemulsions	123
5.3.5	Characterization Methods	123
5.3.5.1	Fourier Transform Infrared Spectroscopy	123
5.3.5.2	Nuclear Magnetic Resonance Spectroscopy.....	123
5.3.5.3	Epoxy Titration.....	123
5.3.5.4	Size Exclusion Chromatography	124
5.3.5.5	Critical Micelle Concentration Determination	124
5.3.5.6	Dynamic Light Scattering.....	124
5.3.5.7	Isothermal Titration Calorimetry.....	124
5.3.5.8	Electron Microscopy	125
5.3.5.9	Oscillatory Rheology.....	125
5.4	Experimental Details for Chapter 4.2.4	126
5.4.1	Materials.....	126
5.4.2	Preparation of Amine and Epoxy Miniemulsions	126
5.4.3	Preparation of PIK-Systems	128
5.4.4	Characterization Methods	128
5.4.4.1	Absorption and Emission Spectroscopy.....	128
5.4.4.2	Dynamic Light Scattering.....	128
5.4.4.3	Fluorescamine Assay.....	128
5.4.4.4	Film Formation.....	129
5.4.4.5	Turbidity Measurements.....	129
5.4.4.6	Electron Microscopy	130
5.4.4.7	Thermal Analysis.....	130
5.4.4.8	Oscillatory Rheology	130
5.5	Experimental Details for Chapter 4.3.	131
5.5.1	Materials.....	131
5.5.2	Synthesis of the Dyes used for DC-STED	131

5.5.3	Synthesis of Nanofibers	133
5.5.4	Characterization Methods	133
5.5.4.1	Fiber Spinning	133
5.5.4.2	Electron Microscopy	134
5.5.4.3	Simulations	134
5.5.4.4	Dual Color Stimulated Emission Depletion Microscopy	134
5.5.4.5	Thermal Analysis.....	134
5.5.4.6	Fourier Transform Infrared Spectroscopy	135
5.5.4.7	High Pressure Liquid Chromatography	135
5.5.4.8	Linear Sweep Voltammetry.....	135
5.5.4.9	Salt Water Corrosion Tests.....	135
6	Summary and Outlook	136
7	Zusammenfassung und Ausblick	139
8	References.....	142
9	Appendix.....	I
9.1	List of Figures.....	I
9.2	List of Tables	III
9.3	List of Abbreviations	IV
9.4	List of Symbols.....	VII
9.5	Curriculum Vitae	IX
9.6	Scientific Contributions	XI

1 Motivation

“In terms of sustainable development all countries are now developing countries.”¹

This statement was made in a study by the Bertelsman Foundation on how the higher income countries are currently performing with regard to the “Sustainable Development Goals” defined on the UN summit which was held on Sept. 25-27 in 2015 and published under the title: “Transforming our world: The 2030 Agenda for Sustainable Development”.¹ These words highlight two aspects, firstly that all countries are far from being sustainable and secondly, that rich countries are no longer considered role models with regard to these challenges. This requires fundamental changes, especially with regard to consumerism and production which also affects the focus of scientific research.

As a consequence, from a scientific point of view there is plenty of room and need for the development of new technologies, alternative resources and more effective processes. The reduction of volatile organic compounds (VOCs) has already accelerated the transformation of many classically solvent based processes like coatings into aqueous colloidal systems. This changed focus is also reflected by the release of new scientific journals like Green Chemistry (1999), ChemSusChem (2008) and ACS Sustainable Chemistry and Engineering (2013), which focus on the development of new functional materials from sustainable feedstocks or more sustainable synthesis routes. The use of renewable feedstocks to obtain raw-materials which can be subsequently used for the production of fine chemicals as a substitution to the classical petro chemistry is one way to address the problem. Within the last years, much work has been done to synthesize functional monomers and to apply them in traditional processes. By doing this, many challenges need to be accomplished since a one on one exchange is seldomly possible, especially in highly optimized processes. The logical consequence would be to invest in a reformation of the processes as well.

Therefore, another approach is the investigation of more efficient ways to use the resources at hand. Many examples show that with the help of catalysis milder, more efficient synthesis routes can be used to obtain materials of similar function and also to decrease the amount of resources used or maybe even to reuse some of the byproducts to create additional value. The objective is always the introduction of new functions to any material to create value and new properties.

Two questions arise from that: How much function is actually needed? To go even further- is function really needed at all times? The more heterogenic a product becomes, the greater the possibility to add functions. Especially in colloid science, the options are manifold, since organic, inorganic or hybrid materials can be used to obtain composite materials. Function can be introduced into colloids either by molecular composition or by the morphology of the colloid itself. In many cases, only the interface of a colloid needs to be functional, which allows a more efficient way of using functionality and results in a huge reduction of resources needed.

The question as to when function is needed is closely linked to the investigation of latency in colloidal state. In this thesis, latency was selectively introduced to deactivate reactivity without altering the molecular structure of the reactive species. Encapsulation of active materials like catalysts or drugs in polymer nanocapsules are one of the most commonly used approaches, mainly to protect the active materials, to facilitate their transport and to control their release. The size reduction to the nanometer range of the capsules allows them to be readily used for drug release, to be applied in thin coatings or used for infusion processes. By introducing a responsive polymer shell, for example a catalyst can be switched active by a stimuli selective release. Compatibility is another important factor, especially for the preparation of thermosets or composite materials. In many cases, not only the size but also the presence of a polymer shell as a barrier system decreases the compatibility or negatively influences the overall mechanical properties. Instead, the use of functional surfactants aiming at a surface deactivation instead of a dense encapsulation were investigated for the stabilization of reactive emulsions. A third example, where latency is needed are self-healing materials, where reactivity is preserved in a dormant state for as long as a material or a coating is intact.

This thesis is subdivided into five main chapters. Firstly, the overall motivation for this thesis is expressed, followed by the theoretical part summarizing relevant physico-chemical and chemical aspects needed for the transformation of the comprehensive ideas into experimental practice. The third chapter emphasized the general working-principle and setup for the most important analytical tools used throughout this work. The experimental results are presented and critically discussed in the fourth chapter and are subdivided into three major projects, each addressing latency in colloidal systems from a different point of view. The experimental details on these findings can be found in the last chapter.

2 Theoretical Background

In the theoretical part, colloidal properties and their stabilization including the underlying physical processes are discussed. The preparation of reactive surfactants, nanoparticles and -capsules, as well as fundamentals on polyaddition reactions for the preparation of thermosets are summarized. This work mainly focusses on epoxy-amine systems, especially with regard to latent reactions.

2.1 Colloidal Systems

Colloids are heterogeneous systems consisting of one material which is entitled disperse phase and is ideally not soluble and homogeneously distributed in another material which is called continuous phase. Graham coined the name colloid in the 1870's and defined them by "their inability to pass through a fine membrane".² Hence, the term colloid was always size-dependent. Later, it was linked to sizes from a few micrometers down to a few nanometers. Many colloids are in the size range of the wavelength of visible light, thus causing scattering and making them appear opaque. They are classified depending on the physical state of both phases and are summarized in Table 1.³ Main characteristics for all colloids include their large interfacial area which allows tunability over a wide range of properties and interactions.

Table 1. Summary of common heterophase systems and their composition.

Name	Continuous Phase	Disperse Phase
Mixture/Alloy	solid	solid
Gel	solid	liquid
Solid foam	solid	gaseous
Dispersion	liquid	solid
Emulsion	liquid	liquid
Foam	liquid	gaseous
Solid Aerosol	gaseous	solid
Liquid Aerosol	gaseous	liquid

2.1.1 Emulsions

Emulsions are in a metastable state and consist of two immiscible fluids with the dispersed phase being homogeneously distributed in the continuous phase in the form of droplets. Typically, emulsions are kinetically stabilized by surfactants which will be further explained in 2.2. They are classified as oil-in-water (o/w) or water-in-oil (w/o) emulsions. Depending on their size, preparation and (thermodynamic) stability macro-, mini- and microemulsions can be

distinguished.⁴ A macroemulsion is prepared by weak forces like shaking and the resulting droplets sizes and size distribution is large (1-90 μm). Macroemulsions are thermodynamically unstable and they will phase separate over time.² Microemulsions in contrast, are spontaneously formed, thermodynamically stable isotropic and in many cases consist of clear mixtures with droplet sizes of 5-50 nm.⁵ The surfactant concentration is usually high and exceeds the critical micelle concentration (chapter 2.2), so in many cases free micelles are present. In addition, for microemulsions a co-surfactant, mostly a short-chained alcohol which further reduces the surface tension but does not form micelles itself is needed.⁶ Miniemulsions in contrast are kinetically stabilized against collision and diffusion. The term was first announced by Chou et al.⁷ They are 30 – 500 nm in size and exhibit narrow size distributions. Miniemulsions are prepared by high shear forces for example via ultrasonication or high pressure homogenization. The amount of surfactant is low and usually no free micelles are present and the droplet-water interface is not fully covered with surfactant.⁸

2.1.2 Stability

For the successful stabilization of miniemulsions, two destabilization mechanisms, droplet fusion and molecular exchange by diffusion through the continuous phase need to be overcome as illustrated in Figure 1.⁹

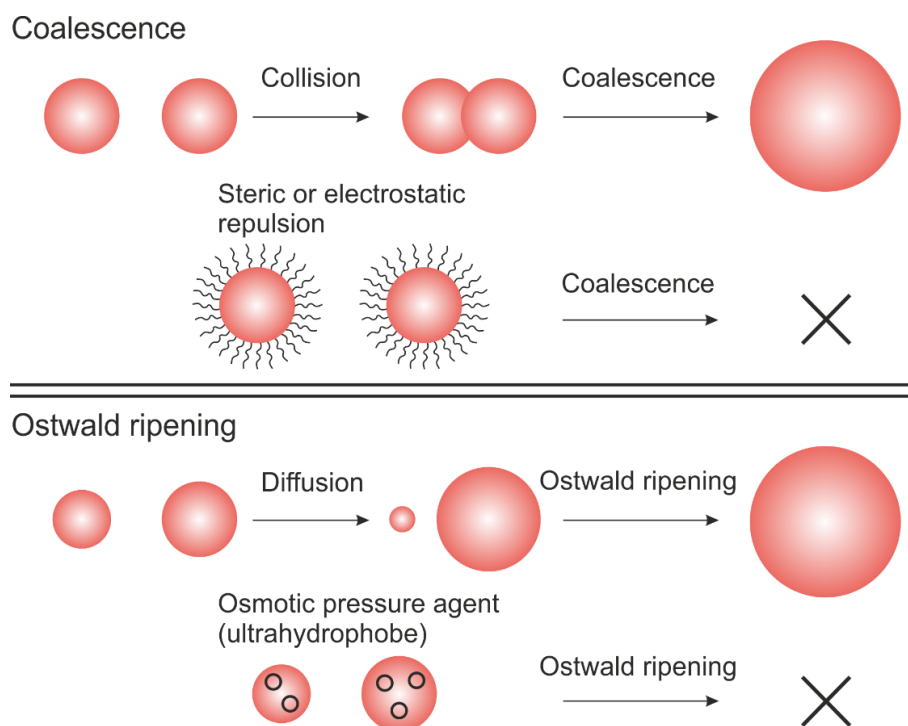


Figure 1. Mechanism of coalescence (upper part) and Ostwald ripening (lower part) which destabilize emulsions and strategies to suppress them by the addition of surfactants to prevent coalescence and osmotic pressure agents to suppress Ostwald ripening.

The former is explained by looking into the interaction energy of two approaching particles in dispersion as described in the DLVO-theory by Derjaguin, Landau, Verwey and Overbeck as a function of their distance and is firstly described for electrostatic stabilization. In their theory, the attractive and repulsive forces of approaching charged particles are correlated. The potential curve in Figure 2 on the left side is composed of electrostatic double-layer repulsion, Van der Waals attraction and Born repulsion. If the particle-particle distance is ∞ , the colloids do not interact with each other. As they approach each other, they start to interact and the attractive and repulsive forces increase. As long as the Van der Waals attraction is weaker than the electrostatic repulsion, the system is colloidally stable. At a certain distance, a local flat secondary minimum may lead to reversible flocculation of the particles. Further approach leads to irreversible particle-particle aggregation once the potential barrier is overcome. The height of this barrier is dependent on the surface charge of the particles and the ionic strength of the continuous phase. Low charge densities in combination with high ionic strengths decrease this barrier, since this reduces the thickness of the Debye length of the electric double-layer, whereas the Van der Waals forces are nearly independent on the salt concentration.

In the case of steric stabilization as shown in Figure 2 on the right side, repulsive forces are generated by I) entropy loss once the polymer chains approach each other since this would decrease their segment flexibility and rotational freedom and II) an osmotic pressure increase. The overlapping polymer chains displace the surrounding solvent molecules. For the counterbalancing of this pressure difference, solvent molecules diffuse into these areas which causes a separation of the particles.

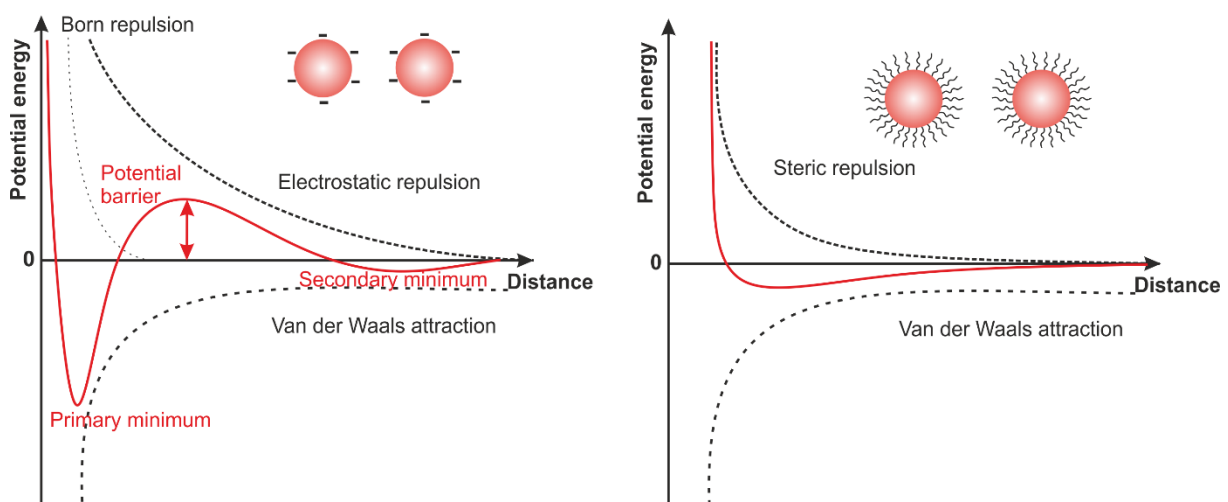


Figure 2. Potential curve of two approaching, electrostatically (left) and sterically (right) stabilized particles as a function of distance.

According to the DLVO-theory, if two particles that are not sufficiently stabilized by surfactants get in contact, they will coalesce. The choice of surfactant can significantly reduce this destabilization mechanism and will be further explained in chapter 2.2. Another possibility is to change the diffusion coefficient of the dispersed phase for example by increasing the viscosity of the continuous phase or by the addition of dissolved polymers.¹⁰⁻¹²

The second destabilization mechanism of a miniemulsion is called Ostwald ripening as shown in Figure 1 (lower part).¹³ Due to polydispersity in droplet size, bigger droplets are formed over time at the expense of smaller ones.¹⁴⁻¹⁶ The diffusion is caused by differences in Laplace pressure ($P_{Laplace}$, equation 1), which is dependent on the surface tension (γ_{ij}) between the continuous and dispersed phase, as well as on the hydrodynamic diameter (D) of the droplets:¹⁷

$$P_{Laplace} = \frac{4\gamma_{ij}}{D} \quad 1$$

As a consequence, diffusion from smaller droplets to bigger ones decreases the Laplace pressure and leads to a phase separation over time. To suppress this, the Laplace pressure needs to be counterbalanced which can be achieved by the addition of an osmotic pressure agent (ultrahydrophobe). It is homogeneously distributed in the dispersed phase and expresses the lowest solubility in the continuous phase.¹⁸ Equation 2 describes the built up of an osmotic pressure ($\Pi_{osmotic}$) inside the droplets which increases until it equals the Laplace pressure:

$$\Pi_{osmotic} = \frac{cRT}{M} \quad 2$$

With: c = concentration of ultrahydrophobe, R = universal gas constant, T = Temperature, M = Molecular weight.

Very recently, a third destabilization mechanism was investigated by Roger et al. which they called contact ripening.¹⁹ It was noticed by the authors that emulsions, which were effectively stabilized against both coalescence and Ostwald ripening were destabilized quickly which led them to the assumption that molecular exchange at the droplet interfaces was possible which they could prove by neutron scattering experiments of a model system. In this mechanism molecular exchange is possible by two approaching droplets without irreversible coalescence but rather upon reversible contact.

2.2 Surfactants

The formation of small droplets in water as a continuous phase leads to an increased droplet-water interface which is thermodynamically unfavorable and needs to be stabilized by surfactants. Surfactants are defined as amphiphilic molecules which consist of a water and an oil soluble part.²⁰ They are able to significantly reduce the surface tension and to form micelles after a certain characteristic threshold concentration (critical micelle concentration, CMC) is exceeded. At this point, the interface is fully covered by surfactant molecules and further increase in surfactant concentration does not decrease the surface tension further. Micelles are formed due to entropic reasons, since the formation of aggregates leads to a decreased number of molecules needed for the solvation of individual surfactant molecules. In colloidal systems, their adsorption at the newly formed interface can, besides stabilizing the additional surface area, significantly alter the morphology, solubilization behavior and properties of the colloid. Surfactants can be classified by their hydrophilic-lipophilic-balance (HLB), a concept which was first introduced by Griffin and further modified by Davies according to:^{21, 22}

$$\text{HLB} = 7 + \Sigma \text{hydrophilic increments} + \Sigma \text{hydrophobic increments} \quad 3$$

Table 2 summarizes the general applications of surfactants according to their HLB values.²³ For the purpose of this work, surfactants for o/w miniemulsions were synthesized, so the necessary condition for their HLB is to be between 7- 18 as calculated in chapter 4.2.3.2.

Table 2. Applications of surfactants and classification according to their HLB value.

HLB	Application
1.5-3	Anti-foaming agent
3-8	Water-in-oil emulsifier
7-9	Wetting agent
8-16	Oil-in-water emulsifier
13-15	Detergents
15-18	Solubilizing agent

Surfactants can either be further divided by their molecular weight into low molecular weight stabilizers or macromolecular stabilizers. Another possibility is to categorize them by their stabilization mechanism which can be via electrostatic repulsion for ionic surfactants or via steric hindrance for non-ionic surfactants.

Ionic surfactants like sodium-dodecylsulfate (SDS), which was used in chapter 4.1.2 for the preparation of nanocapsules stabilize the colloids by the formation of a negatively charged interface which forms a diffuse double layer. The particles are stabilized due to coulomb repulsion as explained in the previous chapter on emulsion stability in chapter 2.1.2.

2.2.1 Non-Ionic Surfactants

In most cases, nonionic surfactants are macromolecular stabilizers, of which the majority are formed by diblock copolymers. Charged polyelectrolytes are also used for colloid stabilization but throughout the course of this work macromolecular surfactants are understood as nonionic oligomers/polymers. They are capable of stabilizing both aqueous as well as organic continuous phases. The necessary condition is, that the hydrophilic segment is long enough and easily dissolved in the continuous phase. Otherwise, the chains entangle which may lead to coalescence. Macromolecular surfactants display certain differences in adsorption behavior compared to ionic low molecular weight stabilizers. For example, they are able to self-assemble into micellar structures of different morphology already at very dilute conditions.²⁴ Also, they are not sensitive to changes in ionic strength as are ionic stabilizers. It was furthermore shown, that they diffuse slower and that the adsorption is kinetically irreversible which generally leads to denser adsorption layers at the interface of the stabilized colloids. Therefore, they exhibit slower exchange rates with their surrounding medium.²⁵ In terms of suppressing the diffusion and mass transfer through the aqueous phase, for example as intended for the amine miniemulsion in this work, these properties are highly desired as further stated in chapter 4.2.3 and 4.2.4.

2.2.2 Functional Surfactants

Parts of this chapter are based on a review summarizing the current literature on functional surfactants for the stabilization of colloids (to be submitted). Most commonly, functions are added to colloids by functional monomers. The route to add functionality via stabilizers is less exploited but can be a promising alternative, since the functionality is directly added at the interface where it is usually needed.

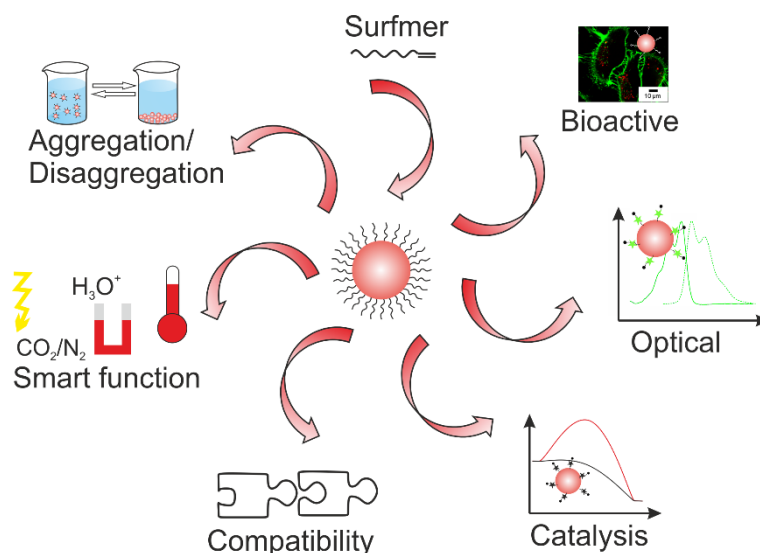


Figure 3. Summary of functions which can be added to surfactants.

The term functional surfactant is used for stabilizers having additional functional groups included in their molecular structure. In the simplest case, the stabilizer contains a reactive group, which covalently bonds to the colloid during their preparation which is called surfmer (surf-actant + mono-mer). Surfmers based on vinyl double bonds are already well-known for the emulsion polymerization of acrylates.^{26, 27} The polymerization mechanism will be discussed in more detail in the next chapter (2.3). In order to maintain the stability during the course of the polymerization, the reactivity of the double bond had to be decreased to avoid the burying of surfactant under the latex.^{28, 29} The covalent attachment of the surfactant to the colloids provides several advantages, like an increased stability, as well as reduced water uptake in films due to decreased migration.³⁰ Surfmers have been frequently used for miniemulsion polymerizations.³¹⁻³⁵ Furthermore, the surfactant can increase the compatibility in films (chapter 2.5) or in composite materials.^{36, 37} The film formation of polymer lattices can be improved by the use of polymeric surfactants which can actively participate in the cross-linking upon film formation. They can also act as a mediator between incompatible phases which usually results in better mechanical properties of composite materials or might even result in new properties. An increased compatibility was achieved by the use of two ammonium-based

cardanol (chapter 2.4.1) surfactants for the incorporation of clays into thermosetting epoxide matrices by the incorporation of OH and NH₂-groups as cross-linking junctions.^{38, 39} However, all surfmers have in common that they are no longer functional after the polymerization is completed. Beyond that, stimuli responsive surfactants have been widely under investigation, where the properties inherited by the surfactant are transferred to the colloids.⁴⁰ This is a very elegant way to perform a, in many cases reversible, aggregation and disaggregation of colloids in a controlled way by using triggers like pH⁴¹⁻⁵², temperature^{53, 54} or CO₂/N₂.⁵⁵⁻⁶³ Even magnetic^{64, 65} or light^{66, 67} responsive surfactants have been prepared for these purposes. The pH response is generated by protonation induced change in solubility or swelling behavior of macromolecular surfactants mostly by the incorporation of dialkylamino ethyl methacrylates or (meth)acrylic acid. Applications exceeding a sole (de)stabilization are sensors or drug delivery and release.⁶⁸⁻⁷¹ By the introduction of a thiopropionate linker, cleavable, acid labile micellar aggregates made by these surfactant could even be disassembled.^{72, 73} Macromolecular surfactants displaying a preferably low lower critical solution temperature (LCST) can be used to create thermoresponsiveness. This allows for example the controlled desorption of the surfactant from the interface for purification processes.⁷⁴ In another example, thermoresponsive surfactants could be used to make nanoparticles adhesive by heating above their LCST.⁷⁵ Many surfactants function as carrier systems for biomedical applications like wound dressings or drug release. Light responsiveness is an attractive trigger within this field because radiation can be applied with high precision, tunable wavelength and intensity. The irradiation leads to photoisomerization or even the cleavage of bonds which then leads to a change in stabilizing properties. One example of note switched amphiphilicity and allowed the transformation of polylactic acid nanoparticles from an organic solvent based environment to an aqueous one.⁷⁶ Within this field, biocompatibility or degradability is often required which can be achieved by the use of for example polysaccharide or amino acid based surfactants.^{25, 77-80} A function which has already proven useful especially for the investigation of colloids and their interactions with surfaces or their cellular uptake is the incorporation of fluorescent moieties into the surfactant.⁸¹⁻⁸³ This renders additional labelling of particles redundant and if surfmers are used, also prevents leakage of free dye into the environment.

In general, functional surfactants can be a good alternative to a functionalization of the entire colloid to obtain responsive materials. Furthermore, as will be discussed in chapter 2.6.2 and 4.2.3 such stabilizers can be applied in systems where it is mandatory to preserve reactivity and the common encapsulation techniques cannot be used.

2.3 Preparation of Nanoparticles by (Mini)Emulsion Polymerization

Usually, emulsion droplets are only an intermediate state to prepare polymer dispersions. Throughout this chapter, polymerization methods for the preparation of (functional) nanoparticles and capsules are discussed. Chain-growth or a step-growth mechanisms are discussed in this respect.

2.3.1 Chain-Growth Polymerization in (Mini)Emulsions

Free radical emulsion polymerization is the most abundant type within the former and can be carried out as heterophase polymerization method for the preparation of functional particles, besides suspension- or microemulsion polymerization.⁴ In a classical emulsion polymerization, the chain growth proceeds by monomer addition at the chain ends in a three stage process. During the I) initiation, the rate of polymerization increases fast and remains constant during the II) propagation stage and decreases, as the reaction is terminated in stage III).⁸⁴ There are three possible pathways for the initiation in emulsion polymerization: I) in monomer-swollen micelles, II) in the aqueous phase, followed by diffusion or precipitation of the growing oligomers or III) in the monomer droplet itself.⁸⁵ In a classical emulsion, the probability for the third scenario is rather low. In miniemulsion polymerization in contrast, it becomes the dominant mechanism. Ugelstad et al. were the first to describe the initiation in sufficiently small (0.7 μm) styrene monomer droplets in the presence of an emulsifier and a fatty-alcohol as co-stabilizer.⁸⁶ In an ideal miniemulsion, the particles have the same identity before and after polymerization and can therefore be regarded as a one to one copy with each droplet being a nano-reactor.⁸⁷

A typical protocol for a miniemulsion polymerization is shown in Figure 4. A macroscopic emulsion is obtained by mixing the organic phase, which contains the monomers and the ultrahydrophobe (often hexadecane), with an aqueous surfactant solution. Nanosized droplets with narrow size distributions are generated by high shear forces, like ultrasound or high pressure homogenization.⁸⁸ In the case of free radical polymerization, the temperature is increased and an oil or water soluble initiator is added to start the polymerization.

Whereas emulsion polymerization is mostly limited to free radical polymerization, a much broader range including step-growth polymerizations (chapter 2.3.2), ionic or catalytic polymerizations can be carried out in miniemulsions.⁸⁹

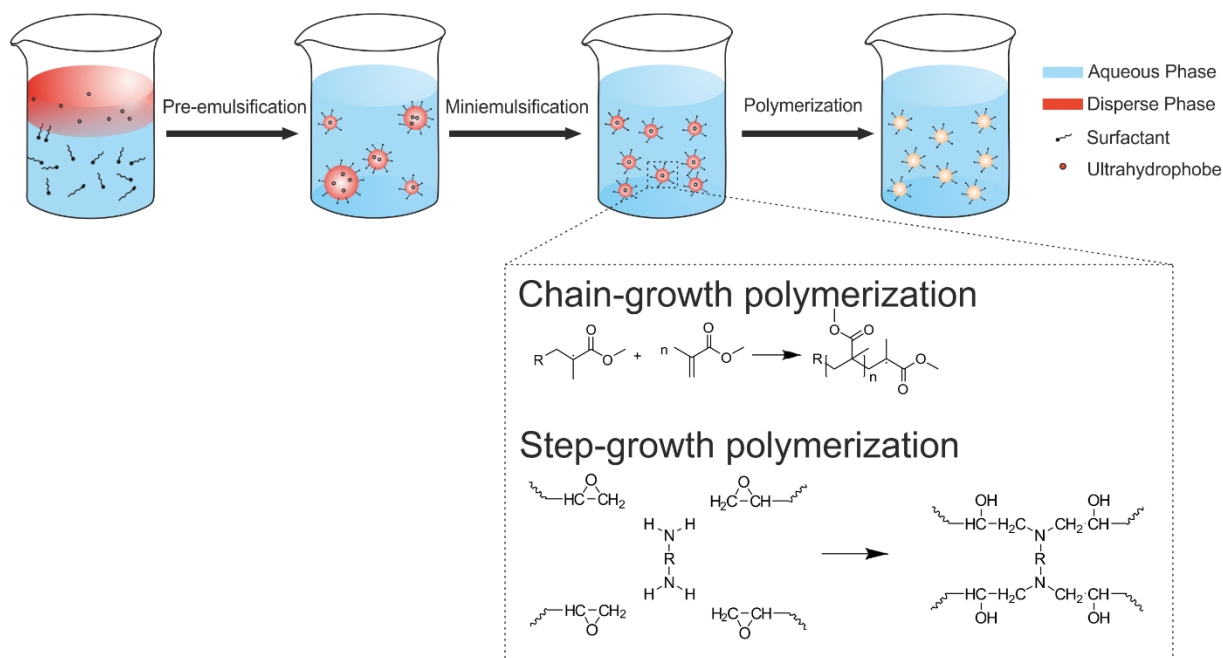


Figure 4. Schematic principle of miniemulsion polymerization involving a pre-emulsification step prior to miniemulsification by high shear forces. Subsequently, polymerization can be carried out via chain-growth or via step-growth mechanism as exemplarily shown to generate polymer dispersions of various compositions.

Additionally, the miniemulsion polymerization can be used for the preparation of nanocapsules. In this work, they are prepared by a polymerization-induced phase separation (chapter 4.1), however nanocapsules can also be prepared via interfacial polymerizations or by solvent evaporation from miniemulsion droplets.⁹⁰⁻⁹² For a polymerization-induced phase separation, the hydrophobic oil, which later forms the capsule core, needs to be miscible with the shell-forming monomers. Upon polymerization, the formed polymer becomes insoluble, thus leading to a phase separation and the evolvement of a core-shell morphology, if the following requirements are met:

Torza and Mason developed a model which allowed the prediction of the thermodynamically most stable morphology of two immiscible liquids (1 and 3), dispersed in an aqueous phase (2) by using the spreading coefficient (s_i , equation 4) which is dependent on the interfacial tensions between the three phases:⁹³

$$s_i = \gamma_{ik} - (\gamma_{ij} + \gamma_{ik}) \quad 4$$

With: γ = interfacial tension between the phases i,j,k .

Three possible scenarios arise from this interdependence: If phases 1 and 3 are comparably hydrophilic and their interfacial tensions are high, separate droplets are obtained ($S_1 < 1$, $S_2 > 0$, $S_3 < 0$). Partially engulfed morphologies are obtained, in case phases 1 and 3 are again comparably hydrophilic but display a low interfacial tension ($S_1 < 0$, $S_2 < 0$, $S_3 < 0$). Instead, a core-shell morphology is the result of phase 3 being considerably more hydrophilic than phase 3 and their interfacial tensions being low. This leads to a complete engulfing of phase 1 by phase 3 ($S_1 < 0$, $S_2 < 0$, $S_3 > 0$). From a thermodynamic perspective, the driving force for the resulting morphology are based on the minimization of the Gibbs free energy (ΔG , equation 5), generated by the formation of new interfaces:⁹⁴

$$\Delta G = \sum \gamma_{ij} A_{ij} - \gamma_0 A_0 \quad 5$$

With: A = interfacial area between the phases ij and γ_0 , A_0 = initial interfacial tension and area.

The possibilities to alter the thermodynamic morphology are manifold, for example the interfacial tension is dependent on the nature of surfactants used, on the hydrophobicity, mobility and concentration ratios of the polymer phases, as well as on the temperature. In addition, the phase separation may also be affected by several kinetic factors, for example by the increasing viscosity inside the droplet upon polymerization.⁹⁵

2.3.2 Step-Growth Polymerizations in Miniemulsions

Step-growth polymerizations, like polyadditions or polycondensations are defined by individual, intermolecular reaction steps between monomers that are di- or multifunctional.⁹⁶ Upon polymerization of either $nA-B$ or $nA-A + nB-B$ molecules, firstly di-, tri- and oligomers and finally polymers are formed. Since all reaction products carry the same functionality, there is no loss in reactivity with the proceeding polymerization reaction. So, in principle oligomers can be isolated at any point and there is no termination. In reality however, the reaction may be terminated kinetically due to an increasing viscosity at high conversions. In step-growth polymerizations, high conversions and in A-A B-B systems exact stoichiometries are needed to produce high molecular weight polymers, as expressed by the Carothers equation describing the dependency of the degree of polymerization on the conversion (equation 6). If higher functional monomers are used, cross-linked systems may be obtained:

$$P_n = \frac{1 + r}{1 + r - 2pr} ; \quad r = \frac{N_a}{N_b} \quad 6$$

With: p = conversion, P_n = Degree of polymerization, r = ratio of reactants, N = number of A or B molecules.

Step-growth polymerizations can be carried out in miniemulsion droplets or at the respective droplet interfaces. Compared to free-radical polymerization, the formation of nanoparticles may already proceed at room temperature without the addition of an initiator.⁹⁷ Astonishingly, the formation of nanocapsules in water was also demonstrated by the interfacial polycondensation to form polyurethane and polyuria capsules.⁹² Generally, miniemulsion polymerization allows the generation of a variety of hybrid particles or capsules, which may be organic, inorganic or hybrid materials with applications in biomedical fields, energy related topics, catalysis, coatings or cosmetics.^{89, 98-100}

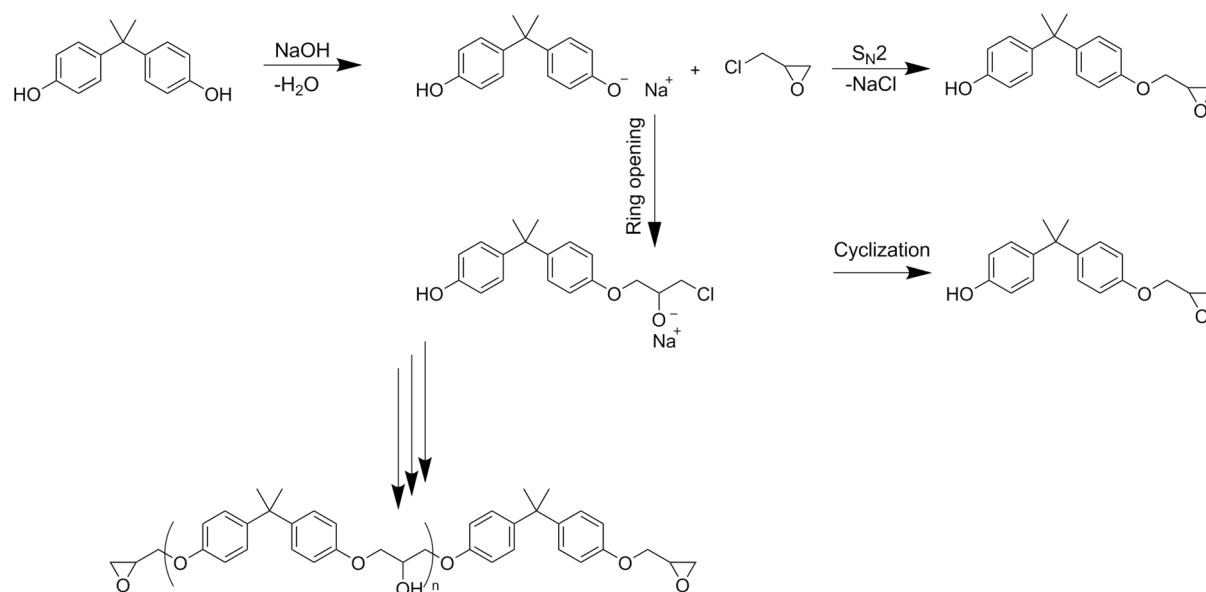
2.4 Thermosetting Polymers

Polymers can be divided into thermosets and thermoplastics according to their processability. Thermoplastic polymers consist of linear or graft, high molecular weight polymer chains which, are associated through intramolecular forces but are not chemically linked. They show a phase change above their glass transition temperature (T_g), which allows their re-processability.¹⁰¹ Chain growth polymerizations predominantly produce thermoplastics. Thermosets in contrast, are according to their IUPAC definition materials consisting of multifunctional monomers, which “change irreversibly into an infusible, insoluble network by curing”⁷³ either by a spontaneous reaction or induced by heat or irradiation. Their properties are strongly dependent on the molecular composition and the density of cross-linking junctions. Thermosets make up about 20% of the overall plastic production.¹⁰² The most prominent materials are epoxide resins, polyurethanes, polyester resins and phenolic resins like bakelite.¹⁰³ Step-growth reactions can be used to prepare thermosets as well as thermoplastics.⁹⁶

2.4.1 Epoxy-Amine Thermosets

Epoxide resins are one of the most important building blocks for thermosetting materials. They consist of monomeric or oligomeric backbones with more than one epoxide group per molecule. Monofunctional resins are also used, but function as reactive dilutents. Resins with aliphatic, cycloaliphatic and aromatic backbones are commercially available. Epoxide resins were first synthesized by Schlack in 1934 by a coupling reaction of bis(4-hydroxyphenylene)-2,2-propane (bisphenol-A) with 1-chloroprene 2-oxide (epichlorhydrine, ECH) to obtain bisphenol-A-diglycidyl ether (BADGE) in aqueous sodium hydroxide solution as shown in Scheme 1.¹⁰⁴ The ECH attacks the active hydrogens of the bisphenol-A, followed by dehydrohalogenation in two competitive mechanisms. The cleavage of the C-Cl bond can either occur via a one-step S_N2 nucleophilic substitution or via a two-step mechanism which proceeds via a ring-opening reaction of the ECH by the phenate group followed, by intramolecular cyclization.¹⁰² Both require the formation of phenate groups with the NaOH, which can reduce the yield and purity of the glycidylized products. Oligomerization takes place by further addition of bisphenol-A. Depending on the stoichiometry and the reaction conditions, the degree of polymerization can be adjusted. The BADGE monomer ($n = 0$) is a crystalline solid and is obtained by using a large excess of epichlorhydrine and thus not of industrial relevance. Already at very low degrees of oligomerization ($n = 0.15-0.5$), liquid resins are obtained, the most relevant being about $n = 0.15$ which was also used in the cause of this work and is further referred to as BADGE.

Theoretical Background

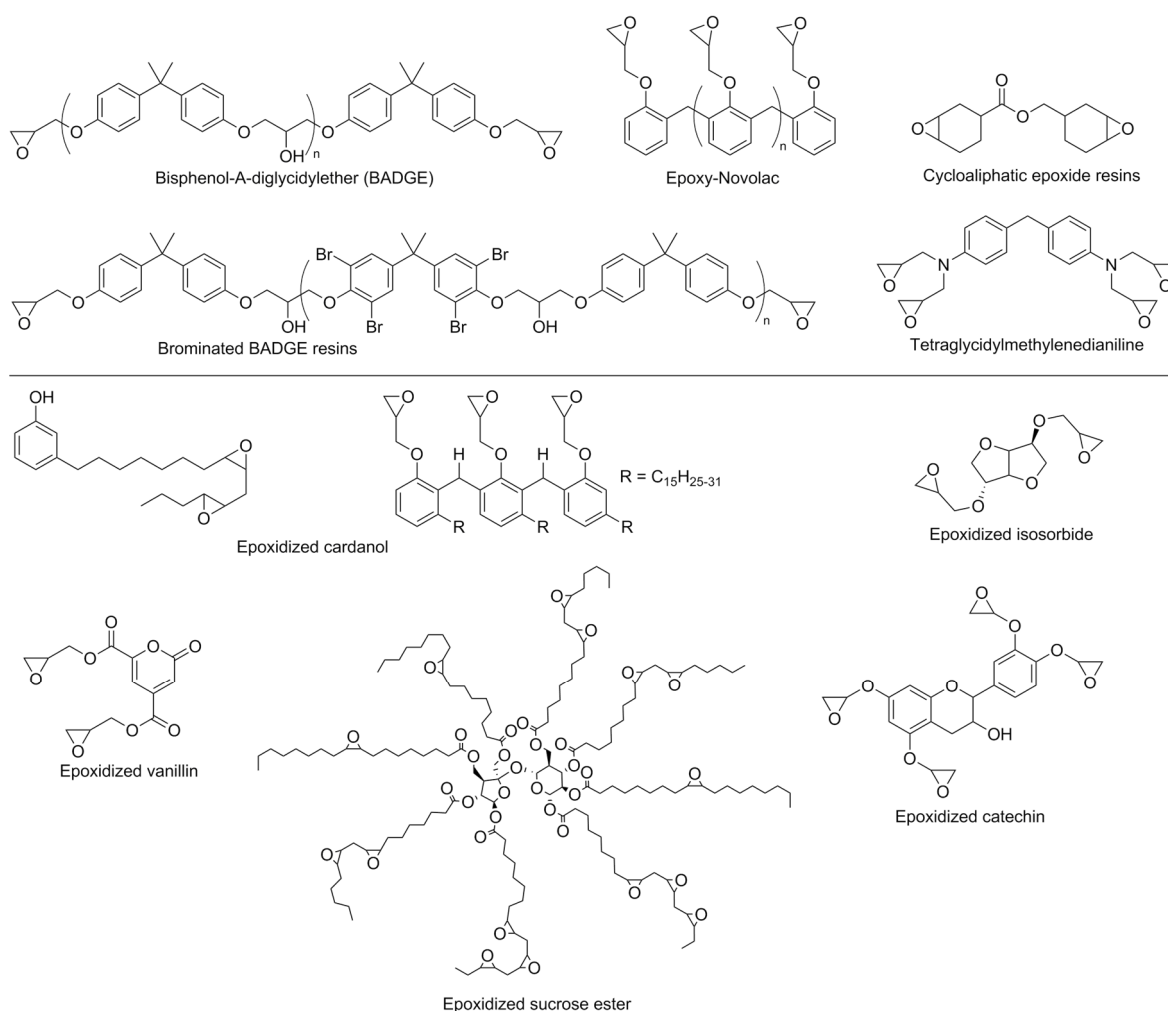


Scheme 1. Glycidylation of bisphenol-A with epichlorohydrin to produce BADGE resins. The degree of oligomerization can be varied by altering the stoichiometries.

The industrial relevance of this building block was not realized until Castan patented the curing reaction of BADGE with phthalic anhydride for dental applications.¹⁰⁵ Commercialization took place in the 1940s with applications ranging from protective coatings, which now make about 50% of the epoxy market, automotive primers, adhesives, semiconductors to composites for aerospace.¹⁰⁶ Still today, about 75% of all epoxy resins are bisphenol-A based. Other industrially relevant resins are phenol-formaldehyde (novolac) based epoxides or brominated resins as flame retardants, cycloaliphatic epoxide resins or reaction products of aromatic amines with ECH (Scheme 2 upper part). Their key properties are high mechanical strength, dimension stability also at high temperatures, as well as high chemical, moisture and corrosion resistance and good thermal, electrical and adhesive properties.¹⁰⁷⁻¹⁰⁹ For BADGE resins, the thermal stability is achieved via the aromatic ring of the bisphenol-A.

To apply coatings from high-viscos or solid epoxy monomers, solvents had to be used. Volatile Organic Compound (VOC) regulations forced a development towards water based epoxide dispersions in the 1960s, which even added value by allowing a direct application, also on wet substrates. Epoxide dispersions were for example used for cathodic deposition in automotive industry and in can coatings.¹⁰⁶ Other concerns regarding the use of epoxy resins refer to the use of bisphenol-A, especially in food contact, since it is known to be reprotoxic and an endocrine disruptor.¹¹⁰ Therefore, new bio-based alternatives are strongly investigated. However, the substitution of BADGE without performance and property loss is a challenge.^{102, 108, 111, 112}

One possible route is the epoxidation of naturally occurring aliphatic double bonds from natural feedstocks, like vegetable oils by the use of hydrogen peroxide as oxidative agent.^{113, 114} Natural (poly)phenols like e.g. tannins, catechine, or cardanol (see Scheme 2 lower part) are under investigation.¹¹⁵⁻¹¹⁸ Sugars, like isosorbide were epoxidized with ECH but show low water resistance.¹⁰² Vanillin was used to produce epoxides as well.¹¹⁹ However, the toxicity of these natural phenols is still unclear in many cases. Also, some products are too flexible to be considered true BADGE alternatives. Anhydride cured thermosets were obtained from epoxidized sucrose esters of fatty acids with high mechanical moduli.¹²⁰ However, those materials need higher temperatures (85 °C) for curing. As a consequence, a lot of industrial and academic research is focused on finding solutions to generate new classes of thermosetting epoxide systems.

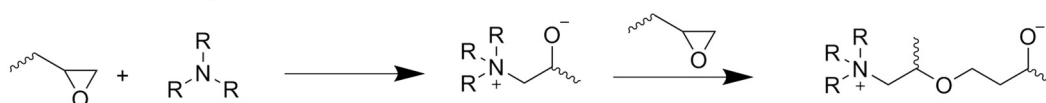


Scheme 2. Industrially relevant epoxide resins (top) and selected bio-based alternatives (bottom).^{102, 106}

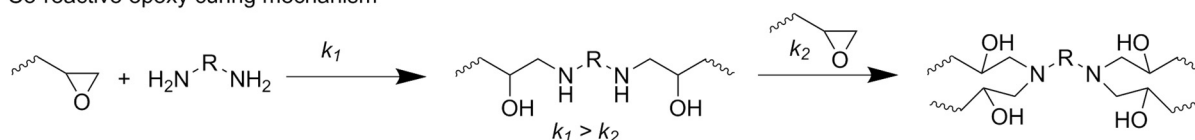
Epoxy resins are typically characterized by their epoxy-equivalent weight (EEW) which represents the amount of resin containing one equivalent of epoxide groups and is calculated by dividing the molar mass of the resin (g mol^{-1}) by the epoxy functionality (g eq.^{-1}). In this work, the EEW was used to calculate the stoichiometric amount of hardener needed which was measured by potentiometric titration with perchloric acid (see chapter 5.2.3.1)

Epoxy resins are reactive towards both nucleophiles and electrophiles and can be homo- or copolymerized. Homopolymerization takes place via catalyzed anionic or cationic mechanisms. Most commonly, Lewis bases like for example tertiary amines are used as demonstrated in Scheme 3. The reaction via a co-reactive mechanism is called curing. Epoxy resins can be cured with a variety of hardeners like amines, amides, anhydrides, thiols, phenols or isocyanates. Lewis or carboxylic acids can be added to accelerate the curing reaction. The choice of curing agent is strongly dependent on the desired properties of the final product. The focus of this work is on epoxy-amine curing. The reactivity within this family is increasing with increasing nucleophilicity from aromatic < cycloaliphatic < aliphatic amines. Upon reaction with primary amines, a secondary amine and a secondary alcohol are formed. The reactivity of the secondary amine is decreased ($k_1 > k_2$) as shown in Scheme 3 and might require higher curing temperatures.^{121, 122} Upon reaction with secondary amines, the cross-linking density of the formed thermoset is increased. The reaction is self-catalyzed by the generated hydroxyl groups due to the formation of a trimolar complex which favors the nucleophilic attack of the amine. If stoichiometric amounts of amine are provided, the reaction between epoxides and the hydroxyl groups themselves is not competitive.¹²³ However, especially in the presence of catalysts, the secondary alcohol can be gradually converted into the corresponding ether.

Catalytic epoxy curing mechanism



Co-reactive epoxy curing mechanism

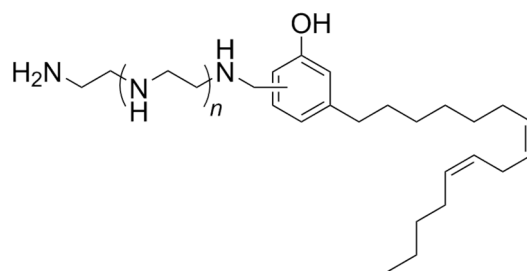


Scheme 3. Catalytic curing of an epoxy resin with a tertiary amine and co-reactive curing reaction of an epoxy resin with a diamine.

Since hardeners are often mixtures and not of high purity, the stoichiometric amount necessary for the epoxy curing is calculated via the amine hydrogen equivalent weight (AHEW [g eq.⁻¹]) which is calculated by the molar mass divided by the number of active amine-hydrogens. For mixtures, it can be determined similar to the EEW by potentiometric titration as described in chapter 5.2.3.1 and can be used to calculate the hardener amount by:

$$M_{amine} = \frac{M_{epoxy} AHEW}{EEW} \quad 7$$

The cross-linking density of the cured thermoset, as well as the curing speed and temperature can be adjusted by the type of hardener and its functionality. In industrial applications, sometimes off-stoichiometric amounts with a slight excess of epoxide (0.85/1) are used to fine tune the mechanical properties. In this work, stoichiometric amounts were used and special focus was on the use of very reactive hardeners which exhibit fast curing already at ambient temperatures. At first, this seems contradictory to the concept of latent systems, but will be further clarified in chapter 2.6.. Another requirement for this work was a high hydrophobicity of the curing agent, to allow its emulsification. Especially phenalkamines proved to be good candidates, as investigated in a previous PhD thesis by Melanie Hagenbucher.¹²⁴ They are synthesized from cardanol, which is gained from the cashew nutshell as renewable feedstock by a Mannich type condensation reaction as shown in Scheme 4 and described in more detail in chapter 4.2.2.1 with interesting structural properties.



Scheme 4. Simplified structure of phenalkamines obtained from cardanol.

2.4.2 Thermosets and Miniemulsion Polymerization

As described in chapter 2.3.2, it is possible to perform step-growth polymerizations in water by the use of the miniemulsion process. Epoxy-amine curing in nanodroplets was shown to be possible by polyaddition in miniemulsion and was first carried out by mixing different epoxide resins with polyamines, thiols and diols to produce very uniform and narrowly distributed thermosetting nanoparticles.⁹⁷ The same was shown later on for polyurethane particles.¹²⁵ Furthermore, they are frequently used for the preparation of micro- or nanocapsules by interfacial reactions at the droplet interfaces.⁹² Usually, the more hydrophobic component, for example the epoxy resin, is dispersed in the aqueous phase. Afterwards, the second component is added through the aqueous phase where it reacts or condenses to form a shell around the droplet core. The advantage of this technique is, that mild conditions can be used in both direct and inverse systems. However, since the formation of a protective shell around a payload needs to be an orthogonal reaction to prevent cross-linking with the payload as well, the choice of core materials is limited.

2.5 Film Formation

In many cases, polymer coatings are applied to surfaces to improve their performance and resistance against environmental impacts or to enhance their aesthetic appearance. Traditionally, they are prepared from organic solutions and film formation takes place upon solvent evaporation. Film formation of polymer dispersions instead is a widely used economically friendly alternative to apply coatings of water insoluble materials to overcome the need of organic solvents.¹²⁶ However, compared to the solvent based approaches, certain drawbacks like inhomogeneities in film thickness and component distribution had to be overcome and were widely improved in the last decades.^{5, 127, 128}

There are different, partially inconsistent theories on the driving forces for film formation, the main being polymer/air surface tension, polymer/water interfacial tension and capillary forces. Brown opposed the main forces preventing a film formation (deformation resistance F_G) to those that support it (surface and interfacial forces, capillary forces F_C , Van-der-Waals forces and gravitational forces).¹²⁹ He found, that for a successful film formation the following requirement: $F_C > F_G$ needs to be met.

Generally, film formation of dispersions takes place upon water evaporation and can be described as a four stage process: I) evaporation of water, II) ordering of latex particles, III) contact and deformation of particles and IV) coalescence and polymer chain interdiffusion as illustrated in Figure 5.¹³⁰ I) In the first stage, water evaporates at a constant rate of about 85% compared to pure water and is accompanied with a strong increase in viscosity. Usually, the stabilized particles are not in contact until a concentration of about 50 wt.% is exceeded. II) As the viscosity increase proceeds, the water evaporation rate is reduced. Attractive capillary forces (F_C) increase as the particles approach each other. The particles arrange themselves into agglomerates and continuously into a more ordered state, until ideally a cubic-closed packed state is reached. The process is strongly dependent on the nature of the dispersion and its stabilization. III) The particles are further deformed to dodecahedrons into a state of irreversible agglomeration. IV) In the final stage, particle coalescence takes place and the interdiffusion of polymer chains becomes the rate limiting factor in the film formation process. These rates are dependent on their molecular weight as well as on the type of surfactant used for the stabilization of the colloids. At this stage, also cohesive and adhesive interactions with the substrate take place. The final mechanical strength of a film is reached, once the polymer chains are diffused approximately half their gyration length.¹³¹

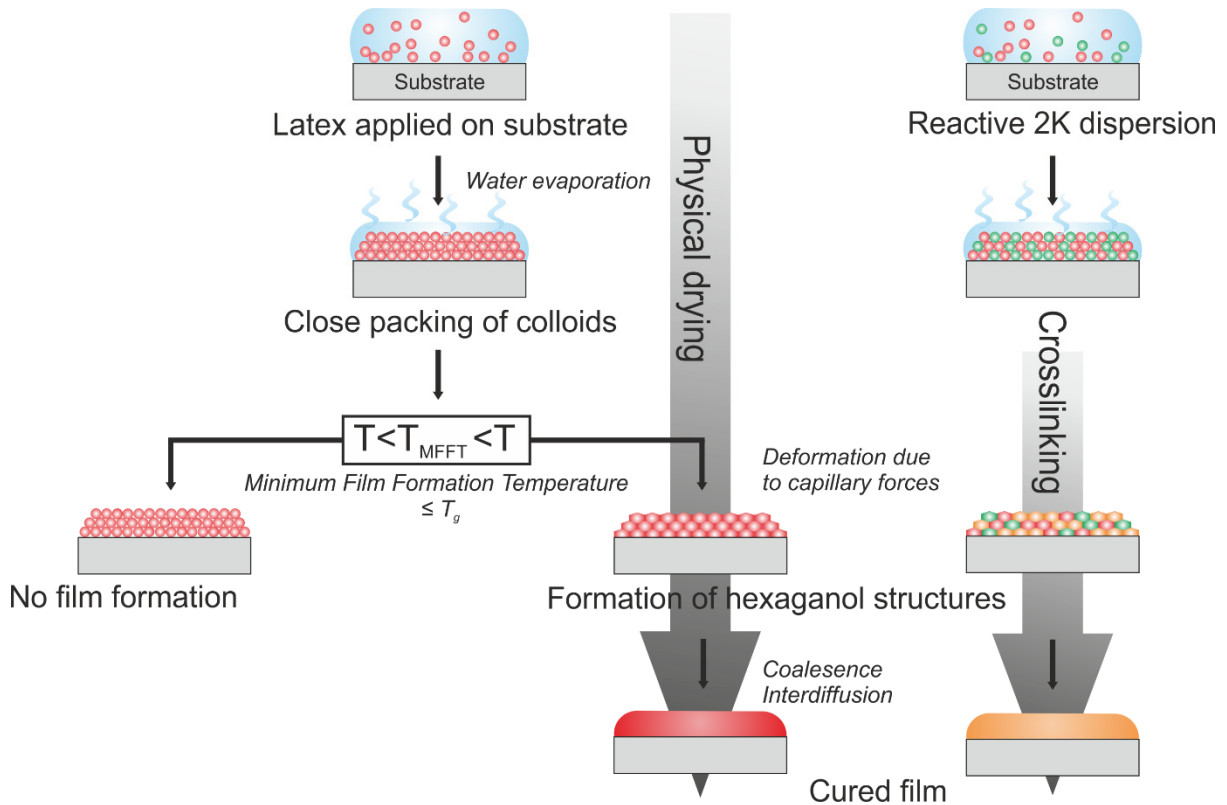


Figure 5. Film Formation Principle of a nonreactive latex (left). Stage I: water evaporation, II ordering of particles. Below MFFT: no film formation takes place whereas above MFFT film formation proceeds: Stage III: particle contact and deformation and IV: coalescence and interdiffusion. Film formation for reactive 2K dispersions (right) additionally involves cross-linking reactions.

A coherent film is only formed, if a certain movement is possible across the particle interfaces, which is expressed by the minimum film formation temperature (MFFT). Above MFFT, an optically clear film is obtained. In contrast, if the drying temperature is lower than the MFFT, the polymer chains are in a glassy state and a turbid film with cracks is obtained. The MFFT is usually lower than the T_g of the latex because the residual water content from the former continuous phase and the surfactants have plasticizing effects. The MFFT is measured by applying a temperature gradient and was used to roughly estimate the degree of premature reaction in the P1K system in chapter 4.2.4.

Whereas stage I-II are purely physical processes, the particle deformation in stage III can be accompanied by chemical cross-linking between reactive compartments, as shown on the right side of Figure 5. Examples are polyurethane dispersions or epoxy-amine systems. In this case, the degree of cross-linking additionally defines the rate limiting factor in the film formation of the system. A complete interdiffusion in dense polymer networks can usually not be realized.

It was shown for some systems that the hexagonal geometry was preserved after curing, because the cross-linking at the former droplet interfaces inhibits further diffusion which, as a consequence, decreases the mechanical performance and strength of the material.¹³² These issues can be overcome by thermal or chemical post-curing the films. Furthermore, it was shown that, especially low molecular weight surfactants tend to form cavities or migrate within the network which favors water uptake and thus reduces the anti-corrosion performance of the coating.¹²⁶ The use of macromolecular surfactants or surfmers like those described in chapter 4.2.3 are possible candidates to overcome this issue.

2.6 Reaction Latency in Colloidal Systems

“Causality is the relation between an event (the cause) and a second event (the effect) where the first event is understood to be responsible for the second.”¹³³

“Latency is the time interval between the stimulus (the cause) and the response (the effect)”. So, latency can be regarded as “the condition of being temporarily inactive”.¹³⁴

In many cases, latency is regarded a “waste of time”, however the ability of controlling the time when a response actually takes place can be very helpful in many fields. In material science, there are many different approaches to achieve latency which may be approached either chemically by the introduction of functional groups being temporarily inactive or physically by spatial separation or phase transitions.

2.6.1 Latent Catalysis

At first, it seems contradictory to discuss latency in connection with catalysis, since the purpose of a catalyst is to accelerate a reaction rather than to retard it. However, in biological systems, enzymatically catalyzed processes and reactions can be precisely regulated.¹³⁵ The idea to switch the activity of a catalyst from an inactive to an active state at will, has already gained much interest, especially in the field of homogeneous catalysis.¹³⁶⁻¹³⁸ Latent homogenous catalysts mainly function by the dissociation of ligands, which makes them more active compared to the complexed and more stable state. The off/on switch of reactivity can be triggered by various stimuli like light, pH, temperature, supramolecular interactions or mechanical forces.^{136, 139, 140} In principle, the use of precisely switchable catalytic activity makes it possible to carry out several reactions in one pot.^{136, 137}

Especially the concept of a thermolatent catalysis has gained interest in applied research.^{141, 142} For many applications, it is desired to apply a film or coating at elevated temperatures to lower the viscosity and thereby ensure the processability of the raw materials. Increased open-times are especially needed in infusion processes, where the raw materials are pumped into molds and a complete filling of the molds needs to be ensured before the curing is initiated. At the same time, the actual curing time is supposed to be as short as possible, which means the system is preferably catalyzed immediately after the mold is filled. So the ideal thermolatent catalyst would be completely inactive with a sudden tunable “on-switch” temperature. In homogenous catalysis, the on-switch often involves complex synthesis of suitable ligands which also has the drawback of the necessary registration of new chemicals and labelling issues when those systems shall be used commercially.

In colloidal systems, these properties can be more easily achieved than from a molecular oriented point of view. Instead of altering the molecular structure of the catalyst itself, a polymer serves as responsive barrier which protects and prevents premature catalysis. Encapsulation and release enables great varieties with regard to the barrier properties and the triggers applied. This colloidal approach was used for the preparation of thermolatent catalytic nanocapsules in chapter 4.1.

2.6.2 Latency Triggered by Film Formation

The idea of what is called a *pseudo-one-component* (P1K)-system throughout this work, is to further transfer the concept latency in colloidal state towards the coexistence of two reactive colloids, which are stable and separate for as long as they are in dispersion as illustrated in Figure 6. For coating or adhesive applications, such a system would be highly beneficial, since it combines the reactivity of a classical two component system and at the same time can be applied similar to a one component system. In 2K adhesives, both components immediately react upon contact. As a consequence, they need to be kept separate upon storage and a mixing step is necessary, immediately before their application on for example a substrate. One component systems in contrast display a decreased or latent reactivity which requires energy input by for example heat or UV-radiation to initiate the curing reaction. The P1K-system combines these two benefits. The key features of a miniemulsion, as well as the use of functional surfactants are used to allow a coexistence of A&E type colloids, which are separated by the continuous phase as demonstrated in chapters 4.2.3 and 4.2.4. After the P1K-dispersion is applied on substrate, the solvent evaporates and the colloid identity is not preserved any further, the two components start to crosslink and form a continuous film as described in chapter 2.5.

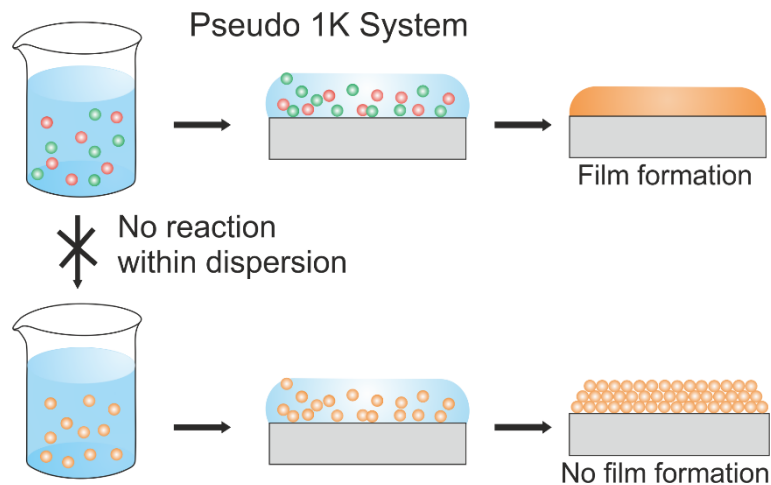


Figure 6. Schematic principle of the P1K-concept with reactive A&E-type colloids present in the P1K-dispersion. Premature reaction needs to be suppressed in order enable homogeneous film formation.

2.6.3 Latency in Self-Healing Films

Self-healing polymers are a class of materials being able to autonomously respond if damage is applied to them, which allows for an increased lifespan. The physical energy caused by the damage is transferred into a chemical or physical response, which heals the material by recovering its initial properties or shape.¹⁴³ The triggers which cause the material damage are in most cases mechanical rupture or crack formation, as well as temperature or corrosion induced events. Successful examples of self-healing are found in living matter like tissue, which can be regenerated to restore the initial properties instead of a replacement. The applied damage induces the formation of a new interface, where the self-healing needs to take place. This often requires physical processes, like for example diffusion or swelling, mostly accompanied by a chemical reaction like covalent cross-linking or supramolecular assembly. It can also be a physical process by for instance, temperature induced chain entanglement.¹⁴⁴ So, regarding the importance of latency for self-healing events, both concepts are inseparately tied to each other.

The self-healing event can be either intrinsic as shown in Figure 7 I, which means the material itself inherently contains the ability to heal. Healing can also occur extrinsic, for example by the introduction of self-healing agents as shown in Figure 7 II. In intrinsic self-healing, multiple healing events are usually possible.¹⁴⁵

Extrinsic self-healing can be further subdivided into capsular or vascular systems, the former usually being a one-time healing event, whereas a vascular network structure which is integrated as interconnected network may be refilled several times. Toohey et al. developed a microvascular system for multiple healing, which contained an epoxide resin and amine hardener.¹⁴⁶

The capsule based approach was first presented by White et al.¹⁴⁷ The published system contained a Grubb's catalyst, homogeneously distributed in a cured epoxy matrix and dicyclopentadiene filled microcapsules which were ruptured and subsequently polymerized with a healing efficiency of about 60% virgin fracture load, measured by fracture tests. Other prominent healing-reactions are Diels-Alder, thiol or click reactions, polyurethane or epoxy curing, Michael additions or metathesis reactions.¹⁴³

The use of thermosetting materials for the self-healing reaction allows the generation of highly crosslinked networks, which enables a good recovery of the initial properties. Blaszik et al. further categorized the capsular approach by systems which contain a) one encapsulated healing-agent and a homogeneously distributed catalyst in the matrix, b) one encapsulated healing agent and a second healing agent which is phase separated in the matrix, c) one encapsulated healing-agent and a latent reactant dispersed in the matrix or d) encapsulation of two reactive healing agents in individual capsules (Figure 7).¹⁴⁸ The last method was only recently realized for an epoxy-amine system because the encapsulation of the traditional amine curing agents was found to be challenging.¹⁴⁹

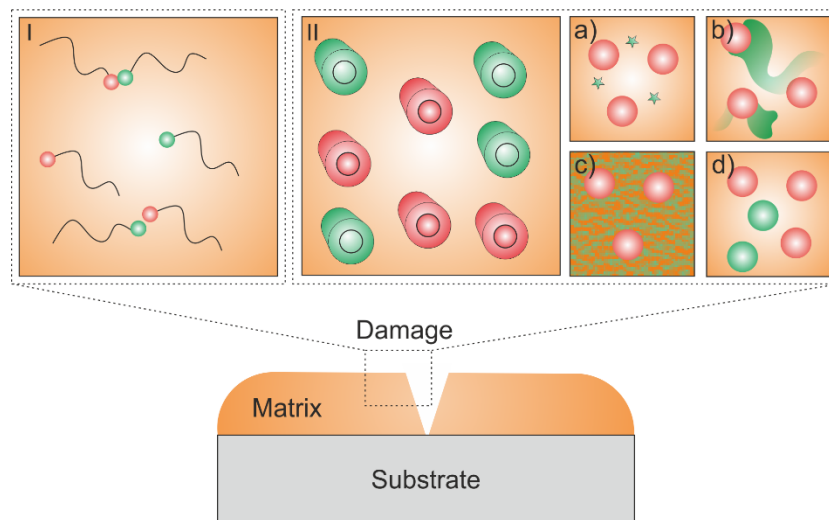


Figure 7. Self-healing principle. I) intrinsic self-healing, with the material itself inherently containing the ability to heal II) extrinsic self-healing, by the introduction of healing-agents. Middle: vascular type, providing the healing-agents by an integrated network. Right: capsular type with a) catalyst and encapsulated healing-agent, b) phase separated and encapsulate 2K healing-agents, c) latent reactive and encapsulate 2K healing-agents and d) separate encapsulation of 2K healing agents.

3 Preparation and Characterization Techniques

3.1 Dynamic Light Scattering (DLS)

With dynamic light scattering, the hydrodynamic radius and the size distribution of colloidal systems can be determined.¹⁵⁰ In a typical light scattering experiment, the diffusion coefficient is measured by irradiation of the sample with coherent light, emitted by a laser in a defined angle. Scattering occurs due to differences in the refractive index of the continuous and dispersed phase. The scattered photons interfere with each other either in a constructive or destructive way, which results in either stronger or weaker intensities. The interference pattern is dependent on the position of the respective scattering centers. Brownian motion causes all colloids to randomly move in space. Smaller colloids move faster than bigger ones, which leads to fluctuations in the scattering intensity.¹⁵¹ In a light scattering experiment, these intensities are measured over time to give an autocorrelation function to determine the diffusion coefficient. Since the size and fluctuations are directly related to the diffusion coefficient of the colloids, the hydrodynamic radius can be calculated by the Stokes Einstein equation:

$$r_h = \frac{k_B T}{6\pi\eta D_s} \quad 8$$

With: r_h = hydrodynamic radius, k_B = Boltzmann constant, T = Temperature, η = dynamic viscosity and D_s = diffusion coefficient.

In this calculation, the dispersed colloids are assumed to be hard spheres. For monodisperse colloids, the autocorrelation function can be fitted by using a single exponential decay-function. For a polydisperse system, a sum of e-functions needs to be fitted. Depending on which function is used different particle-sizes can be obtained. Throughout this work, the Z_{av} value was used for the determination of particle sizes which is calculated by fitting a single e-function in a cumulative way. As a result of the cumulative analysis, a Gaussian curve is obtained. From its width, the polydispersity (PDI) of the colloids can be calculated.

In this work, DLS analysis was used to determine the sizes of droplets, particles and capsules.

3.2 Imaging Techniques

High resolution imaging techniques are crucial for evaluation of nanoparticle morphologies or to visualize their distribution in a matrix. The resolution of conventional optical microscopes is too small to resolve nano-structures of less than 200 nm in size, especially when being in close vicinity, due to the Abbe diffraction limit which is defined by:

$$d = \frac{\lambda}{2n \sin(\alpha)} \quad 9$$

With d = diffraction limit, λ = wavelength of light, $n \sin(\alpha)$ = numerical aperture.

Electrons which are of smaller wavelength can be used instead. They are emitted and focused as an electron beam to interact with the substrate which requires high-vacuum conditions.

3.2.1 Scanning Electron Microscopy (SEM)

Scanning electron microscopy allows for resolutions from a few μm down to several nm. The focused electron beam scans the sample with tunable intensities from 30 eV to 0.5 eV depending on the nature of the substrate it shall interact with. As a consequence to the electron irradiation, several elastic and inelastic interactions occur which can be used for detection like the emission of secondary electrons and X-rays.¹⁵² The former are used to generate an image of the sample surface, whereas the latter can be used for element-specific mapping. Since polymers are generally rather soft materials, low electron intensities are used. Because the samples are usually not conductive, a small layer of gold needs to be deposited on their surface by sputtering. In this work, SEM is used to determine the morphology of the nanofibers and nanocapsules as well as their distribution in composite matrices.

3.2.2 Transmission Electron Microscopy (TEM)

TEM in contrast to SEM does not detect scattered but transmitted electrons which are projected for imaging, which requires rather thin substrates.¹⁵³ With TEM, it is possible to also access the inner morphology of e.g. nanocapsules. The intensity is dependent on sample thickness and composition. The former allows the distinction between for example a capsule shell and core and the latter between elements with low or high atomic number, which appear darker. Since the structural differences in polymer samples are often rather small, staining agents like OsO_4 can be used to enhance the contrast. In some cases the polymer sample is degraded due to the energy input of the electron beam, like for example in the PMMA containing catalyst

nanocapsules.^{154, 155} The degradation can be suppressed by operating the TEM under cryogenic conditions at $-170\text{ }^{\circ}\text{C}$.¹⁵⁶

3.2.3 Confocal and Dual Color-STED Microscopy (DC-STED)

Confocal microscopy is a method based on fluorescent labelling of samples, thus allowing measurements under ambient conditions, which is especially important for biological applications. The diffraction limit was pushed by a reduction of the focal spot size and a point-like detection to eliminate out of focus light, since only fluorescence close to the focal plane is detected. Thus, the optical (in depth) resolution is increased. It can however not exceed the diffraction limit. One possibility to actually break the diffraction limit is stimulated emission depletion (STED) microscopy. Stefan Hell pioneered in the development of this method and was awarded the Nobel Prize in 2014 for his work. In brief, the resolution is increased by a selective depletion of the surrounding fluorescent molecules, except for the fluorescence at the focal point itself. The depletion is performed by a second laser pulse which has a “doughnut”-shaped profile. This allows a modification of the Abbe equation (equation 9) by:^{157, 158}

$$d = \frac{\lambda}{2n \sin(\alpha) \sqrt{1 + \frac{I}{I_s}}} \quad 10$$

With I = intracavity intensity and I_s = saturation intensity.

It is also possible to perform dual color (DC)- STED, by subsequently exciting two different fluorophores under the condition that their absorbances and emissions are well separated. Dual color STED microscopy was used in the nanofiber project to distinguish the epoxy and amine compartments, which are assembled in very close vicinity (see chapter 4.3).

3.3 Thermal Methods

The thermal properties of polymers are crucial for two reasons. Firstly, the glass transition temperature (T_g) in nanocapsules can be used for a triggered release of payloads. Secondly, the determination of reaction enthalpies in thermoset curing gives insights into their curing kinetics.

3.3.1 Thermogravimetric Analysis (TGA)

With TGA, the mass-loss of a sample is measured as a function of temperature or time. Mass-loss can be caused by physical processes like evaporation, sublimation or degradation, or by chemical reactions like oxidation and reduction. In this work, TGA is used to determine degradation temperatures of polymers and to monitor the release of volatile components from nanocapsules.

3.3.2 Differential Scanning Calorimetry (DSC)

With DSC, difference in the heat flow of a sample are measured as a function of temperature or time, in comparison to a reference. Such differences can be caused by physical processes like evaporation, sublimation, crystallization, melting or the transition from a glassy to an amorphous state (glass transition temperature) in polymers. Also, chemical processes like reaction enthalpies in thermoset cure can be determined. DSC was employed to determine the properties of nanocapsules and their payload release and to determine the curing characteristics of the epoxy amine thermosets in films and in fibers.

3.3.3 Isothermal Titration Calorimetry (ITC)

With ITC, molecular interactions like ligand-binding or adsorption of surfactants, as well as biological reactions like protein adsorption, which absorb or release heat are measured as a function of time. The reaction is triggered by stepwise titration of the reactant under isothermal conditions. Hence, ITC allows to directly and quantitatively monitor droplet/particle-surfactant interactions in emulsions with high sensitivity.^{159, 160} In a typical experiment, the reactant is titrated stepwise to the sample, the absorbed or released heat is measured in every step until saturation is reached and no more heat changes are detected. Every measurement needs to be corrected by subtracting the heat of dilution of the titrant in usually water. Upon fitting the integrated results, reaction enthalpies, binding affinities and the number of binding sites can be determined as shown in Figure 8.

In this work, ITC was used to prove the interfacial reaction of the epoxy surfactant with the amine miniemulsion droplets (see 4.2.3).

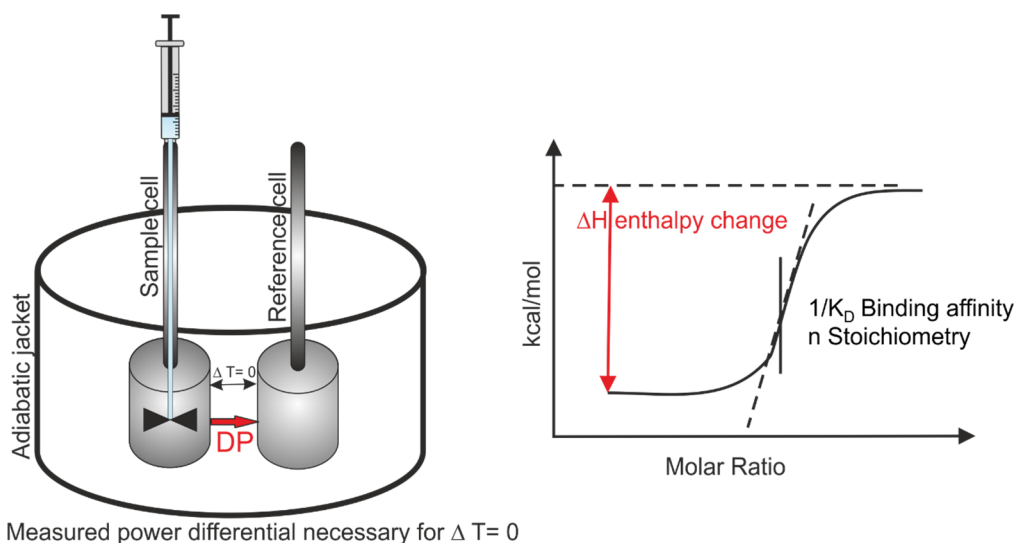


Figure 8. Measurement principle for isothermal titration calorimetry.

3.4 Mechanical Properties

The determination of the mechanical properties of thermosetting polymers and films is crucial to evaluate their performance in the desired application, like the maximum forces, temperatures or stress which can be applied without destroying the integrity of a coating. This chapter is mainly based on a textbook explaining the principles of rheology.¹⁶¹

3.4.1 Oscillatory Rheology

Oscillatory rheology belongs to the group of dynamic mechanical analysis methods and allows the time- and temperature dependent determination of viscoelastic properties over a wide range of materials from solids, gels, polymer-melts and -solutions to emulsions and dispersions. Rheology can be understood as the “science of deformation and flow of matter”.¹⁶¹ Polymers often display viscoelastic properties upon applied stress, which means in a certain range they show elastic behavior (which is typical for solids), which may switch towards viscos behavior which is common for liquids (and gasses) and their ratios can be determined. For oscillatory rheology measurements, the sample is placed between two plates with a defined gap, one plate is stationary and the other one is rotated “back and forth” to shear the sample in a controlled fashion as shown in Figure 9. The necessary condition is, that the sample is homogeneously deformed throughout the entire area under shear and the sample is fixed to both plates, so it cannot slide. A sinusoidally oscillating strain (deformation) is applied with:

$$\gamma = \gamma_0 \sin(\omega t) \quad 11$$

With γ_0 = strain amplitude; ω = angular frequency,

causing an oscillating stress of identical frequency which is shifted by the phase angle δ .¹³⁰

The complex shear modulus (G^*) is a material constant and represents its stiffness. Since according to Hook’s law:

$$G^* = \frac{\tau_t}{\gamma_t} [Pa] = const. \quad 12$$

For a purely elastic behavior, the phase angle between γ and τ is 0 and the shear rate is shifted by 90°, so it appears as a cosinusoidal curve.

For purely viscos behavior, according to Newton's law:

$$\mu^* = \frac{\tau_t}{\dot{\gamma}_t} [Pas] = const.$$

31

The τ curve is in phase with the shear rate and they are both shifted by 90° compared to the γ curve as schematically shown in Figure 9.

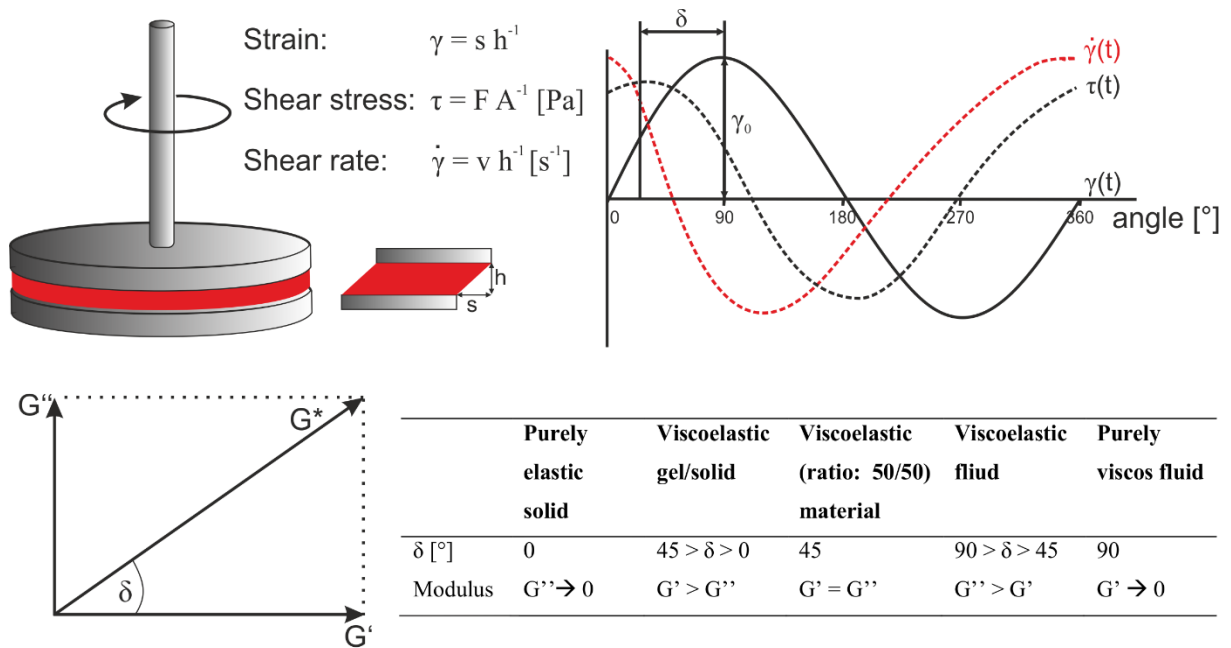


Figure 9. Measurement principle for oscillatory rheology.

The relationship between the complex shear modulus and the complex viscosity is given by:

$$|G^*| = \omega |\eta^*| \tag{14}$$

G^* (or η^*) is the vectorial sum of the elastic (G' (or η'')) and viscous (G'' (or η')) portion of the viscoelastic material, as illustrated in the vector graphic in Figure 9. G' is defined as the storage modulus and represents the reversibly stored deformational energy. After the strain is removed, the sample fully returns to its initial state. The loss modulus G'' in contrast, represents the energy portion which is lost upon shearing the material.

The energy is consumed by relative movements, which causes friction and irreversible deformation of the sample and is often accompanied by heat release. They are typically plotted with a logarithmic scale. The loss factor represents the relation of these portions as summarized in the table in Figure 9 according to:

$$\tan\delta = \frac{G''}{G'} \quad 15$$

The temperature-dependent course of the $\tan\delta$ function can be used for the determination of the T_g of a polymer under the condition, that no chemical reaction takes place. The curve shows a distinct maximum at the point where the ratio of the loss modulus (G'') to the storage modulus (G') is at its maximum and was used for the determination of the T_g s of the polymer films in the P1K project.

The curing of a thermoset can also be monitored by the course of the $\tan\delta$, which usually shows a dominantly viscos behavior in the beginning. The sol-gel transition point is reached at $\tan\delta = 1$ and was therefore used to compare the curing of a polyurethane matrix in the catalyst capsule project. However, to obtain fully cured, non-tacky materials, the storage modulus must exceed the Dahlquist criterion which is about 10^5 Pa.^{162, 163} For the investigations of the curing kinetics in chapter 4.1, an NIR-coupling was used to directly correlate the mechanical properties with molecular information by the appearance or disappearance of functional groups.¹⁶⁴

3.5 Electrospinning

Electrospinning is a versatile tool to produce micron- or nano sized fibers with a large variety of functions and compositions.^{165, 166} It can be used to fabricate all kinds of 1D-structures with possible applications ranging from tissue engineering, drug delivery, filters and energy applications.¹⁶⁷⁻¹⁷⁰ Fibers can be spun from polymer solutions, melts or sol- gel precursors, which are pumped into a fine metallic nozzle with a syringe pump. An electric field is applied by a high power supply between the nozzle and the conductive collector as schematically shown in Figure 10. This causes charging of the droplet which is formed at the tip of the nozzle. This leads to the formation of a Taylor cone, which is further stretched towards the collector as a liquid jet once the surface tension is overcome. During this stretching, the solvent evaporates and randomly oriented fibers form, which can be collected from the collector.^{171, 172} The morphology, thickness and properties of the nanofibers can be adjusted by several parameters. For example, an increase in voltage and tip-collector distance or a decrease in flow rate and viscosity of the spinning solution may lead to smaller fibers. It is furthermore possible to encapsulate liquids or particles in fibers by colloid-electrospinning to add functionality.^{173, 174} It is possible to encapsulate various loads like drugs, peptides or nanoparticles into such fiber structures.^{175, 176} In many cases, the fiber matrix is used for triggered delivery upon various stimuli. Colloid-electrospinning was used to create a latent system for self-healing applications, by assembling and immobilizing epoxy and amine colloids as separate compartments within a polymer nanofiber as described in the nanofibers project in chapter 4.3.

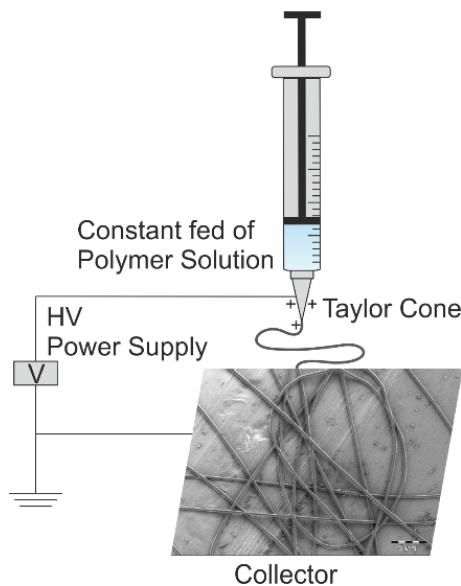
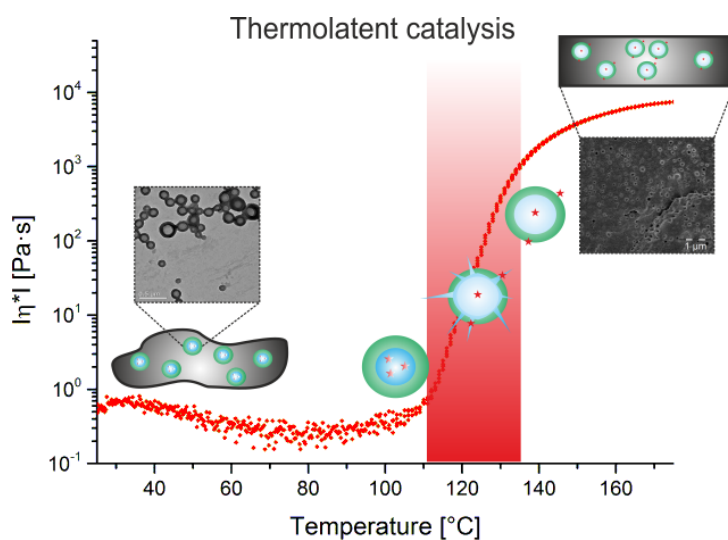


Figure 10. Principle of electrospinning.

4 Results and Discussion

4.1 Reaction Latency by Triggered Catalysis

A physical approach towards temperature-switchable catalysis is investigated. In theory, thermolateness is needed whenever an application requires a system to remain inactive, unless a threshold temperature is reached. After exceeding this temperature, the reaction is immediately catalyzed and proceeds rapidly. For the first time, these properties could be gained by a nanocapsules-based approach. Therefore, polymer nanocapsules (200 nm), containing a catalyst and a low boiling hydrocarbon were synthesized to achieve a “release-on-demand” for polyurethane curing. The release kinetics can be tailored by the cross-linking density and/or the catalyst loading. The approach can be used for infusion processes in reinforced fiber composites, since the nanocapsules are unsusceptible to filtering in such applications.



4.1.1 Motivation

Composites and coatings made from reactive, multifunctional resins have been widely investigated in the last decades to develop novel properties and applications. Amongst those, often polyurethanes, epoxides, polyester- or alkyd-resins, silicones, ϵ -caprolactones or polyimides are used. Many examples show the reinforcement with (nano)-particles or fibers to yield superior, for example mechanical or thermal properties.^{177, 178} Especially for aliphatic isocyanate based systems, often catalysts are required to accelerate the polymerization and to reduce the curing temperature. A high catalytic activity on the hand is highly desired but on the other hand reduces the potlife of polyurethane (PU)-materials, since the reaction will be immediately catalyzed.^{179, 180} As a solution, several methods have been established, which include the use of blocked isocyanates, surface deactivated micronized isocyanate powders or UV-curable hybrid systems.^{181, 182} All of these alternatives suffer from certain drawbacks which limit their applicability, e.g. high temperature requirements, restriction to thin, transparent films and/or significant changes in terms of cross-linking and polymer network structure. As a consequence, for many applications the concept of a "delayed action" or thermolatent catalyst as described in chapter 2.6.1 is highly desired. The catalyst remains inactive until a certain stimuli is applied, which is usually a threshold temperature.¹⁸³ This principle enables an improved handling for adhesive and coating applications, as well as for reinforced materials, obtained by infusion or injection processes. Looking at the problem from a molecular point of view, few examples report the introduction of thermolabile ligands into the catalyst. Zoeller et al. developed Tin (II) and Tin (IV) alkoxy catalysts with a kinetically labile $N \rightarrow Sn$ coordination for this purpose.¹⁸⁴ To overcome the need of rather complex synthesis protocols, we looked at the thermolatency concept from a physical point of view. For example, it was shown, that the catalytic activity could be switched by encapsulation and release of a photoredox catalyst in a macromolecular assembly.¹⁸⁵ Furthermore, a double hydrophilic micellar diblock copolymer system enabled the temperature and solvent switchable catalytic activity in esterolysis reactions.¹⁸⁶ This chapter focusses on creating a polymer shell around a common catalyst, which serves as a responsive barrier (chapter 2.6.1). There have been several attempts to use microcapsules as barrier systems for the encapsulation of catalysts.¹⁸⁷⁻¹⁸⁹ However, none of those publications investigated the capsules with regard to thermolatency. In addition, microcapsules are often too large to be applied in thin coatings ($<100 \mu\text{m}$). They furthermore cannot be used for infusion processes, especially if reinforced fibers are used, since they will be filtered out. Also, microcapsules are prone to sedimentation and creaming and the shear stability of microcapsule dispersions is low. In many cases, microcapsules can negatively

influence the mechanical properties of the cured material. Nanocapsules instead have proven to be excellent carriers for various payloads and allow triggered release by stimuli responsive shell materials without affecting those properties. An early example demonstrated the encapsulation of a Grubb's catalyst in silica nanocontainers.¹⁹⁰ In a recent example, Tran and co-workers used encapsulated Grubbs Howeda second generation catalyst for autonomous corrosion protection as further development of previous works by Brown et al. and Cho et al.¹⁹¹⁻¹⁹³ The ideal thermolent catalyst shows a distinct “non-Arrhenius” behavior due to a sharp increase in reaction rate. This can be achieved by the introduction of a physical phase transition of the polymer shell at its glass transition temperature, which allows the release of the catalyst, thus immediately initiating the polymerization. In this work, nanocapsules with a cross-linked shell and a PU-catalyst (dimethyltin dineodecanoate as less toxic dibutyltin dilaurate (DBTL)-alternative),¹⁸⁰ dissolved in a hydrophobic, low-boiling hydrocarbon as core material are presented. The use of a commercially available catalyst diminishes the need of labelling and classification, for example by GHS, REACH, etc. as needed for new compounds. The presence of the hydrocarbon assists in the release of the catalyst as a so called “release agent”. Upon temperature increase, the hydrocarbon vaporizes and builds up pressure inside the capsules as shown in several microcapsule systems for foaming applications.^{194, 195} However, as already stated before, those microcapsule-based approaches suffer from size-related drawbacks. Nevertheless, the idea to increase the pressure inside the nanocapsules to assist the catalyst release can be very helpful to achieve a “release/catalysis-on-demand”, once the capsule shell is heated above its T_g as shown in Figure 11 and investigated throughout this project.

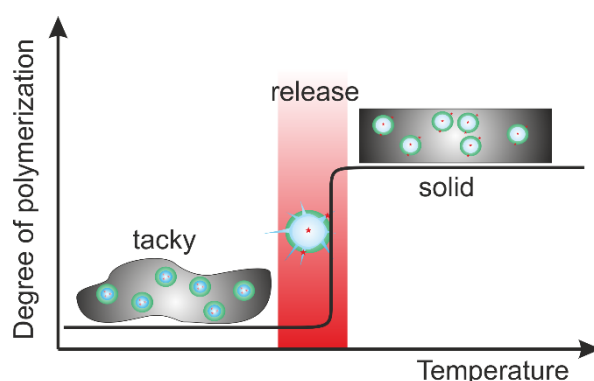


Figure 11. Schematic presentation of the release profile of an ideal thermolent catalyst. Below the threshold temperature the catalyst is completely inactive, whereas by passing the threshold temperature, the polymerization proceeds rapidly until full conversion is achieved.

4.1.2 Nanocapsule Synthesis

Thermolent-catalyst-nanocapsules (TLCN) were prepared via miniemulsion analogous free radical polymerization. The capsule core consists of isooctane as release-agent as well as dimethyltin dineodecanoate as catalyst. The polymer shell consists of poly(methyl methacrylate-*co*-butyl methacrylate-*co*-methacrylic acid) (PMMA_{0.79}-*co*-PBMA_{0.105}-*co*-PMAA_{0.105}) and is cross-linked with 1,4-butanedioldimethacrylate (BDDMA) in various concentrations from 0 to 5 wt.% (Table 3). Phase separation of the shell and the core material(s) takes place due to an increasing incompatibility with the polymer as discussed in chapter 2.3.1. and investigated before for the encapsulation of volatile compounds.¹⁹⁷ Hofmeister et al. correlated the encapsulation efficiency of a core material in a polymeric nanocapsule with the Hansen Solubility Parameters and found high encapsulation efficiencies for materials with a very low value for hydrogen bonding.⁹⁰

In the system herein presented, we used a comparable polymer shell and isooctane with a value of $\delta_H = 0 \text{ MPa}^{1/2}$ for hydrogen bonding as main core component except for the TLCN 3 sample.¹⁹⁶ So, a very good encapsulation efficiency can be expected. To measure the encapsulation efficiency, defined amounts of the emulsion were freeze-dried and the solid content (SC) was determined. A theoretical solid content (SCT) including isooctane as volatile compound was calculated. Deviations from these values originate from free material which evaporated upon the freeze drying process and thus lower the encapsulation efficiency (EE) which is given in % by subtracting SCT – SC.

Table 3. Composition, colloidal properties and encapsulation efficiencies of the synthesized nanocapsules.

Entry	Cross-linker [wt.%] ^{a)}	Catalyst [wt.%] ^{b)}	Z_{av} (PDI) [nm]	EE [%] ^{c)}	EE _{Catalyst} [%] ^{d)}
Ref	2.5	0	193 (0.09)	85	-
TLCN 1	2.5	15	192 (0.07)	81	81
TLCN 2	2.5	30	204 (0.02)	87	85
TLCN 3	2.5	100	197 (0.06)	94	80
TLCN 4	0	15	223 (0.17)	83	-
TLCN 5	1	15	191 (0.06)	92	88
TLCN 6	5	15	coagulation	-	-

^{a)} Based on the total quantity of the polymer shell. ^{b)} Based on the total quantity of the capsule core. The core/shell ratio of 0.57/1 was maintained constant. ^{c)} Encapsulation efficiency (EE) of the core material (isooctane and catalyst) by gravimetric determination of the freeze-dried samples. ^{d)} EE of the catalyst determined by XRF-spectroscopy of the freeze-dried samples.

High encapsulation efficiencies of 80-90% were obtained (see Table 3). The ratio of shell to core was maintained constant throughout these investigations. The catalyst loading was varied from 0 to 100% with respect to the capsule core and did not significantly influence the overall encapsulation efficiency. Capsules containing pure isooctane were prepared as a nonreactive reference.

Additionally, the encapsulation efficiency of the catalyst was calculated by quantification of the Sn-content with X-ray fluorescence spectroscopy. Beforehand, samples were dialyzed to remove free catalyst from the system. High recovery rates of > 80% are obtained, again independent on the catalyst loading. Furthermore, the composition of the polymer shell was altered by varying the cross-linker amount from 0 to 5 wt.%, to allow a tunable release of the core materials. Apart from the TLCN 6, the sample with the highest cross-linker content which coagulated upon polymerization, uniform particles with a diameters of ~ 200 nm were obtained according to the DLS measurements. All dispersions were found to be colloiddally stable for more than six months.

4.1.3 Morphology

SEM and cryo-TEM microscopy images of the isooctane reference capsules displayed in Figure 12 show nanocapsules of about 200 nm in diameter with a uniform size distribution. Core-shell morphologies were found throughout the whole sample and almost no particles were found.

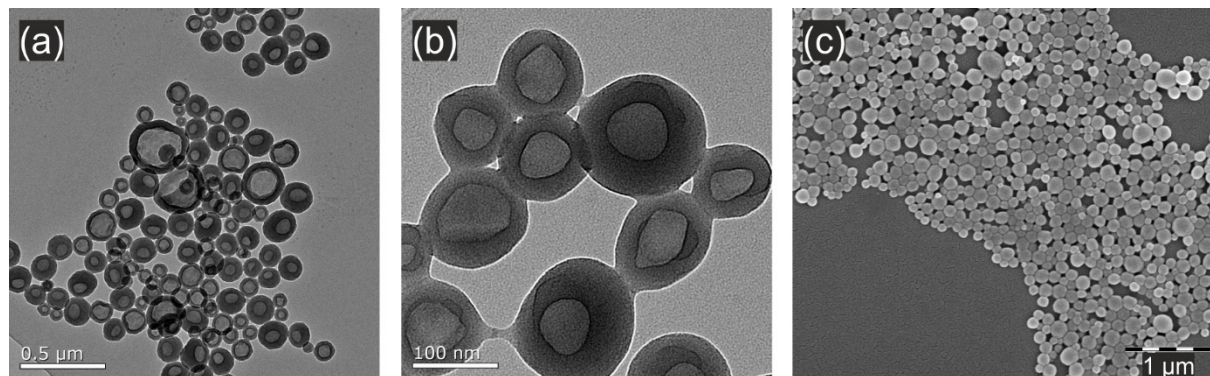


Figure 12. Morphology of the isooctane nanocapsules observed with cryo-TEM in a) low and b) high magnification, showing a core shell structure in nearly all cases. Images were kindly recorded by Ingo Lieberwirth. SEM images of the capsules are shown in c).

Figure 13 displays the morphology of the catalyst-loaded nanocapsules by cryo-TEM, as schematically shown in b). The catalyst load increases from c) 15 wt.% (TLCN 1) to d) 30 wt.% (TLCN 2) and in the TEM image in e) the core consists solely of the catalyst with no isooctane present anymore (TLCN 3). For all samples very uniform core-shell morphologies are obtained independent on the catalyst loading. For the TLCN 1 sample, also an SEM image is given in a). The TLCN 3 was investigated with higher detail by performing Scanning Transmission Electron Microscopy (STEM) on the sample to obtain additional information on the distribution of Sn within the capsules. With this technique, the focused electron beam rasters the sample and can be used to simultaneously obtain elemental information by energy dispersive X-ray (EDX) analysis. It was not possible to perform these measurements on the other samples, since the Sn-concentration was not high enough. Figure 14 a) shows one nanocapsule and the spots where a complete EDX spectrum was taken in the center of the capsule as marked with a + and shown in b). The elemental composition, as expected shows that besides C and O, Sn is present in the nanocapsules. More importantly, the EDX line scan in c) reveals the elemental composition along the capsule axis as an overlay of the carbon and the tin channel. The Sn-signal is homogeneously distributed in the capsule with a decreasing concentration towards the capsule walls, as expected from the core-shell morphology. Still the results suggest, that at least partially the catalyst is also present in the capsule wall.

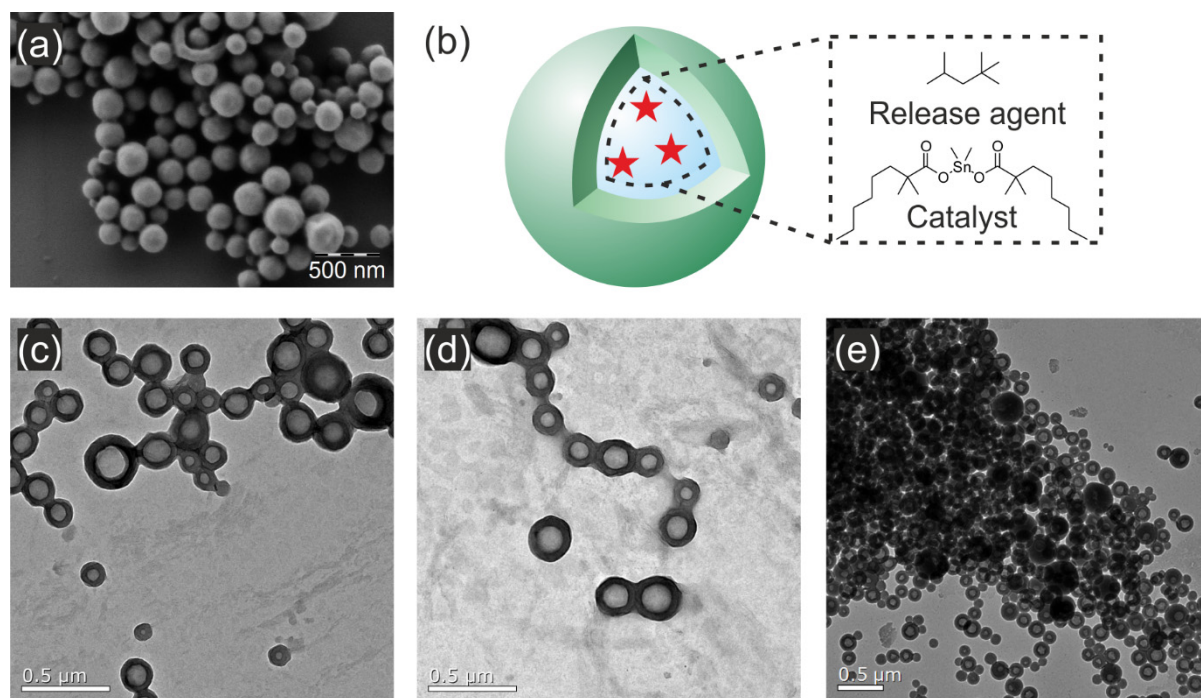


Figure 13. Morphology of the nanocapsules containing different amounts of catalyst. a) SEM image of the TLCN 1 sample. b) Schematic drawing of the nanocapsules. TEM images of the c) TLCN 1, d) TLCN 2 and e) TLCN 3 nanocapsules obtained under cryogenic conditions to avoid degradation. Images were kindly recorded by Ingo Lieberwirth and Gunnar Glasser.

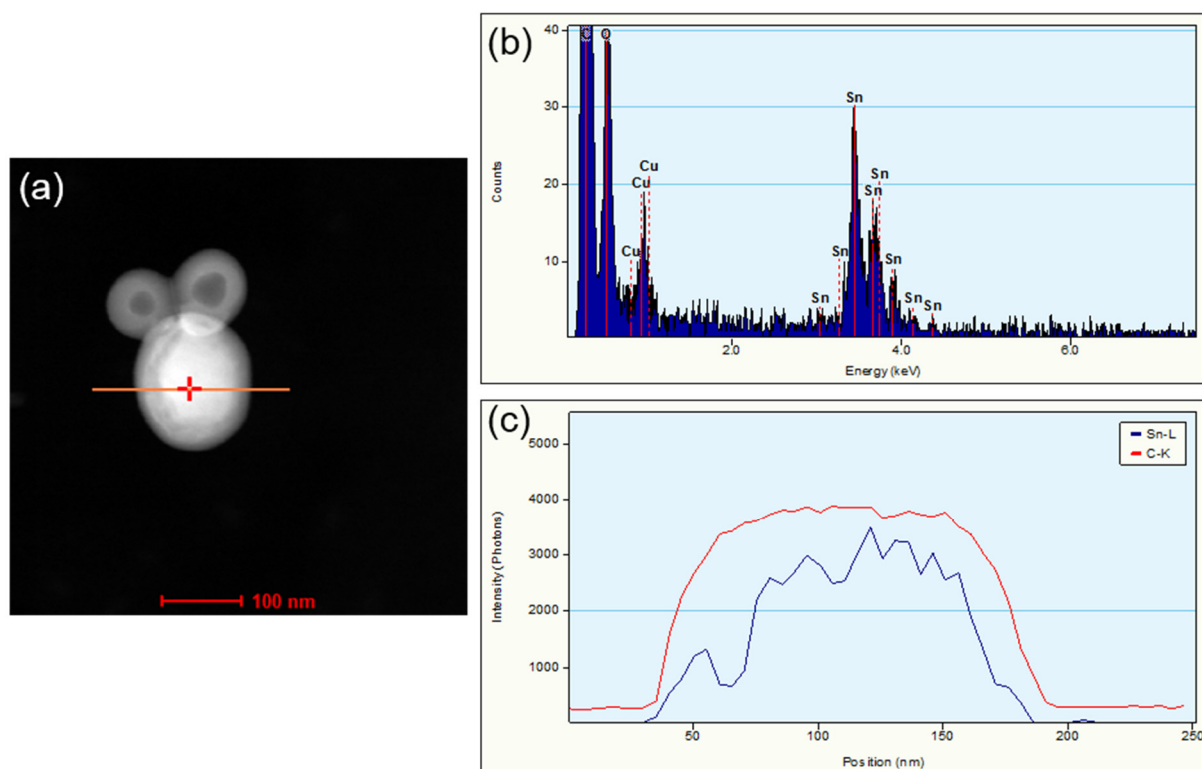


Figure 14. STEM analysis of the TLCN 3 nanocapsules depicted in a). The red cross marks the position where the EDX image is taken and the orange line marks where the EDX line scan was performed. b) Elemental composition present in the center of the capsule where Sn from the catalyst can be detected. The Cu derives from the copper grid sample holder. c) Intensity profiles of C and Sn along the capsule axis.

4.1.4 Thermal Properties

High T_g values are an important prerequisite to obtain a high barrier performance and to prohibit premature release. The isooctane release was investigated by DSC and TGA (Figure 15). In the TGA analysis, the TLCN 1 capsules show a mass loss at ~ 120 °C of about 21% which is due to the isooctane evaporation and is in good agreement to the theoretical mass loss of about 23%. At higher temperatures of around 300 °C, the acrylic polymer-shell starts to degrade. The mass remaining after the measurement cycle was completed is about 8% due to Sn-species formed upon catalyst degradation at high temperatures. The first heating cycles obtained by DSC analysis, depicted in Figure 15b) show a strong endothermic signal for the isooctane reference sample with an onset temperature of 127 °C, which corresponds to the evaporation of isooctane (boiling point 99 °C). Evaporation is delayed by the cross-linked nanocapsule shell. Compared to the isooctane reference, the TLCN 1 sample shows a shifted evaporation peak towards lower temperatures, which indicates that the catalyst either influences the polymerization of the capsule shell or that some catalyst-shell interactions are present. The onset temperature is further shifted towards lower temperatures for the TLCN 2 sample. Compared to the TLCN 1 sample, the peak is also much broader. The glass-transition temperatures of the acrylate copolymer shells were determined by running second heating cycles as summarized in Table 4 and found to be around 130-150 °C. Since the TLCN 3 sample does not contain any isooctane, the curve shows the T_g already in the first heating cycle, which with about 103 °C and are again distinctly shifted towards lower temperatures. Since the catalyst does not evaporate it still can act as softening agent, i.e. the measurement of the unperturbed T_g is basically impossible via DSC.

Secondly, the influence of the crosslinking density on the isooctane release (samples TLCN 4-5) were investigated. The overlay in Figure 15c) shows the tunability of the isooctane release kinetics. The onset temperatures decrease with decreasing amount of cross-linker until the onset temperature of 109 °C nearly equals the boiling temperature of the isooctane in case of the linear copolymer in sample TLCN 4.

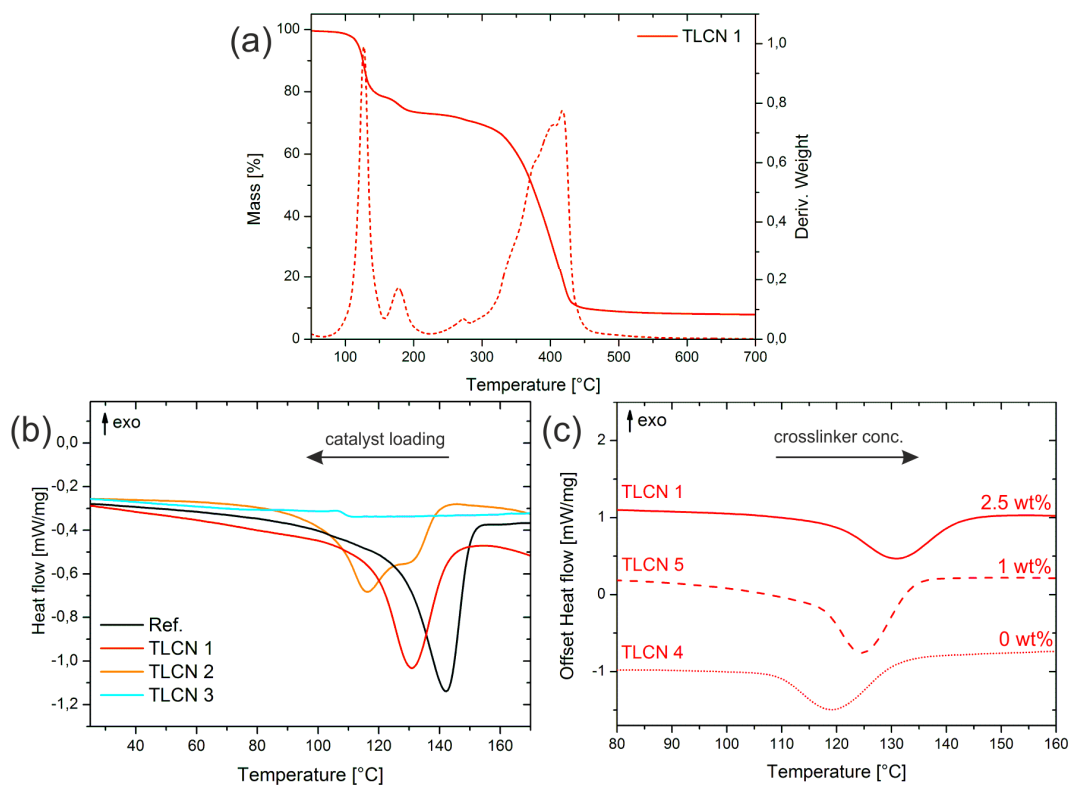


Figure 15. Thermal properties of the synthesized nanocapsules. a) TGA measurements showing the mass loss of the TLCN 1 capsules from 50-700 °C and the derivative weight loss (dashed line). b) First heating cycles of the DSC analysis showing the isooctane release as an endothermic peak. c) DSC measurements comparing the influence of the cross-linker concentration on the isooctane release temperature.

Table 4. Comparison of onset-, peak- and glass transition temperatures of the nanocapsules measured with DSC.

Entry	T_{Onset} 1 st heating cycle [°C]	T_{Peak} 1 st heating cycle [°C]	T_g 2 nd heating cycle [°C]
Ref.	127	142	147
TLCN 1	119	131	132
TLCN 2	103	116	157
TLCN 3	n.a.	n.a.	103*
TLCN 4	109	119	139
TLCN 5	116	125	146

*Since no isooctane was present in this sample, the T_g was determined on basis of the first heating cycle.

4.1.5 Thermolatent Catalysis

To determine the catalytic activity of the capsules, a polyfunctional aliphatic isocyanate-based hardener and castor oil as polyol, which were also used later for the preparation of reinforced glass fiber composites (chapter 4.1.5.3). The castor oil is used as a substitute for the usually non bio-based polyol component. Obtained from vegetable oils as renewable feedstocks, castor oil has already proven a good candidate to obtain cross-linked PUs, since it contains in average three hydroxyl groups.^{198, 199} The catalyst concentration was fixed at 0.1 wt.% of the polyol for all samples, to allow comparability. In each set of experiments, the influence of the thermolatent catalyst nanocapsules were compared to I) the pure polyurethane matrix without any catalyst, II) the PU-matrix mixed with the free, nonlatent Sn-catalyst, III) the PU-matrix mixed with the isooctane reference nanocapsules in the same quantity as the TLCN 1 to exclude effects caused by the capsules and not by the catalyst.

4.1.5.1 Rheology

The evolution of viscoelastic properties of the polyurethane composites were monitored over time and at different temperatures by oscillatory rheology measurements. Upon curing, the mechanical moduli of the sample change over several orders of magnitude. The measurement profiles were optimized to depict the whole curing processes which is why in some cases, especially in the low viscous regime at the beginning of the curing reaction there are some deviations which however do not interfere with the overall analysis.

Firstly, isothermal measurements were conducted. We chose 50 °C as inactive and 120 °C as active scenario. Figures 16 and 17 display the individual evolvments mechanical moduli for each sample individually, whereas additionally and for a better comparability the complex viscosities are summarized in Figure 18. At 50 °C, the complex viscosity of the pure matrix does not increase over time, indicating that no reaction takes place under these conditions (Figure 18a)). The results for the reference capsules mixed with the matrix show almost identical results. The TLCN 1 and 2 samples show only a moderate increase in viscosity over time. Their final storage moduli are however far below the Dahlquist criterion (10^5 Pa) which defines the marginal value to obtain non-tacky films. Thus, it is still possible to process the mixture even after several hours of storage at 50 °C.^{162, 200} The final viscosity of the TLCN 2 sample is roughly twice as high as for the TLCN 1 sample. A plausible explanation could be increasing trace amounts of catalyst entrapped in the polymer-shell with increasing catalyst loading, which can diffuse out at higher temperatures. This becomes even more prominent for the TLCN 3 sample where the core only consists of the catalyst. The curve shows a nonlinear

increase in viscosity directly from the beginning of the measurement, i.e. this sample lacks a pronounced thermolatent behavior as already suspected from the STEM analysis in chapter 4.1.3. However, with the pure Sn-catalyst present, a strong increase in viscosity takes place immediately which means the free catalyst cannot be used for infusion processes under these conditions.

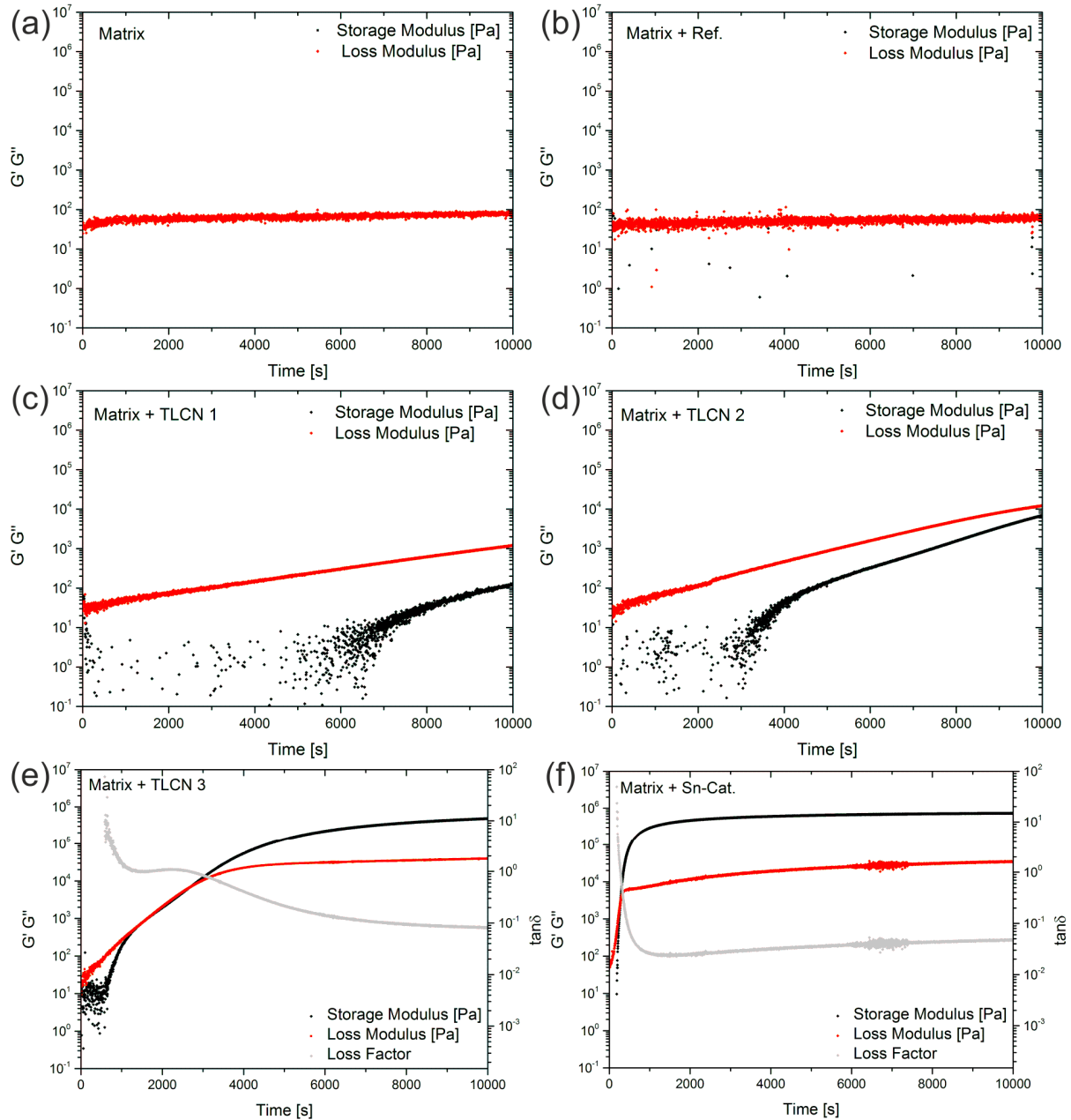


Figure 16. Isothermal rheology measurements at 50 °C. a-b) The pure matrix and the matrix+reference show a completely viscous behavior and no increase in loss modulus over time. b-c) The TLCN 1&2 samples also show a predominantly viscous behavior with only slight increases in storage modulus over time, not exceeding the Dahlquist criterion ($G' > 10^5$ Pa). e) The TLCN 3 sample shows an increase in $G' G''$ and exceeds the Dahlquist criterion, indicating an insufficient thermolatency. f) The free catalyst immediately promotes the reaction, prohibiting further processability.

We then increased the operation temperature to 120 °C, since the DSC results showed a rapid isooctane release above this temperature (Figure 18b)). After about 35 min, the pure matrix shows an increase in viscosity also without any catalyst present, since the activation energy is sufficient to promote the cross-linking reaction. The sample containing the reference capsules shows a similar behavior indicating that the quantity of nanocapsules has only minor influence on the mechanical properties of the matrix materials. The TLCN 1 sample instead shows a completely different behavior. After a short induction period of about 15 min, the viscosity increases rapidly. As discussed in the introduction this is highly desired, since especially in infusion processes for reinforced fiber composites, open-times are needed to ensure the fibers are completely wetted with the matrix before the curing proceeds. Comparing the slopes, the TLCN 1 catalyzed sample shows a 2.8-fold increased acceleration compared to the isooctane reference. The free catalyst could not be measured with this rheometer setup anymore, since the sample had already hardened before the spindle trimming position was reached. The shape of the TLCN 2 sample is similar to the TLCN 1, however, the increase in viscosity is shifted towards shorter reaction times. For the TLCN 3 sample the maximum viscosity is already reached after less than 5 min. The curve does not show a measureable induction period anymore and the reaction appears to be catalyzed immediately. The final viscosities and the G' moduli depicted in Table 5 comparing the catalyzed sample with encapsulated catalyst ones also do not differ notably, showing that the quantity of nanocapsules is not decreasing the mechanical properties of the material within this low concentration regime. A plot of the acceleration (slopes of the curves in Figure 18a-b) versus catalyst loading as shown in Figure 18c) even suggests a linear dependency, thus allowing a tunable release on demand.

Table 5. Mechanical properties of the catalyst nanocapsules at different temperatures comparing the maximum G' -moduli and the reaction times until the sol-gel point ($\tan\delta = 1$) is reached.

Entry	Temperature [°C]	$t_{\tan\delta=1}$ [s]	$G'_{t=10000\text{ s}}$ [Pa]
Matrix	120	2450	$6.94 \cdot 10^5$
Matrix + Sn- Cat.	120	n.d.	n.d.
Matrix + Ref.	120	3030	$4.90 \cdot 10^5$
Matrix + TLCN 1	120	1210	$9.82 \cdot 10^5$
Matrix + TLCN 2	120	782	$1.00 \cdot 10^6$
Matrix + TLCN 3	120	<3	$1.37 \cdot 10^6$
Matrix	50	>10 000	n.d.
Matrix + Sn- Cat.	50	276	$7.31 \cdot 10^5$
Matrix + Ref.	50	>10 000	n.d.
Matrix + TLCN 1	50	>10 000	$1.23 \cdot 10^2$
Matrix + TLCN 2	50	>10 000	$6.88 \cdot 10^3$
Matrix + TLCN 3	50	1350	$4.85 \cdot 10^5$

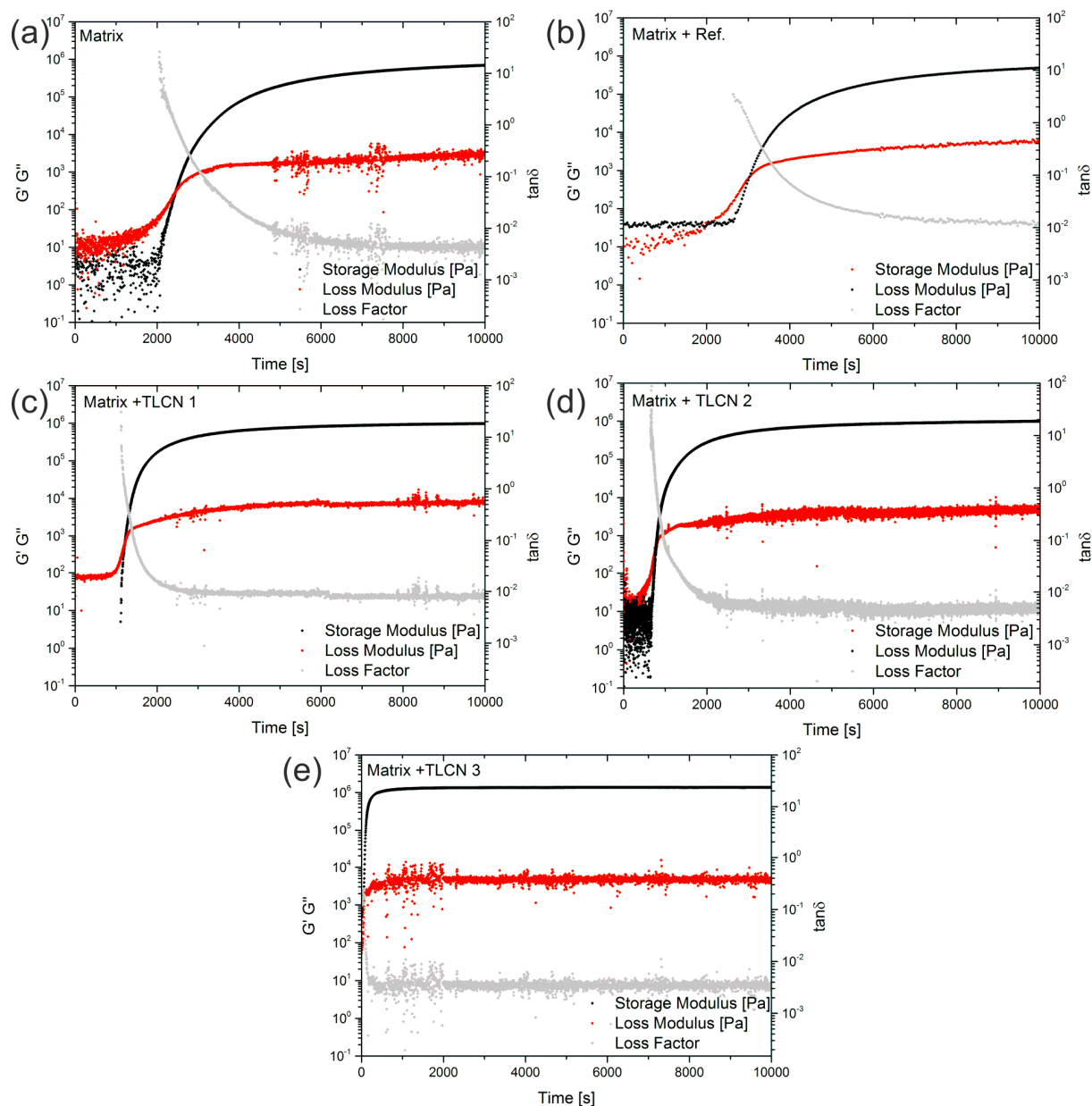


Figure 17. Isothermal rheology measurements at 120 °C. All samples show increasing moduli over time, the Dahlquist criterion is met in all cases and high G' moduli are obtained. Compared to the references in a-b), the TLCN catalyzed samples c-e) show a rapid catalysis with a short induction period which decreases with increasing catalyst load.

As already stated before, the ideal thermolatent catalyst shows a distinct non-Arrhenius behavior by being completely inactive until a certain threshold temperature is reached. We therefore ramped the temperature from RT to 180 °C as shown in Figure 18d). The TLCN 1 sample shows an almost ideal behavior. No increase in viscosity is noticed until the threshold temperature of 115 °C is reached, immediately causing a strong increase in the degree of polymerization. The reaction is completed within 900 s. The slope after linear regression between 115 and 130 °C was 0.146 Pa s K⁻¹. To demonstrate the tunability of the system, the influence of the cross-linking density on the rheological behavior of the system was measured. All graphs show the same sigmoidal shape and a delayed catalysis. As expected from the DSC measurements, the threshold temperature decreases with decreasing cross-linking density. For the TLCN 5 sample with a reduced cross-linker content of 1 wt.%, it is decreased by 14 °C to about 101 °C with an almost identical slope of 0.149 Pa s K⁻¹ (after linear regression between 101-122 °C). In contrast, the TLCN 4 sample which is not cross-linked shows a much earlier increase in viscosity starting at about 80 °C with a slope of 0.102 Pa s K⁻¹ (80-105 °C). By this comparison, the beneficial effect of the delayed “burst” release caused by the evaporation of the isooctane becomes visible. The cross-linked polymer shell can withstand a higher internal pressure due to the isooctane evaporation, whereas for the linear copolymer the diffusion is less hindered. As a consequence, the acceleration of the curing reaction is reduced, which allows the gradual adjustment of the curing profile according to technical needs.

Furthermore, the storage stability of the nanocapsules was investigated by dispersing them in the polyol component and storing the mixture at room temperature. Even after 18 days of storage, no significant loss in catalytic activity was noticed as shown in Figure 18f). Also, no measurable loss in the barrier properties of the capsule wall were noticed as revealed in the 50 °C measurements in e). Otherwise, if the polyol would swell the capsule wall, this would lead to some degree of catalyst leaking thus causing catalysis already at lower temperatures.

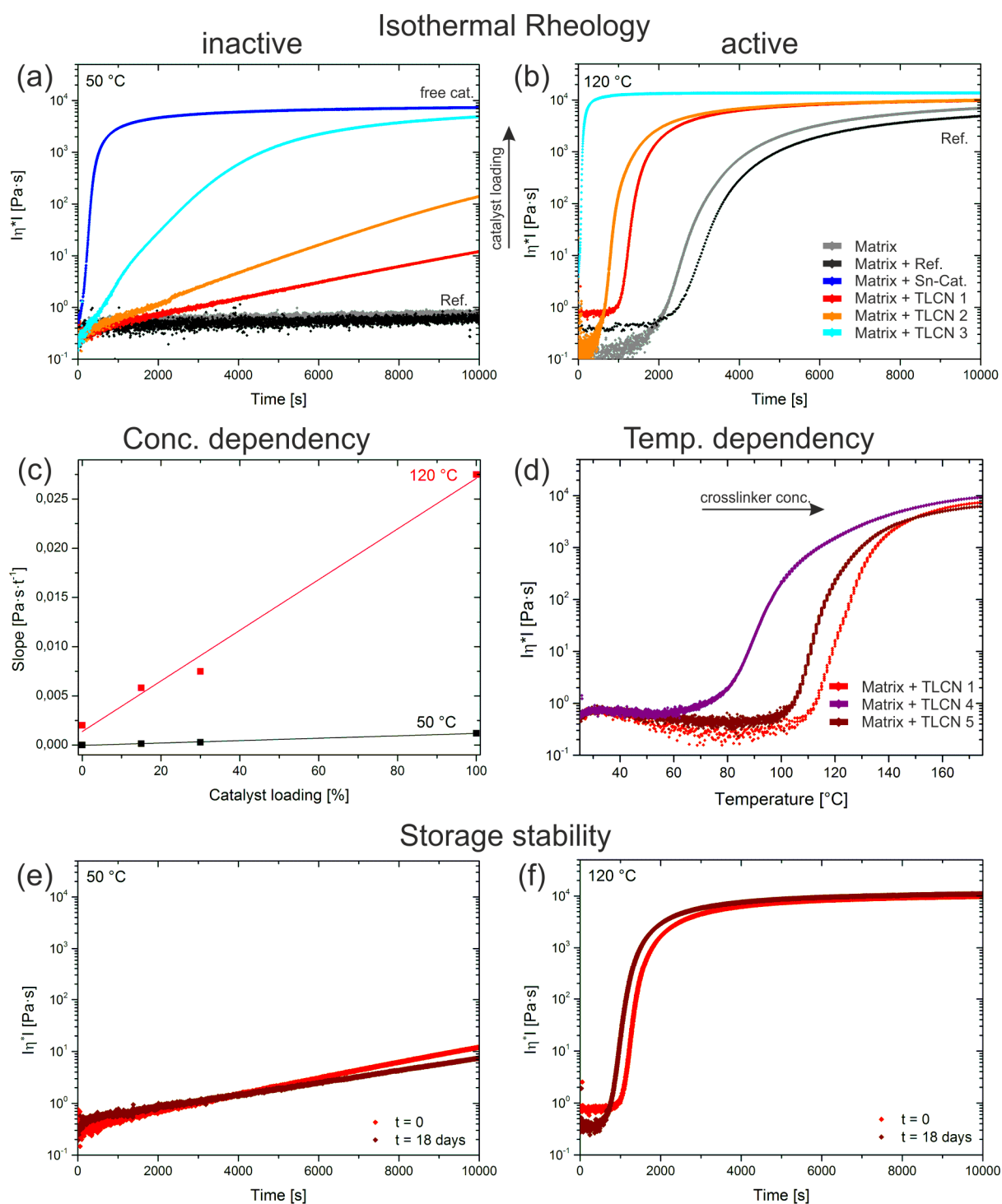


Figure 18. Isothermal rheology showing the complex viscosity as a function of time at a) 50 °C and b) 120 °C. c) Catalyst loading versus the acceleration derived from the $|\eta^*|$ -curves in a-b) and linear regression. d) Temperature versus viscosity plots with different cross-linker concentrations showing an almost ideal thermolent behavior. Comparison of the catalytic activity after storage of the TLCN 1 sample in the polyol at e) 50 °C and f) 120 °C showing no significant loss in activity or latency.

4.1.5.2 FT-IR/NIR Analysis

In addition, spectroscopic information on the degree of curing was obtained, firstly by infrared spectroscopy on the films before curing (Figure 19a) red curves) and after their rheological analysis at 120 °C (black curves). Initially, all samples show the characteristic N=C=O stretching vibration at 2250 cm⁻¹ and a broad peak at about 3550 cm⁻¹ assigned to the OH valence vibration, which are both consumed upon reaction. Upon urethane formation, the characteristic C=O valence vibration at 1687 cm⁻¹, the NH deformation at 1525 cm⁻¹ and the NH valence vibration 3360 cm⁻¹ of the secondary amide evolve. For the samples c-f) which contain the Sn-catalyst either added directly, or encapsulated, the NCO peak vanishes. The TLCN 2 sample shows a very small remaining peak which might be due to minor inhomogeneities. Comparing the non-catalyzed samples however, a-b) still show a pronounced N=C=O peak, indicating that under the given conditions the conversion was less than 100%.

To get further insights into the curing mechanism at 120 °C, we used *in-situ* coupled NIR-spectroscopy. This technique allows the simultaneous determination of the viscoelastic properties and spectroscopic information, which are otherwise difficult to access for highly cross-linked systems.^{164, 201} The isocyanate reaction can be monitored by for example either the consumption of the hydroxyl groups of the polyol or the formation the amide NH peak from the urethane formation, as already shown in the FT-IR study.^{202, 203} Figure 20a) exemplary shows selected spectra recorded over time for the curing of the PU-matrix with the TLCN 1 sample. Since there are some OH-groups (7045 cm⁻¹) present in the nanocapsule shell as well, the 2ν-NH (6749 cm⁻¹) band was chosen for further analysis. The increase of integrated relative peak areas over time are depicted in Figure 20b). Comparing the results, the NIR curves show a different behavior, since they do not show any induction period anymore. The urethane formation starts immediately. The TLCN 3 catalyzed sample shows the fastest increase. The TLCN 1 and 2 catalyzed samples in contrast to the rheology measurements are no longer distinguishable. One possible explanation might be, that the presence of the nanocapsules initially interferes with the network formation, thus allowing for a longer chain segment flexibility. Since there are twice as many capsules (mass) present in the TLCN 1 catalyzed sample, the effect is more prominent.

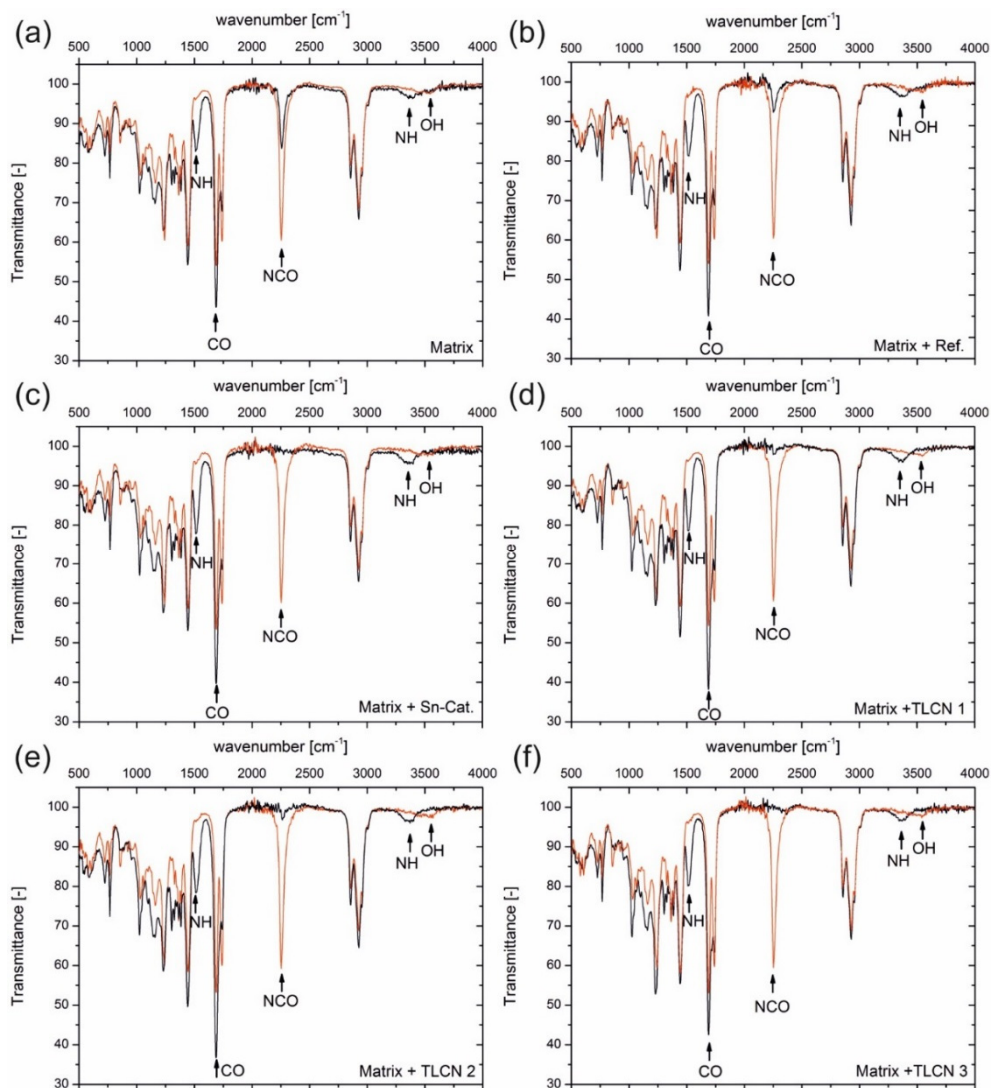


Figure 19. FT-IR spectra comparing the cured PU-film before (red) and after curing (black) for 2 h at 120 °C.

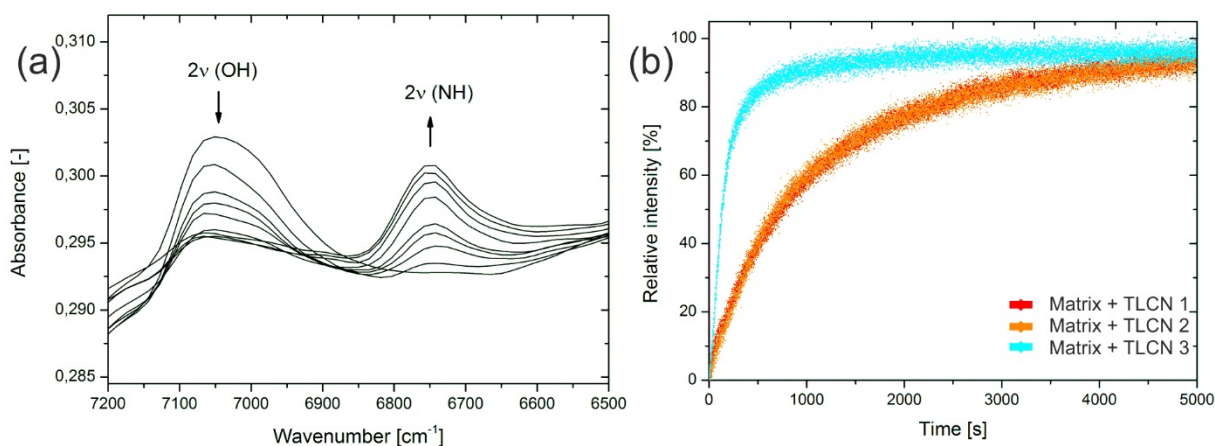


Figure 20. *In-situ* NIR-analysis of the curing at 120 °C. a) Selected spectra of the TLCN 1 catalyzed sample showing the consumption of the OH-groups of the polyol and the evolution of the urethane group over time. b) Urethane formation showing the absence of an induction period. Relative intensities are plotted over time.

4.1.5.3 Composite-Morphology

The distribution of capsules in the PU-matrix was analyzed via SEM measurements in cross-sections, made by a microtome. Figure 21 shows a very uniform distribution of individual particles or particle residues in the matrix. Their sizes are about 150 nm and they seem to be well enwrapped by the matrix. Also, no agglomerates were found in the analyzed areas.

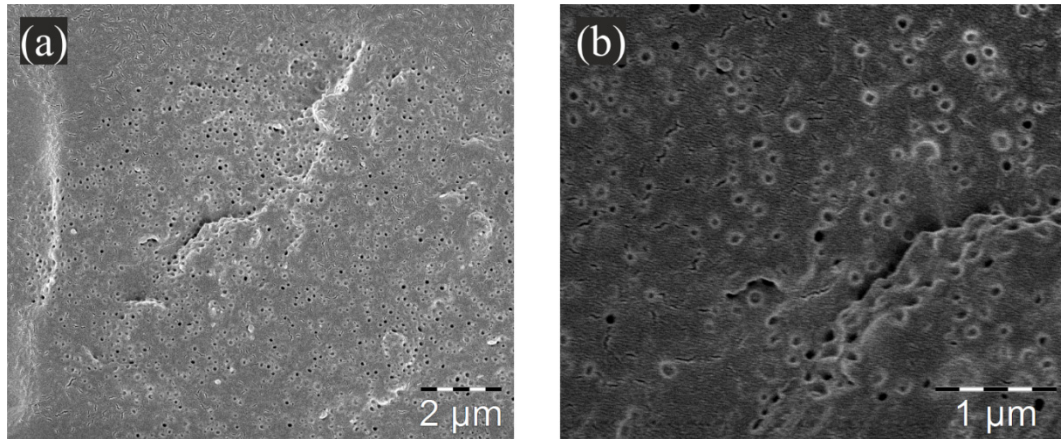


Figure 21. SEM measurements of the TLCN 1 cured PU-composite in a) lower and b) higher magnification showing uniformly distributed particles or particle residues of about 150 nm size.

We then used the very same system (PU+TLCN 1) to produce a reinforced glass-fiber composite by resin transfer molding. The set-up is schematically shown in Figure 22e). Several layers of $\pm 45^\circ$ biaxial glass-fibers are fixed within the mold and sealed. They are infused by pumping the PU+TLCN 1 mixture through the mold in the direction of the red arrows to produce a composite with a total fiber volume of 50%. It is crucial for a successful preparation of such composites, that no filtering occurs during the infusion process which usually eliminates the use of microcapsules in these processes. However, with the TLCN 1 nanocapsules, we obtained a homogenous, completely infused composite. Figure 22 compares the non-catalyzed matrix a) with the TLCN 1 catalyzed sample b) to show the macroscopic differences in mechanical moduli. We checked for complete curing by performing dynamic mechanical analysis (DMA) on different positions as marked in Figure 22e) and determined a T_g of $44 \pm 0.8^\circ\text{C}$ by the peak maximum of the loss factor as shown in f). We did not see any differences along the infusion direction, which proves that no significant filtering of the nanocapsules occurred during inception molding. Furthermore, the composite morphology was analyzed by SEM. Figure 22c) shows the composite at a low magnification. The micron-sized fiber-bundles are visible, as well as the surrounding PU-matrix. In d), the morphology can be seen at a higher magnification. On the left side, a single fiber is visible which is surrounded by the PU-matrix. Many possibilities arise based on this model system, for instance further studies

using different polyols and isocyanates will be carried out to specifically tune the adhesion to the glass fibers.

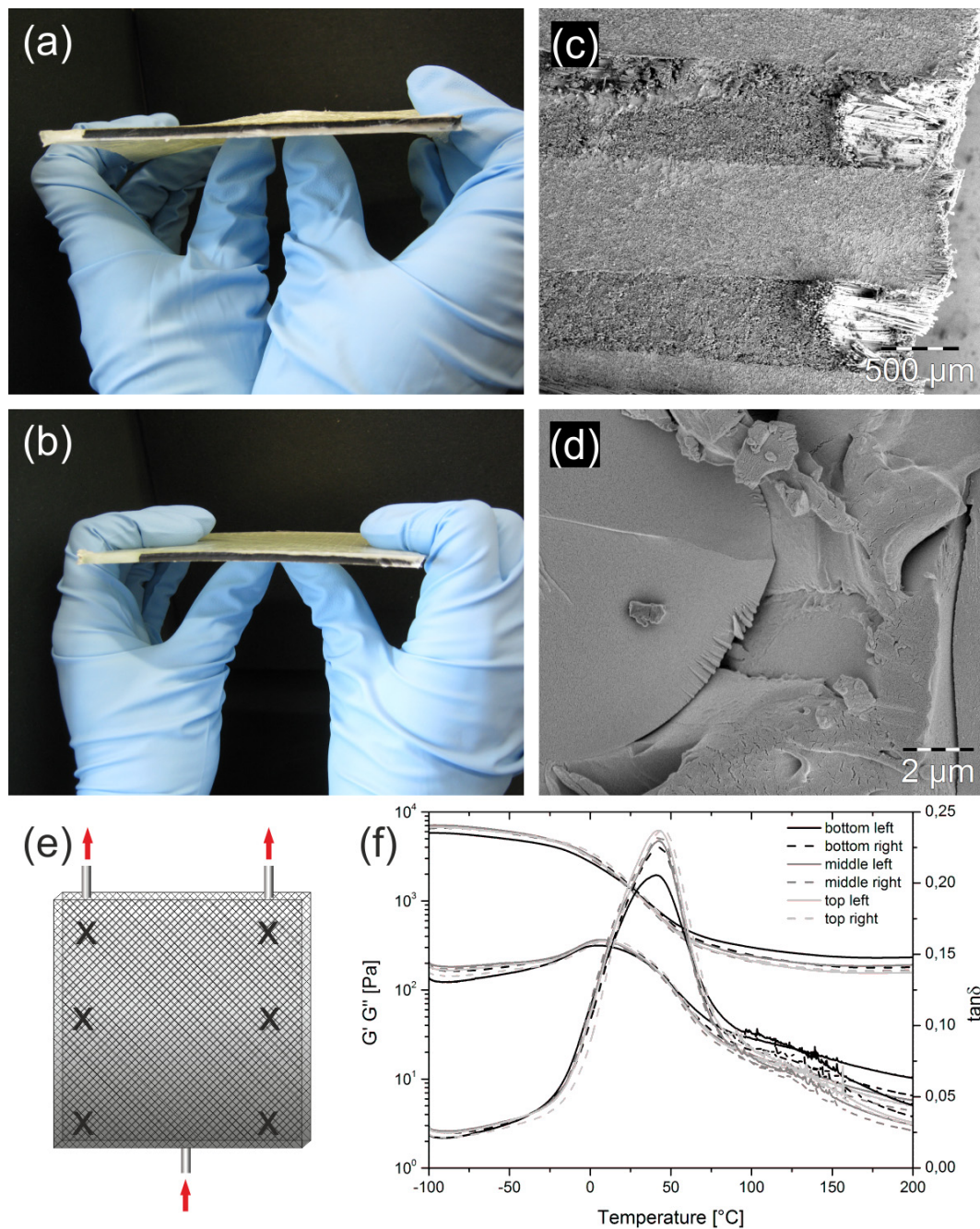


Figure 22. Optical images of a) the non-catalyzed and b) the TLCN-1 catalyzed composite after 2 h of curing. SEM images showing a cross-section of the TLCN-1 cured composite with c) low and d) high magnification depicting one fiber enwrapped in the PU matrix. e) Schematic representation of the reinforced composite and direction of flow. DMA analysis was performed on the sports marked with an X. f) DMA measurements showing the loss/storage modulus of the marked spots and the loss factor as a function of temperature.

4.1.6 Conclusion

In conclusion, a colloidal approach for switchable catalysis with a pronounced non-Arrhenius behavior was investigated. Due to the encapsulation into polymer nanocapsules, it was possible to yield a thermolent behavior, in principle for any catalyst. The approach was proven successful for the curing of reactive systems, which was demonstrated by the curing of an aliphatic polyurethane system as a model system. It was possible to prepare uniform and stable nanocapsules with various loads of a commercially available PU-catalyst, thus rendering complex synthesis and labelling issues of new compounds redundant. The release profiles could be tuned either by varying the catalyst loading due to an increased plasticizing effect on the polymer shell which lowered the release temperature. Another possibility was the variation in the degree of cross-linking. The threshold-temperature range was in between 80 and 120 °C. The possibility to use this nanocapsule-approach in infusion processes, where remarkably no filtering occurred due to the small sizes of the nanocapsules, may especially be useful for applications in the automotive or aerospace sector.

Further studies will be carried out on basis of these findings. One is the investigation of inductive heating as an alternative release mechanism by the incorporation of magnetite nanoparticles into the catalyst capsules. The second approach focusses on the storage stability of the capsules in different polyols, since the polymer shell investigated in this chapter may be sensitive towards swelling, especially if polyols with a high Hansen Solubility Parameter for hydrogen bonding, like 1,4-butanediol are used. To increase the storage stability, the formation of an additional shell on the capsules, e.g. by silica will be studied. In summary, the transformation of a homogenous catalyst into a colloidal system is a very versatile tool to significantly tune the activity of a standard catalyst.

4.2 Reaction Latency in “pseudo” 1K Systems

4.2.1 Motivation

The previous chapter demonstrated one approach, where latency was triggered by temperature in a system of moderate reactivity, thus requiring a catalyst. Within this section in contrast, as stated in chapter 2.6.2, latency was investigated in a highly reactive, so-called “pseudo-one-component” (P1K)-system, consisting of two types of reactive colloids in one dispersion. As a consequence, the only trigger needed is their application on a substrate as shown in Figure 23. Upon evaporation of the aqueous phase, both components start to crosslink and form a continuous film. Latency is generated solely by their spatial separation in colloidal state. Epoxides and amines were used as model compounds for the preparation of A&E-type colloids. The key issue for the preparation of a P1K-system is to allow their coexistence in dispersion, despite their predominant tendency to react. Any type of collision or molecular diffusion results in premature reactions, which need to be suppressed efficiently. This involves not only a deep understanding of their curing kinetics in bulk and upon film formation but also involves several requirements:

For the materials:

- a) Identification of hydrophobic and reactive amines which can form stable emulsions
- b) Fast curing in bulk and homogeneous film formation
- c) Moderate or high cross-linking density and T_g to form thermosetting polymers.

For the colloids:

- a) Stabilization of amine emulsions
- b) High colloidal stability
- c) Similar particle sizes for both A&E type colloids to hinder Ostwald ripening
- d) Suppression of molecular diffusion
- e) Determination of a suitable characterization method to detect premature reaction without triggering the film formation.

The following section is therefore subdivided into three parts. The first describes the properties and curing kinetic of the P1K-systems in bulk, the second deals with the stabilization of hydrophobic amines by the use of functional epoxy surfactants and the last section describes the behavior of P1K-systems in colloidal state and investigates their film formation.

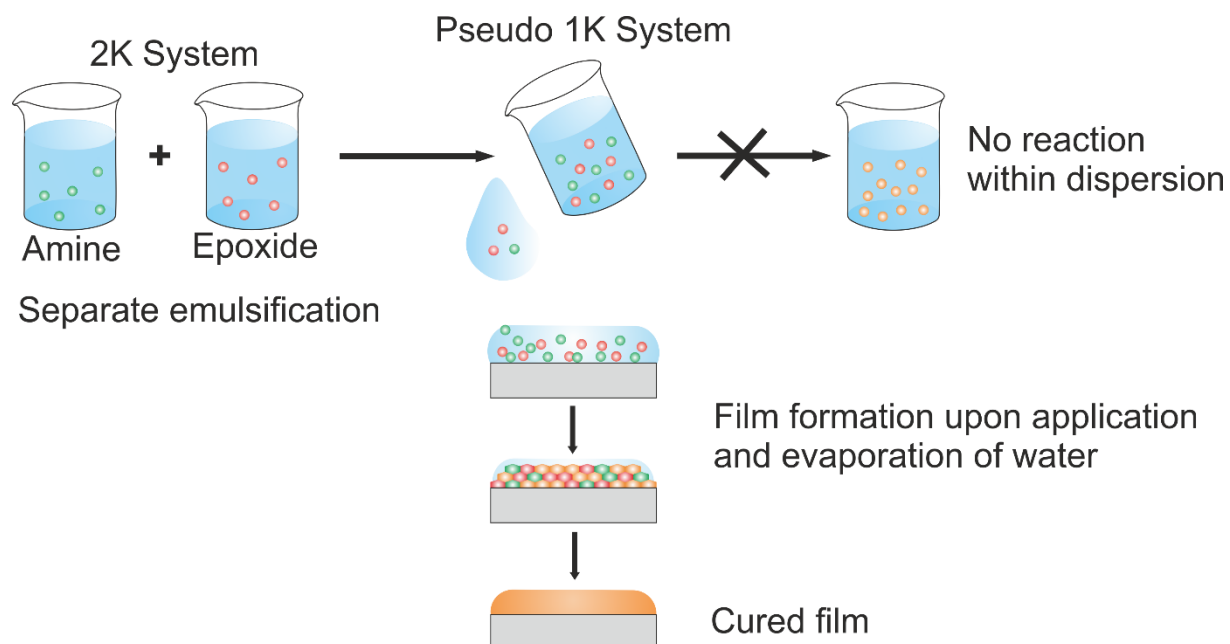
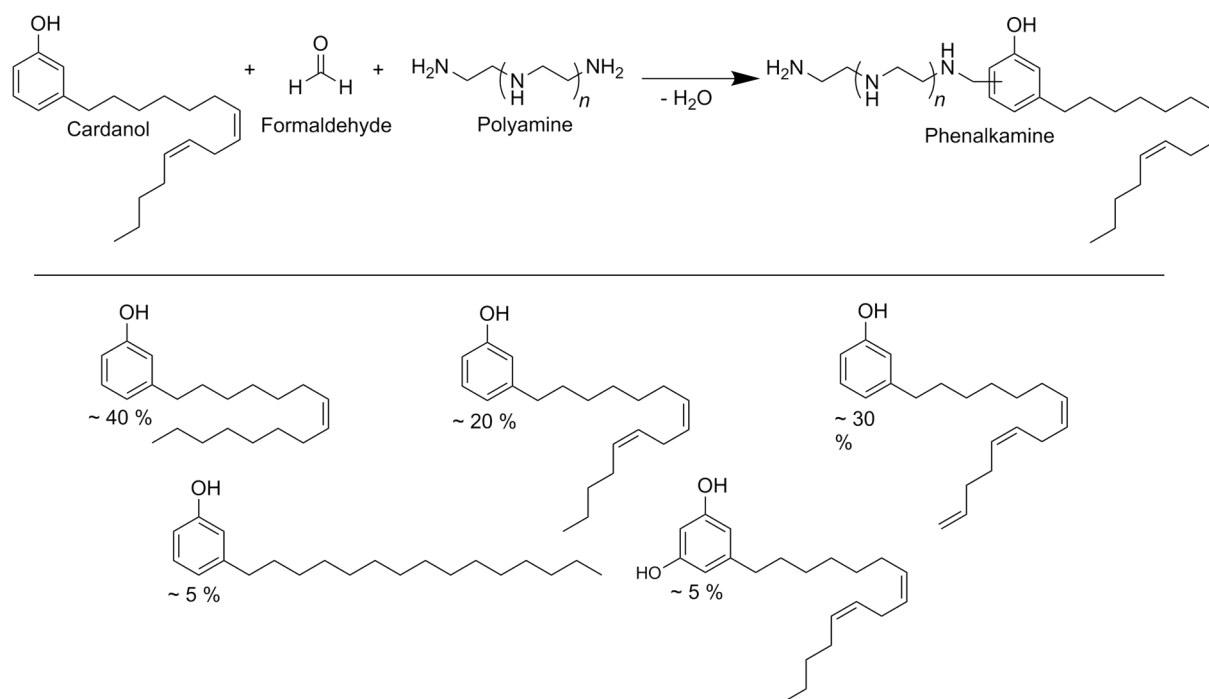


Figure 23. Preparation and principle of a P1K-system from epoxy resins and polyamines.

4.2.2 P1K-Thermosets

4.2.2.1 Hydrophobic Polyamines

As described in chapter 2.4.1, phenalkamines fulfill the requirements of a hydrophobic and at the same time reactive curing agent, thus making them good candidates for the preparation of P1K-systems. The phenalkamines used throughout this work are obtained by a Mannich type condensation of cardanol with a different (poly) amines and formaldehyde as shown in Scheme 5. The cross-linking density after curing can be varied by the type of polyamine used. The OH-group from the phenol enables fast curing, also at ambient or low temperatures and additionally improves the adhesion to the substrate.²⁰⁴ The long carbon chain from the cardanol provides a high hydrophobicity and therefore a good water and corrosion resistance. The unsaturated double bonds along the chain also result in an increased flexibility and allow for further chemical modification.²⁰⁴ The cardanol itself varies in degree of unsaturated bonds in the side chain, as summarized at the bottom of Scheme 5, which makes spectroscopic analysis of the phenalkamines very challenging. For their use in P1K-systems, they are best characterized in terms of their functionality and reactivity.



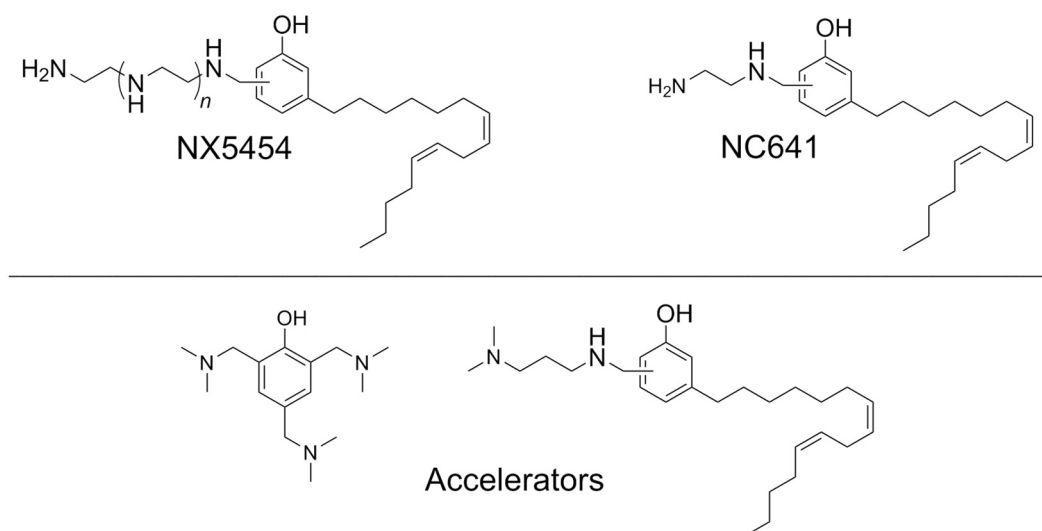
Scheme 5. Top: Synthesis and tentative structure of the phenalkamines by Mannich type reaction of cardanol with polyamines and formaldehyde. Bottom: Average composition of the distilled cardanol.

Throughout this work, two slightly different phenalkamines were used. Their exact structure is trade secret, therefore only a tentative structure which was also reported earlier is given in Scheme 6.²⁰⁵ The amine moiety of the NX5454 is mainly based on diethylenetriamine (DETA), whereas the amine moiety of the NC641 is mainly based on ethylenediamine (EDA). Both are mixtures of oligomers and not pure chemicals. They also contain low molecular weight impurities, which had to be removed by solvent extraction with water for at least three times until the aqueous phase was clear. The water solubility was twice determined gravimetrically on the basis of OECD Guideline 105 to be $107 \pm 18 \text{ mg L}^{-1}$.²⁰⁶ The molecular weight for the NX5454 after purification was determined to be $M_w = 429 \text{ g mol}^{-1}$; PDI = 1.3 via SEC measurements in THF. Elementary analysis gave a composition of 79.25% C, 10.30% H and 4.85% N. The amount of nitrogen present in the sample was further confirmed via potentiometric titration resulting in an average number of 1.5 nitrogen groups per molecule. About 60% of those were determined to be primary nitrogen. The number of functional groups was determined by potentiometric titration of give an AHEW of 220 g eq^{-1} . Compared to the non-purified sample, the AHEW has decreased significantly (see Table 6), which means that the formulation contained a considerable amount of water soluble amines. This will later on cause premature reactions in the P1K-system. For the slightly more hydrophobic NC641, the AHEW after purification was 142 g eq^{-1} , which is only slightly decreased compared to the non-purified sample, indicating that lower amounts of water soluble amine were present in the formulation. The Nitrogen titration also revealed the presence of tertiary amines, which were not removed upon the purification. They most likely origin from two accelerators present, which are supposed to promote the epoxy curing, as shown in the lower part of Scheme 6. One is 2,4,6-tris (dimethylaminomethyl)phenol, which is often used in epoxy curing and the second one is most likely a Mannich condensate of 3-aminopropydimethylamine with the cardanol as well.

Table 6. Nitrogen content and AHEW of the phenalkamines by potentiometric titration after their purification.

Name	N _{total} [%]	N _{Prim.} [%]	N _{Sek.} [%]	N _{Tert.} [%]	AHEW _{before} [g eq ⁻¹]*	AHEW _{after} [g eq ⁻¹]**
NX5454	4.85	2.79	0.94	1.19	133	220
NC641	6.71	4.65	1.27	0.79	130	142

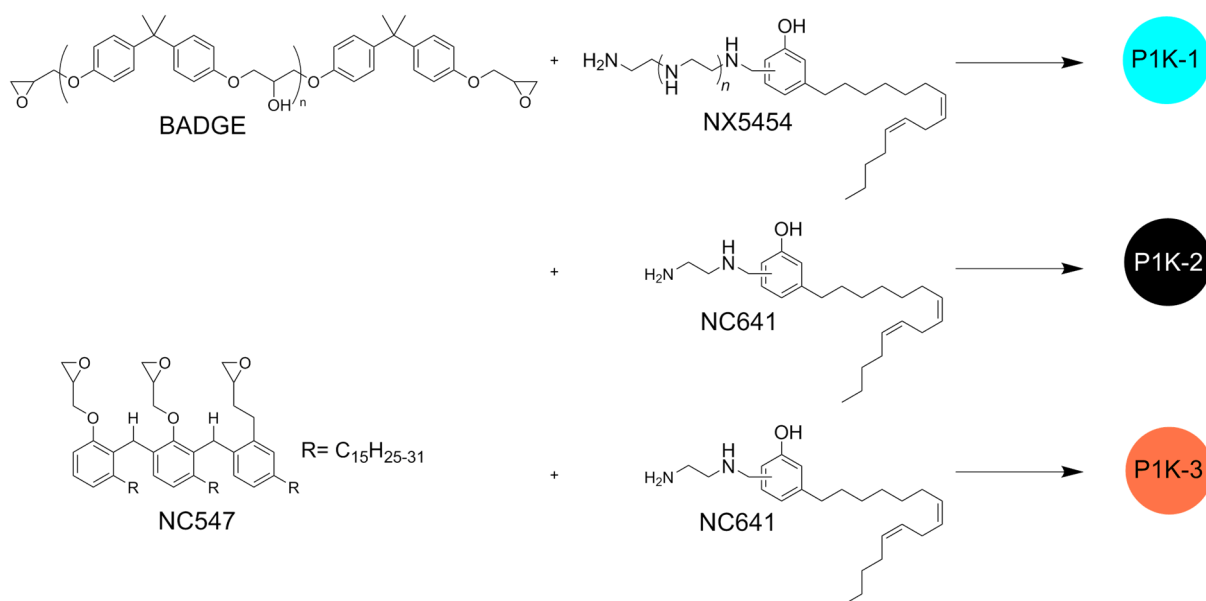
* According to MSDS of the supplier, ** By potentiometric titration.



Scheme 6. Simplified structure of the NX5454 and NC641 phenalkamines and possible structures of the accelerators present in the formulations to promote the epoxy curing.

4.2.2.2 P1K-Systems

Three different combinations of epoxides with phenalkamines were investigated to see if they can be used for the formation of P1K-systems (Scheme 7). The P1K-1 consists of BADGE as benchmark in epoxy curing and was combined with the phenalkamine NX5454. BADGE was further combined with the slightly more hydrophobic phenalkamine NC641 to give the P1K-2. In the P1K-3 system, this phenalkamine was combined with the cardanol-based epoxide (NC547), which is originally used as functional modifier in epoxy formulations. The systems were mixed stoichiometrically for their curing according to their EEW and AHEW.



Scheme 7. Simplified compositions of the different P1K-systems.

4.2.2.3 Properties

In a first step, the thermal properties of the educts were characterized by DSC and rheology measurements. Figure 24a) shows the stacked DSC curves in a temperature range from -50 °C to 50 °C. It is well known for the BADGE to crystallize at low temperatures, which can be seen in the red curve, showing a distinct melting peak at -15 °C. The cardanol-based epoxide in contrast does not show any tendency to crystallize. Both phenalkamines show similar behaviors. Their low crystallization tendency can be explained by the C₁₅-hydrocarbon tail of the cardanol. The cis-configuration of the double bonds require more space and thus decrease the overall order to an extend, which disables crystallization of the materials over wide temperature range.

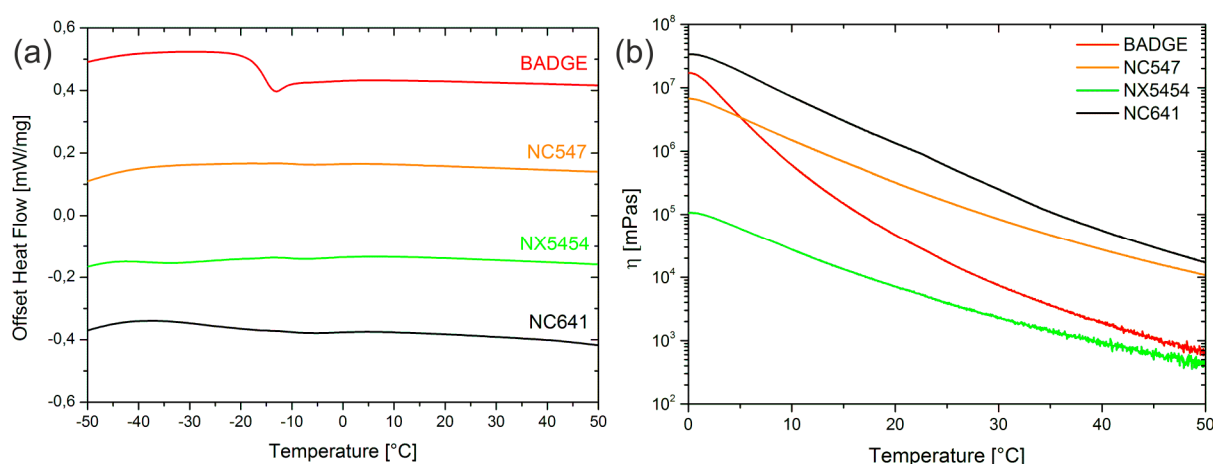


Figure 24. a) DSC curves of the epoxides and amines to show their crystallization tendencies at low temperature. b) Viscosity of the epoxides and amines as function of temperature from 0 to 50 °C as a logarithmic plot.

As described in chapter 2.5, interdiffusion is important for the formation of coherent films which is among other factors, significantly dependent on the educt-viscosities. Figure 24b) summarizes the temperature dependent viscosities of both epoxides and amines. They strongly increase in the order NX5454 < BADGE < NC547 < NC641, which will most likely decrease the overall mobility of the forming polymer chains upon their film formation in the same order. The NC547 and the NC641 remain viscos even at elevated temperatures.

Table 7. Properties of the educts used for the preparation of the different PIK-systems.

Name	M_w [g mol ⁻¹]	AHEW [g eq ⁻¹]	EEW [g eq ⁻¹]	η @ 25 °C [mPa s]
NX5454	429	220	n.a.	3930
NC641	372*	142	n.a.	160000
BADGE	380	n.a.	187	17600
NC547	2289*	n.a.	763	585000

*Calculated based on idealized structure.

As a consequence, in a second step the reactivity and the properties of the cured P1K-thermosets were investigated as a comparative study in bulk. To determine their reactivity, oscillatory rheology measurements were carried out at RT and the complex viscosity is shown as a function of time on a logarithmic scale. The potlife is defined by DIN EN 14022 as the time needed for a system to double its initial viscosity at 25 °C. All systems show an immediate increase in viscosity with very short potlives of about 10 to 20 min, as summarized in the inlay in Figure 25. This only serves as a rough comparison, since the systems strongly differ in their initial viscosities. As expected, their viscosities increase from P1K-1 < P1K-2 < P1K-3 over several orders of magnitude as the curing proceeds. The trend of the complex viscosity is very similar for the P1K-1 and P1K-2 with an increase of approximately 4 orders of magnitude. The P1K-3 only shows an increase in η^* of about two orders of magnitude, with a slightly longer potlife of about 18 min. By comparing the P1K-1 to the P1K-2, the effect of the type of phenalkamine becomes visible, since the epoxide is the same. Both amines are structurally comparable, yet they strongly differ in their viscosities by a factor of approximately 16. An initial lower viscosity generally enables a faster diffusion of the two components towards each other and therefore enables a faster reaction. Secondly, the reactivity is also dependent on the nature of functional groups. As already explained in chapter 2.4.1, primary amine groups are more reactive than secondary and will be the first to react with the epoxide. The secondary amines will only gradually increase the network density of the thermoset, if the diffusion is not hindered too much by the already cross-linked polymer chains. Judging from that point of view, the reactivity of the two phenalkamines should be comparable as is their curing behavior despite the differences in initial viscosities. Both systems reach a steady state after a curing time of about 4 h. By comparing the P1K-2 and P1K-3 instead, the effect of the epoxide on the overall reactivity can be seen. Both epoxides differ in viscosity by a factor of two. Nevertheless, for the P1K-3 the viscosity only gradually increases over time. This can more likely be attributed to reactivity differences between both epoxides. As expected, the bisphenol-A based epoxide seems to be more reactive than the epoxidized cardanol. This may be due to steric reasons, as well as due to the presence of hydroxyl groups in the BADGE, which also additionally catalyze the curing reaction.

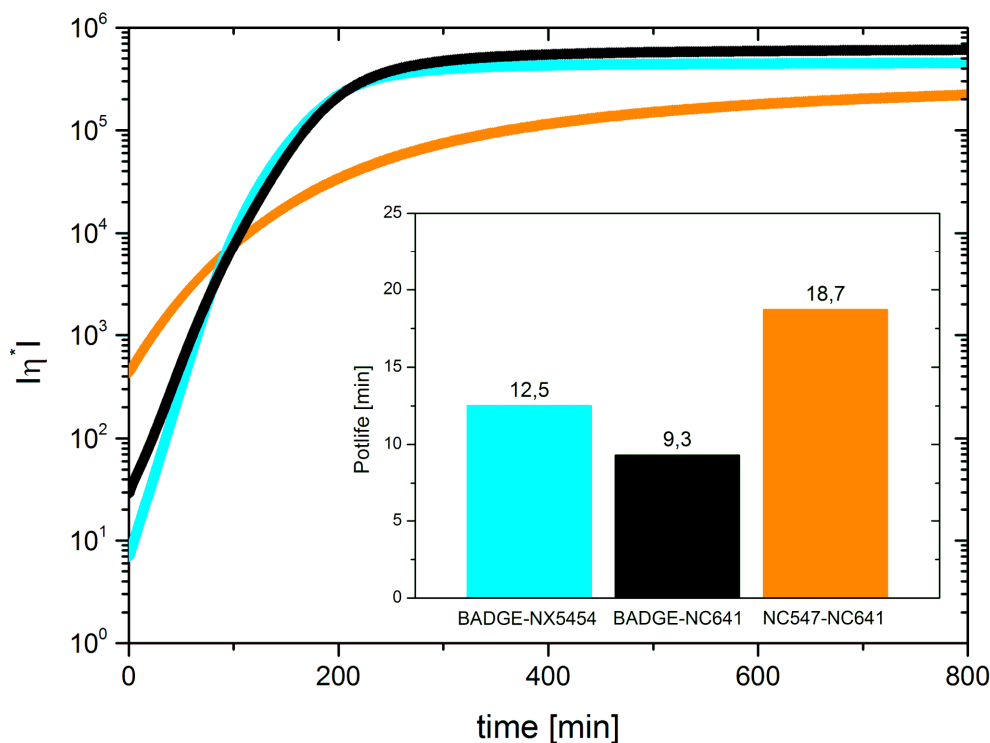


Figure 25. Curing kinetics of the different P1K-systems at RT in bulk. Inlay: Comparison of the potlives of the P1K-1 to 3.

Also, the gelation-point where G' equals G'' and the loss factor becomes one, is reached in comparable times for all three systems (Figure 26, upper part). For the P1K-2 it is reached after about 2.6 h, for the P1K-1 after about 3 h and for the P1K-3 after approximately 3.2 h. Subsequently, the samples were heated to ensure complete curing and their T_g s were determined. For all systems including the purely cardanol-based P1K-3, they are well above RT, as required for most thermosetting materials.

The storage modulus (G') above the T_g can be used to compare the network density as shown in Figure 26 (bottom) and summarized in Table 8. A denser network in general corresponds to higher G' values. Dense networks are obtained for all three systems, displaying storage moduli in the same order of magnitude. The highest values are obtained for the P1K-2.

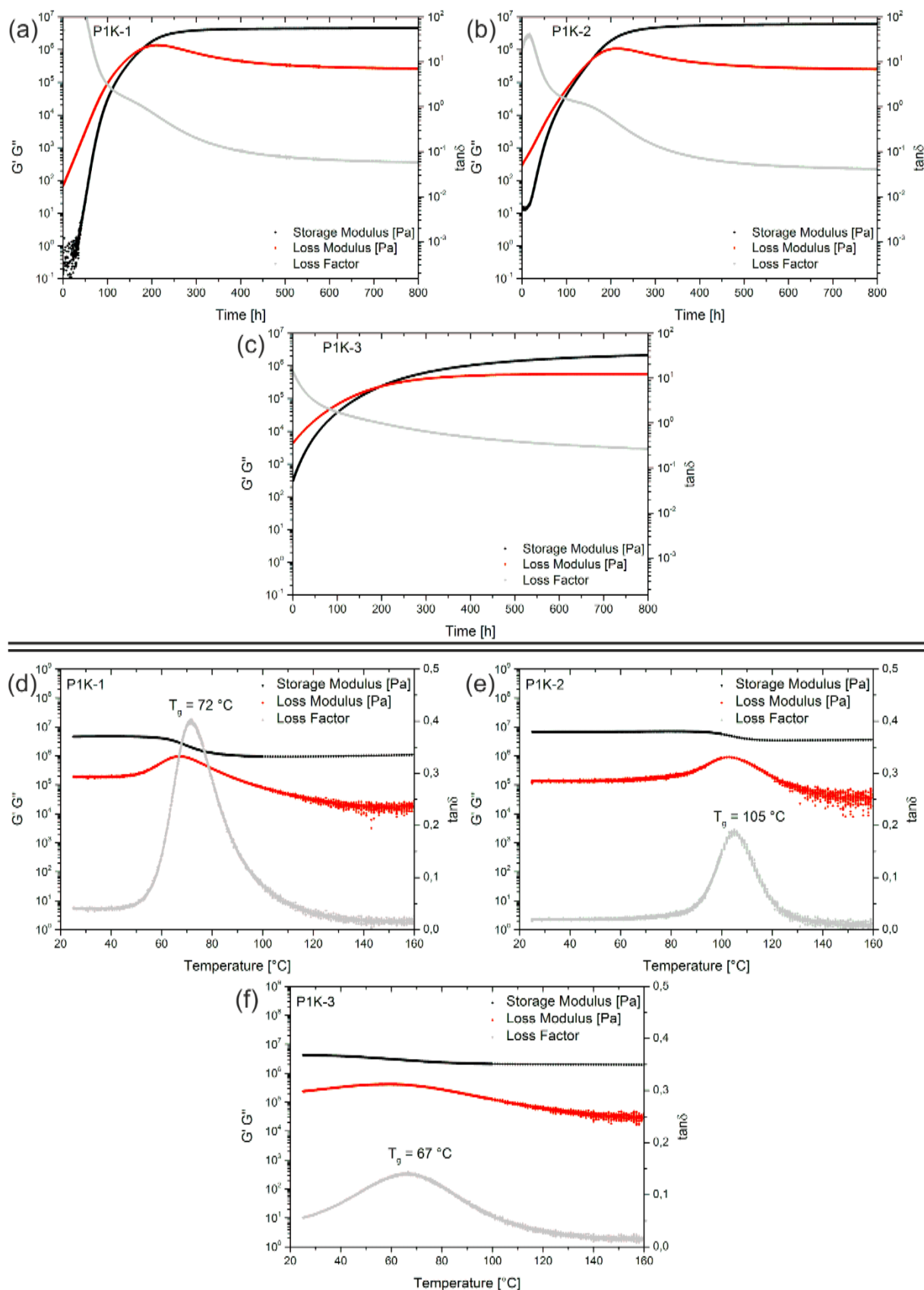


Figure 26. Top: Evolution of mechanical properties of the different P1K-systems upon room-temperature cure. Bottom: Rheological determination of the T_g s of the different P1K-systems after their post-cure at 160 °C for 2 h.

The curing enthalpy of the P1K-systems was investigated via DSC measurements as shown in Figure 27, in a stacked plot of the exothermal curing process. Here, the systems strongly differ from each other. For better comparison, the enthalpies were normalized to Joules per epoxy group. The curing of the P1K-1 is the most exothermic with about $238 \text{ J g}_{\text{epoxy}}^{-1}$. In comparison, the curing enthalpy of the P1K-2 is less than half. For the P1K-3, the overall functionality compared to the BADGE based systems is lower, which results in a smaller enthalpy change, however also the normalized enthalpy is again compared to the P1K-2 only about 1.6 times less.

In comparison, the rheology provides more conclusive results, since high moduli and densely cross-linked networks can only be obtained in fully cured systems.

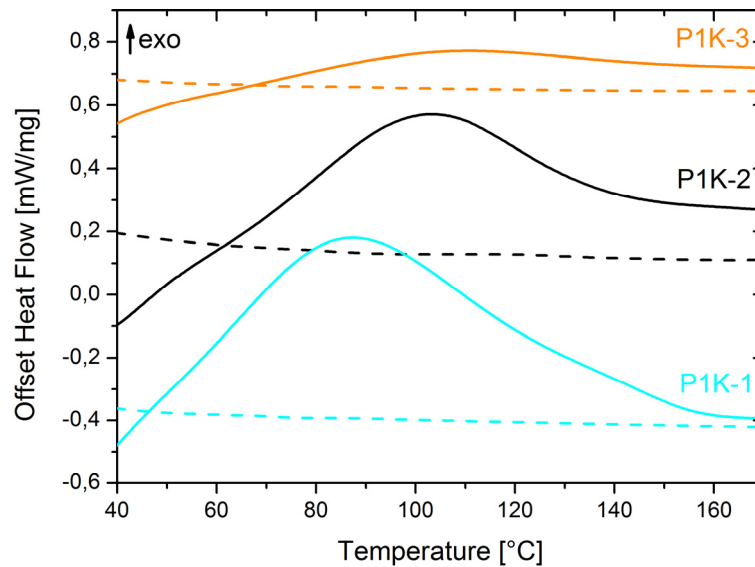


Figure 27. Stacked curing enthalpies (prior to their normalization to $\text{J g}_{\text{epoxygroup}}^{-1}$) of the different P1K-systems from RT to $170 \text{ }^\circ\text{C}$. 2nd heating cycles are depicted as dashed lines.

Table 8. Summary of the curing and thermal properties of the different P1K-systems.

Entry	ΔH [J g^{-1}]	ΔH [$\text{J g}_{\text{epoxygroup}}^{-1}$]	Potlife [min]	$G'_{120^\circ\text{C}}$ [Pa s]	$\tan\delta=1$ [min]	T_g [$^\circ\text{C}$]
P1K-1	253	238	9.40	$9.66 \cdot 10^5$	180	72
P1K-2	163	123	6.20	$3.46 \cdot 10^6$	157	105
P1K-3	36	75	10.85	$2.04 \cdot 10^6$	197	67

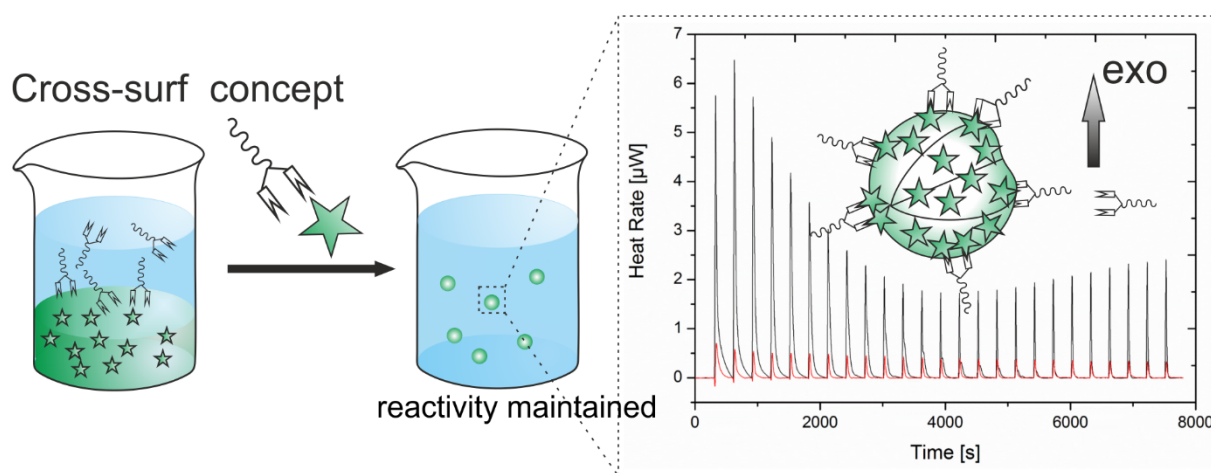
Summarizing the results so far, all three systems meet the requirements set for a P1K-system. It was possible to prepare thermosets from all three combinations with very short curing times and high reactivities at room temperature.

Furthermore, all raw materials are highly hydrophobic. Judging from Table 8, the system which best meets the requirements for the P1K-concept would be the P1K-1, since it is the most reactive amongst the three. On the contrary, the P1K-3 consists solely of bio-based raw materials, which makes it the most appealing in terms of the development of sustainable products.

The next crucial step for the preparation of a P1K-dispersion is now the stabilization of amine emulsions in water, which is subject of the next chapter.

4.2.3 Cross-Linkable Surfactants*

Highly reactive emulsions were stabilized by employing a surfmer analogous concept. An interfacial reaction between an emulsion droplet and a cross-linkable reactive surfactant was used to provide colloidal stability and simultaneously maintain the majority of the reactive groups by a polyaddition-type reaction between epoxy and amine to spontaneously and covalently bond the surfactant to the emulsion droplets. The interfacial reaction was monitored via isothermal titration calorimetry analysis. With this method, the increased colloidal stability could be attributed to a reaction rather than a pure physical adsorption. The maintained reactivity of the emulsion droplets enables their use in the PIK-systems since no dense shell is formed which would prohibit their film formation.

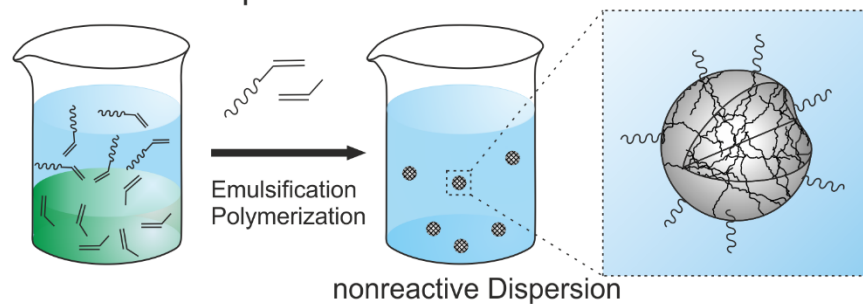


This chapter is based on the publication “Alternative Pathway for the Stabilization of Reactive Emulsions via Cross-Linkable Surfactants” by Ann-Christin Bijlard, Svenja Winzen, Kenji Itoh, Katharina Landfester and Andreas Taden published in 2014 in *ACS Macro Letters*, 3(11), pages 1165-1168.^[250] Reprinted with permission. Copyright 2016 American Chemical Society.

4.2.3.1 Motivation

As previously described, the stabilization of hydrophobic amines in water is challenging because they tend to be at least partially hydrophilic, due to the nature of their functional groups. It was not possible to obtain stable emulsions with commercial surfactants like SDS or cetyltrimethylammonium bromide (CTAB). Nonionic surfactants improved the stability but only allowed for a limited storage stability. Hence, a functional surfactant needed to be developed, which increased colloidal stability. Reactive surfactants have proven to exceed the performance of pure physisorbed surfactants in many cases due to their covalent incorporation into the polymer structure as described in chapter 2.2.2.³⁴ Those surfmers, they consist of amphiphilic molecules with a polymerizable unit and are especially known for free radical emulsion polymerization to obtain systems with improved coating adhesion and water resistance.^{28, 207} The surfmer concept was further employed for polyaddition reactions, i.e. in benzoxazine³⁷ or polyurea/polyurethane²⁰⁸⁻²¹³ based systems. The film formation of polymer lattices can be improved by the use of polymeric surfactants which can actively participate in the cross-linking upon film formation. This was demonstrated by the use of different types of benzoxazine (BOX)surfmers (linear and gemini type) which were used for the stabilization of BOX-nanoparticles.³⁶ The surfmer was however not covalently attached to the particles, but reacted upon temperature induced curing of the applied BOX films to increase the compatibility and reduce the water uptake of the film. What all these approaches all have in common is: i) the functionality of the surfmer equals the functionality of the monomer and ii) that the reactive species are fully consumed upon the respective polymerization reactions. Since it is crucial for the majority of the amine to remain reactive to be used in the PIK-system, we chose to stabilize the emulsion by an interfacial reaction between the active material and the reactive surfactant (schematic representation in Figure 1). Polyaddition-type reaction between an amine and a reactive cross-linkable surfactant (“cross-surf”) containing epoxy groups was used as a model system. High shear force miniemulsification was utilized to obtain small, narrowly distributed nanodroplets. Miniemulsion droplets are typically not densely covered with surfactant molecules and often referred as “critically stabilized”.⁸ In this respect the cross-surf concept and its ability to react with amine droplets can hardly be considered as encapsulation mechanism or dense shell formation, and might be seen as soft interface functionalization (or deactivation) instead.

Surfmer concept



Cross-surf concept

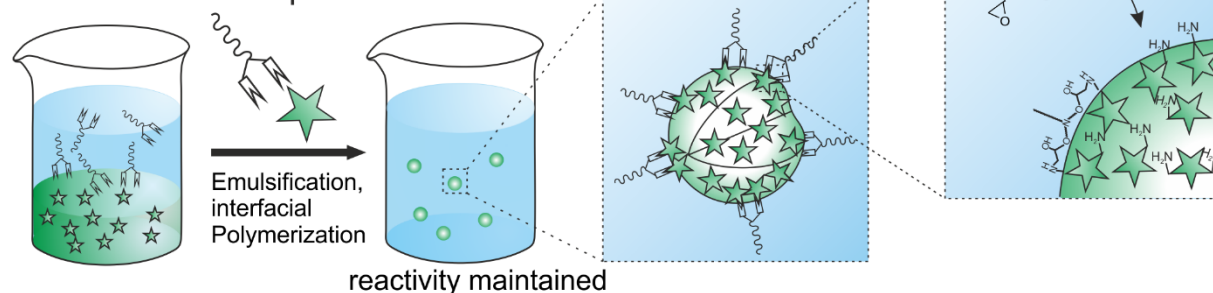


Figure 28. Comparison of the surfmer concept to the cross-surf concept, which allows the effective stabilization of active materials via interfacial reactions.

Therefore, oligomeric epoxy surfactants (ES) were synthesized, comprising a bifunctional reactive glycidyl headgroup and a nonionic, mainly poly(ethylene oxide) (PEO) based tail (Scheme 8). The length of the hydrophilic tail was systematically varied as well as the stoichiometry of the addition reaction (see Table 9). The HLB values were calculated and summarized in Table 10, showing that in principle all surfactants are classified for the stabilization of oil-in-water (o/w) emulsions.²¹

Table 9. Composition of the synthesized surfactants.

Hydrophobic head	Hydrophilic tail	M [g mol ⁻¹]	Epoxy functionality	Ratio _{PPG/PEO}
BADGE	-	380	2	-
	L100	1000	-	3/19
	L200	2000	-	2/42
	L300	3000	-	8/58

between the formed hydroxyl groups occurred, which was monitored by measuring the EEW over time as shown in Figure 29 b). The initial content was calculated since no solvent was used therefore the polyetheramine had to be molten prior to the reaction which had already started upon mixing the two components. If the alkoxide or alcohol groups would attack the epoxide, the epoxide groups would be fully consumed during the reaction which is not the case.

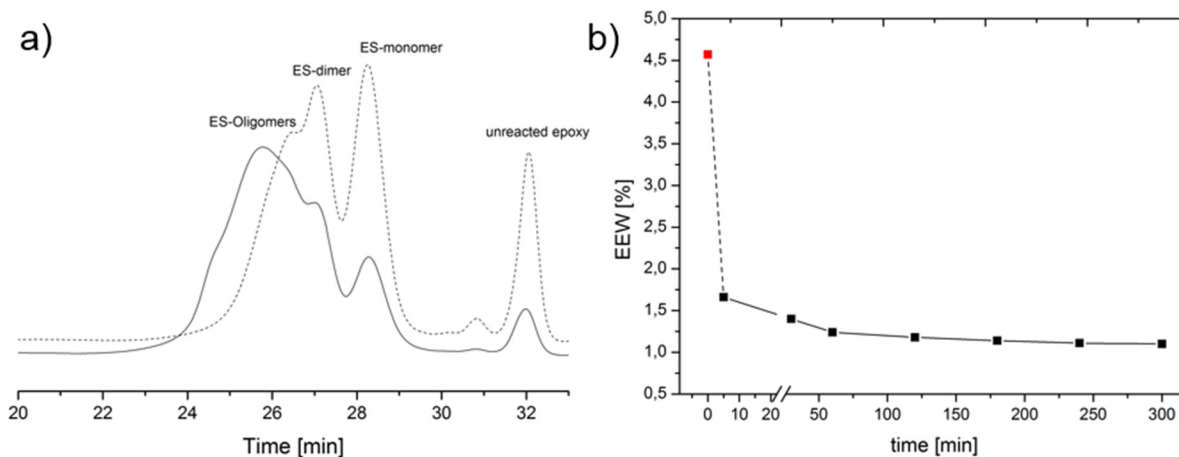


Figure 29. a) SEC elugrams of the stoichiometric (2:1) polyaddition reaction (dashed line) and the 4:3 stoichiometry (solid line). b) EEW vs. reaction time for the 4:3 stoichiometry ES. First the EEW decreases quickly and reaches a steady state after approx. 120 min.

Surface tension measurements were performed to prove the surface activity of the ES series, as summarized in Table 10. Commercially available surfactant Lutensol AT50 was chosen for comparison, since it is a nonionic surfactant with a PEO₅₀ chain as hydrophilic tail and a C₁₆/C₁₈ alkane hydrophobic head group, thus making it comparable to the ES surfactants. All surfactants tested clearly show surface active behavior by strongly decreasing the surface tension already at low concentrations. Comparing the different types of surfactants the following trends can be seen: The ES₁₀₀ based surfactant with a rather short PEO chain shows the strongest decrease in surface tension. For the longer PEO chain epoxy surfactant, ES, the minimum surface tensions was determined to be around 55 mN m⁻¹ with a CMC value comparable to the Lutensol surfactant. For the ES₃₀₀ based surfactant, a slightly higher CMC was found.

Surface tension measurements of the nonreactive reference (nrES) also show surface active behavior. Compared to the ES surfactant it is derived from, the nrES shows only a slightly decreased ability to reduce the surface tension. The corresponding CMC is about 39 mg L⁻¹. This might be caused by the reduced hydrophobicity of the head of the surfactant.

Table 10. Properties of the epoxy surfactant series.

Surfactant	Stochio- metry	M_n [g mol ⁻¹]	HLB	γ_{min} [mN m ⁻¹]	CMC [mg L ⁻¹]	EEW _{theo} [%]	EEW _{exp.} [%]
ES_100	2:1	3069	9.7	n.d.	n.d.	2.7	2.8
ES_100	4:3	4885	11.3	50.4	35.5	1.8	1.8
ES	2:1	5397	13.5	n.d.	n.d.	1.6	1.8
ES	4:3	8025	14.9	53.1	31.5	1.1	1.1
ES_300	2:1	7320	11.4	n.d.	n.d.	1.2	1.4
ES_300	4:3	9462	14.7	56.3	41.6	0.9	0.6
Lutensol	n.a.	~ 2000	18*	46.8	32.1	n.a.	n.a.
nrES	comparable to ES 4:3			59.8	39.1	0.0	0.0

*According to Technical Data Sheet.

Figure 30a) shows the ¹H-NMR spectra for the ES: For the epoxide surfactants, the peaks at 7.1 and 6.8 ppm correspond to the aromatic protons of the benzene ring of the epoxy headgroup. The methyl groups of the epoxide appear at 1.6 ppm. The peaks of the methylene as well as the methine groups of the epoxide ring as well as the CH₂N group can be found at 2.7 and 2.9 ppm, indicating that the surfactant still carries reactive epoxide groups. The signals at 3.4 to 3.7 ppm origin from the methylene groups of the PEO chain of the hydrophilic tail. The peak at 1.1 ppm corresponds to the methyl groups of the PEO units. The ethylene oxide groups of the epoxide as well as the CH-OH group of the opened ring is found at 3.7-4.2 ppm. The peaks at 7.3 and 2.1 ppm origin from the solvent and water traces. Since the synthesized surfactant contains multiple oligomeric structures, the conversion of the reaction was not investigated quantitatively.

The nonreactive surfactant displayed in Figure 30b) shows the ring opening of the epoxy groups into the corresponding ester upon reaction with formic acid. The peaks at 2.7 and 2.9 ppm originating from the methylene groups of the epoxy ring disappeared thus indicating a successful reaction. Additional peaks at a chemical shift of 5.3 and 5.5 ppm can be attributed to the CHOH as well as 8.1 ppm to HC=O of the formed ester.

IR spectra of the ES (see Figure 30c)) show a characteristic peak at 935 cm⁻¹ originating from the valence vibration of the epoxy ring. Furthermore, the peaks at 1037 cm⁻¹ and 2872 cm⁻¹ show the CN and the CH₂-N valence vibration of the bonds formed due to the reaction with the polyether amine. The absence of the characteristic double N-H stretching peaks at 3000-3300 cm⁻¹ indicate the full consumption of the polyetheramine upon the reaction. The IR spectra

of the nrES reference (red line) shows the characteristic C=O peak as well as the disappearance of the epoxide peak which is also true for the phenalkamine “endcapped” nrES2 (blue line).

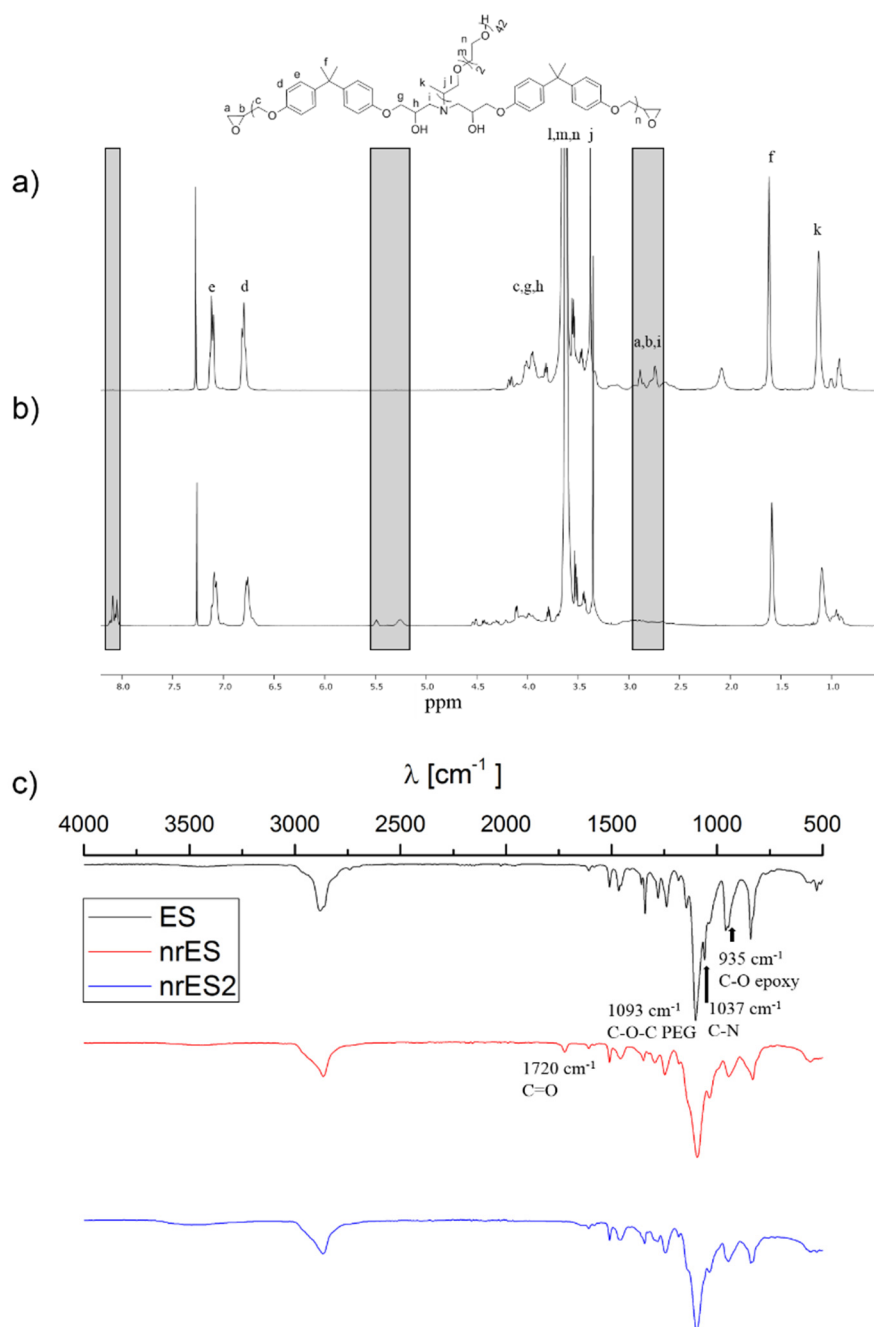


Figure 30. Spectral characterization of the ES and its nonreactive references with a) $^1\text{H-NMR}$ and b) FT-IR.

4.2.3.3 Colloidal Stability

The ability of the ES to stabilize the phenalkamine emulsion was investigated by varying the concentration ratio of the ES to the disperse phase. Figure 31a) illustrates that the Z-average particle size decreases from 415 nm to 124 nm when the surfactant to amine ratio (R_{SA}) is increased from 0.5 wt.% to 9 wt.%. Secondly, the colloidal stability was monitored over time by firstly comparing the influence of the length of the hydrophilic tail (Figure 31b)). Initially, the particle sizes of the ES_100 and ES_300 surfactants were almost identical, however after one day of storage, already an increase in particle sizes was observed. It was more prominent for the longer L300 based tail. After five days of storage, also the ES_100 stabilized particles started to increase, indicating an insufficient stabilization. For the ES stabilized emulsion instead, no increase in particle size was obtained, even after six months of storage as shown in Figure 31c). The use of the nonionic surfactant Lutensol AT50 ($C_{16/18}EO_{50}$) initially produced stable emulsions of very similar particle size but also had a limited long-term stability to a few days. A strong increase in particle size and partial phase separation was observed. To show that the increased stability was attributed to an interfacial reaction, emulsions with the nrES were prepared that also showed an even stronger increase in particle size. An analogously prepared miniemulsion with the nrES2 as surface active, but non-reactive surfactant had a particle size of $Z_{av} = 228$ nm compared to $Z_{av} = 134$ nm for the ES stabilized emulsion. This may be a hint that not only nrES2 is formed at the interface, but also cross-linked products. However, the overall amount of polymer formed is fairly low.

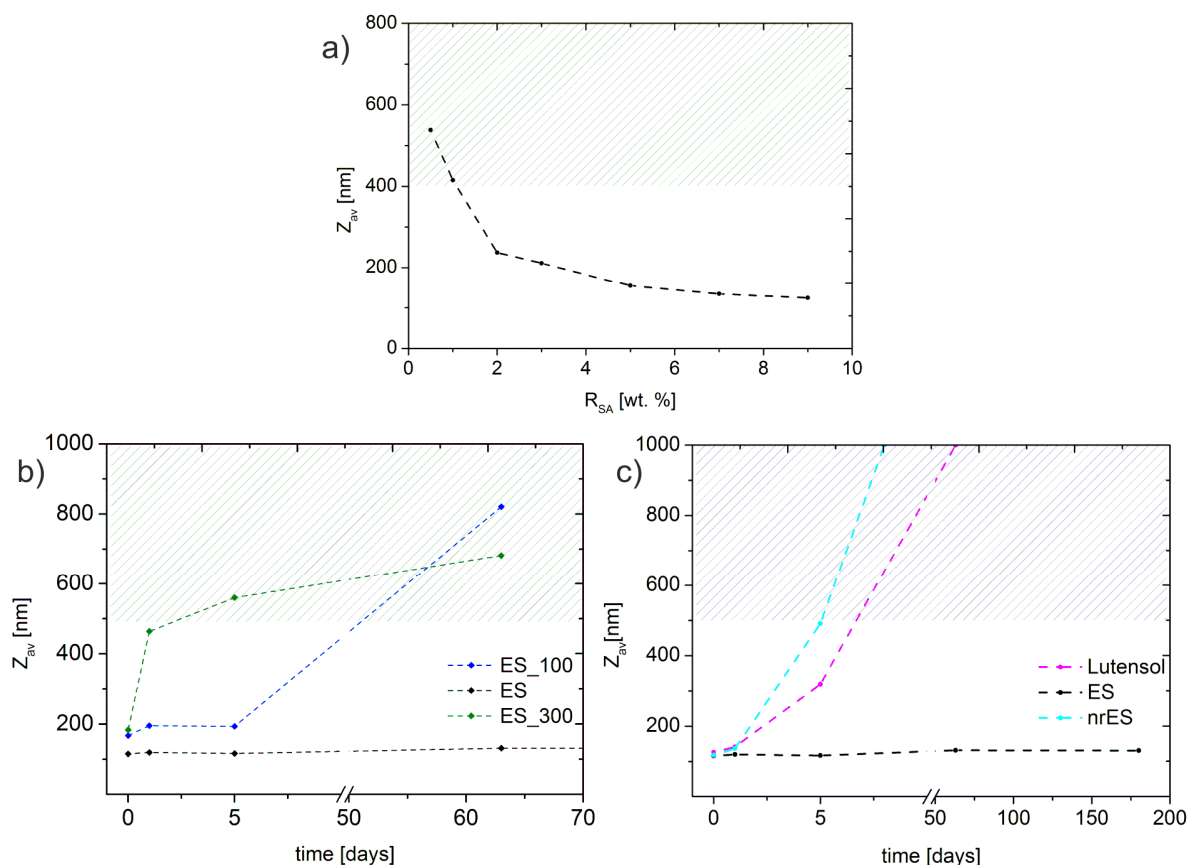


Figure 31. Colloidal stability of the amine emulsions. a) Dependency of the Z_{av} on the ES-concentration. Stability versus time plots comparing b) the different ES surfactants and c) the nonreactive references, showing the beneficial effect of the epoxy groups. Lines are meant to guide the eye.

4.2.3.4 Interfacial Stabilization

Isothermal titration calorimetry (ITC) was chosen to closer investigate the droplet surfactant interaction.^{160, 214-216} ITC is a well-known method to follow polymer-surfactant interactions, micellation or to investigate interfacial processes in emulsion.²¹⁷ A freshly prepared emulsion which was prestabilized with Lutensol was diluted to a droplet concentration of $1 \cdot 10^{-6}$ M as calculated according to the DLS data (153 nm). A 1 mM surfactant solution was titrated into the emulsion and into distilled water as a blank experiment to subtract the heat of dilution as shown in Figure 32a). Two experiments were carried out as references. Firstly, the nonreactive surfactant was titrated into the amine miniemulsion with all other parameters kept constant. Secondly, the reactive surfactant was titrated into a nonreactive miniemulsion. For this purpose, an epoxy miniemulsion was chosen, since it is structurally comparable to the headgroup of the surfactant. A number concentration in the cell was estimated similar to the amine miniemulsion on the basis of the DLS data (241 nm).

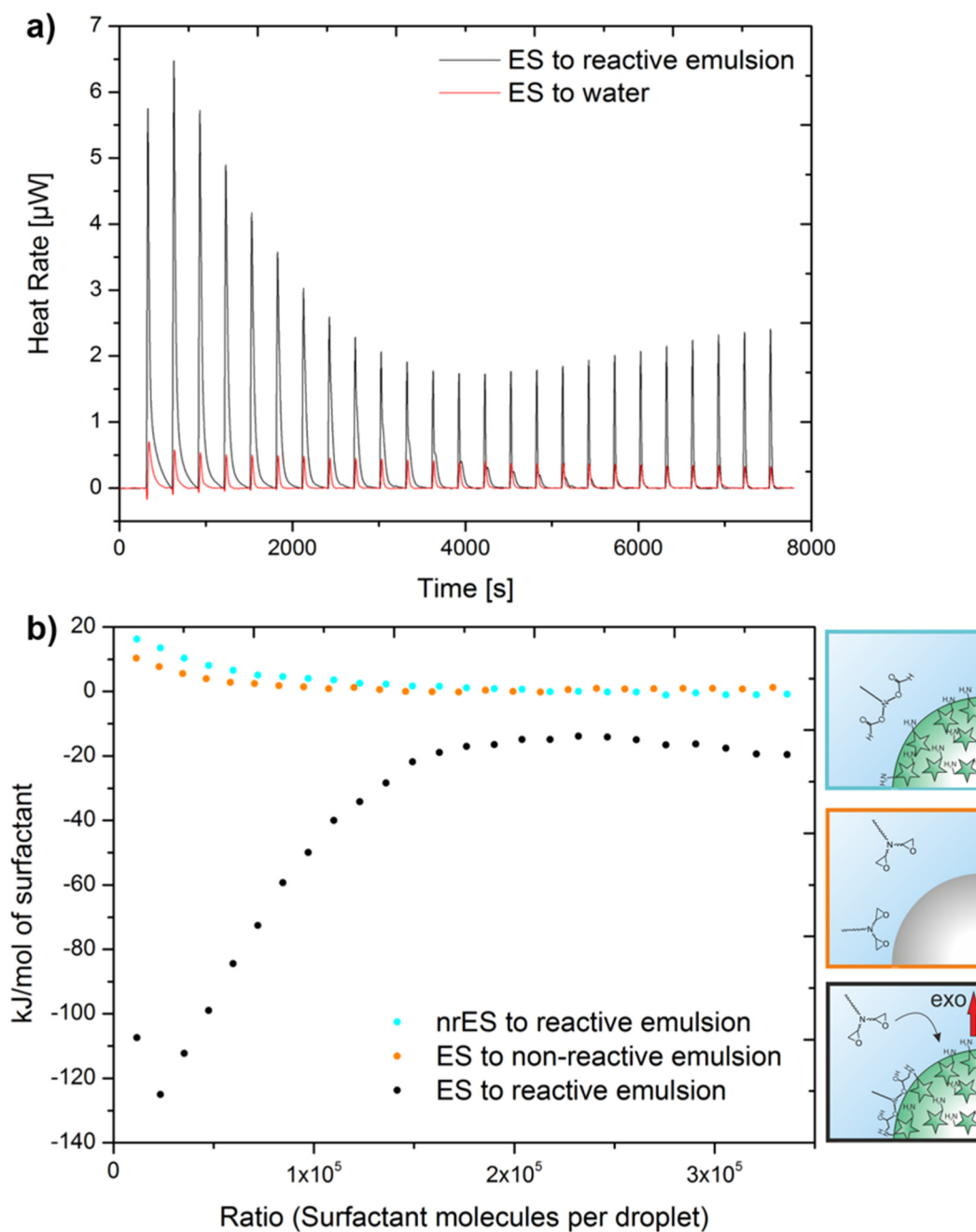


Figure 32. a) Exemplary raw ITC signals from the titration of the ES to the amine miniemulsion and to water to subtract the heat of dilution. b) Integrated results of the heat change per mole surfactant versus the surfactant to droplet ratio showing, the cross-linking of the ES at the interface.

For the titration of the epoxy surfactant to the amine emulsion as shown in Figure 32b) a strong heat release can be observed which reaches a plateau after approx. 14 titration steps. The enthalpy of the process was determined by a fit according to an independent binding model and was found to be about -343 kJ mol^{-1} of surfactant.^{159, 218}

The reference experiments however show different trends. The titration of the nonreactive surfactant to the amine miniemulsion shows a slightly endothermic process. The second control experiment shows a comparable result. It can thus be concluded, that the generated heat observed for the reactive surfactant is not attributed to a physical adsorption process but rather to the exothermic reaction between the epoxy group and the amine at the interface. The result, that the reaction between the ES and the reactive amine miniemulsion reaches a plateau also shows that the reaction seems to be restricted to the droplet-water interface due to the high reactivity of the amine.

4.2.3.5 Reactivity

To prove that the majority of the amine was still reactive and can be used for consecutive reactions was demonstrated by polymerizing an epoxide resin. A thermosetting polymer network could be formed by stoichiometrically mixing with the epoxy emulsion which already served as reference for the ITC experiments. Homogenous, non-tacky and free-standing films were obtained after drying at room temperature (Figure 33b)). The curing reaction was determined via rheology measurements at $70 \text{ }^\circ\text{C}$ to enable the evaporation of the aqueous phase within reasonable time. The moduli displayed in Figure 33a) show a strong increase and hardening reaction upon film formation, further signified by the damping factor $\tan\delta$, which shows the conversion from a predominantly viscous ($\tan \delta > 1$) towards an elastic material ($\tan\delta < 1$). TEM measurements were carried out to confirm that no dense shell was formed upon the reaction. No particles or shell like remains could be found, instead molten film like parts could be found on the TEM grid. SEM measurements of the cured film showed a very homogeneous film with no traces of shell or shell like remains visible.

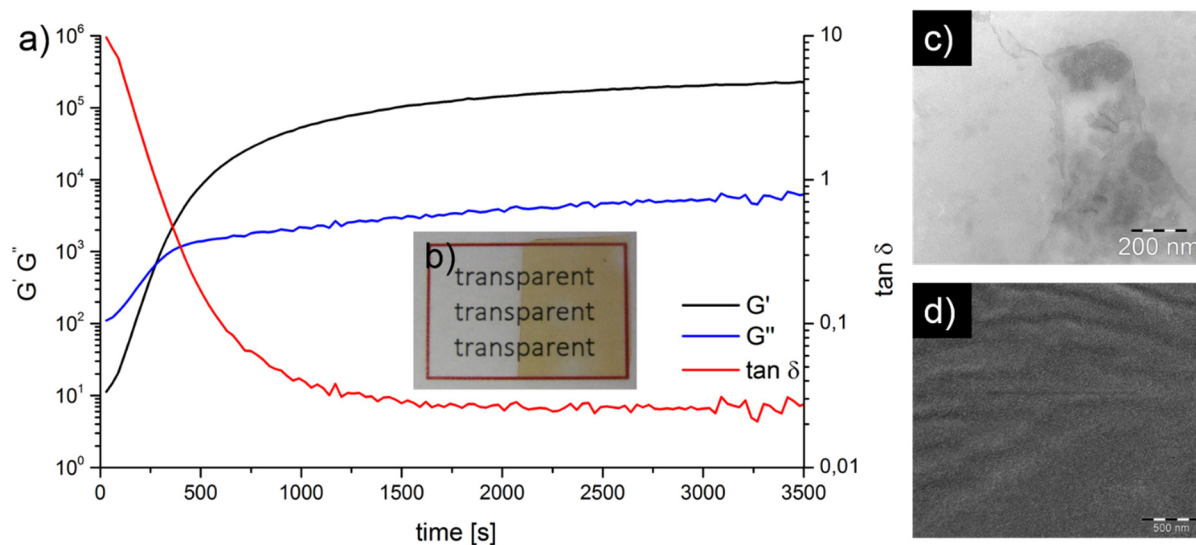


Figure 33. a) Oscillatory rheology measurement upon curing reaction, to demonstrate the maintained reactivity of the amine. b) Optical image of a room temperature cured film. c) TEM image of the diluted amine emulsion showing molten residues of the sample and d) SEM image of the cured film.

4.2.3.6 Conclusion

In conclusion, reactive epoxy surfactants are able to stabilize reactive compounds without the need of dense encapsulation. They are able to undergo interfacial polyaddition reactions with amine nanodroplets as followed by ITC experiments which indicate an interface “deactivation” with a stabilization layer formed. The vast majority of the active amine component remains unaffected and can be utilized for the preparation of P1K-dispersions. By this concept, the first requirement for the colloidal stability of the P1K is fulfilled. Furthermore, the overall characteristics render the cross-surf concept highly interesting also for various other applications and products, e.g. coatings, adhesives, self-healing systems and corrosion protection.

4.2.4 Colloidal Latency in the P1K

On basis of the bulk properties and the reactive stabilization of amine droplets in water, all necessary conditions for the preparation of a P1K-dispersion are met. As described in chapter 2.2, differences in size or a large size distribution can cause an emulsion to phase separate because bigger droplets are formed by molecular diffusion through the continuous phase. It was shown in the previous chapter, that Ostwald ripening of the NX5454 emulsion was not observed, since the particle size remained constant over a very long time period within the limits of the characterization method. For the P1K-dispersion however, additional driving forces become relevant. In contrast to an emulsion, which consists solely of one type of particles (A), droplet coalescence and Ostwald ripening are thermodynamically driven and purely physical processes. In a P1K-dispersion consisting of A&E type droplets which are highly reactive towards each other, a destabilization is much more likely. In case A and E get in contact, they will immediately react, so coalescence is likely to happen. Also, if diffusion through the continuous phase takes place, which would be more likely to happen for the amine component (A), its reaction with the epoxide droplets (E) results in the constant removal of component A from the system. This is usually applied as a trick in classical synthesis protocols to increase the yield of a reaction but is highly unfavorable for a P1K-dispersion. Therefore, as shown in Figure 34, the time dependent stability and reactivity of the P1K-dispersion was investigated. Additionally, the epoxy-amine polyaddition reaction in miniemulsion droplets was carried out to prepare positive control samples where the conversion was 100%.

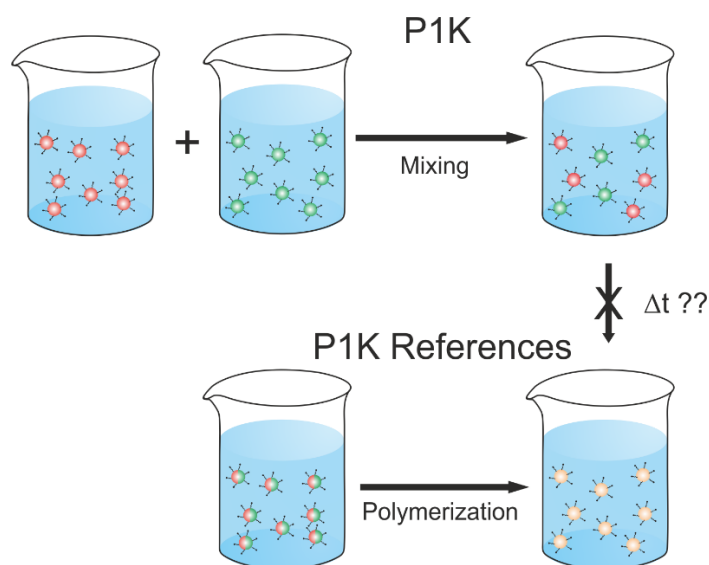


Figure 34. P1K-concept. The P1K-dispersions are prepared by mixing epoxy and amine emulsions of similar particle size and their time-dependent stability is investigated. Cured references are obtained by performing polyaddition in the emulsion droplets.

4.2.4.1 Colloidal Stability

The first requirement for the colloidal stability of the P1K-dispersions is a similar particle size and narrow size distribution to suppress a physical destabilization. Therefore, a library of A&E miniemulsions was prepared by varying the concentration of epoxy surfactant used and comparing their particle sizes. The epoxy surfactant was used for the preparation of the epoxy dispersions as well because its headgroup is structurally comparable to the epoxy phase. Small sizes with narrow PDI were obtained for all types of emulsions over a wide concentration range. Figure 35a) shows the dependency of particle size for the NX5454 emulsion as previously described. Also the NC641 emulsion shows very small Z_{av} values and PDIs over a wide concentration range. Compared to the NX5454 emulsion, the particle sizes of the NC641 miniemulsions do not show any significant increase in size even at only 1 wt.% epoxy surfactant. Interestingly, the color of the dispersion changed from a faint orange to a deep pink with increasing ES concentration. Figure 35b) shows the dependencies of the epoxide dispersion where the stabilization is a non-reactive one. In comparison to the amine emulsions, the particle sizes are in the same range with slightly bigger average sizes but are in general comparable, especially at ES concentrations exceeding 5 wt.%. At lower surfactant concentrations, both dispersions show a bigger increase in size compared to the reactive stabilization. Some phase separation was observed for the NC547 dispersion at 1 wt.% ES concentration. The particle sizes for the BADGE emulsions are slightly smaller compared to the NC547 ones. Judging from these results, all four educts can be potentially used in the P1K-dispersion.

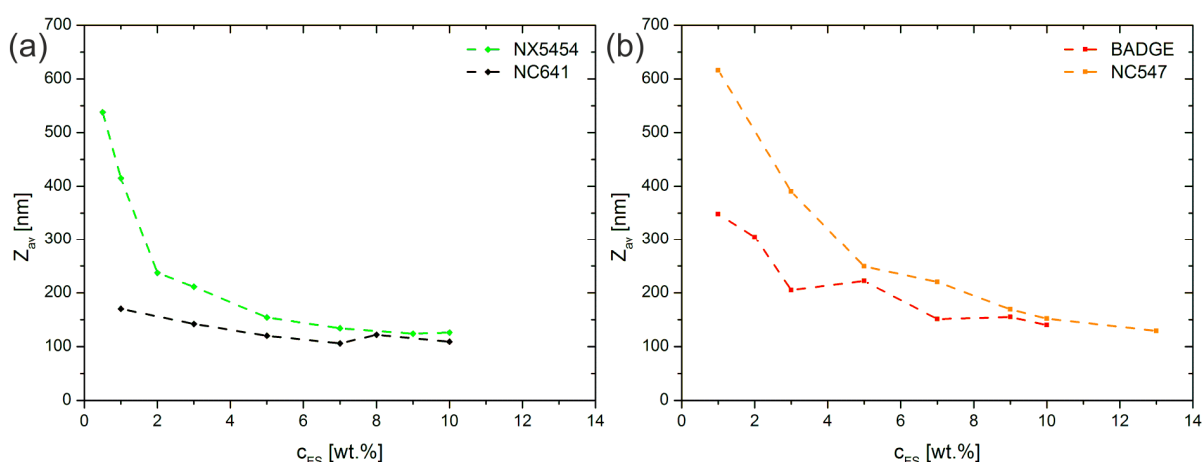


Figure 35. Size versus epoxy surfactant (ES) concentration plots for the a) NX5454 (green) and NC641 (black) amine emulsions and the b) BADGE (red) and NC547 (orange) epoxide dispersions. All graphs show an increase in particle size with decreasing surfactant concentration. Lines are meant to guide the eye.

In a second step, the time-dependent stability of these emulsions was investigated at an ES concentration of 10 wt.% with respect to the disperse phase and at a solid content of 20%. Both amine emulsions which are depicted in Figure 36a) are very stable over time. For the epoxy emulsions shown in Figure 36b) however, the BADGE emulsion was not long-term stable and showed a rather rapid increase in particle size already after two days of storage. The cardanol based epoxide emulsion however, did not show any significant increase in particle size over time and can hence be regarded as stable.

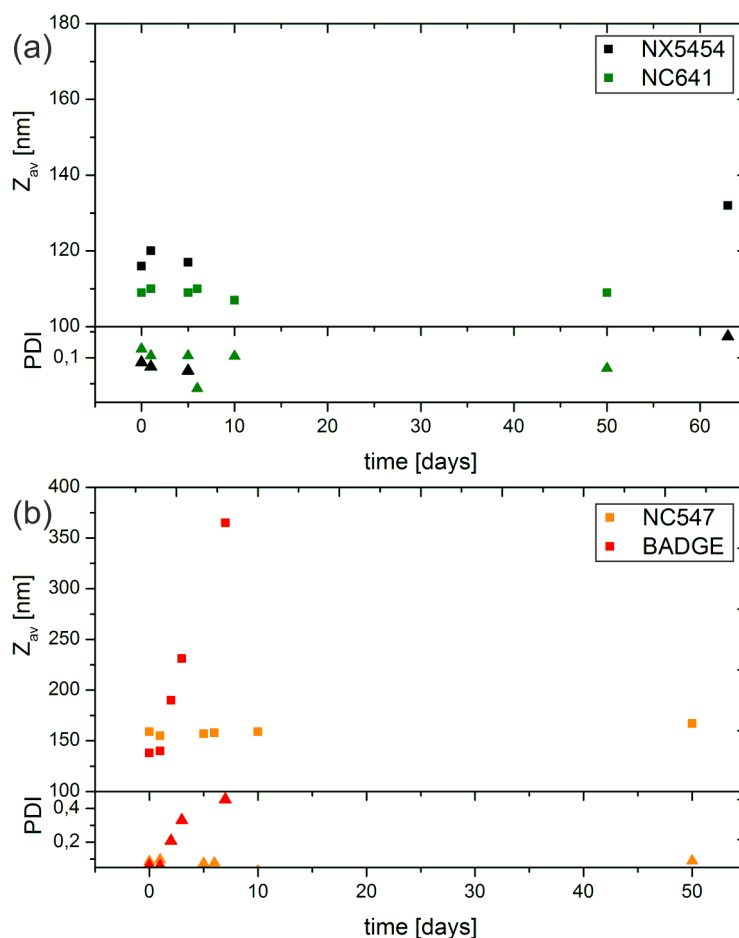


Figure 36. Particle sizes and size distributions of the a) amine emulsions made from the NX5454 (cyan) and the from the NC641 (green) and b) epoxy dispersions made from BADGE (red) and from the NC547 (orange) as a function of time to determine their colloidal stability at fixed surfactant concentration of 10 wt.% based on the dispersed phase.

Subsequently, the PIK-dispersions were prepared according to Figure 34 by stoichiometrically mixing (1 min), the two types of A&E emulsions which is defined as $t = 0$, with a vortexer. Upon mixing, no visible changes like coagulation or phase separation occurred. Their stability was monitored by measuring DLS of the mixed systems over time. The particle sizes of both components before mixing are given in Table 11.

Table 11. Particle sizes of A&E before their mixing to form P1K-dispersions.

Entry	BADGE-10		NC547-10		NX5454-10		NC641-10	
	Z_{av} [nm]	PDI	Z_{av} [nm]	PDI	Z_{av} [nm]	PDI	Z_{av} [nm]	PDI
P1K-1	140	0.060	-	-	126	0.049	-	-
P1K-2	140	0.060	-	-	-	-	109	0.117
P1K-3	-	-	152	0.976	-	-	109	0.117

Interestingly, for the P1K-1 (Figure 37a)) the initial particle size is slightly bigger (~145 nm) than the individual components alone. The average particle size of the mixture shows a slight but reproductive (3x) increase within the first 5 h to about 150 nm and afterwards remains constant. Still, the variations are very close to the region of experimental error, so the possibility of nonsense correlation cannot be completely excluded. Also the PDI does not significantly change upon time. For the P1K-2 (Figure 37c)), the trend looks very similar. In the beginning, the average particle size increases slightly and remains constant over the course of the measurement. Compared to the P1K-1, the size distributions are slightly bigger but also do not significantly increase over time. From the time dependent behavior of the sole BADGE emulsion, a totally different behavior would be expected. The drastically increased stability may be an indication, that some premature reaction took place, which added to the stability of the epoxy emulsion, for example by the formation of a cross-linked layer around the epoxide which prevents its destabilization. This would suggest rather a diffusion induced process, as droplet coalescence would lead to an increase in size distribution over time. This might explain the minor increase in size within the first hours of storage but further analysis is necessary to explain this behavior. This however is challenging by standard methods, since the samples easily lose their original identity and form films.

The P1K-3 dispersion shown in Figure 37e) in contrast, does not show an increase in particle size at the beginning. There are slight variations in size and PDI but the overall particle size and distribution remains constant over time. Also, after months of storage no significant change in size was observed for all systems.

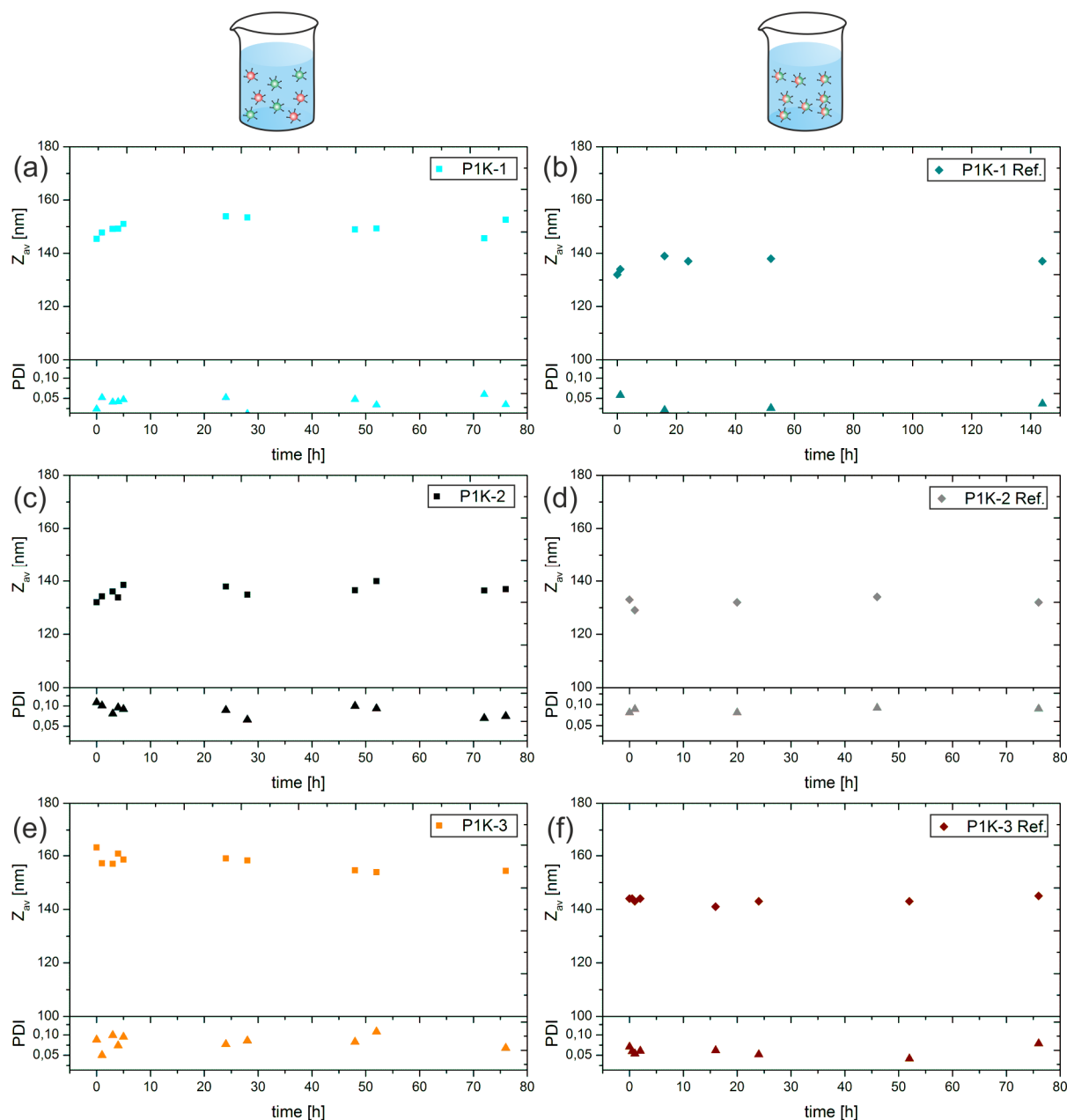


Figure 37. Particle sizes and size distributions of the a) P1K-1, c) P1K-2 and e) P1K-3 as well as their cured reference b) P1K-1 Ref., d) P1K-2 Ref. and f) P1K-3 Ref. as a function of time, showing no significant changes in particle sizes.







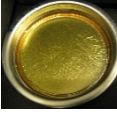










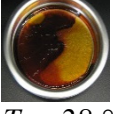



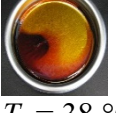
For comparison, references were prepared for all systems as positive controls, where the nano-reactor concept was used to perform the polyaddition of epoxy and amine within the individual droplets to obtain cured particles, which are not reactive anymore. Therefore, the disperse phase contained both components dissolved in ethyl acetate and was immediately emulsified and similar particle sizes (P1K-1 \sim 132 nm, P1K-2 \sim 133 nm and P1K-3 \sim 144 nm) were obtained. Also for the references, no significant change in particle size was observed over time as shown in Figure 37b,d,e).

In summary, the colloidal stability of any P1K-mixture is surprisingly high, with no visible coagulation or agglomeration taking place. The increased stability for the BADGE-based systems however suggests, that some degree of premature reaction must have taken place, since a destabilization was observed for the BADGE emulsions alone. This should also take place in the P1K-systems, if no premature reaction occurred. Still, the observations by DLS alone cannot completely exclude the absence of coalescence, since many parameters influence the measurement such as dilution of samples even though the dilution was kept constant for all measurements. Secondly, what needs to be taken into account is the possibility of a gradual transition from an emulsion to a dispersion in case premature reaction takes place in the P1K-systems. Also, in case of the references, where a definite transformation towards solid particles occurs, the results of the measurements might be affected (see chapter 3.1). Still, the Stokes Einstein equation (equation 8) used for the calculation of the hydrodynamic radii was proven valid for emulsions in many cases.²¹⁹⁻²²² Furthermore, the emulsions used for the preparation of the P1K-systems as such are quite viscous materials already, compared to a classical emulsion consisting of low viscous monomers only. As a consequence the usage of the Stokes Einstein equation should be valid. Still, further complimentary analysis is needed.

4.2.4.2 Film Formation

A simple, but effective method to evaluate if premature reaction took place in the P1K-dispersion is their film formation. In the ideal case, where no premature reaction in dispersion occurred, a homogeneous film should be obtained after evaporation of water as described in chapter 2.6.2. On the contrary, in case premature reaction took place in colloidal state a film formation should not be possible anymore, since highly cross-linked particles usually cannot form continuous films. The intentionally cured P1K-references serve as a 100% positive control for these investigations.

Table 12. Optical evaluation of the P1K-systems after film formation over a time period of 10 days. Also the T_g s are determined for those samples which formed a homogeneous film.

time	P1K-1	P1K-2	P1K-3
t_0			
	$T_g = 50\text{ }^\circ\text{C}$	$T_g = 93\text{ }^\circ\text{C}$	$T_g = 41\text{ }^\circ\text{C}$
t_{1h}			
	$T_g = 54\text{ }^\circ\text{C}$		$T_g = 39\text{ }^\circ\text{C}$
$t_{1\text{ day}}$			
	$T_g = 52\text{ }^\circ\text{C}$		$T_g = 40\text{ }^\circ\text{C}$
$t_{2\text{ days}}$			
			$T_g = 41\text{ }^\circ\text{C}$
$t_{3\text{ days}}$			
			$T_g = 40\text{ }^\circ\text{C}$
$t_{4\text{ days}}$			
			$T_g = 38\text{ }^\circ\text{C}$
$t_{7\text{ days}}$			
			$T_g = 39\text{ }^\circ\text{C}$
$t_{10\text{ days}}$	n.d.	n.d.	
			$T_g = 38\text{ }^\circ\text{C}$

Films of approximately 50 μm thickness were prepared from the P1K-dispersions over time and left curing for 48 h at RT. The films were first evaluated optically as shown in Table 12. Subsequently, if coherent films were formed, their T_g s were determined via oscillatory rheology. The pictures confirm what was already suspected from the DLS measurements. The BADGE based P1K-systems fail to form continuous films already after very short storage times. Whereas the P1K-1 can still form a film after one day, the P1K-2 fails already after 1 h of storage. This can be attributed to the lower viscosity of the NX5454, enabling a better interdiffusion compared to the NC641 as shown in chapter 4.2.2.3. Taking the P1K-3 into consideration, this cannot be the sole origin of the film formation failure, since here a continuous film is formed even after 10 days of storage. The T_g s for the P1K-3 were determined after heating the samples to 160 $^{\circ}\text{C}$ for 2 h to obtain fully cured films. They were about 40 $^{\circ}\text{C}$ and did not significantly change over time. Compared to the in bulk cured systems in chapter 4.2.2.3, the T_g s are systematically about 25 $^{\circ}\text{C}$ lower. Similar observations were made for the P1K-1. This is a common phenomenon caused by plasticizing effects of the surfactant and residual water.

The film formation was investigated in more detail by the minimum film formation temperature (MFFT). The MFFT determines the minimum temperature necessary to obtain a homogeneous, non-hazy film. The measurement is performed by casting a film with a 500 μm doctor blade on a steel plate, where a temperature gradient was applied under a constant stream of dry air to promote solvent evaporation and to prevent condensation. The MFFT was determined optically for the P1K-dispersions as well as for their references as a function of time. To determine the maximum MFFT, the cured references were sealed and heated to 70 $^{\circ}\text{C}$ for 12 h. They are depicted as dashed horizontal lines in Figure 38. As expected, the MFFT_{max} is systematically lower than the corresponding T_g s.

The MFFT of the P1K-1 was 0 $^{\circ}\text{C}$ for the first hours of storage but showed a steep increase after one day. The trend of the MFFT curve is best represented by a bounded growth function which reaches a steady state after about four days of storage. For its reference, an MFFT was observed right from the beginning of about 11 $^{\circ}\text{C}$ increasingly rapidly over time, as the curing in the droplets proceeded. For the P1K-2, a MFFT of 13-16 $^{\circ}\text{C}$ was observed right after mixing. In contrast, for the cured reference, the initial MFFT was 0 $^{\circ}\text{C}$ but, as expected, increased rapidly afterwards. The maximum MFFT was found to be 75 $^{\circ}\text{C}$. After two days of storage, the MFFT of the reference had almost reached the MFFT_{max} , indicating again the high reactivity of the system. For the P1K-2 in comparison, the MFFT increase was found to be less in absolute numbers but also showed an exponential increase in between one to four days of storage,

reaching a MFFT of about 50 °C after five days. Afterwards, no further increase was observed and the MFFT was still significantly lower than the $MFFT_{max}$, which might be due to hindered diffusion, since cross-linked particles were likely formed over time, thus hindering further diffusion and reaction of A&E. Nevertheless, the difference in MFFT comparing the P1K-dispersions with their positive controls is surprisingly small. Still, the potlife of both systems could be prolonged by the P1K-approach.

For the P1K-3, the maximum MFFT is much lower and very close to RT, most likely due to a decreased cross-linking density as described in chapter 4.2.2.3. Initially, the reference as well as the P1K-3 display an MFFT of 0 °C, as shown in Figure 38c). The reference shows a rapid increase in MFFT after two days of storage to about 20 °C. The P1K-3 instead does not show an increase in MFFT over the observed timeframe. These findings are promising but can only be taken as an indication, premature reaction might still be possible. Still the results suggest a significantly improved potlife for the P1K-3.

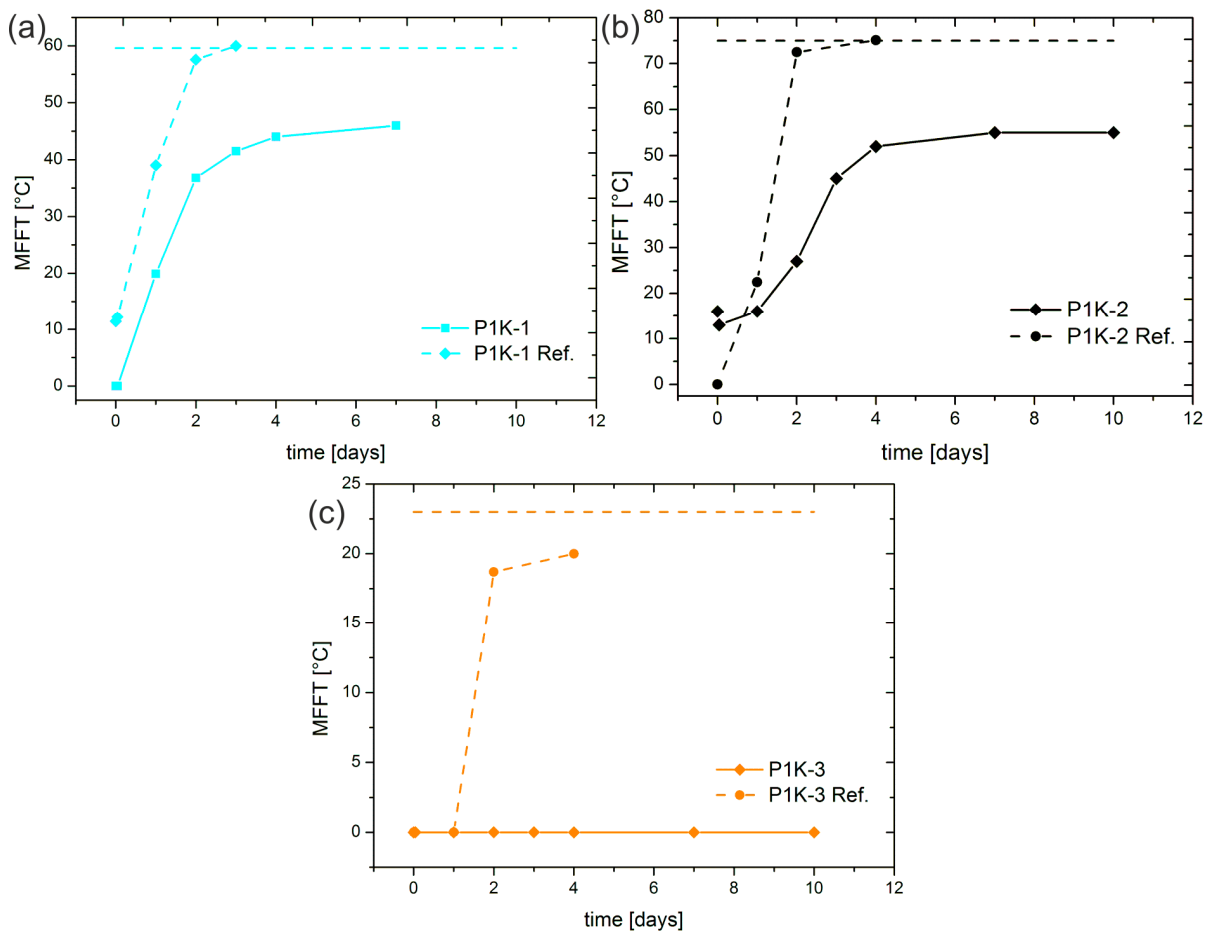


Figure 38. Minimum film formation temperatures (MFFT) as a function of time for the P1K-dispersions and their references. The vertical lines represent the $MFFT_{max}$ for a fully cured particle.

SEM analysis was performed on the RT-cured films for further insights into their nanostructures. Therefore, the films used for the MFFT analysis at 25 °C were sputtered with a thin layer of gold. The results for the P1K-1 are summarized in Table 13. Initially, a homogeneous film was obtained, however as already expected from the previous results, over time more and more particles become visible. As expected, the P1K-1 reference as positive control just shows particles of very similar size and does not form any film at all.

For the P1K-2 the pictures are very similar (Table 14). Already after one day of storage, particle formation becomes visible. The particles seem to be slightly deformed as well but cannot form a continuous film anymore. The reference like the P1K-1 reference, shows almost ideal spherical particles of narrow size distribution.

Table 13. SEM images of the P1K-1 films cured at RT in low and high magnification in comparison to the P1K-1 reference as positive control.

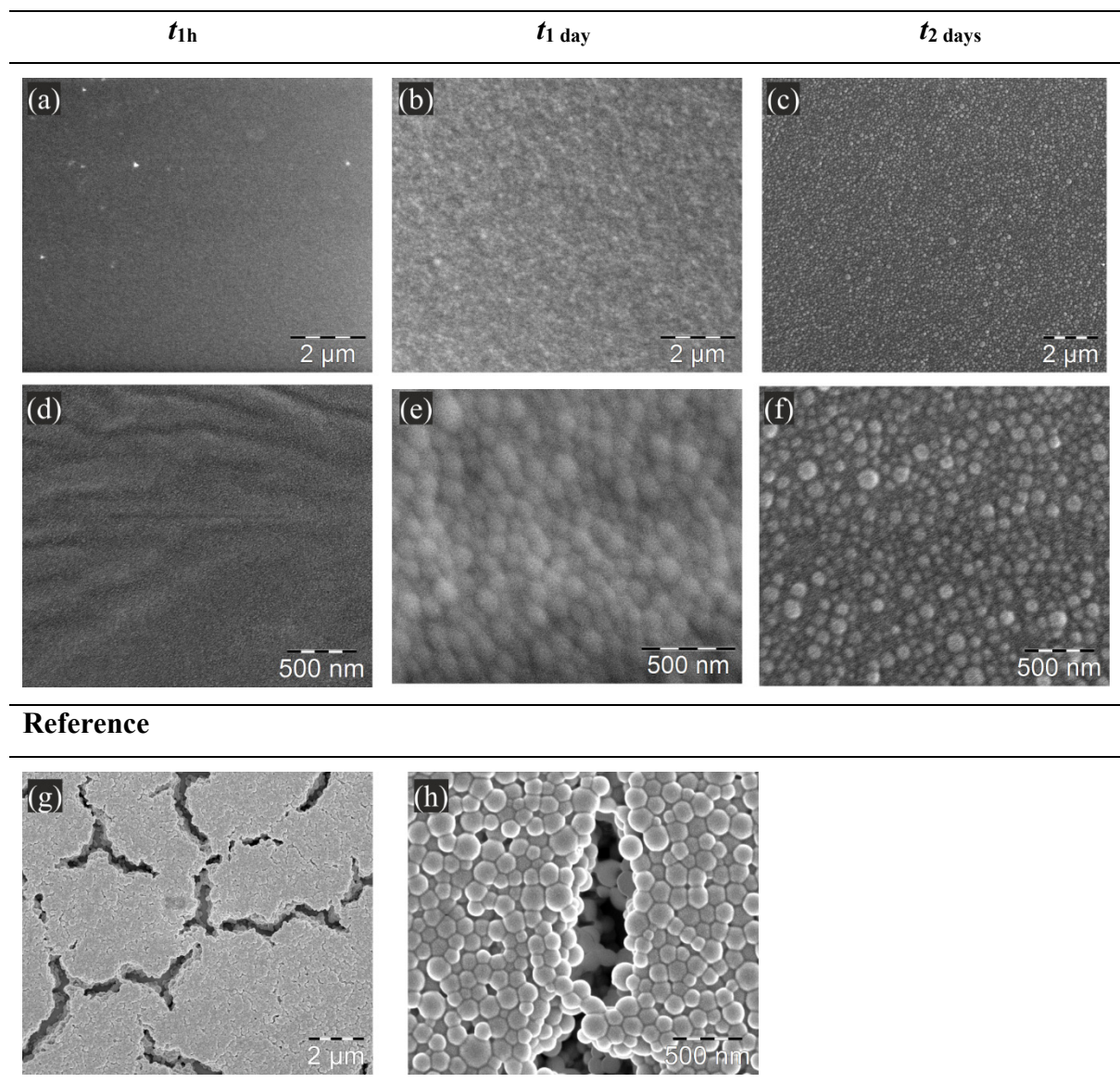
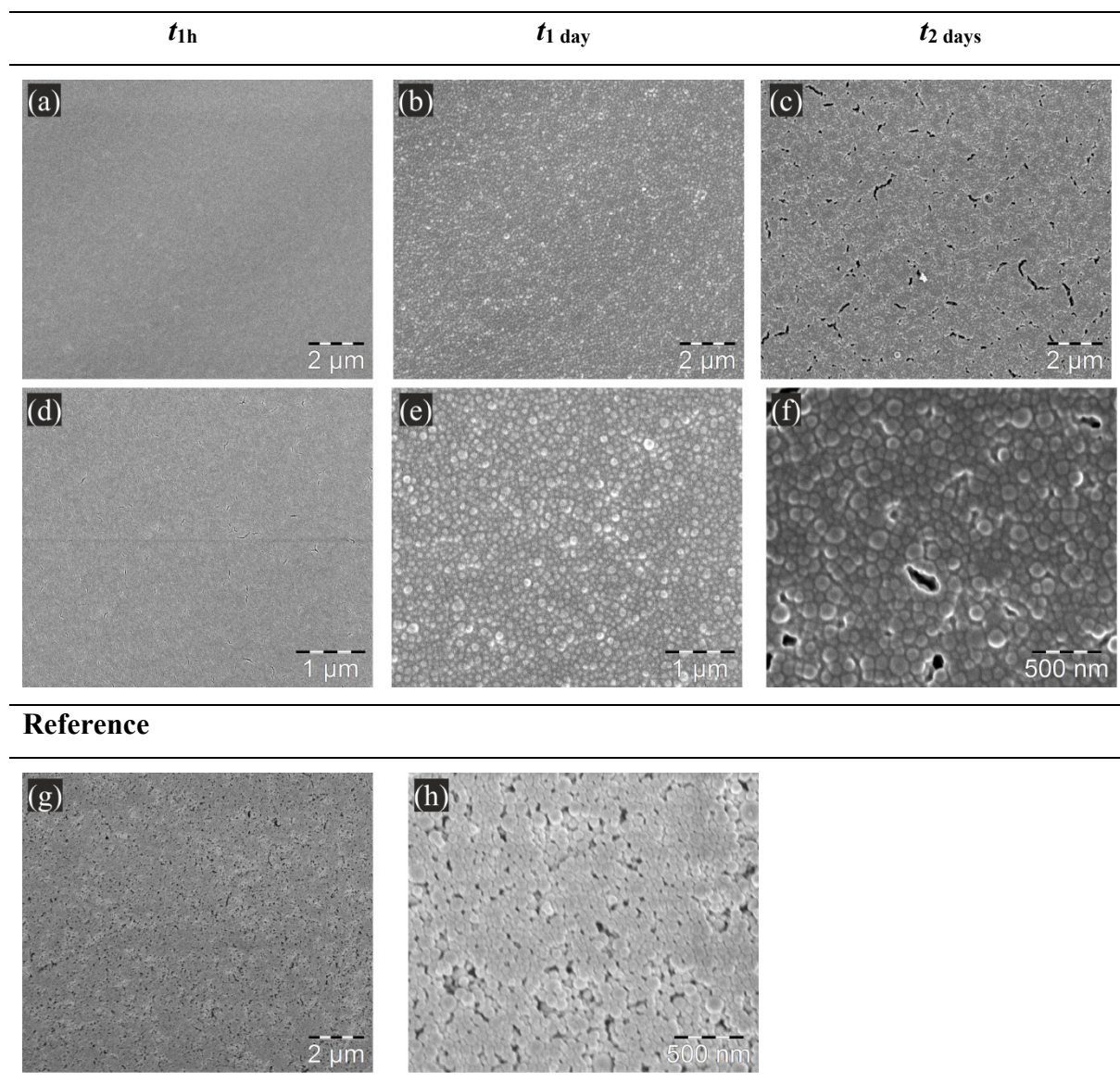
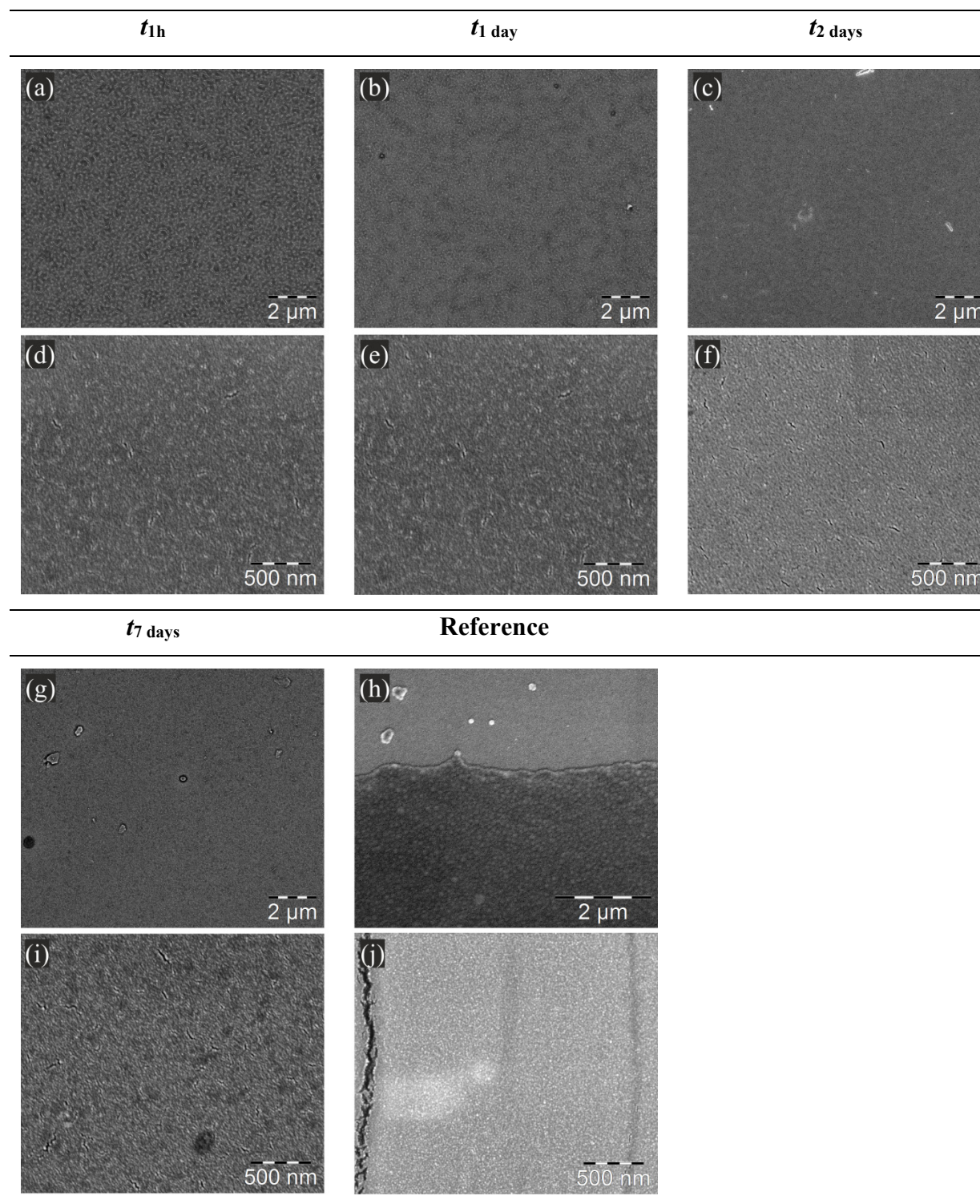


Table 14. SEM images of the P1K-2 films cured at RT in low and high magnification in comparison to the P1K-2 reference as positive control.



For the P1K-3 in contrast, similar to the observations made in the MFFT analysis, no particle formation was observed over time as shown in Table 15. The structures present in the higher magnification images do not correspond to the sample itself, but are rather due to the necessary Au-sputtering since, the same structures were also found on the sputtered but otherwise empty substrate. However, also for the P1K-3 Ref. no defined particles were found, probably due to their comparably low T_g . It was possible to observe partially fused particles of approximately 150 nm in size at the edge between the film and the substrate, which were not observed for the other samples where no clear edge was visible. The results support the above stated trends for the stability of the P1K increasing in the order P1K-2 < P1K-1 < P1K-3. However, also with SEM no direct prove could be made.

Table 15. SEM images of the P1K-3 films cured at RT in low and high magnification in comparison to the P1K-3 reference as positive control.



TEM analysis was furthermore carried out since we suspected, that interfacial epoxy-amine cross-linking took place, to see if the film formation failure could be attributed to some degree of shell formation. TEM measurements were carried out after one day of storage as shown in Figure 39. For the P1K-1 and 2, diffuse particles were visible which were surrounded by some material which spread out on the grid. No core-shell morphologies were found. For the P1K-3, as expected only diffuse spots with no clear morphology were visible.

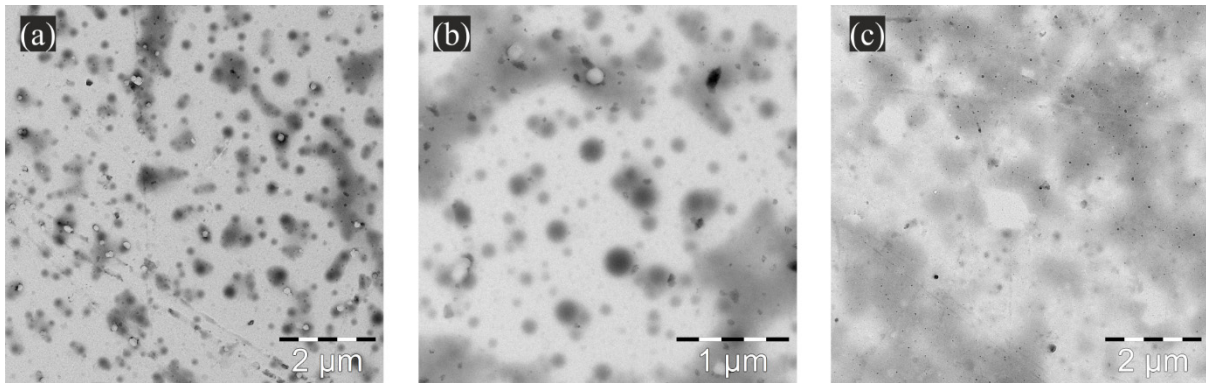


Figure 39. TEM measurements of the a) P1K-1, b) P1K-2 and c) P1K-3 systems one day after their preparation showing no clear morphology but some particles present for the P1K-1 and P1K-2.

4.2.4.3 Turbidity Measurements

As film formation failure can directly be correlated to an increase in cross-linking density within the colloids, turbidity measurements were employed as an indirect measure to determine the degree of cross-linking. Therefore, small amounts of the P1K-dispersions were dissolved in ethyl acetate. For better comparison between the different systems, samples were measured at a fixed amine concentration of 0.05 g L^{-1} . Aliquots were taken over time and the turbidity of the mixtures was determined with a photometer. Initially, all educts are dissolved by the solvent and clear solutions were obtained with a transmittance of 100%. With proceeding premature reaction in the P1K-dispersion, cross-linked polymers are formed which cannot be dissolved anymore, thus leading to a decrease in transmission. Figure 40 compares the decrease in transmission of the three P1K-systems as a function of time. For the P1K-1 and 2, a rapid decrease in transmittance was observed within the first 6 h after their preparation and becomes constant after about one day. The trend of the curves can be best fitted by an exponential decay as represented by the dashed lines (the corresponding functions are given in chapter 5.4.4.5). The P1K-3 in contrast can be fully dissolved in the first hours of measurement and afterwards shows a rather slow and constant decrease in transmittance. It was found to be best correlated by a linear fit, as indicated by the orange dashed line in Figure 40. These results support the findings from the MFFT analysis, suggesting that premature reaction can be suppressed best in the P1K-3 system.

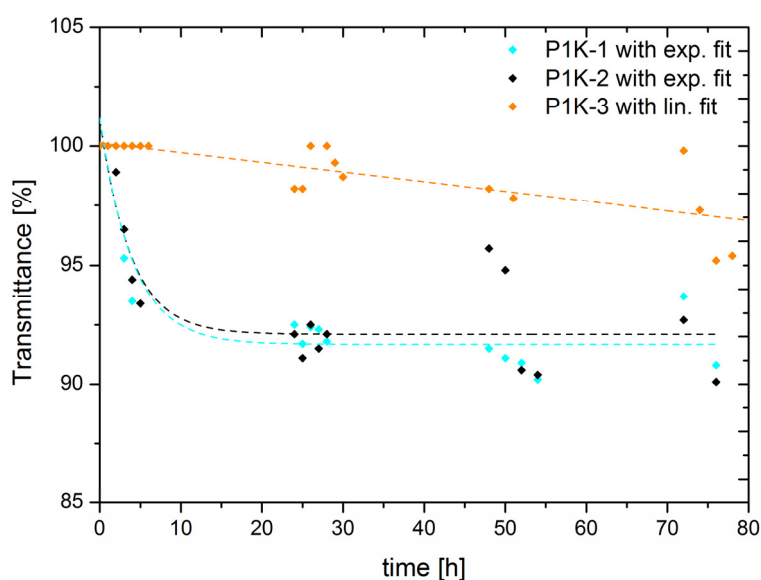


Figure 40. Turbidity measurements of the dissolved P1K-systems as a function of time. A decrease in transmission indicates an increased cross-linking density.

As described in chapter 2.4.1, the cross-linking density is also dependent on the average distance between the cross-linking junctions. For the P1K-1 and 2, judging from a molecular point and of view and also from the findings in oscillatory rheology (chapter 4.2.2.3), the cross-linking density of the fully cured systems is quite similar. Comparing the BADGE with the NC547, also similar cross-linking densities were found for the P1K-3. However, to ensure that the measured difference in transmittance do not result from differences in molecular structure, the P1K-3 was directly compared to its nonreactive reference. Figure 41 demonstrates the result which shows strong differences between both samples. The cured reference shows an immediate decrease in transmittance. The value for t_0 is already below 100% transmittance, likely because the curing reaction already started during the preparation of the sample. The best fit for the course of the curve was again an exponential decay, as represented by the dashed line. As a conclusion, the differences between the different P1K-dispersions are not caused by their different chemical composition but are rather a consequence of premature reaction which seems to be suppressed more efficiently in the P1K-3 system.

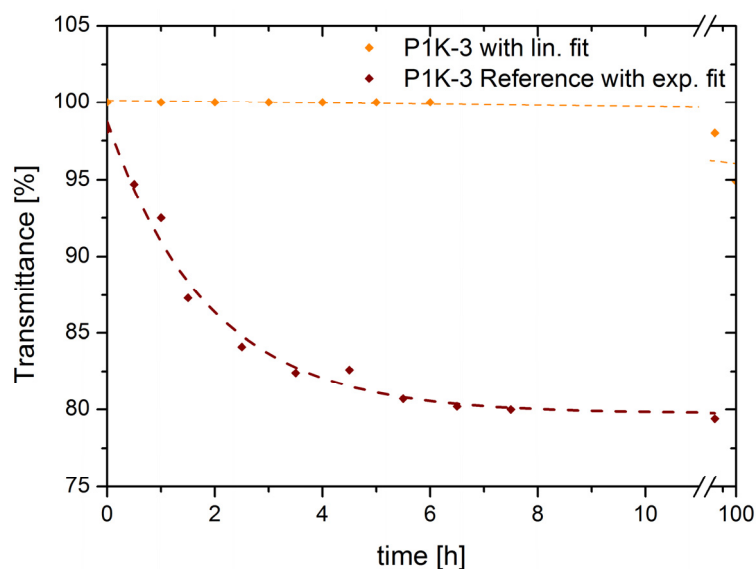
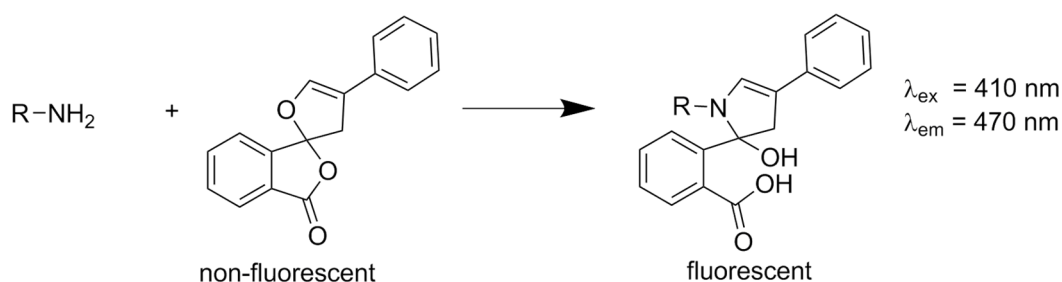


Figure 41. Turbidity measurement of the dissolved P1K-3 compared to its reference as a function of time.

4.2.4.4 Fluorescence Characterization

The characterization methods so far led to the conclusion, that premature reaction indeed takes place in the PIK-systems to different extends and provided deeper insights into the underlying processes which are likely to happen upon storage of the dispersions. However, none of these methods allows a direct quantification, since spectroscopic methods in dispersion are challenging to perform. We tried to quantify the amount of amine by derivatization with a fluorescent dye instead. This fluorescamine assay is originally used for the quantification of primary amine groups in protein and peptide solutions. As shown in Scheme 10, the reagent itself is non-fluorescent, whereas the reacted form gives highly fluorescent products which can be detected down to picomolar concentrations. The reaction is selective for primary amines in aqueous solutions and proceeds almost instantaneously at RT.²²³ Figure 42 shows the absorption and emission spectra for the fluorescamine after its reaction with the NX5454 in ethyl acetate. This method was reported earlier for the quantification of primary amine groups at the interface of polyurethane particles, to determine the number of functional groups present at the surface.²²⁴



Scheme 10. Selective fluorescent titration of primary amines.

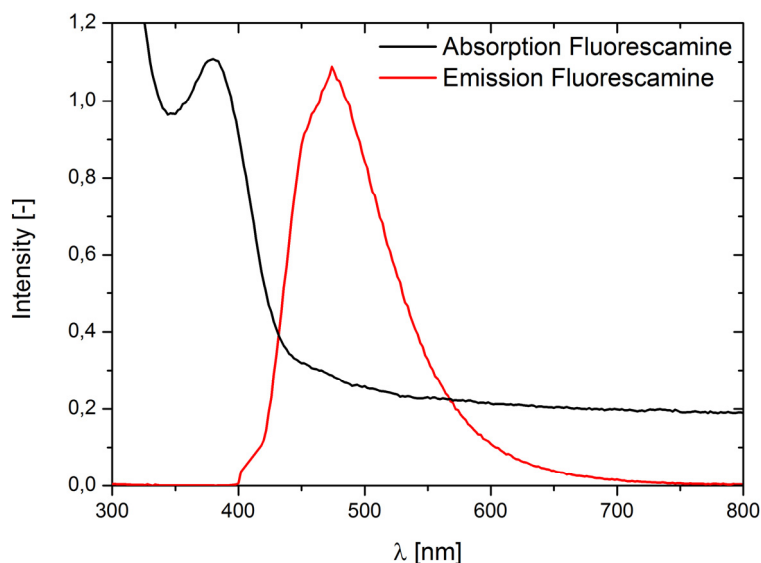


Figure 42. Absorption and emission spectra for the fluorescamine-NX5454 derivate.

In principle, the method can be used to determine the concentration of primary amines over time as representative for the degree of premature reaction, since they will be the first to react with the epoxide. The process had to be slightly modified, since we were interested in the total quantity of amine within the sample, not just the functional groups present at the surface. Furthermore, the derivatization in solution was found to slightly cause a destabilization of the amine emulsions. As a consequence, the P1K-systems were dissolved in ethyl acetate as already done for the turbidity measurements. Afterwards, the mixtures were derivatized immediately and quantified after irradiation with a 410 nm excitation wavelength and subsequent detection at 470 nm, by using a plate reader. Since the amount of insoluble polymer increases over time, thus causing scattering which might interfere, a blank was measured for every sample where no fluorescamine was added. As for the turbidity measurements, an initial fixed amine concentration of 0.05 g L^{-1} was used for better comparability. Calibration was performed by dissolving the amine emulsions NX5454-10 and NC547-10 in ethyl acetate as shown in Figure 43.

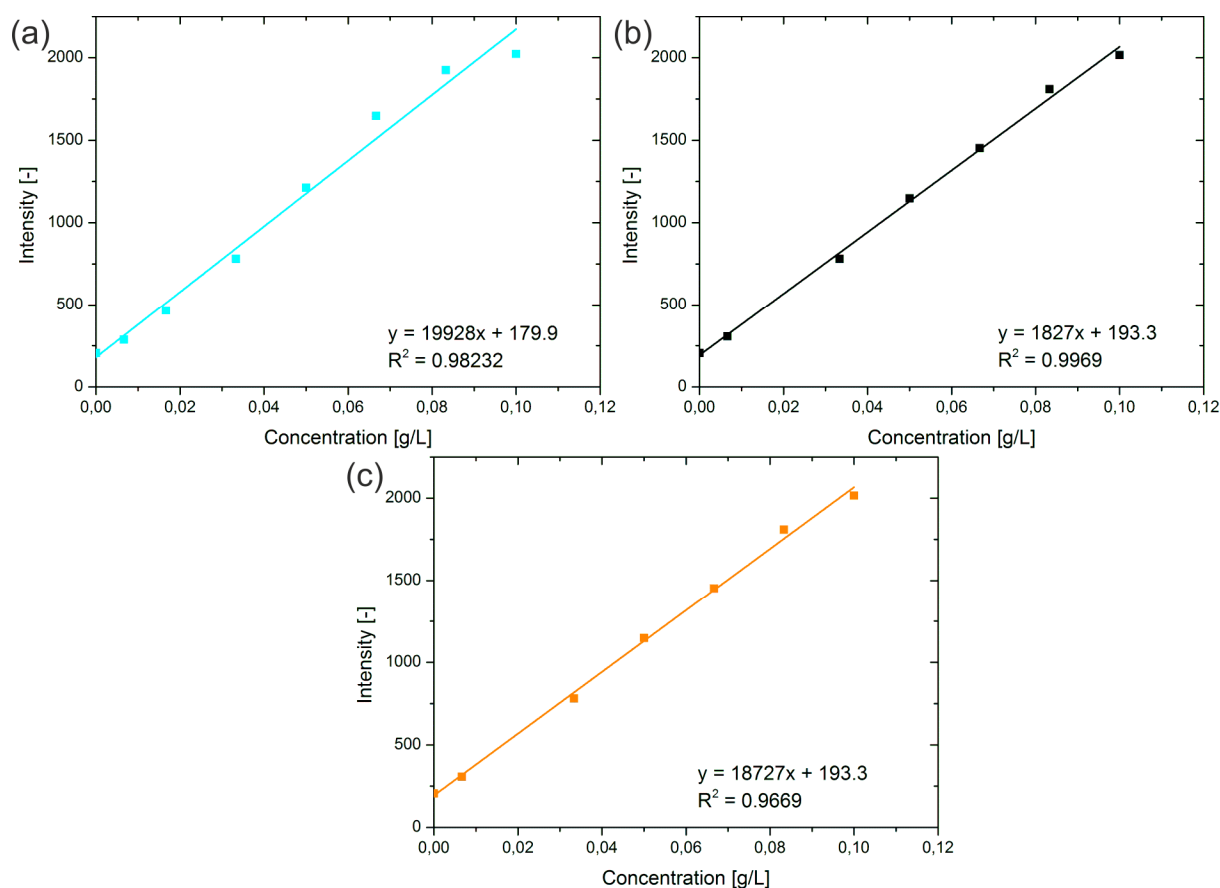


Figure 43. Calibration curves for the fluorescamine assay for the different P1K-systems in ethyl acetate. The curves for the P1K-2 and 3 are identical, since the same amine was used for their preparation. The initial amine concentration used in the P1K-samples was fixed to 0.05 g L^{-1} which allows their detection within the linear range of the calibration curves.

Figure 44 compares the results from the fluorescamine assay for the different P1K-dispersions. Concentrations are normalized to allow a direct comparison. The initial concentrations were found to be systematically already about 20% less than the calculated concentrations for t_0 . This already indicates, that premature reaction took place immediately after the P1K-systems were prepared. It could however also be possible, that A&E reacted during the sample preparation where they were dissolved in ethyl acetate. In this case, this would be a systematical error for all samples but it was not possible to determine which one is more likely because it was not possible to perform the experiments in dispersion directly. Comparing the different systems over time, a trend similar to the observations in the turbidity measurements was found. The P1K-1 and P1K-2 samples show a very rapid decrease in primary amine content which was best fitted exponentially, as represented by dashed lines in Figure 44. For the P1K-1 no NH_2 could be detected anymore already after 5 h of storage. For the P1K-2 the rate of premature reaction was a bit slower but also after about 24 h of storage no primary amine could be detected anymore. The P1K-3 in comparison showed a more linear decrease over time. After 24 h about 50% of the NH_2 -groups were consumed indicating a reduced reaction rate in this system. After about two days of storage they were still not fully consumed. The P1K-3 reference was measured for a direct comparison as shown in Figure 45. The initial concentration at $t_{30\text{min}}$ was only about 50 % of the theoretical concentration. The trend of this curve could be better fitted exponentially as represented by the dashed line. After about 24 h of storage no primary amine could be detected anymore. Judging from this behavior, the decreased premature reaction rate cannot fully be explained by the reactivity differences between the BADGE and NC547 epoxide. The increased stability of the P1K-3 might be the result of the increased colloidal stability of the NC547 emulsion. Nevertheless, it becomes quite obvious, that the idea of the P1K-concept cannot be realized by the approach we tried, since the systems need to be stable over a much longer time period. Nevertheless, the potlife could be significantly prolonged for the P1K-3 system.

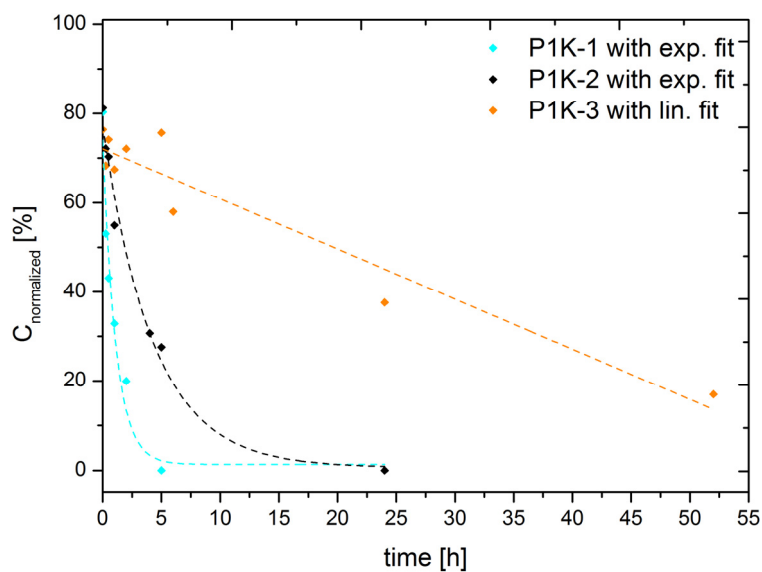


Figure 44. Relative concentrations of primary amines according to the fluorescamine assay for the different P1K-systems as a function of time, fitted with exponential decay functions in case of the P1K-1 and P1K-2 and a linear fit in case of the P1K-3.

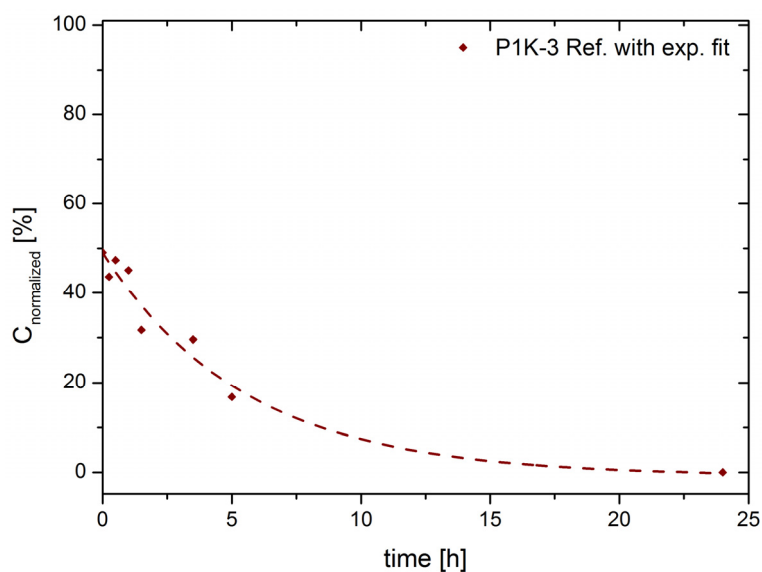


Figure 45. Relative concentrations of primary amines according to the fluorescamine assay for the P1K-3 reference showing an exponential decay over time.

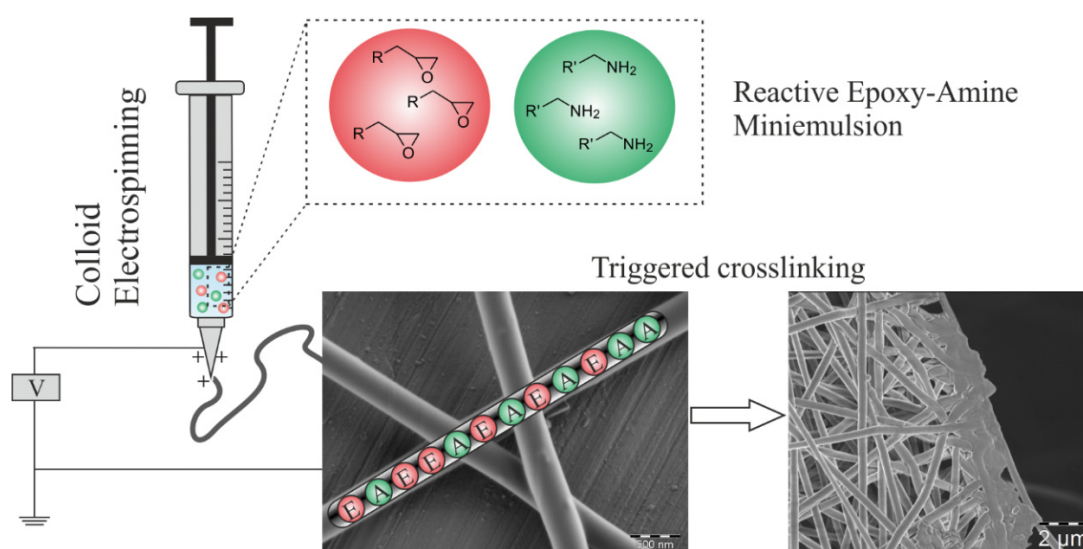
4.2.4.5 Conclusion

Summarizing the above mentioned results on the colloidal stability of the P1K-systems, it was possible to obtain highly stable amine miniemulsions by using reactive, cross-linkable epoxide surfactants over a wide concentration range. These surfactants were furthermore found to produce stable cardanol-based epoxy dispersions, whereas for the BADGE based dispersions only a limited colloidal stability was found. Also, the P1K-dispersions displayed a high colloidal stability even though premature reaction took place for all three systems. A combination of mechanical analysis and fluorescence titration could be used to quantify the degree of premature reaction which decreased in the order of P1K-1 > P1K-2 >> P1K-3. For the P1K-3, a significantly improved potlife was obtained. Based on these findings, it can be concluded, that the hydrophobicity or the surface-activity of the phenalkamine plays a role in the destabilization of the system. The colloidal stability of the epoxy dispersion seems to be another important factor, since the substitution of the BADGE by the epoxidized cardanol significantly improved the stability of the system. Apart from these findings, the P1K-3 is a very promising candidate with respect to sustainability, since it consists of two bio-based raw materials dispersed in water. Furthermore, neither toxic solvents nor low molecular weight surfactants were used. The DLS results suggest, that the premature reactions are not likely to be the subject of droplet coalescence which points into the direction of molecular diffusion. This would be more likely to be the case for the amine than for the epoxide, due to the surface-active character inherited by the amine functionality. But DLS analysis alone cannot be taken as prove, since the diameters calculated can be influenced by various events including the dilution of the samples.

One possible method which will be subject of further studies is to investigate the destabilization mechanism by dual-color fluorescence cross correlation spectroscopy (FCCS). The measurement principle is based on measuring fluctuations in fluorescence intensity over time to determine hydrodynamic radii, similar to DLS. This method could already be used to determine the mechanism of nanoparticle formation by the solvent evaporation method or by miniemulsion polymerization.^{91, 225} To use this method for the determination of coalescence in the P1K-systems, both types of colloids need to be fluorescently labelled, preferably by two fluorescent polymers of different wavelength, to ensure there is no diffusion of free dye. After their excitation, they either diffuse independently from each other in case no coalescence takes place and their fluctuations are random. In case of coalescence however, both fluctuations are correlated and the degree of coalescence can be determined to investigate the mechanism of premature reaction in the P1K-system over time.

4.3 Reaction Latency in Nanofibers**

Even though the stability of the P1K-dispersion as such was limited, the P1K-concept can be very promising with regard to self-healing applications. The high reactivity of the system can be used to enable efficient cross-linking at room temperature after some damage is applied to for example a protective coating. The main challenge which still needs to be overcome is the storage stability of the P1K. Therefore, colloid electrospinning with poly(vinyl alcohol) as confining matrix is used for the encapsulation of the epoxy and the amine as separated compartments. Uniform fibers are produced with a matrix/colloid weight ratio of 3/1. The internal fiber morphology was investigated via dual-colour stimulated emission depletion (STED) microscopy and TEM. The results show a statistical distribution of epoxy and amine compartments and indicate average particle-particle distances of < 100 nm, which is supported by computations. The fibers are highly storage stable under ambient conditions and yet allow efficient cross-linking and self-healing. The curing reaction can be initiated upon thermal or mechanical stimuli, as demonstrated by electron microscopy and electrochemical testing of fiber containing coatings. The reactivity and latency for reaction is furthermore proven by calorimetry and chromatography methods.



**This chapter is based on the publication “Dual-compartment nanofibres: separation of two highly reactive components in close vicinity.” by Ann-Christin Bijlard, Anke Kaltbeitzel, Yuri Avlasevich, Daniel Crespy, Marc Hamm, Katharina Landfester and Andreas Taden published in 2015 in *RSC Advances*, 5 (118), pages 97477-97484.^[251] Reprinted with permission. Copyright 2016 The Royal Society of Chemistry.

4.3.1 Motivation

As described in chapter 3.5, electrospinning has been proven a powerful technique for the preparation of functional materials. Usually, the fibers are spun from a dispersion of the dissolved polymer forming the fiber matrix and the colloids in water and is thus well suited for processing the P1K-dispersions. Recent publications report the successful preparation of multi-compartment nanofibers with incorporated functional nanoparticles.^{173, 226, 227} The incorporation of particles can not only add functionality to the fibers but can also significantly alter their morphology and properties.²²⁸ For example, Yuan et al. studied the morphology changes of poly(vinyl alcohol) (PVA) fibers as confining template for the assembly of polystyrene particles with different sizes and concentrations.²²⁹ Most importantly for our approach, by using this technique, it was demonstrated possible to use the nanofibers as protection of the load from environmental influences like oxygen due to better barrier properties, caused by the double encapsulation offered by the wall of the nanocapsules and the fibers matrix.²³⁰ Also, encapsulation of different payloads as separated domains as well as multi-agent delivery from nanofibers was successfully shown.²³¹

However, in the above mentioned examples, the encapsulated compartments were not reactive towards each other. In this project, we tried to encapsulate the two highly reactive epoxy and amine colloids used in the P1K-1 system in one electrospun fiber. To prolong the lifespan of the P1K, we aim at separating the two compartments on the nanoscale by the polymeric fiber matrix and to “freeze” them within the fiber. Upon stimuli induced contact, both compartments shall immediately react. The possibility to create a high concentration of both components in close vicinity inside these dual-component fibers can provide very short diffusion distances for polymerization, which can be very interesting for self-healing applications. Many examples of autonomous self-healing materials make use of two component systems that form thermosetting polymers either directly upon contact or by catalysts.^{143, 147, 232-234} One key issue is the spatial separation of both and at the same time the facilitation of both components getting in contact when the self-reaction is needed.²³⁵⁻²³⁷ Often mechanical stress or temperature increase is used as a trigger for the initiation of the cross-linking reaction.^{238, 239} Epoxy-amine curing has already gained much interest in this field because the high reactivity, dense cross-linking ability and strong adhesion properties of epoxy/amine-systems can provide significant advantages for self-healing.^{149, 240, 241} It would be beneficial, to assemble and keep the E&A colloids in close vicinity, which can be realized by the colloid-electrospinning approach. At the same time it is mandatory to prevent their premature cross-linking which may be realized by the surrounding fiber matrix and was investigated throughout this work. In theory, the nanoscale dimensions

and a statistical distribution of both parts favor an improved stoichiometry for reaction and therefore enable efficient cross-linking. The self-healing reaction can be triggered either upon temperature increase or by mechanical stress.

4.3.2 Nanofiber Synthesis

For the encapsulation of the epoxide and amine (E&A) as distinct compartments they need to be immiscible with the spinning solution and the fiber matrix itself and premature reaction needs to be suppressed. PVA was chosen as the fiber matrix. We used the same synthesis protocol as for the P1K-1, except that the amine emulsion was mixed with the PVA matrix solution for 3 min with a vortexer before the epoxy miniemulsion was added. The P1K-1 dispersion was used for these study, since a low educt viscosity was needed to facilitate their immediate interdiffusion as soon as the matrix material is damaged. This viscous hybrid dispersion was again prepared by stoichiometrically mixing the A&E colloids according to their amine hydrogen- and epoxy equivalent weight (AHEW and EEW). The calculated number concentration of amine and epoxy droplets is approximately 1.9:1 as displayed in Table 16. Compared to the aqueous P1K-1 system, the likelihood of premature reaction should be decreased due to the viscos PVA solution, still the mixture was submitted for immediate colloid-electrospinning as shown in Figure 46 to prevent premature reactions.

Table 16. Summary of the colloidal properties of the emulsions, details regarding the fibers and their epoxy-amine loads. From the calculations, a number ratio of amine nanoparticles to epoxy nanoparticles of 1.91/1 can be deducted.

Entry	Mean diameter [nm] (PDI)	droplet number/g EA dispersion ^a	Ratio PVA/ EA	C _{PVA} [wt.%]	Mean fiber diameter ^b [nm]
Amine Me	137 (0.093)	4.4*10 ¹⁵	-	-	-
Epoxy Me	153 (0.099)	2.3*10 ¹⁵	-	-	-
PVA control	-	-	-	10	361 ± 14
PVA-EA 0	-	-	6:1	12	319 ± 54
PVA-EA	-	-	3:1	10	311 ± 50
PVA-EA 2	-	-	2:1	8.6	165 ± 18
PVA-EA 3	-	-	1:1	5	73 ± 31

^a) Calculated on basis of the DLS data (with $\rho_{\text{epoxy}} = 1.16 \text{ g cm}^{-3}$; $\rho_{\text{amine}} = 0.979 \text{ g cm}^{-3}$ (measured with a pycnometer); AHEW = 220 g eq⁻¹, EEW = 187 g eq⁻¹). ^b) Calculated via SEM. The viscosity (25 °C) of the amine was 1530 mPas and of the epoxide about 12 000 mPas.

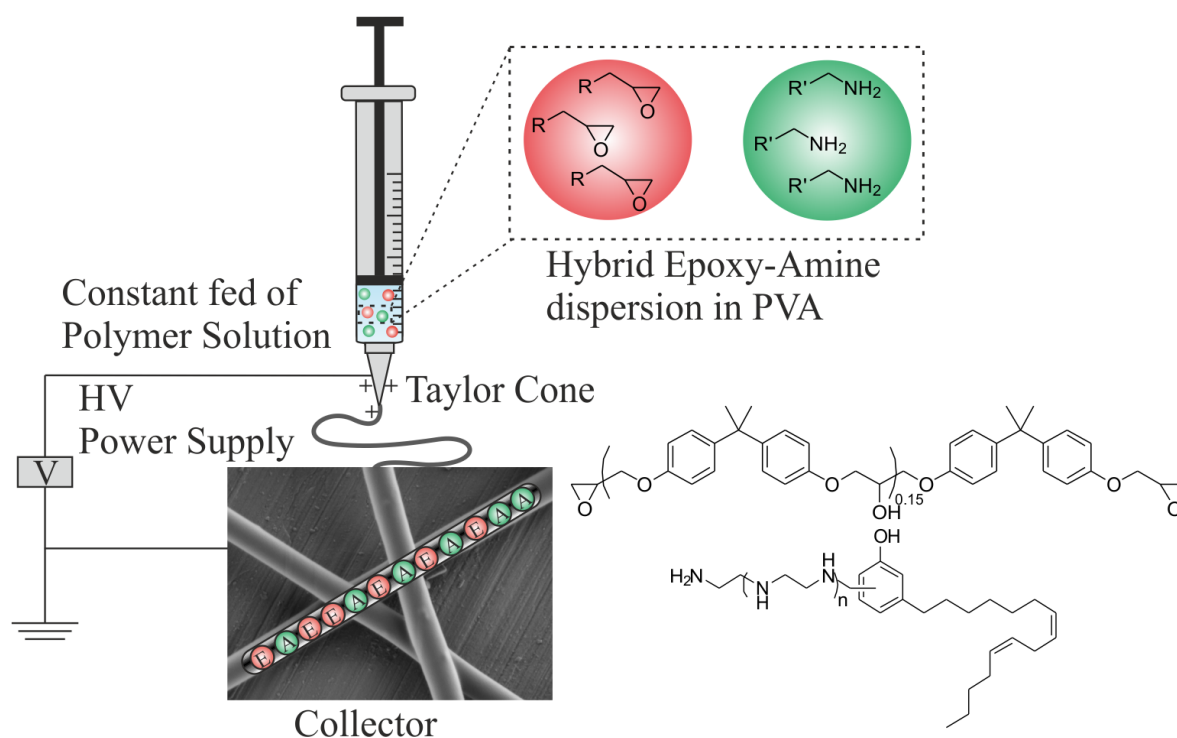


Figure 46. Schematic presentation of the colloid electrospinning process and the statistical distribution of the epoxy and amine compartments in the obtained nanofibers on basis of the PVA-EA 3:1 sample. PVA serves as matrix polymer keeping the reactive colloidal domains separated. Furthermore, the simplified chemical structures of the epoxy and amine are displayed.

4.3.3 Morphology and Distribution of Compartments

4.3.3.1 External Morphology as studied by SEM

During the spinning process, various parameters influence the morphology of the nanofibers: Jet thinning, water evaporation, increasing viscosity and possible reactions of both compartments play important roles. Depending on the concentration ratios of the PVA matrix to the colloids, the fiber morphology will be either dominated by the matrix or by the epoxy-amine colloids. Therefore, the PVA-EA ratio was varied from 6:1 to 1:1 based on dry weight, in order to maximize the load of A&E while maintaining uniform fibers. The SEM image in Figure 47c) shows the electrospun fibers at a ratio of 3:1, which appear smooth and uniform with 310 ± 50 nm thickness and with no unencapsulated material present, i.e., absence of free amine or epoxy nanoparticles. Lower ratios and pure PVA fibers gave almost identical results. Fiber spinning with higher concentration of the dispersion yielded a more irregular morphology. In contrast, also beads were formed due to decreased viscosity, converting the polymer jet into droplets.²⁴² For the 1:1 ratio (Figure 47e)) also some free material was visible as particles on the substrate. It can be speculated, that at high particle concentrations premature reaction of

A&E at least partially takes place during the colloid-electrospinning. In fact the 1:1 nanofibers appear partially fused together, with a tendency to cross-link especially in the beaded regions.

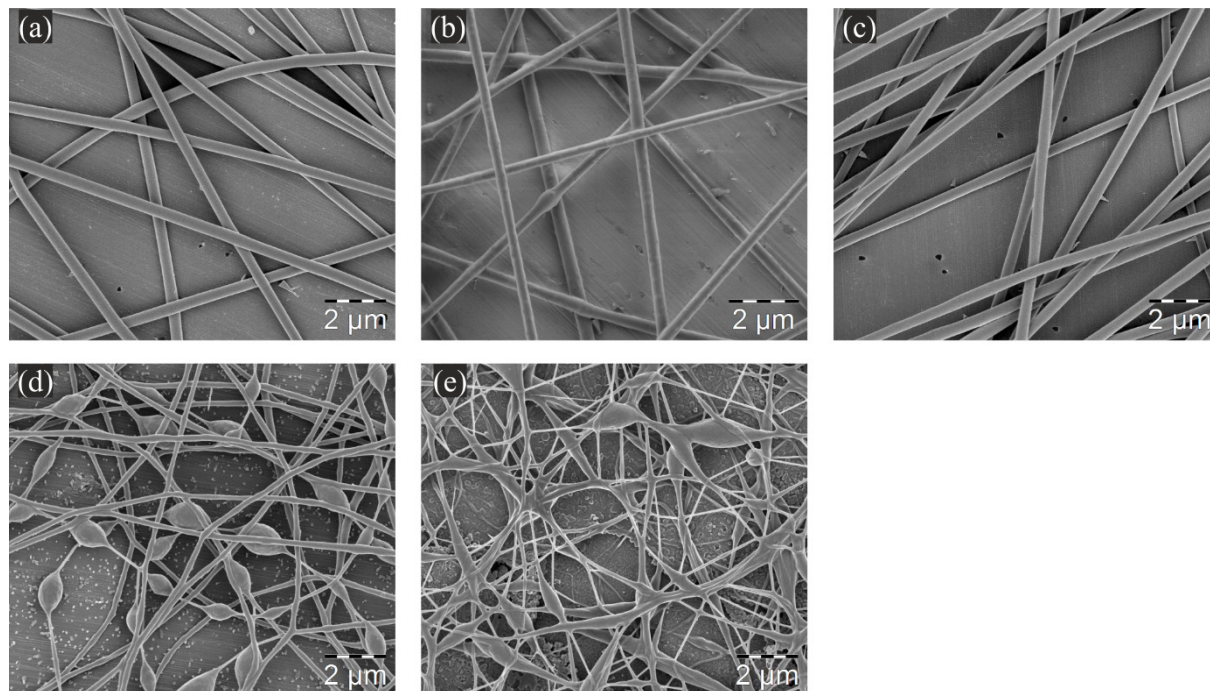


Figure 47. SEM images of the dual compartment (PVA-EA) fibers with different matrix to colloid ratios a) pure PVA b) 6:1 c) 3:1 d) 2:1 e) 1:1.

4.3.3.2 Internal Morphology as studied by (DC-STED)

To visualize the distribution of both components within the nanofibers, we utilized fluorescence labelling in combination with dual-color stimulated emission depletion (STED) microscopy.^{157, 158} This method was reported earlier to resolve and locate nanoparticles immobilized in nanofibers.²⁴³⁻²⁴⁵ Two hydrophobic dyes were synthesized for this purpose: A BODIPY and a bathochromically shifted perylene dye, since they provide high fluorescence quantum yield, photostability, STED suitability and large extinction coefficients.⁸¹ A detailed description of their synthesis can be found in the experimental part (chapter 5.5.2). Their absorption and emission spectra are shown in Figure 48c). The amine component was labelled in green (diphenylperylene) and the epoxy component in red (BODIPY). Both dyes were subsequently excited at $\lambda_{\text{Diphenylperylene}} = 458 \text{ nm}$ and $\lambda_{\text{BODIPY}} = 514 \text{ nm}$ with an Ar-laser. The fluorescence was depleted at 592 nm, which is suitable for both dyes.

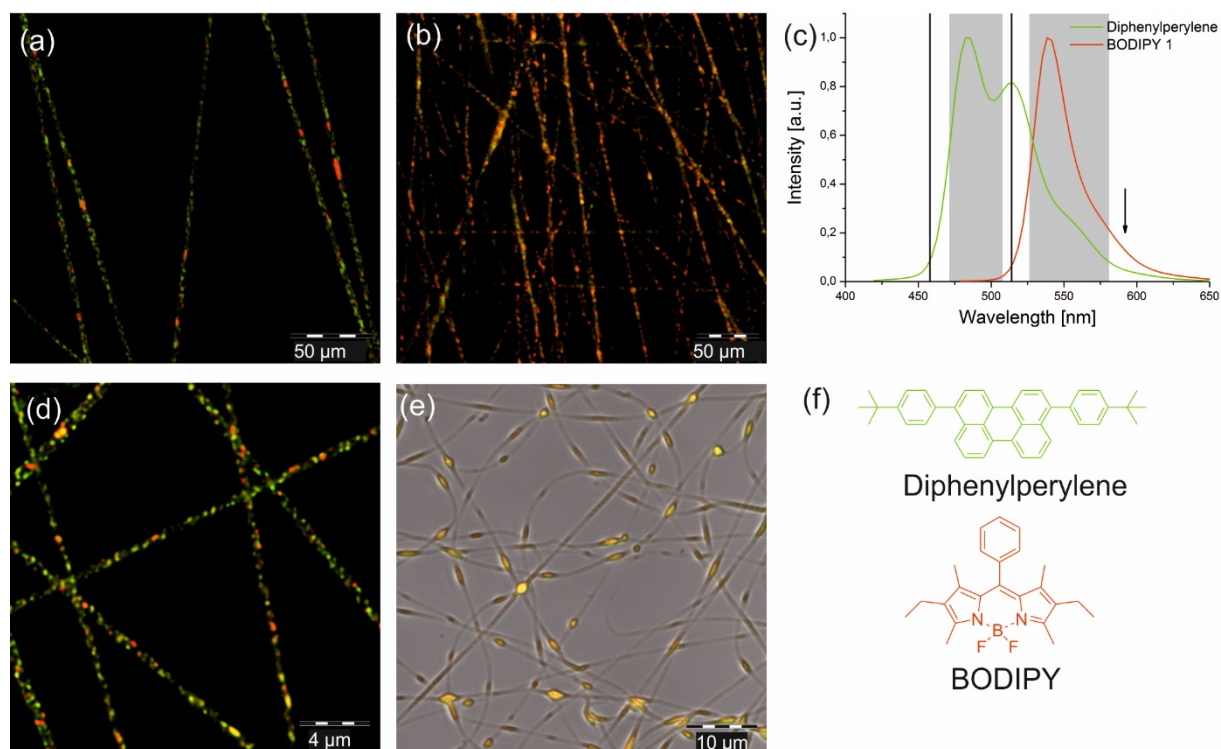


Figure 48. Characterization of the electrospun two component nanofibers. Dual-color STED image (deconvoluted) of the PVA-EA 3:1 sample a) at room temperature and b) after thermal treatment (150 °C). c) Emission spectra and detection windows (grey) for the STED imaging. Excitation wavelengths for both dyes are marked as black lines and the depletion wavelength with an arrow. d) Confocal microscopy image (deconvoluted) of the PVA-EA fibers immersed in glycerol. e) Confocal image of the PVA-EA 1:1 sample. f) Chemical structure of the dyes used. Images were kindly recorded by Anke Kaltbeitzel.

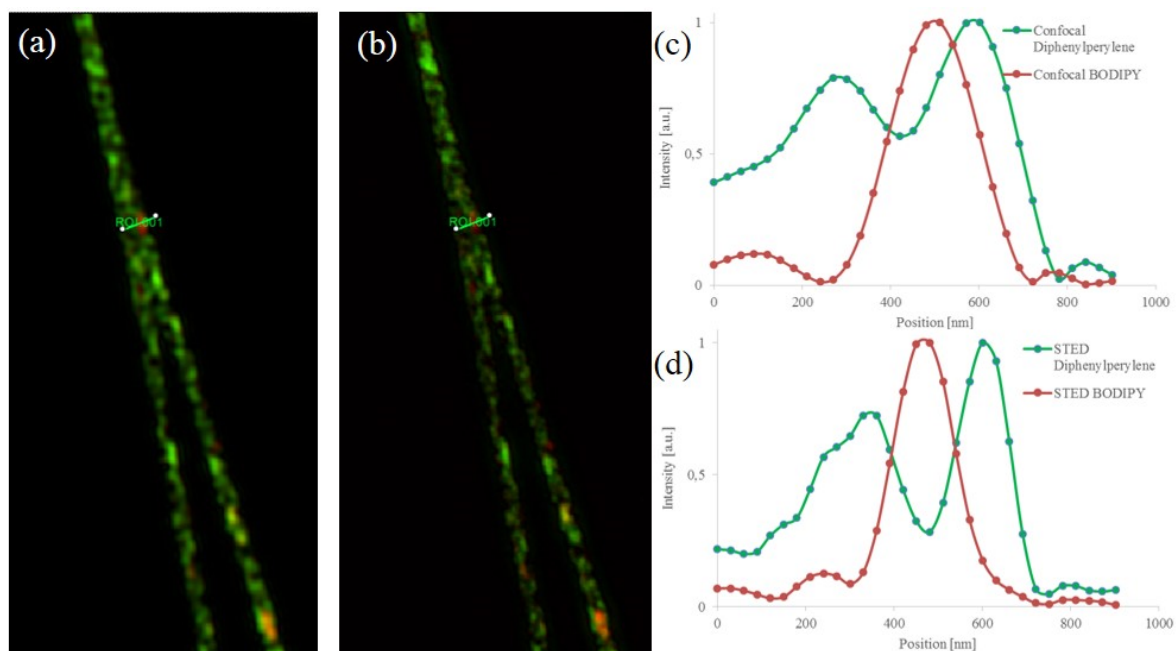


Figure 49. Comparison of a) confocal image versus b) STED image. The graphs show the intensity for both color channels along the line profile shown in both images for the c) confocal image and d) for the STED image.

Figure 48a) displays the PVA-EA 3:1 nanofibers as an overlay of the red and the green channel. A comparison of STED versus confocal imaging can be found in Figure 49. For this comparison, a section of Figure 48a) was enlarged (Figure 49b)) and compared to the same section in confocal imaging (Figure 49a)). For confocal deconvolution, the same algorithm/parameters were used as for the STED image, except for the PSF, assuming a Gaussian distribution of 230 nm. In Figure 49c-d) the intensity profiles along the lines marked in a) and b) are depicted for the diphenylperylene and BODIPY channel. It is obvious, that the usage of STED allows for a better separation and resolution of the compartments. Full width half maximum (FWHM) of the BODIPY compartment is ~ 230 nm in confocal mode as compared to 170 nm using STED imaging. For the diphenylperylene compartment, STED shows FWHM of ~ 130 nm as compared to ~ 230 nm in the confocal mode.

From the absence of background fluorescence, it can be concluded that the self-healing material is fully encapsulated within the PVA fibers. Furthermore, both components are randomly distributed among the fibers with more “green” droplets present, due to the differences in number concentration as calculated in Table 16. Despite the nanoscale dimensions, the particles appear well separated from each other in almost all cases. Some of the “red” epoxy droplets seem elongated. We used glycerol as immersion fluid to swell the PVA matrix which displayed an increased average fiber diameter of about 670 nm (Figure 48d)). The image shows that at this stage, except from very few orange appearing spots, the red and green labelled compartments are clearly separated from each other. For evaluation, we performed statistical analysis of both components. In total, 450 objects were analyzed. It needs to be noted however, that we are operating close to the detection limit, which only allows a vague quantitative discussion. The analysis was performed using object recognition. In average, in a fiber volume of $1 \mu\text{m}^3$, 10 objects were found for the swollen state. In the non-swollen state, the concentration is about 4-5 times higher. The ratio of green/red was found 1.9:1 which is in good agreement with the theoretically calculated 1.91:1 number concentration. We found partial overlapping between the A&E compartments, which we could not resolve accurately due to the detection limit. Nevertheless, the analyzed image is a 2D projection, so overlapping signals could also be a consequence of this projection and are investigated further.

Additionally, we had a closer look at the PVA-EA 1:1 sample. The confocal microscopy image shown in Figure 48 e) shows a complete co-localization of the red and green dye. As suspected, we also found an increased concentration of the dyes in the beaded regions, showing that cross-linking had likely taken place during the spinning process. In this sense, the intrinsic reactivity approach can be used for the generation of new structures and fiber morphologies, suitable for

advanced material and tissue engineering, which will be subject of further studies. The focus of this contribution maintains on dual-compartment fibers with a very close vicinity of A&E without significant reaction to enable for example enhanced self-healing ability. Therefore, the 3:1 ratio was used for all further investigations.

4.3.3.3 TEM and Simulations

To estimate the particle-particle distances within the fibers, firstly computations and secondly TEM measurements were performed. For the computation of the nearest neighbor particle-particle distances, the following assumptions were made: a) the concentration ratios after the electrospinning equal the initial concentrations, b) to simplify the model no distinction between the A&E compartments was made, c) the compartments were described as hard spheres and the confining fiber as cylinder and d) the spheres perform a random walk on a cubic grid with a step size of 2.5 nm within the cylindrical confinement. We used $R_{\text{Fiber}} = 175$ nm and $r_{\text{EA}} = 75$ nm and $f_{\text{EA}} = 0.28$ representing the fraction of spheres compared to the overall amount of polymer (fiber+ spheres) for the computation (see Table 17). The nearest neighbor distribution is close to an exponential distribution as one would expect for a uniform point distribution in one dimension.²⁴⁶ For the simulation, the spheres were located along the cylinder axis as initial scenario (Figure 50c) left). Starting from this conformation, the spheres were allowed to move within the confined space. The second cylinder shows their position after approximately 80000 moves. The initial 40000 steps were discarded to avoid artefacts originating from the chosen starting conformation. The statistics were carried out on basis of the remaining 40000 steps.

Table 17. Parameters used for the computations.

R_{Fiber} [nm]	r_{EA} [nm]	f_{EA}	ρ_{EA} [g cm ³]	ρ_{PVA} [g cm ³]
155	75	0.284	1	1.19

$$f_{\text{EA}} = \frac{1}{\left(1 + \frac{3 \cdot \rho_{\text{EA}}}{\rho_{\text{PVA}}}\right)} \quad 16$$

f_{EA} represents the fraction of both amine and epoxy compartments compared to the total amount of polymers in the system (A&E + PVA). For this calculation, it is assumed that the densities in the nanofibers equal those of the bulk polymers.

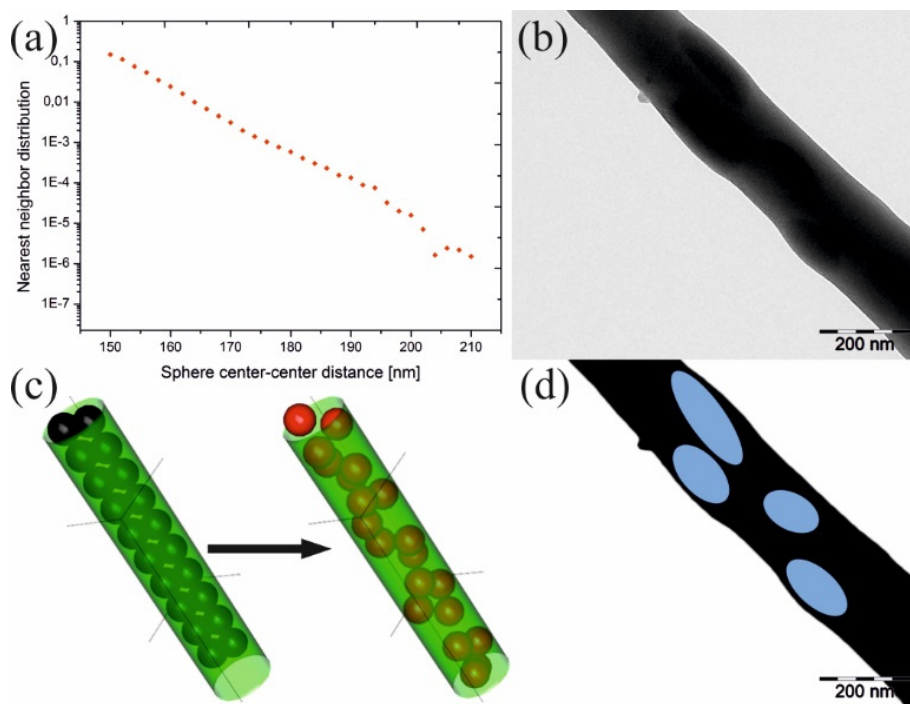


Figure 50. a) The graph shows the probability density for the nearest neighbors as a function of the sphere center to center distance as a logarithmic plot. b) TEM images of the PVA-EA 3:1 sample. c) Computed model of the fibers showing the sphere-filled cylinder with a chosen initial conformation where all spheres (black) are located at the cylinder axis. The red spheres in the second cylinder represent their position after 80000 moves. d) False colored reproduction of image b) showing the elongated particles.

The depicted density allocation in Figure 50 a) shows the particle-particle distances in the nanometer range. The distance (in units of r_{EA}) between the majority of individual particles is even less than one, thus proving this method viable to assemble highly reactive components in very close vicinity to each other. Similar results were obtained by choosing a different starting scenario, where the spheres are located close to the cylinder wall.

The localization of nanoparticles in the fibers with TEM is usually difficult because of their low differences in electron density. It was possible to enhance the contrast with OsO_4 staining (Figure 50b)). For better understanding, we false-colored the particles in Figure 50d)). Also in TEM the particles seem elongated, a phenomenon which already has been described for colloid-electrospinning several times.²⁴⁷ The aspect ratio was 2.9 ± 1.0 . The particle-particle distances are on the nanometer length scale with 91 ± 63 nm. Compared to the computed model, the center to center distances are higher. This could have several reasons: The model does not consider the observed anisotropic deformation of the particles and also the model disregards deviations in particle as well as fiber sizes. Another explanation might be a changed concentration ratio before and after the electrospinning took place. However, we did neither observe any free, unencapsulated material in SEM nor in the STED measurements.

4.3.4 Reactivity

In a second step, we tried to investigate the reactivity of the system. The curing of the epoxy-amine system itself at RT is very fast with a pot-life of about 12 min (chapter 4.2.2.3). At first, we tried to quantify the amount of unreacted epoxide within the fibers by DSC and HPLC measurements. From the DSC, a very broad signal for the cross-linking in bulk with an enthalpy change per gram epoxide of about 230 J g^{-1} with a T_g of $103 \text{ }^\circ\text{C}$ was obtained (Figure 51a)). For these investigations, the epoxy was balanced into the DSC crucible and the amine into the lid. They were pressed against each other immediately before the measurement was run. Thus, we compared the PVA reference fibers and the PVA-EA fibers and also found a broad exothermic peak for the latter, indicating that the curing reaction is possible within the nanofibers, which is however hard to describe quantitatively. To exclude that the exothermia results from anything other than the epoxy amine curing, two sets of reference experiments were carried out. In Figure 51a) bulk reactions, obtained by mixing the pure PVA with the epoxy and amine in the same quantities as in the nanofibers are shown. We saw a similar very broad peak which increased in area as we shifted the ratio towards higher epoxy-amine concentrations. To exclude side reactions between for example the PVA matrix and the epoxy, we additionally mixed the PVA with only the epoxy or the amine as shown in Figure 51b). Neither showed any exothermia, so it can be concluded, that epoxy-amine curing is possible in the nanofibers. For the HPLC measurements, the amine as well as the PVA fibers were cross-linked with glutaraldehyde and the epoxide was extracted from the mixture by swelling the samples in chloroform. The extract was analyzed with HPLC-UV (see Figure 51 d)). Despite uncertainties, like premature reaction during chemical fixation/solvent treatment or the complete extraction, we found about 65% of unreacted epoxide, which means the majority of both components remains reactive within the nanofibers and can be used for triggered reactions, due to for example temperature increase or mechanical stress.

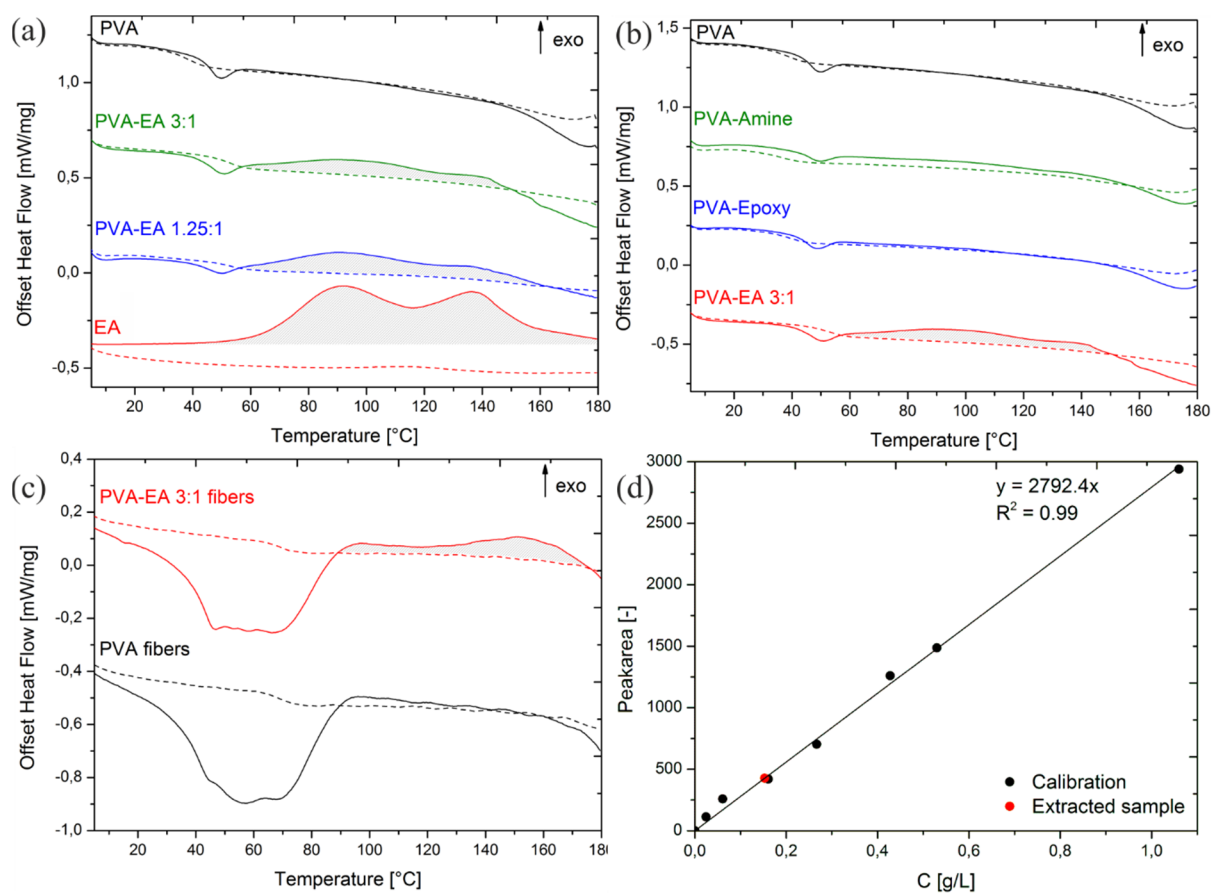


Figure 51. DSC curves of the epoxy-amine curing as bulk references. 2nd heating cycles are depicted as dashed lines. a) Black: pure PVA powder; green: PVA powder mixed with epoxy and amine (ratio 3:1); blue: artificially increased ratio of 1.25:1; red: pure curing reaction. b) Mixtures of PVA powder with the individual components, to ensure that the measured enthalpy change originates from the curing reaction only. c) Comparison of the pure PVA fibers (black) and the PVA-EA fibers (red). d) Black: Calibration curve for the epoxide including linear regression and correlation coefficient. Red: Extracted sample after cross-linking of the amine and the PVA fibers with glutaraldehyde (GAH).

To get further insights into the curing mechanism, we compared the fibers at RT and after heating to 120 °C and 150 °C for 5 h. Afterwards, the PVA matrix was removed by immersing the sample in 500 μ L deionized water for 3 min and subsequent drying in a N₂ stream. The dual-compartment fibers heated from RT up to 120 °C (Figure 52a-b)) show an inhomogeneous film, also with some cured particles and partially fused particles present on the substrate. A further increase in temperature to 150 °C enables a preservation of the fiber morphology as shown in Figure 52c). Furthermore, the fibers seem to be partially fused together, which for self-healing materials can be regarded as a desired effect, since it adds to the overall integrity of the composite material.

FT-IR spectroscopy (Figure 52d)) comparing the fibers before and after this treatment (150 °C) also indicate a temperature induced cross-linking reaction by the disappearance of the peak

shoulder corresponding to the characteristic valence vibration of the epoxide ring at 915 cm^{-1} . From the FT-IR measurements it can also be seen, that the PVA becomes partially trapped within the fiber-network and could not be removed by immersion in water anymore. Since the hydroxyl groups of the PVA are present in large excess, it can be expected that they cross-link with the epoxide or with themselves at high temperatures.

We also looked at the cured fibers at $150\text{ }^{\circ}\text{C}$ with STED in a less concentrated region. The STED microscopy image in Figure 48b) shows that now both channels almost completely overlay. It is no longer possible to distinguish between the red and the green channel which again indicates a successful curing.

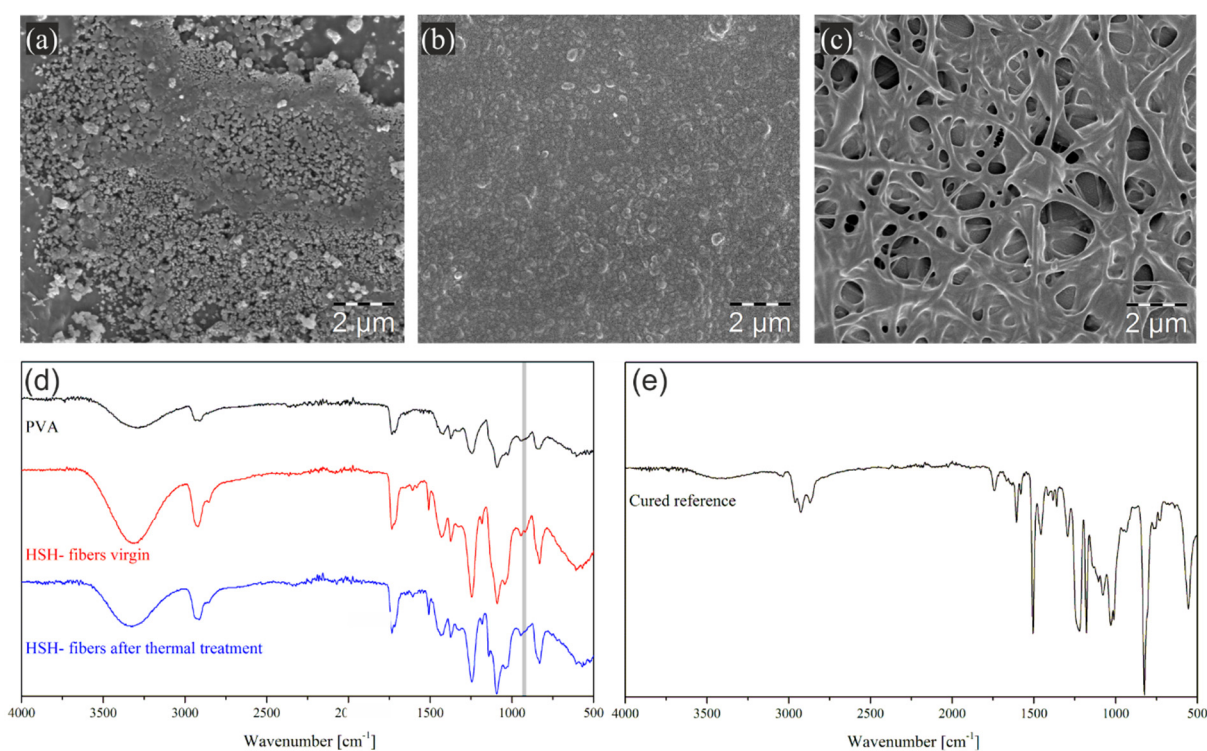


Figure 52. SEM images after dissolving of the PVA at a) RT, b) $120\text{ }^{\circ}\text{C}$ showing an inhomogeneous film and c) $150\text{ }^{\circ}\text{C}$ showing a partially fused fiber matt. d) FT-IR of the nanofibers before and after curing and the PVA reference. e) Reference spectrum of a fully cured film.

4.3.5 Self-Healing

To demonstrate the approach viable for self-healing applications, the electrospun fibers were coated with an amine cured epoxy matrix which was scribed with a razorblade as shown in Figure 53a). Pure PVA fibers were also embedded in the same matrix to serve as a reference as did the matrix without any fibers. Linear sweep voltammetry was performed 96 h after the samples were cut. A three electrode cell with the Al-foil glued onto an Au-electrode was used and subsequently the sealed sample was immersed into a KCl-electrolyte solution. The graph in Figure 53b) shows that for the virgin coating no current was detected, whereas a significantly increased current was measured for the scribed coating without any fibers present. Similar results were obtained for the pure PVA-fiber control sample. In contrast, the PVA-EA fibers did not show an increase in current, but provided significant passivation of the substrate and hence an efficient self-healing.

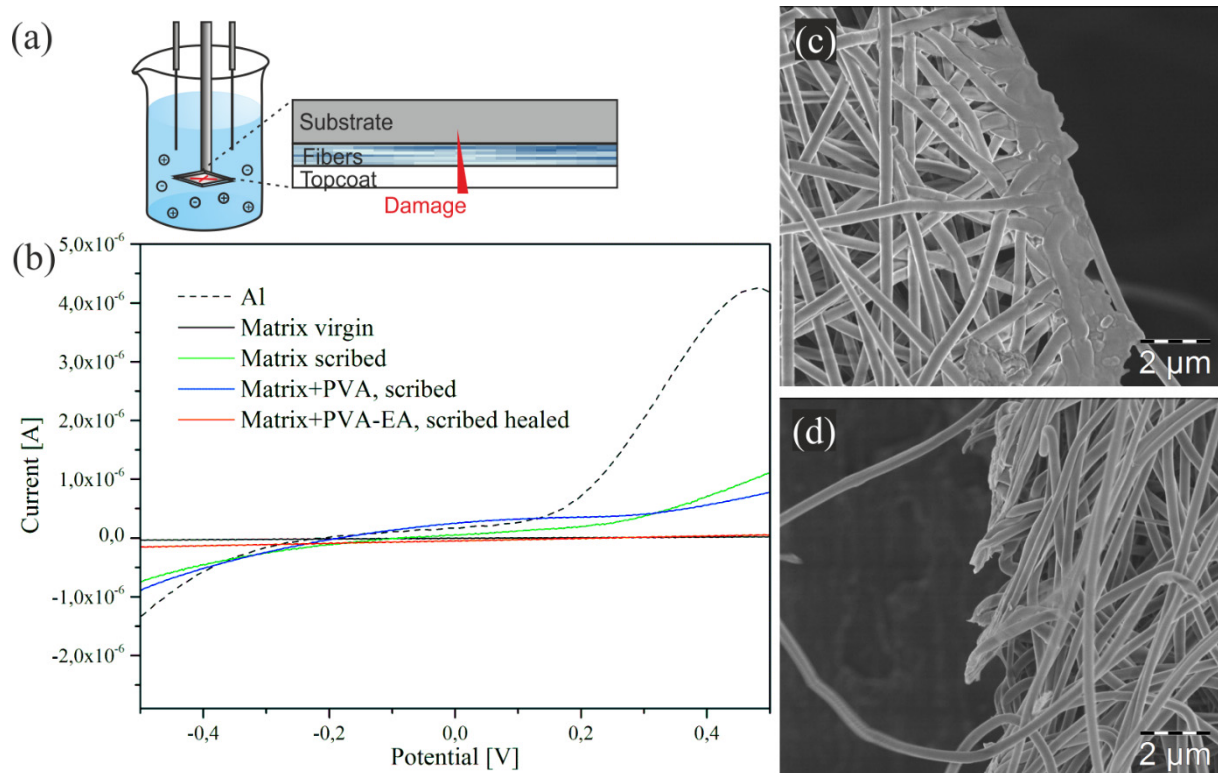


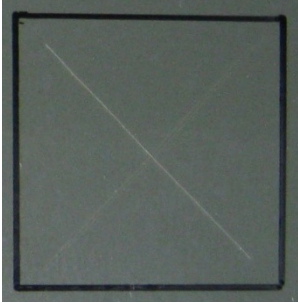
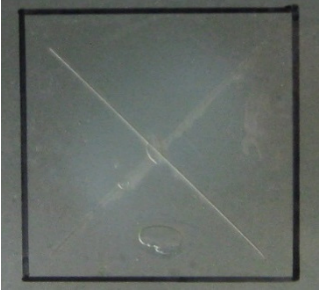

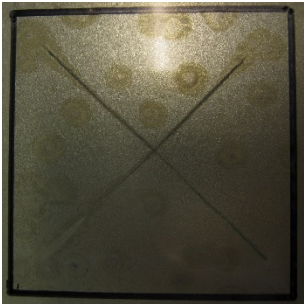
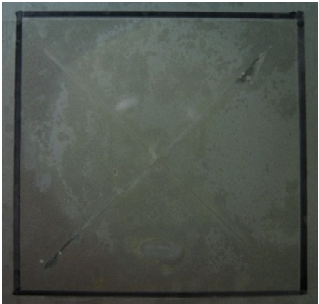
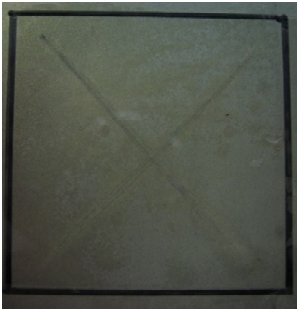
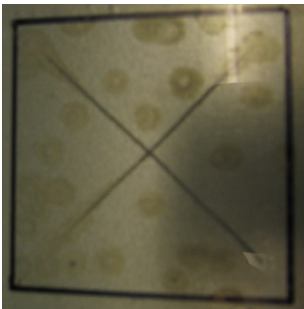
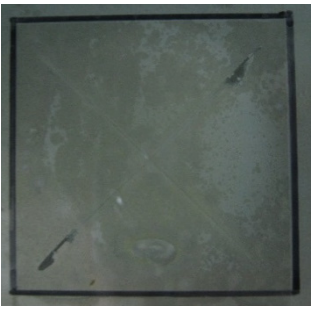

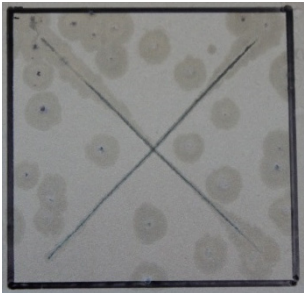


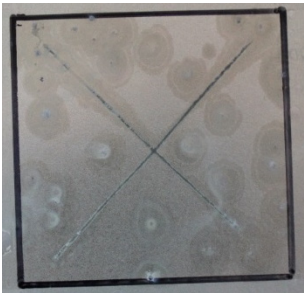


Figure 53. Self-healing ability of the PVA-EA 3:1 sample. a) Schematic drawing of the setup for the voltammetry measurements. b) Current versus Potential curves comparing the virgin coating (black), the pure Al-foil (black, dashed) with the scribed non-healing (green and blue) and the self-healing coating (red). SEM image of the scribed c) PVA-EA sample versus d) the scribed PVA nanofibers.

Additionally, the reactivity and self-healing capability of the reactive dual-compartment nanofibers are shown in a simple fiber cutting experiment. Samples were scribed with a razor blade and left healing at room temperature for 24 h. These investigations were made after 3 months of storing the fibers at RT, to prove the long-term stability and maintained reactivity of the system. Figure 50c-d) compares the pure PVA fibers and the PVA-EA fibers. The PVA-EA fibers are completely fused due to the release of both compartments and their subsequent cross-linking, whereas the PVA fibers remain ruptured.

Another common method to determine the anti-corrosion performance of a coating in a reasonable time is performed by immersing coated steel substrates into salt water to promote their corrosion. This method is also widely used in industry. In this experiment, the performance of the self-healing nanofibers was compared to the pure PVA fibers and the coating without any fibers present. Therefore, the fibers were directly spun onto the corrosive substrates and coated with the epoxy-amine matrix (PIK-1) that is also present in the fibers themselves.

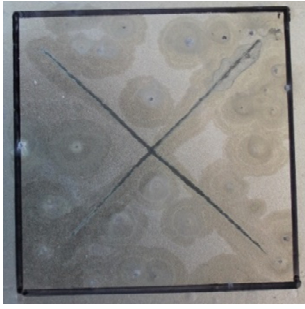
The optical images depicted in Table 18 show their anti-corrosion performance over time. After one day, the PVA reference already shows some degree of staining at the corners of the cut area. During the course of the test all samples show progressive corrosion of the underlying steel which becomes obvious after the polymer was removed. The PVA-EA sample seems to retard the corrosion compared to the PVA reference, where the topcoat of the PVA sample started to detach from the substrate after about 60 h. However, compared to the pure coating no beneficial effect can be noted. Since the PVA fiber matrix itself is water soluble, water could penetrate through the damaged area over time, causing the system to fail which was not observed in the electrochemical testing. As a consequence, for further applications in the field of corrosion protection, the effect of different fiber matrices should be studied to tune the adhesive properties of the fibers to the substrate.

Table 18. Optical evaluation of the salt water corrosion test.

Time [h]	Topcoat	Topcoat +PVA fibers	Topcoat +PVA-EA
0			
24			
48			
60			
72			

Results and Discussion

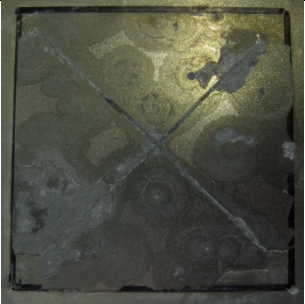
84



96



After
topcoat
removal



4.3.6 Conclusion

In conclusion, dual-compartment nanofibers encapsulating epoxy and amine as two highly reactive components in one polyvinyl alcohol fiber are investigated. They are prepared by colloid-electrospinning of the P1K-1 dispersion with poly (vinyl alcohol) in different concentration ratios. Uniform fibers are produced using a fiber/colloid ratio of 3:1. Computations in combination with fluorescent labelling and high resolution microscopy methods confirm that well separated epoxy and amine domains in very close vicinity (< 100 nm) are obtained. Despite their immediate proximity, premature reaction is suppressed efficiently. The fiber matrix is able to keep them separated over several months of storage. Cross-linking of the compartments can be initiated either upon temperature increase or mechanical damage. Self-healing at room temperature is achieved as shown by electrochemical testing and scanning electron microscopy measurements. The concept represents a non-classical, colloidal approach to carefully adjust reaction latency. Additionally, extremely short diffusion distances for two component cross-linking polymerization offers fundamental advantages and new possibilities for self-healing systems and autonomous repair of material damage. For further studies, the adhesive properties of the fiber matrix to the substrate should be tuned to obtain better adhesive properties of the fibers themselves.

5 Experimental Part

5.1 Experimental Details for Chapter 4.1

5.1.1 Materials

Methyl methacrylate (MMA, $\geq 99\%$ stab. Merck Chemicals), butyl methacrylate (BMA, $\geq 99\%$ stab., Merck Chemicals), methacrylic acid (MAA, 99.5% stab., Acros Organics) and the crosslinker 1,4-butanediol dimethacrylate (BDDMA, $\geq 95\%$, Sigma Aldrich) were used without further purification. Desmodur Z 4470 (IPDI-trimer, 70% in butylacetate, NCO = 355 g eq.⁻¹, Bayer Materials) and the castor oil (OH number = 158 mg KOH g⁻¹, VWR International), isooctane (IO, $\geq 99.5\%$, Carl Roth), hexadecane (HD, $\geq 99\%$, Merck Chemicals), dimethyltin dineodecanoate (Fomrez UL-28, 50-100%, Momentive), potassium peroxydisulfate (KPS, p.A., Merck), sodium dodecyl sulfate (SDS, 99%, Lancaster) were used as received.

5.1.2 Synthesis of the Nanocapsules containing a PU-Catalyst

The disperse phase was prepared by dissolving various amounts of Sn-catalyst and HD (250 mg) as ultrahydrophobe in isooctane and by mixing with the shell forming monomers MMA (3 g), BMA (0.4 g), MAA (0.4 g) and various amounts of the cross-linker BDDMA according to Table 19. The mixture was slowly poured into 22 g aqueous solution of SDS (23 mg).

Table 19. Preparation of the catalyst nanocapsules.

[g]	Ref.	TLCN 1	TLCN 2	TLCN 3	TLCN 4	TLCN 5	TLCN 6
MMA	3	3	3	3	3	3	3
BMA	0.4	0.4	0.4	0.4	0.4	0.4	0.4
MAA	0.4	0.4	0.4	0.4	0.4	0.4	0.4
BDDMA	0.1	0.1	0.1	0.1	-	0.04	0.2
HD	0.25	0.25	0.25	0.25	0.25	0.25	0.25
IO	2	1.7	1.4	-	1.7	1.7	1.7
Fomrez	-	0.3	0.6	2	0.3	0.3	0.3
H ₂ O	24	24	24	24	24	24	24
SDS	0.023	0.023	0.023	0.023	0.023	0.023	0.023
KPS	0.08	0.08	0.08	0.08	0.08	0.08	0.08
SC [%]	14	14	14	15	13	13	13

A pre-emulsion was obtained by mixing with an ultraturrax at 16000 rpm for 3 min. Miniemulsification was carried out by ultrasonication (Branson W450 Digital sonifier, equipped with a 0.5'' tip) for 3 min at 90% amplitude in a pulsed mode (10 s pulse, 5 s pause) under ice cooling. Afterwards, the miniemulsion was transferred into a 100 mL round bottom flask equipped with a magnetic stirrer and the free radical polymerization was initiated by adding 80 mg of KPS, dissolved in 2 mL water at 72 °C. The polymerization time was 5 h. The solid content was 14%. If not otherwise stated, the final dispersions were dialyzed for 24 h with deionized water to remove possible traces of unencapsulated material and monomers. Afterwards, the dispersions were freeze-dried to obtain the pure nanocapsules.

5.1.3 Catalytic Cure of PU-Composites

To demonstrate the thermolatency of the synthesized catalytic nanocapsules, we chose a polyurethane system comprising of Desmodur Z 4470 as trifunctional, aliphatic isocyanate in combination with castor oil as polyol component. In a typical experiment, 1 g of the castor oil was stoichiometrically mixed with 0.9945 g of the IDPI-Trimer and immediately submitted for rheological analysis. Typically, 0.1 wt.% of catalyst are added to reduce the curing time. They were either added directly (1 mg) to the castor oil directly or encapsulated (TLCN 1: 20.98 mg). Nonreactive isooctane capsules were also added in the same quantity.

For the preparation the reinforced fiber composites by resin transfer molding (RTM) 1.258 g of the TLCN1 capsules were mixed with 60 g of castor oil and 59.67 g of the isocyanate. The mixture was pumped into a 13x13x0.4 cm mold, containing 6 layers of $\pm 45^\circ$ biaxial fiber rovings from Saertex (surface weight 658 g m⁻²), with a peristaltic pump (Europump PA-ST1 basic) from IKA Labortechnik at room temperature to obtain a total fiber volume of 50%. Afterwards, the mold was closed and placed in an oven for 2.5 h at 120 °C for curing.

5.1.4 Characterization Methods

5.1.4.1 Dynamic Light Scattering

Dynamic light scattering (DLS) measurements were carried out using a Malvern Zetasizer instrument at 25 °C with a scattering angle of 173°. Beforehand, the samples were diluted with deionized water. The Z_{av} value was taken for analysis.

5.1.4.2 Electron Microscopy

Scanning Electron Microscopy (SEM) measurements were carried out on a Zeiss Gemini 1530 SEM (Carl Zeiss, Germany). Diluted samples were drop cast on silica wafers and left drying at RT.

Transmission Electron Microscopy (TEM) images were recorded on a Jeol JEM-1400 TEM under cryogenic (-170 °C) conditions and low dose electron beam irradiation to avoid polymer shell degradation.

5.1.4.3 Thermal Analysis

Thermogravimetric analysis (TGA) was performed on a TA Instruments TGA Q5000 IR instrument with heating rates of 10 K min⁻¹ under N₂ atmosphere in a temperature range from 20 to 700 °C.

Differential Scanning Calorimetry (DSC) measurements were carried out on a Netzsch 204 F1 Phoenix differential scanning calorimeter with heating rates of 10 K min⁻¹ under N₂ atmosphere in a temperature range from 20 to 180 °C. 5-10 mg were used for the measurements.

5.1.4.4 X-Ray Fluorescence Spectroscopy

Quantification of the Sn-content in the nanocapsules was determined with an Axios Advanced, Fa. Panalytical (WD-RFA) X-ray fluorescence spectrometer equipped with a LiF200 crystal, a 300 μm collimator and a scintillation counter operating at 60 kV/ 66 mA. Analysis was performed using a 2θ-angle of 14.0318°. Fluorescence was detected using the K_α line. Sn-extraction was performed on about 100 mg of the freeze dried samples which were melted at 800 °C with a mixture of LiNO₃, NaNO₃ and NaB₄O₇ and afterwards heated to 1100 °C to quantitatively extract Sn.

5.1.4.5 NIR-Coupled Oscillatory Rheology

For the evaluation of the catalytic activity of the nanocapsules, near infrared spectroscopy-coupled rheology was used. Therefore, an Anton Paar MCR 302 rheometer was coupled with a

Bruker MPA FT-NIR spectrometer to allow simultaneous determination of the viscoelastic properties, as well as monitoring the disappearance/evolution of functional groups upon curing. Measurements were carried out in a plate-plate configuration with one quartz glass plate and one aluminum plate ($d = 25\text{mm}$) with an initial gap of 0.2 mm and the normal force was set to zero with automatic gap control throughout the measurement. The measurements were carried out at a frequency of 100 rad s^{-1} with a deformation of 0.1%. NIR spectra were recorded with a resolution of 16 cm^{-1} at a constant sampling rate of about 2 spectra s^{-1} . For the monitoring of the urethane formation, the peak areas of the $2\nu\text{NH}$ vibration at about 6749 cm^{-1} were integrated. For comparison, the spectra were normalized. Therefore, the peak areas after complete curing reaction were set to 100%.

5.1.4.6 Dynamic Mechanical Analysis

Dynamic Mechanical Analysis (DMA) was carried out on a TA- DMA Q800 instrument using a single cantilever method with a heating rate of 3 K min^{-1} under N_2 atmosphere with a frequency of 1 Hz and an amplitude of $20\text{ }\mu\text{m}$ in a temperature range of -100 to $200\text{ }^\circ\text{C}$. The T_g was determined by evaluation of the maximum of $\tan\delta$. Specimen sizes were $35\times 10\times 4\text{ mm}$.

5.2 Experimental Details for Chapter 4.2

5.2.1 Materials and Purification

Diethylether (>99%), acetic acid (99.9%) and perchloric acid (0.1 M) from VWR Chemicals and tetraethylammoniumbromide (98%, Alfa Aesar) were used as received. Bisphenol-A-diglycidylether (Dow Chemical) and the NC547 (Cardolite Corp.) were used as received. The phenalkamines NX545 and NC641 were purified by solvent extraction. Therefore, 250 g of each amine were dissolved in 250 g of diethyl ether and water soluble impurities were removed by extracting 3 to 5 times with 1 L of deionized water in a separation funnel until the aqueous phase was clear. The solvent was removed *in vacuo* to obtain the purified amines.

5.2.2 Preparation of the P1K-Thermosets

The P1K-systems were prepared by vigorous mixing the epoxy and amine component in stoichiometric amounts according to their EEW and AHEW in a flask which was subsequently degassed for 1 min to avoid bubble formation. Afterwards, the mixture was submitted for immediate analysis.

Table 20. Preparation of the P1K-thermosets.

Entry	Epoxy component	Amine component
P1K-1	BADGE (2.0 g, EEW = 187 g eq. ⁻¹)	NX5454 (2.353 g, AHEW = 220 g eq. ⁻¹)
P1K-2	BADGE (2.0 g, EEW = 187 g eq. ⁻¹)	NC641 (1.519 g, AHEW = 142 g eq. ⁻¹)
P1K-3	NC547 (4.0 g, EEW = 763 g eq. ⁻¹)	NC641 (0.744 g, AHEW = 142 g eq. ⁻¹)

5.2.3 Characterization Methods

5.2.3.1 Epoxy Titration

The epoxy equivalent weight (EEW) was determined via potentiometric titration adapted from ASTM D 1652 with perchloric acid to from bromohydrine which after consumption of the epoxide groups gives free hydrobromic acid. The inflection point was taken for determination and each measurement was repeated three times and the average was taken for calculation of the EEW. Titration was performed on a Metrohm T50 Titrator from Mettler Toledo.

5.2.3.2 Amine Titration

The total amount of nitrogen was determined by dissolving the sample in acetic acid and titrating with 0.1 M trifluoromethanesulfonic acid and the consumption at the inflection point was determined (DGF H-III 20a (98)). For the determination of tertiary nitrogen the sample

was dissolved in acetic acid, put in a 250 mL autoclave, acetic anhydride was added and the mixture was heated to 60 °C for 30 min. The inflection point after titration with 0.1 M trifluoromethanesulfonic acid was determined (DGF-H-III 20b (98)). The sum of tertiary and secondary nitrogen was determined by dissolving the sample in propanol and adding salicylaldehyde and leaving the mixture at 80 °C for 15 min. The mixture was titrated with 0.1 M HCl and the primary nitrogen content was determined by subtracting the sum from the total nitrogen content (DGF-H III 20b (98)).

5.2.3.3 Thermal Analysis

DSC measurements were carried out on a Netzsch 204 F1 Phoenix differential scanning calorimeter with heating rates of 10 K min⁻¹ under N₂ atmosphere in a temperature range from 20 to 180 °C. 5-10 mg were used for the measurements. The measurements were carried out immediately after the two components were mixed. Two heating cycles were performed for each measurement.

5.2.3.4 Oscillatory Rheology

Oscillatory rheology measurements were carried out in a plate-plate configuration ($d = 25\text{mm}$) with an initial gap of 0.8 mm and the normal force was set to zero with automatic gap control throughout the measurement. The measurements were carried out at a frequency of 10 rad s⁻¹ with a deformation of 0.1 %. For the curing at RT the temperature was set to 25 °C for 15 h.

For the determination of the T_g the samples were subsequently heated to 160 °C at 2 K min⁻¹ held, at 160 °C for 2 h to ensure complete curing and cooled to RT with a cooling rate of 0.5 K min⁻¹. The T_g was determined by evaluation of the peak maximum in the loss factor curve upon cooling.

5.3 Experimental Details for Chapter 4.2.3

5.3.1 Materials

The hydrophobic phenalkamine (NX5454) was kindly provided from Cardolite Corp.. Bisphenol-A-diglycidylether (BADGE, DER331) with an epoxy equivalent weight (EEW) of 187 g eq⁻¹. was purchased from Dow Chemical, Germany and the surfonamine (L200 with an average number of 2 PPG and 42 PEG units; M_w = 1960; PDI= 1.16 by SEC) from Huntsman, The Netherlands. The nonionic surfactant Lutensol AT 50 and the ionic surfactant sodium dodecyl sulfate (SDS BASF, Germany), cetyltrimethylammonium bromide (CTAB, Sigma Aldrich) and hexadecane (HD, \geq 99%, Merck Chemicals) as well as the solvent ethyl acetate (p.a., Sigma Aldrich, Germany) were used as received. Formic acid (98%) was purchased from Bernd Kraft, Germany.

5.3.2 Synthesis of the Epoxy Surfactants

BADGE (12.67 g; 0.033 mol) was put in a 250 mL round bottom flask and was mixed with the polyether monoamine (50.00 g; 0.025 mol). The reaction was carried out at 150 °C for 5 h to obtain a slightly yellow wax in quantitative amounts. Under the chosen conditions, no noticeable competitive reaction between the formed hydroxyl-groups occurred, which was monitored by measuring the EEW over time by taking aliquots and freezing them in liquid nitrogen.

5.3.3 Non-Reactive Epoxy Surfactants

nrES

For the synthesis of the nonreactive surfactant (nrES) the epoxy groups were quantitatively esterified by dissolving 2 g of the epoxy surfactant in 10 g formic acid. The mixture was left stirring overnight, distilled and dried *in vacuo*.²⁴⁸

nrES2

- a) 3 g ES (0.375 mM) dissolved in 20 g THF were put in a 50 mL flask and were mixed with 0.32 g of the phenalkamine (0.75 mM). The mixture was left stirring at RT for 24 h. After removal of the solvent a yellow waxy product was obtained which could only be swollen but not dissolved afterwards, indicating that cross-linking took place under this conditions.

- b) 3 g ES (0.375 mM) dissolved in 20 g THF were put in a 50 mL flask and were mixed with 0.64 g of the phenalkamine (1.50 mM). The mixture was left stirring at RT for 24 h. After removal of the solvent and repeatedly washing with THF and diethyl ether a yellow viscous product was obtained which was still soluble.

5.3.4 Preparation of Amine Miniemulsions

In a typical experiment, the disperse phase contained 20 g of the amine dissolved in 20 g of ethyl acetate. Hexadecane (4 wt.%) was used as an ultrahydrophobe to prevent Ostwald ripening of the emulsion droplets. The disperse phase was slowly poured into an aqueous solution of the synthesized epoxide surfactant or the nonreactive reference in various amounts. A pre-emulsion was obtained by using an ultraturrax for 3 min. Miniemulsification was carried out under ice cooling by passing the emulsion 4 times through a M-100Y high pressure homogenizer (Microfluidics) at 10000 psi. The interaction chambers used were H230Z (400 μm) and H210Z (200 μm). Afterwards the ethyl acetate was carefully removed with a rotary evaporator without affecting the stability of the emulsion.

For the ITC experiments a pre-stabilization of the amine miniemulsion with Lutensol AT50 as a surfactant was achieved by using the same preparation procedure. The nonreactive reference emulsion was prepared by using an epoxy resin which was prepared analogously to the above mentioned procedure.

5.3.5 Characterization Methods

5.3.5.1 Fourier Transform Infrared Spectroscopy

IR spectroscopy measurements were carried out on a Bruker ALPHA FT-IR spectrometer equipped with an ATR diamond, a SiC light source and a DTGS detector. Measurements were carried out at room temperature.

5.3.5.2 Nuclear Magnetic Resonance Spectroscopy

^1H -NMR spectra were measured on a Bruker DRX spectrometer (400.13 Hz). CDCl_3 was used as a solvent and the spectra calibrated according to its chemical shift of 7.25 ppm.

5.3.5.3 Epoxy Titration

The epoxy equivalent weight (EEW) was determined via potentiometric titration, adapted from ASTM D 1652 with perchloric acid to from bromohydrine which after consumption of the epoxide groups gives free hydrobromic acid. The inflection point was taken for determination

and each measurement was repeated three times. The average was taken for calculation of the EEW.

5.3.5.4 Size Exclusion Chromatography

The molecular weight distribution was determined via size exclusion chromatography (SEC) on an Agilent PSS SEcurity SEC equipped with a Shodex RI 101 detector at 30 °C. Samples were dissolved in THF or DMF to reach a concentration of 5 mg mL⁻¹, the flow rate was 1.0 mL min⁻¹ and the calibration was done with a polystyrene standard from Polymer Standard Services GmbH.

5.3.5.5 Critical Micelle Concentration Determination

The critical micelle concentration (CMC) of the epoxy surfactant was investigated with a SITA science t60 bubble pressure tensiometer. The measurement was carried out at 21 °C with an average bubble lifetime of 60 s. The CMC was determined by dosing a 5 mg L⁻¹ solution of ES into 150 mL of deionized water and by measuring the surface tension. From the surface tension versus concentration plot which ideally shows a linear decrease followed by a sharp change in slope to zero, the CMC can be calculated by determination of the intersection point after linear regression of both lines.

5.3.5.6 Dynamic Light Scattering

Dynamic light scattering (DLS) measurements were carried out using a Malvern Zetasizer instrument at 25 °C with a scattering angle of 173°. Beforehand, the samples were diluted with deionized water. The Z_{av} value was taken for analysis.

5.3.5.7 Isothermal Titration Calorimetry

Isothermal titration calorimetry (ITC) was performed on a NanoITC Low Volume instrument from TA instruments, Germany. The cell temperature was constantly kept at 25 °C. The reference cell contained distilled water. For the measurements a freshly prepared pre-stabilized miniemulsion using 7 wt% Lutensol AT50 as surfactant was chosen. The total cell volume was 190 µL and permanently stirred at 350 rpm. The emulsion was diluted to a droplet concentration of 1·10⁻⁶ mM. The concentration was estimated according to the average droplet diameter determined via DLS measurements. A 1 mM solution of the reactive epoxy surfactant as well as the nonreactive surfactant was used as a titrant. The total titration volume was 50 µL (20 x 2.5 µL). In between each titration step a 40 s delay was chosen to ensure the system had reached its equilibrium state. Blank measurements were performed by titrating the same amount of surfactant into distilled water to determine the heat of dilution. Thermal heat flow was measured

over time to give either positive signals corresponding to an exothermic reaction or negative signals for endothermic reactions. The enthalpy of the reaction was calculated by plotting the heat per mole of titrant against the ratio of titrated surfactant molecules per emulsion droplet. The curves were fitted with the Independent binding model which assumes that every surfactant molecule binds individually and that no cooperative reactions take place, such as the formation of new NH_2 groups that can further react.^{159, 218}

5.3.5.8 Electron Microscopy

SEM measurements were carried out on a Nova NanoSEM (Fei, USA). The undiluted samples were dried for 3 days at RT on a silicon wafer and were sputtered with Au prior to analysis.

TEM measurements were performed on a Philips Tecnai 10 TEM operating at 100 kV. Diluted samples were deposited on 400-mesh carbon coated copper grids and dried prior to analysis.

5.3.5.9 Oscillatory Rheology

Oscillatory rheology was carried out on an Anton Paar MCR 302 Rheometer with parallel plate geometry at 70 °C in the linear viscoelastic region at 0.1% deformation and 10 rad s^{-1} angular frequency with a plate-plate-configuration.

5.4 Experimental Details for Chapter 4.2.4

5.4.1 Materials

Bisphenol-A-diglycidylether (Dow Chemical) and the NC547 (Cardolite Corp.) were used as received. The phenalkamines NX545 and NC641 (Cardolite Corp.) were used after purification. Deionized water was used throughout all experiments. Ethyl acetate (EtAc, 99%, Sigma Aldrich) and the fluorescamine ($\geq 98\%$, Alfa aesar) were used as received.

5.4.2 Preparation of Amine and Epoxy Miniemulsions

For the preparation of amine and epoxy miniemulsions, the dispersed phase contained 30 g of amine or epoxide with hexadecane as ultrahydrophobe and ethyl acetate as auxiliary solvent to lower the viscosity in order to obtain smaller particle sizes, as listed in Table 21. The dispersed phase was slowly poured into an aqueous solution of the epoxide surfactant in various concentrations (0.5 wt% - 13 wt%) and pre-emulsified using an ultraturrax for 3 min. Miniemulsification was carried out under ice cooling by passing the emulsions 4 times through a M-100Y high pressure homogenizer (Microfluidics; M-100Y, interaction chambers H230Z 400 μm and H210Z 200 μm) at 10000 psi. Ethyl acetate was removed with a rotary evaporator at 40 °C without affecting the stability of the emulsions. The solid content was determined gravimetrically and was 20% in all cases.

Table 21. Preparation of amine and epoxy miniemulsions with different surfactant concentrations and the corresponding sizes and size distributions.

	BADGE [g]	NC547 [g]	NX5454 [g]	NC641 [g]	EtAc. [g]	HD [g]	ES [g]	H ₂ O [g]	Z _{AV} [nm]	PDI	
BADGE-1	30	-	-	-	-	30	1.2	0.312	137.28	348	0.228
BADGE-2	30	-	-	-	-	30	1.2	0.624	137.28	305	0.051
BADGE-3	30	-	-	-	-	30	1.2	0.936	137.28	205	0.045
BADGE-5	30	-	-	-	-	30	1.2	1.56	137.28	220	0.159
BADGE-7	30	-	-	-	-	30	1.2	2.184	137.28	151	0.072
BADGE-9	30	-	-	-	-	30	1.2	2.807	137.28	155	0.06
BADGE-10	30	-	-	-	-	30	1.2	3.12	137.28	140	0.06
NC547-1	-	30	-	-	-	30	1.2	0.312	137.28	616	0.131
NC547-3	-	30	-	-	-	30	1.2	0.936	137.28	390	0.237
NC547-5	-	30	-	-	-	30	1.2	1.56	137.28	249	0.147
NC547-7	-	30	-	-	-	30	1.2	2.184	137.28	220	0.121
NC547-9	-	30	-	-	-	30	1.2	2.807	137.28	169	0.071
NC547-10	-	30	-	-	-	30	1.2	3.12	137.28	152	0.097
NC547-13	-	30	-	-	-	30	1.2	4.056	137.28	129	0.06
NX5454-0.5	-	-	30	-	-	30	1.2	0.156	137.28	538	0.569
NX5454-1	-	-	30	-	-	30	1.2	0.312	137.28	415	0.234
NX5454-2	-	-	30	-	-	30	1.2	0.624	137.28	237	0.217
NX5454-3	-	-	30	-	-	30	1.2	0.936	137.28	211	1.860
NX5454-5	-	-	30	-	-	30	1.2	1.56	137.28	154	0.208
NX5454-7	-	-	30	-	-	30	1.2	2.184	137.28	134	0.123
NX5454-9	-	-	30	-	-	30	1.2	2.807	137.28	124	0.079
NX5454-10	-	-	30	-	-	30	1.2	3.12	137.28	126	0.049
NC641-1	-	-	-	30	-	30	1.2	0.312	137.28	170	0.080
NC641-3	-	-	-	30	-	30	1.2	0.936	137.28	142	0.37
NC641-5	-	-	-	30	-	30	1.2	1.56	137.28	120	0.011
NC641-7	-	-	-	30	-	30	1.2	2.184	137.28	106	0.049
NC641-8	-	-	-	30	-	30	1.2	2.807	137.28	122	0.067
NC641-10	-	-	-	30	-	30	1.2	3.12	137.28	109	0.117
Cured references for the PIK systems											
PIK-1 reference	13.7838	-	16.2162	-	-	30	1.2	3.12	137.28	132	0.003
PIK-2 reference	11.364	-	-	8.636	-	20	0.8	2.807	94.43	129	0.089
PIK-3 reference	-	25.2928	-	4.07072	-	30	1.2	3.13	137.28	144	0.070

5.4.3 Preparation of P1K-Systems

For the preparation of the P1K-dispersions, the different epoxy and amine emulsions were stoichiometrically mixed as listed in Table 22 and homogenized with a vortexer for 1 min. Afterwards, the systems were submitted for immediate measurements. The recipes for the cured references, where the polyaddition was carried out ideally in each emulsion droplet to give fully cured thermosetting particles can be found in Table 21.

Table 22. Preparation of the P1K-dispersions.

Name	BADGE-10 [g]	NC547-10 [g]	NX5454-10 [g]	NC641-10 [g]
P1K-1	100	-	117.647	-
P1K-2	100	-	-	75.94
P1K-3	-	100	-	18.6

5.4.4 Characterization Methods

5.4.4.1 Absorption and Emission Spectroscopy

Absorption and emission spectra were recorded on a Tecan Infinite M1000 plate reader. Absorption and emission spectra for the fluorescamine $1 \mu\text{g mL}^{-1}$ were recorded after it was derivatized with the NX5454 to obtain a fluorescent product. Spectra were recorded in ethyl acetate. All spectra were corrected for solvent and background and their intensities were normalized. Triple determinations were carried out for all measurements.

5.4.4.2 Dynamic Light Scattering

Dynamic light scattering (DLS) measurements were carried out using a Malvern Zetasizer instrument at $25 \text{ }^\circ\text{C}$ with a scattering angle of 173° . Beforehand, the samples were diluted with deionized water. The Z_{av} value was taken for analysis.

5.4.4.3 Fluorescamine Assay

Fluorescence spectra were recorded on a Synergy H1 Multi Detection Reader from Bio-tek Instruments GmbH, Bad Friedrichshall, Germany with $\lambda_{ex} = 410 \text{ nm}$ and $\lambda_{em} = 470 \text{ nm}$ in ethyl acetate. Samples were prepared according to chapter 5.4.3. Aliquots were taken from the prepared P1K-systems and dissolved in ethyl acetate in a 100 mL volumetric flask and shaken for 2 min. Subsequently, $2 \times 25 \mu\text{L}$ aliquots were taken and diluted with another $750 \mu\text{L}$ of ethyl acetate. For the fluorescamine assay, $250 \mu\text{L}$ of a fluorescamine stock-solution (0.3 g L^{-1}) were

added and mixed with a vortexer. All spectra were corrected for solvent and background. Therefore, blanks were prepared by adding another 250 μL of ethyl acetate instead of the fluorescamine solution. Triple determinations were carried out for all measurements.

Table 23. Sample preparation and amine concentrations for the fluorescamine assay.

Name	BADGE -10 [g]	NC547- 10 [g]	NX5454- 10 [g]	NC641- 10 [g]	P1K [g]	EtAc [mL]	C^* amine [g L ⁻¹]
P1K-1	2	-	2.353	-	0.052	100	0.05
P1K-2	2	-	-	1.5188	0.066	100	0.05
P1K-3	-	4	-	0.744	0.182	100	0.05
P1K-3 Ref	-	4	-	0.744	0.182	100	0.05

* Calculated, assuming no reaction took place in dispersion.

Table 24. Exponential and linear fits and correlation coefficients for the description of primary amine content in the P1K-systems over time.

Sample	Linear fit	R ²	Exponential decay fit	R ²
P1K-1	-	-	$Y = 72.636 * e^{(-x/1.1119)} + 1.3386$	0.954
P1K-2	-	-	$Y = 76.8248 * e^{(-x/4.2701)} + 0.6127$	0.980
P1K-3	$Y = -1.1245x + 72.078$	0.910	-	-
P1K-3 Ref	$Y = -1.8852x + 41.3378$	0.741	$Y = 49.8184 * e^{(-x/5.5473)} - 0.83358$	0.941

5.4.4.4 Film Formation

Optical images of the RT-cured films were taken after 48 h.

The minimum film formation temperature (MFFT) was determined with a TQC MFFT 10 gradient-plate in a temperature range between 0 and 80 °C. Films were applied with a 500 μm doctor blade from the different P1K-dispersions at 20 wt.% solid content.

5.4.4.5 Turbidity Measurements

For turbidity measurements, the different P1K-systems with a fixed amine concentration of (0.052 g P1K-1; 0.066 g P1K-2 and 0.182 g P1K-3) were dissolved in 100 mL of ethyl acetate. The same samples were used for the amine titration. The turbidity of the solutions was determined at RT on a 662 Photometer from Metrohm Lt., Switzerland after correction for background and solvent. The equations for the fits were:

Table 25. Exponential and linear fits and correlation coefficients for the P1K-systems over time.

Sample	Linear fit	R ²	Exponential decay fit	R ²
P1K-1	-	-	$Y = 9.4918 * e^{(-x/4.0676)} + 91.6753$	0.954
P1K-2	-	-	$Y = 9.0042 * e^{(-x/3.8408)} + 92.1001$	0.980
P1K-3	$Y = -0.0409x + 100.1326$	0.6205	-	-
P1K-3 Ref	-	-	$Y = 18.9854 * e^{(-x/1.8989)} + 79.7493$	0.9839

5.4.4.6 Electron Microscopy

SEM measurements of the cured films were carried out on a Nova NanoSEM (Fei, USA). Samples were sputtered with Au prior to analysis.

5.4.4.7 Thermal Analysis

DSC measurements were carried out on a Netzsch 204 F1 Phoenix differential scanning calorimeter with heating rates of 10 K min⁻¹ under N₂ atmosphere in a temperature range from 20 to 180 °C. Approximately 20 mg were used for the measurements.

5.4.4.8 Oscillatory Rheology

Measurements were carried out in a plate-plate configuration with one quartz glass plate and one aluminum plate (d = 25mm) with an initial gap of 0.8 mm and the normal force was set to zero with automatic gap control throughout the measurement. The measurements were carried out at a frequency of 10 rad s⁻¹ with a deformation of 0.1%. For the determination of the T_g the RT cured samples were heated to 160 °C with 2 K min⁻¹ held at 160 °C for 2 h to ensure complete curing and cooled to RT with a cooling rate of 0.5 K min⁻¹. The T_g was determined by evaluation of the peak maximum in the loss factor curve upon cooling.

5.5 Experimental Details for Chapter 4.3.

5.5.1 Materials

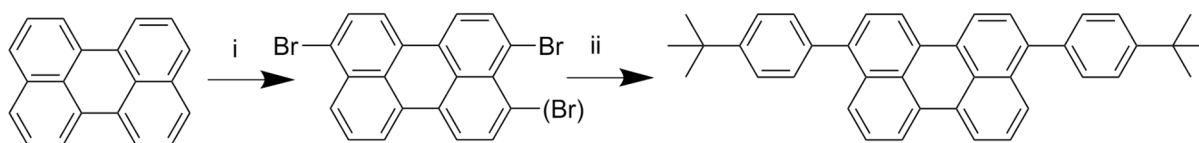
The phenalkamine NX5454 was kindly provided from Cardolite Corp. and purified by extracting 3 times with water (AHEW = 220 g eq.⁻¹). Ethyl acetate (99%), calcium chloride sol. (3M), Nafion per-fluorinated resin sol. (5 wt.%) and glutaraldehyde (25% aq. sol.) from Sigma Aldrich, chloroform (99%, Merck Chemicals), hexadecane (99% Acros Organics), the Jeffamine (D-400 Huntsman), poly(vinyl alcohol) (PVA, $M_w = 130000$, 88 mol% hydrolysis, Kuraray Europe), Bisphenol A-diglycidylether (BADGE, EEW = 187 g eq.⁻¹ Dow Chemical) were used as received.

5.5.2 Synthesis of the Dyes used for DC-STED

The synthesized dyes were prepared and characterized by Dr. Yuri Avlasevich.

3,9(10)-bis(4-*tert*-butylphenyl)perylene

Scheme 11. *i*, Br₂, AcOH; *ii*, 4-*tert*-butylphenyl boronic acid, Pd(PPh₃)₄, K₂CO₃ aq, toluene.



3,9(10)-Dibromoperylene was synthesized by bromination of perylene as described before.²⁴⁹

3,9(10)-Bis(4-*tert*-butylphenyl)perylene. 3,9(10)-dibromoperylene (410 mg, 1 mmol) and 4-*tert*-butylphenyl boronic acid (534 mg, 3 mmol) were dissolved in the mixture of toluene (40 ml) and ethanol (5 ml) in a 100 ml Schlenk flask and flushed with argon. After stirring at 80 °C for 20 min Pd(PPh₃)₄ (100 mg) and aqueous 2M K₂CO₃ (5 ml) were added to the solution. The reaction mixture was stirred at 90 °C for 12 h under argon. After cooling the resulting mixture was washed with water and extracted with toluene. The combined organic extracts were evaporated *in vacuo* and purified by column chromatography on silica gel using petrol ether: dichloromethane, 3:1 as eluent. Yield 400 mg (77.5%). **¹H-NMR (250 MHz, CD₂Cl₂, 25 °C):** $\delta = 8.15\text{--}8.20$ (m, 4H), 7.79 (d, ³*J*=8.44 Hz, 2H), 8.36–7.48 (m, 12H), 1.35 (s, 18H) ppm; **¹³C-NMR (75 MHz, C₂D₂Cl₄, 25 °C):** $\delta = 150.59, 140.25, 140.16, 137.64, 133.14, 131.74, 131.58, 130.70, 130.54, 129.88, 129.14, 128.19, 126.89, 125.63, 120.84, 120.60, 120.51, 120.27, 34.86, 31.76$ ppm; UV-vis (toluene) λ_{max} : 460 ($\epsilon/\text{dm}^3 \text{mol}^{-1} \text{cm}^{-1}$ 48000), 433 (38900) nm. Fluorescence (toluene): 482 nm ($\phi=97\%$). MS (FD): [M⁺], calculated for C₄₀H₃₆, 516.73; found, 517.1 (100%), M⁺.

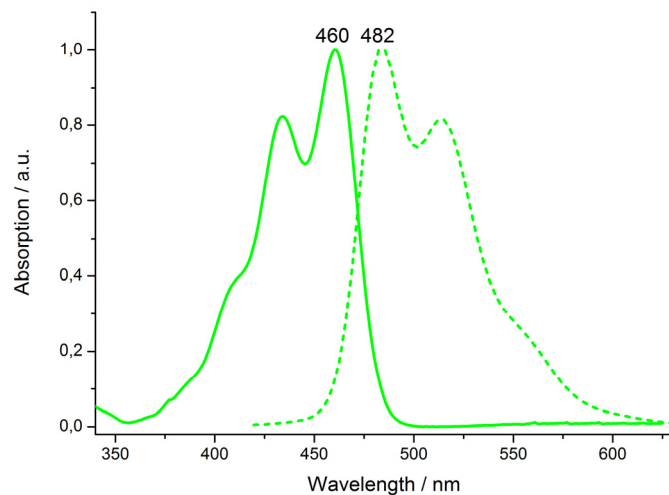
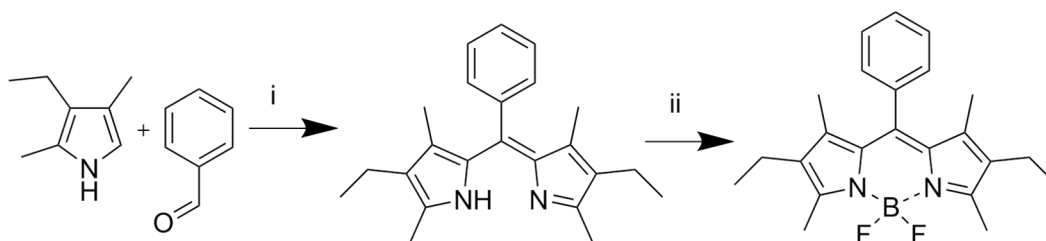


Figure 54. Absorption and emission spectra of diphenylperylene in toluene.

BODIPY (2,6-Diethyl-1,3,5,7-tetramethyl-8-phenyl-4,4'-difluoroboradiaza-indacene)

Scheme 12. i, TFA, dichloromethane, DDQ; ii, BF₃ etherate, Et₃N, dichloromethane.



The two-step synthesis was performed according to the literature.

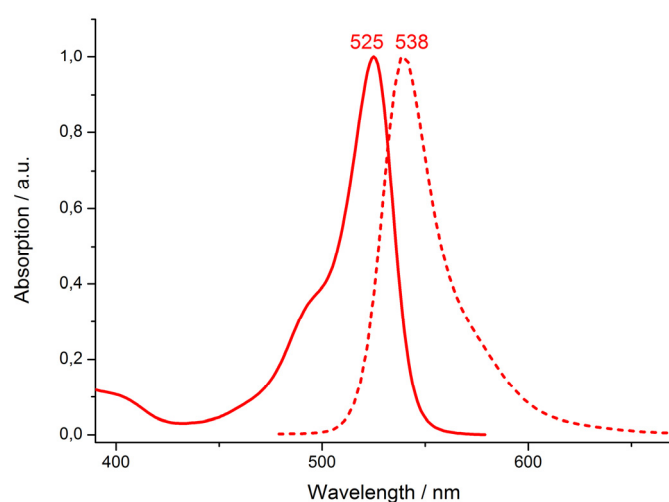


Figure 55. Absorption and emission spectra of BODIPY in toluene.

5.5.3 Synthesis of Nanofibers

The dispersed phase contained 10 g of the amine or the epoxide and 400 mg hexadecane as ultrahydrophobe dissolved in 10 g of ethyl acetate. For the STED experiments, 2 mg of the diphenylperylene (amine emulsion) or 2 mg of the BODIPY (epoxy emulsion) were added. The dispersed phase was slowly poured into an (0.83 wt.%; 112.42 g) aqueous solution of the epoxide surfactant and pre-emulsified using an ultraturrax for 3 min. Miniemulsification was carried out under ice cooling by passing the emulsions 4 times through a M-100Y high pressure homogenizer (Microfluidics; M-100Y, interaction chambers H230Z 400 μm and H210Z 200 μm) at 10000 psi. Ethyl acetate was removed with a rotary evaporator without affecting the stability of the emulsions. The samples were dialyzed for 24 h at RT to remove traces of the dyes in the aqueous phase.

15 wt.% aqueous PVA solutions were prepared by slowly heating the mixture to 90 °C for 2 h until complete dissolution occurred. The EA dispersion was mixed with the PVA solution at different weight ratios based on dry weight.

The EA dispersion was prepared by stoichiometrically mixing the two emulsions (10 g of amine emulsion and 8.42 g of epoxy emulsion) directly before the electrospinning.

For the quantification of the epoxide content, 9.47 mg PVA-EA fibers (equals 1.28 mg of epoxide) of the fibers were cross-linked with glutaraldehyde, which also cross-links the amine and therefore it was possible to extract the epoxide with chloroform for subsequent quantification with HPLC-UV. Extraction was performed by first rinsing the cross-linked fibers with water, freeze-drying subsequent swelling of the fibers in CHCl_3 (4.63 mL) for 18 h at RT under continuous shaking.

5.5.4 Characterization Methods

5.5.4.1 Fiber Spinning

The fibers were spun with a commercial platform (ESIa, Electrospinz) with a positive electrode applied to a spinneret and an aluminum foil as counter electrode. The flow rate of the polymer solution was 0.2 mL h^{-1} and controlled with a syringe pump. The inner diameter of the spinning tip was 0.4 mm and was connected to a 5 mL syringe containing the solution via a silicon rubber tubing. The tip-collector distance was varied from 8 to 12 cm. The electrospinning was carried out at RT. The voltage applied was varied from 10 to 20 kV.

5.5.4.2 Electron Microscopy

SEM measurements were carried out on a Nova NanoSEM (Fei, USA). Samples were measured on the Al-template as spun and were sputtered with Au prior to analysis.

TEM measurements were performed on a Philips Tecnai 10 TEM operating at 100 kV. For the nanofibers project: Samples were directly spun onto 400-mesh carbon coated copper grids and were stained in OsO₄ vapor for 10 min to enhance the contrast prior to analysis.

5.5.4.3 Simulations

Computations were performed using statistical analysis a script in R. For the statistical evaluation of the nearest neighbour density probability, 80000 moves were performed with a step size of 2.5 nm. The initial 40000 steps were discarded to avoid artefacts originating from the chosen starting conformation. The statistics were carried out on basis of the remaining 40000 steps.

5.5.4.4 Dual Color Stimulated Emission Depletion Microscopy

Dual-color Stimulated emission depletion microscopy (STED) (Leica TCS SP5) was used to visualize the distribution of both components within the nanofibers deposited on coverslips. A Leica HCX PL APO CS 1.4/100x oil-immersion objective was used. Both dyes were subsequently excited at $\lambda_{\text{Diphenylperylene}} = 458 \text{ nm}$ and $\lambda_{\text{BODIPY}} = 514 \text{ nm}$ with an Argon-laser. The fluorescence was depleted at $\lambda = 592 \text{ nm}$ with a 1.5 W CW laser. Fluorescence was detected by a Leica HyD-Detector (diphenylperylene) and a Leica photomultiplier (BODIPY). STED images were deconvoluted using the Leica LASAF algorithm "signal energy", a pseudo-inverse filter with stabilized signal energy and linear suppression of noise. Regularization parameter was 0.04, assuming a Lorentz PSF of 90 nm. The ratio and density of epoxy and amine compartments were estimated using Huygens (SVI) software. In a first step, deconvolution allowed for image restoration including noise reduction. Subsequent identification of the A&E compartments was performed by the ObjectAnalyzer module.

5.5.4.5 Thermal Analysis

DSC measurements were carried out on a Netzsch 204 F1 Phoenix differential scanning calorimeter with heating rates of 10 K min⁻¹ under N₂ atmosphere in a temperature range from 0 to 180 °C. 5-15 mg samples were used for the measurements. To monitor the curing for the bulk references the epoxy was first mixed with the PVA and the cooled amine was balanced

into the crucible lid and both components were pressed together immediately before the measurement.

5.5.4.6 Fourier Transform Infrared Spectroscopy

IR spectroscopy measurements were carried out on a Bruker ALPHA FT-IR spectrometer equipped with an ATR diamond, a SiC light source and a DTGS detector. Measurements were carried out at room temperature.

5.5.4.7 High Pressure Liquid Chromatography

HPLC measurements were performed on a Macherey Nagel Pyramid column (Dimensions: 125/4 mm/5 μ m) with CHCl₃/CH₃OH (95/5) as eluent with a flow rate of 1 mL min⁻¹ at 20 °C and a UV-Detector at a detection wavelength of $\lambda = 276$ nm.

5.5.4.8 Linear Sweep Voltammetry

For the embedding of the fibers, 5 g BADGE and 3.075 g Jeffamine D-400 were mixed and degassed. The as spun fibers on Al-foil (1x1 cm) were sealed with 100 mg of the mixture except for a small contact area on the backside for attaching the Au-electrode and left curing for one week at RT. The samples were cut with a razor blade and left at RT for 96 h prior to the measurements. Linear Sweep Voltammetry was carried out on a Metrohm Autolab Potentiostat (204 Potentiostat-Galvanostat) in a conventional three electrode setup. Samples were glued onto the Au working electrode with Nafion polymer to generate a conductive connection between the sample and the electrode. Pt wires served as reference and counter electrode. 3 M KCl solution was used as electrolyte. The potential was ramped from -0.5 V to 0.75 V.

5.5.4.9 Salt Water Corrosion Tests

For the salt water corrosion tests 15 mg of nanofibers (either PVA or PVA-EA 3:1) were directly spun onto hot-dipped galvanized steel surfaces. (19 x 10.5 x 0.1 cm) of which approximately 5 x 5 cm were covered with fibers. Samples were covered with a 200 μ m thick epoxy-amine topcoat (5.0051 g BADGE and 5.884 g NX5454) which was left curing for 24 h at RT. A pure topcoat was also prepared as an additional reference. A 5x5 cm area was scribed in a cross-pattern and the samples were left healing for 24 h at RT. The remaining substrate was fully sealed with duct tape and the samples were fully immersed into a 5 wt.% sodium chloride solution to promote corrosion. The degree of corrosion was evaluated optically on a daily basis for one week. After drying the coating was removed and the corroded area was investigated.

6 Summary and Outlook

This thesis focused on latency in colloidal systems. Latency was created either by encapsulation of active materials into nanocapsules or nanofibers but was also investigated in absence of polymeric barriers. The concepts applied in three examples throughout this thesis can be useful in many technological areas and processes. The colloidal pathway offers several advantages over the molecular approach where molecular structures are altered to synthesize latent reactive compounds. On the one hand, complex synthesis and labelling issues of new compounds become redundant. On the other hand, the introduction of interfacial boundaries allows the introduction and control of additional functions. Aqueous dispersions and if possible raw materials from renewable feedstocks were used to prepare thermosetting polymers. Special focus was on epoxy-amines and their film formation.

In the first project, latency was introduced to control the catalytic curing of reactive systems. By the encapsulation of commercially available catalysts into polymer nanocapsules with high encapsulation efficiencies, unique curing profiles of polyurethane matrices could be obtained. For these composites, castor oil was used as a green substitute for the polyol component. It was possible to obtain curing behaviors with a distinct non-Arrhenius behavior by the introduction of a phase transition by the glass transition temperature of the capsule shell. The release could be tailored by either changing the cross-linking density of the polymer shell or by the catalyst loading in the nanocapsules. The introduction of nanocapsules into a polyurethane matrix had no negative influence on the mechanical properties of the composites and high mechanical moduli were obtained as demonstrated via oscillatory rheology. Furthermore, owing to their small size, these capsules could be used for infusion processes where no filtering occurred. This opens several advantages for the preparation of reinforced composites, since the generated thermolatency allows processability at elevated temperatures and at the same time an immediate catalysis is enabled.

Secondly, latency was employed in a highly reactive system which was triggered simply by film formation. By the transformation of epoxy-amine curing into aqueous systems new possibilities to control their interaction arose. The idea of a pseudo-one-component-system was to create latency in an otherwise highly reactive two-component-system which crosslinks upon contact immediately. By preparing a hybrid dispersion containing amine and epoxy type colloids they are kept separate for as long as they are in colloidal state. The absence of a surrounding barrier shell around the reactive materials allows their reaction to occur

immediately upon contact, as introduced by for example their application on a surface resulting in the formation of a continuous film.

To realize such a system the first obstacle was the stabilization of amine emulsions in water avoiding their dense encapsulation and preserving the amine functionality. Especially phenalkamines, obtained from renewable feedstocks displayed a high hydrophobicity and reactivity towards epoxides. High colloidal stabilities could be realized by the use of polymeric, reactive epoxide surfactants. The increased colloidal stability was attributed to the interfacial reaction between the surfactant and the amine as proven via isothermal titration calorimetry.

Additionally, it was possible to substitute the bisphenol-A based epoxide emulsions by an epoxidized cardanol to obtain a fully bio-based thermoset. Even though it displayed a decreased reactivity compared to the bisphenol-A diglycidyl ether resin as a benchmark, it was possible to obtain fully cured thermosets with glass transition temperatures well above room temperature already at ambient temperatures. Furthermore, the emulsions obtained from the epoxidized cardanol even exceeded the performance of the benchmark with respect to their colloidal stability.

The next crucial step was the transformation of both components into a pseudo-one-component-dispersion. This was achieved by mixing the epoxy and amine colloids of similar particle size to hinder the driving forces which favor emulsion ripening. No change in droplet size could be measured by dynamic light scattering, pointing to the absence of coalescence. However, the minimum temperature needed to form continuous films increased over time, indicating premature reaction took place which was determined by a combination of imaging techniques and the determination of residual amine content in the pseudo-one-component-dispersions. The potlife could be significantly prolonged by the use of the epoxidized cardanol instead of the bisphenol-A diglycidyl ether emulsion. The absence of measurable coalescence points towards molecular diffusion and will be subject of further studies.

However, the idea of the pseudo-one-component-system was found to be a promising candidate for the preparation of self-healing materials. The epoxide and amine dispersions were encapsulated within polymer nanofibers made of poly(vinyl alcohol) as separate compartments by colloid electrospinning. In the nanofibers both compartments are in a dormant state. In contrast to the pseudo-one-component-systems in aqueous state, diffusion and movement is prohibited by the surrounding fiber matrix even though the compartments were in immediate proximity, which was verified by computations in combination with fluorescent labelling and

high resolution microscopy methods. In case of mechanical damage however, the pseudo-one-component-system is released and cross-linking takes place immediately. The concept of maintaining reactive species in close vicinity allows a very effective use of resources.

Summarizing the drawn conclusions, the approaches presented within this work offer alternative pathways for the preparation of thermosetting polymer networks with unusual and controllable curing profiles. The introduction of latency to precisely control when and where the cross-linking of reactive species takes place is a promising concept not only from an academic but also from industrial point of view. Advanced analytical methods were employed to gain deeper insights into the structure-property relationships which may be helpful in other fields as well. In summary, instead of concerning latency “a waste of time” it can be regarded as a concept worth spending time and effort on.

7 Zusammenfassung und Ausblick

Der Fokus dieser Arbeit lag auf der Betrachtung von latentem Verhalten in kolloidalen Systemen. Latenz kann zum einen dadurch generiert werden, dass aktive Materialien in Nanokapseln oder -fasern eingeschlossen werden, zum anderen wurde Latenz aber auch in Abwesenheit kapsel- oder faserbasierter Barriersysteme untersucht. Die diesen drei Beispielen zugrunde liegenden Konzepte können für verschiedenste Technologiefelder und Anwendungen hilfreich sein. Dabei liefert der in dieser Arbeit gewählte kolloidale Ansatz einige Vorteile gegenüber einem molekularen Ansatz, welcher in der Regel auf der gezielten Veränderung molekularer Strukturen zur Synthese latent-reaktiver Verbindungen basiert: Zum einen entfallen sowohl komplexe Syntheseprotokolle, als auch die Einstufung neuer Verbindungen. Zum anderen ermöglicht die Einführung von zusätzlichen Grenzflächen das gezielte Einbringen, sowie die Kontrolle zusätzlicher Funktionalitäten. Im Zuge dieser Arbeit wurde dies, anhand wässriger Dispersionen und wenn möglich auf Basis nachwachsender Rohstoffe, zur Herstellung von Duroplasten gezeigt. Im Speziellen wurden Epoxy-Amin-Systeme und deren Filmbildung untersucht.

Im Zuge des ersten Projektes wurde Latenz gezielt eingesetzt, um die katalytische Härtung eines Reaktivsystems zu kontrollieren. Durch die Verkapselung eines kommerziell verfügbaren Katalysators in Polymeranokapseln, welches mit einer sehr hohen Verkapselungseffizienz gelang, war es möglich, vernetzte Polyurethane mit einzigartigen Härtungsverläufen zu generieren. Dabei fungierte Rizinusöl als biobasierte Rohstoffalternative für die Polyolkomponente. Mit Hilfe der Einführung eines Phasenübergangs, hervorgerufen durch die Glasübergangstemperatur der Polymerhülle und der daraus resultierenden Freisetzung des Katalysators, wurde ein nicht-Arrhenius-Verhalten erzeugt, welches die einzigartigen Härtungsprofile hervorrief. Dabei war es möglich, sowohl den Zeitpunkt, als auch die Freisetzungstemperatur durch Variation des Vernetzungsgrades der Polymerhülle, sowie der Katalysatormenge gezielt einzustellen. Die Präsenz der Nanokapseln hatte dabei keinen negativen Einfluss auf die mechanischen Eigenschaften der Polyurethanmatrix, was mittels oszillatorischer Rheologie gezeigt werden konnte. Ein weiterer Vorteil in der Verwendung von Nanokapseln zeigte sich bei dem Einsatz des Katalysatorsystems in Infusionsverfahren, wo, anders als bei Mikrokapseln, kein Herausfiltern der Kapseln beobachtet wurde. Damit eröffnet das Prinzip der kolloidalen, thermolatenten Katalyse entscheidende Vorteile bei der Herstellung faserverstärkter Verbundstoffe, da sowohl eine gute Verarbeitbarkeit bei erhöhter Temperatur ohne eine verfrühte Aushärtung, als auch eine punktgenaue Katalyse ermöglicht wird.

Im folgenden Projekt wurde Latenz in ein hochreaktives System eingeführt, welches bereits durch ein simples Aufbringen mit nachfolgender Filmbildung aktiviert wird. Durch die Übertragung von Epoxy-Amin-Härtungen in wässrige Systeme entstehen neue Möglichkeiten ihre Wechselwirkung zu steuern. Die Idee des sogenannten „Pseudo-Einkomponenten-Systems“ bestand darin, durch Kolloideigenschaften Latenz in einem klassischen Zweikomponenten-System zu erzeugen, welches unter Normalbedingungen sofort vernetzt. Durch die Herstellung einer Hybriddispersion, bestehend aus Amin- und Epoxid-Kolloiden, sollte sichergestellt werden, dass beide Komponenten dispergiert und getrennt voneinander vorliegen. Durch die Abwesenheit einer Barriere in Form einer Polymerhülle, welche die reaktiven Spezies voneinander abschirmt, soll ermöglicht werden, dass bei Kontakt, beispielsweise hervorgerufen durch das Auftragen und die Filmbildung der Hybriddispersion, die Vernetzung von Epoxid und Amin unmittelbar eintritt. Die erste Hürde bei der Realisierung eines solchen Konzeptes bestand zunächst in der Stabilisierung von Aminemulsionen in Wasser, wobei auf eine Verkapselung verzichtet werden, sowie die Aminfunktionalität erhalten bleiben musste. Dabei stellte sich die Klasse der Phenalkamine als besonders gut geeignet dar, da diese neben ihrer hohen Hydrophobizität und Reaktivität gegenüber Epoxiden zusätzlich auf Basis nachwachsender Rohstoffe hergestellt werden. Durch die Verwendung von reaktiven, makromolekularen Epoxidensiden konnten Aminemulsionen mit hoher kolloidaler Stabilität hergestellt werden. Die erhöhte Stabilität resultierte aus der Grenzflächenreaktion zwischen dem Tensid und dem Amin, was durch isotherme Titrationskalorimetrie bestätigt werden konnte. Weiterhin war es möglich, das typischerweise verwendete Bisphenol-A basierte Epoxidharz durch eine epoxidierte Cardanolverbindung zu ersetzen und somit ein vollständig biobasiertes Duromersystem zu realisieren. Obwohl dessen Reaktivität im direkten Vergleich zu Bisphenol-A-diglycidylether als Benchmark verringert war, wurden dennoch vollständig gehärtete Duroplaste mit Glastemperaturen deutlich über Raumtemperatur bereits bei Härtungen unter Standardbedingungen hergestellt. Weiterhin übertrafen die auf Cardanol basierenden Epoxidemulsionen die zu Bisphenol-A-diglycidylether-Emulsionen deutlich in Bezug auf deren kolloidale Stabilität.

Der nächste entscheidende Schritt bestand in der Überführung beider separat hergestellten Komponenten in eine Pseudo-Einkomponenten-Dispersion. Dies wurde durch das stöchiometrische Mischen der Epoxy- und Amin-Kolloide erreicht. Dabei wurden möglichst ähnlicher Teilchengrößen verwendet, um jene Faktoren, die eine Destabilisierung von Emulsionen begünstigen, bestmöglich zu unterdrücken. Mittels dynamischer Lichtstreuung konnte keine signifikante Veränderung der Teilchengrößen über die Zeit gemessen werden, was

auf die Abwesenheit von Koaleszenz hindeutet. Trotzdem wurde ein steter Anstieg der minimalen Filmbildungstemperatur beobachtet, was einen deutlichen Hinweis auf eine verfrühte Reaktion lieferte, was durch die Kombination von Mikroskopieaufnahmen sowie der titrimetrischen Bestimmung des Amingehaltes in den Pseudo-Einkomponenten-Dispersionen bestätigt wurde. Dabei wurde eine signifikante Verbesserung der Lebensdauer bei der Verwendung des epoxidierten Cardanols im Vergleich zu den Bisphenol-A-diglycidylether basierten Systemen festgestellt. Die Abwesenheit von messbarer Koaleszenz deutet auf einen diffusionsinduzierten Mechanismus hin, welches in weitergehenden Studien bestätigt werden soll.

Die Idee des Pseudo-Einkomponenten-Konzeptes fand eine vielversprechende Anwendung im Bereich selbstheilender Materialien. Dazu wurden die bereits verwendeten Epoxy- und Amin-Kolloide in Nanofasern, bestehend aus Polyvinylalkohol, mittels Kolloid-Elektrospinnen eingebettet, sodass beide Komponenten statistisch verteilt in den Fasern vorlagen. Im Gegensatz zu den wässrigen Pseudo-Einkomponenten-Systemen befanden sich die beiden Komponenten trotz ihrer unmittelbaren Nähe zueinander in einer Art schlafendem Zustand, da Bewegung und Diffusion durch die umgebende Fasermatrix unterbunden werden konnten. Dies wurde mit Hilfe einer Kombination aus Simulationen sowie Fluoreszenzmarkierung in Verbindung mit hochauflösender Mikroskopie bestätigt. Wird nun das System beispielsweise durch das Einwirken mechanischer Kräfte geschädigt, wird das Pseudo-Einkomponenten-System freigesetzt, was eine unmittelbare Vernetzung beider Verbindungen nach sich zieht. Die unmittelbare Nähe beider Komponenten zueinander erlaubt dabei einen äußerst effizienten Rohstoffeinsatz.

In Anbetracht der gewonnenen Erkenntnisse, eröffnen die im Rahmen dieser Arbeit untersuchten Konzepte, neue Möglichkeiten Duromersysteme mit ungewöhnlichen Härtungseigenschaften herzustellen. Der gezielte Einsatz von Latenz zur Kontrolle, wann und wo Vernetzung zwischen reaktiven Spezies stattfindet, stellt dabei einen vielversprechenden Ansatz sowohl aus akademischer, als auch aus industrieller Sicht dar. Die Implementierung der verwendeten analytischen Methoden ermöglichte ein tieferes Struktur-Wirkungs-Verständnis, welches auch für verwandte Fragestellungen hilfreich sein kann. Zusammenfassend wird die Sichtweise, welche Latenz als „Zeitverschwendung“ beschreibt den sich bietenden Möglichkeiten Latenz zu nutzen nicht gerecht. Im Gegenteil handelt es sich um ein Konzept, welches es wert ist Zeit und Mühe zu investieren.

8 References

1. Kroll, C. *Spotlight Europe, August 2015: Sustainable Development Goals: Are the rich countries ready?* Berthelsmann Foundation: **2015**.
2. Cosgrove, T. *Colloid science: principles, methods and applications*. John Wiley & Sons: **2010**.
3. Shaw, D. J. 1 - The colloidal state. In *Introduction to Colloid and Surface Chemistry (Fourth Edition)*, Shaw, D. J., Ed. Butterworth-Heinemann: Oxford, **1992**, 1-20.
4. Dörfler, H.-D. *Grenzflächen und kolloid-disperse Systeme: Physik und Chemie*. Springer: **2002**.
5. Ruckenstein, E.; Chi, J. C. Stability of microemulsions. *Journal of the Chemical Society, Faraday Transactions 2: Molecular and Chemical Physics* **1975**, 71, 1690-1707.
6. Sjöblom, J.; Lindberg, R.; Friberg, S. E. Microemulsions-hase equilibria characterization, structures, applications and chemical reactions. *Advances in Colloid and Interface Science* **1996**, 65, 125-287.
7. Chou, Y.; El-Aasser, M.; Vanderhoff, J. Mechanism of emulsification of styrene using hexadecyltrimethylammonium bromide-cetyl alcohol mixtures. In *Polymer Colloids II*, Springer: **1980**, 599-618.
8. Antonietti, M.; Landfester, K. Polyreactions in miniemulsions. *Progress in Polymer Science* **2002**, 27, 689-757.
9. Evans, D. F.; Wennerstrom, H. *Colloidal domain*. Wiley-Vch: **1999**.
10. Mirhosseini, H.; Tan, C. P.; Hamid, N. S. A.; Yusof, S. Modeling the Relationship between the Main Emulsion Components and Stability, Viscosity, Fluid Behavior, ζ -Potential, and Electrophoretic Mobility of Orange Beverage Emulsion Using Response Surface Methodology. *Journal of Agricultural and Food Chemistry* **2007**, 55, 7659-7666.
11. Kim, N.; Sudol, E. D.; Dimonie, V. L.; El-Aasser, M. S. Poly(vinyl alcohol) Stabilization of Acrylic Emulsion Polymers Using the Miniemulsion Approach. *Macromolecules* **2003**, 36, 5573-5579.
12. Israelachvili, J. N. *Intermolecular and Surface Forces (Third Edition)*, Ed. Academic Press: **2011**.
13. Ostwald, W. Studien über die Bildung und Umwandlung fester Körper. *Z. Phys. Chem* **1897**, 22, 289-330.
14. Taylor, P. Ostwald ripening in emulsions. *Advances in Colloid and Interface Science* **1998**, 75, 107-163.
15. Landfester, K. Recent developments in miniemulsions - formation and stability mechanisms. *Macromolecular Symposia* **2000**, 150, 171-178.
16. Mouran, D.; Reimers, J.; Schork, F. J. Miniemulsion polymerization of methyl methacrylate with dodecyl mercaptan as cosurfactant. *Journal of Polymer Science Part A: Polymer Chemistry* **1996**, 34, 1073-1081.
17. Blythe, P. J.; Klein, A.; Sudol, E. D.; El-Aasser, M. S. Enhanced Droplet Nucleation in Styrene Miniemulsion Polymerization. 2. Polymerization Kinetics of Homogenized Emulsions Containing Predissolved Polystyrene. *Macromolecules* **1999**, 32, 6952-6957.
18. Landfester, K. The Generation of Nanoparticles in Miniemulsions. *Advanced Materials* **2001**, 13, 765-768.
19. Roger, K.; Olsson, U.; Schweins, R.; Cabane, B. Emulsion Ripening through Molecular Exchange at Droplet Contacts. *Angewandte Chemie International Edition* **2015**, 54, 1452-1455.
20. Holmberg, K.; Jönsson, B.; Kronberg, B.; Lindman, B. *Surfactants and polymers in aqueous solution*. Second Edition; John Wiley & Sons: **2003**.

21. Griffin, W. C. Classification of surface-active agents by HLB. *Journal of Cosmetic Chemists* **1949**, 1, 311-326.
22. Davies, J.; Rideal, E. *Interfacial Phenomena*. Academic Press: **1961**.
23. Dörfler, H. D. *Grenzflächen und kolloid-disperse Systeme*. Springer: **2002**.
24. Raffa, P.; Wever, D. A. Z.; Picchioni, F.; Broekhuis, A. A. Polymeric Surfactants: Synthesis, Properties, and Links to Applications. *Chemical Reviews* **2015**, 115, 8504-8563.
25. Durand, A.; Marie, E. Macromolecular surfactants for miniemulsion polymerization. *Advances in Colloid and Interface Science* **2009**, 150, 90-105.
26. Guyot, A.; Tauer, K. Reactive surfactants in emulsion polymerization. In *Polymer Synthesis*, Springer: **1994**; Vol. 111, 43-65.
27. Guyot, A. Recent progress in reactive surfactants in emulsion polymerisation. *Macromolecular Symposia* **2002**, 179, 105-132.
28. Unzué, M. J.; Schoonbrood, H. A. S.; Asua, J. M.; Goñi, A. M.; Sherrington, D. C.; Stähler, K.; Goebel, K.-H.; Tauer, K.; Sjöberg, M.; Holmberg, K. Reactive surfactants in heterophase polymerization. VI. Synthesis and screening of polymerizable surfactants (surfmers) with varying reactivity in high solids styrene-butyl acrylate-acrylic acid emulsion polymerization. *Journal of Applied Polymer Science* **1997**, 66, 1803-1820.
29. Schoonbrood, H. A. S.; Unzué, M. J.; Beck, O.-J.; Asua, J. M.; Goñi, A. M.; Sherrington, D. C. Reactive Surfactants in Heterophase Polymerization. 7. Emulsion Copolymerization Mechanism Involving Three Anionic Polymerizable Surfactants (Surfmers) with Styrene-Butyl Acrylate-Acrylic Acid. *Macromolecules* **1997**, 30, 6024-6033.
30. Asua, J. M.; Schoonbrood, H. A. S. Reactive surfactants in heterophase polymerization. *Acta Polymerica* **1998**, 49, 671-686.
31. Ni, P.; Zhang, M.; Ma, L.; Fu, S. Poly (dimethylamino) ethyl methacrylate for use as a surfactant in the miniemulsion polymerization of styrene. *Langmuir* **2006**, 22, 6016-6023.
32. Luo, Y.; Gu, H. A General Strategy for Nano-Encapsulation via Interfacially Confined Living/Controlled Radical Miniemulsion Polymerization. *Macromolecular Rapid Communications* **2006**, 27, 21-25.
33. Stoffelbach, F.; Belardi, B.; Santos, J. M.; Tessier, L.; Matyjaszewski, K.; Charleux, B. Use of an amphiphilic block copolymer as a stabilizer and a macroinitiator in miniemulsion polymerization under AGET ATRP conditions. *Macromolecules* **2007**, 40, 8813-8816.
34. Li, W.; Min, K.; Matyjaszewski, K.; Stoffelbach, F. o.; Charleux, B. PEO-based block copolymers and homopolymers as reactive surfactants for AGET ATRP of butyl acrylate in miniemulsion. *Macromolecules* **2008**, 41, 6387-6392.
35. Pham, B. T.; Nguyen, D.; Ferguson, C. J.; Hawke, B. S.; Serelis, A. K.; Such, C. H. Miniemulsion polymerization stabilized by amphiphilic macro RAFT agents. *Macromolecules* **2003**, 36, 8907-8909.
36. Sawaryn, C.; Landfester, K.; Taden, A. Benzoxazine Miniemulsions Stabilized with Polymerizable Nonionic Benzoxazine Surfactants. *Macromolecules* **2010**, 43, 8933-8941.
37. Chiou, K.; Froimowicz, P.; Landfester, K.; Taden, A.; Ishida, H. Triggered Precision Benzoxazine Film Formation by Thermally Induced Destabilization of Benzoxazine Nanodroplets Using a LCST-Bearing Surfactant. *Macromolecules* **2014**, 47, 3297-3305.
38. Verge, P.; Fouquet, T.; Barrère, C.; Toniazzi, V.; Ruch, D.; Bomfim, J. A. S. Organomodification of sepiolite clay using bio-sourced surfactants: Compatibilization and dispersion into epoxy thermosets for properties enhancement. *Composites Science and Technology* **2013**, 79, 126-132.

References

39. Puchot, L.; Verge, P.; Toniazzo, V.; Ruch, D.; Fouquet, T.; Bomfim, J. A. S. Tailoring the reactivity of bio-surfactants as a tool for montmorillonite exfoliation in epoxy thermosets. *Applied Clay Science* **2014**, *99*, 35-41.
40. Brown, P.; Butts, C. P.; Eastoe, J. Stimuli-responsive surfactants. *Soft Matter* **2013**, *9*, 2365-2374.
41. Brugger, B.; Richtering, W. Emulsions stabilized by stimuli-sensitive poly (N-isopropylacrylamide)-co-methacrylic acid polymers: microgels versus low molecular weight polymers. *Langmuir* **2008**, *24*, 7769-7777.
42. RezaeeáShirin-Abadi, A. Nitroxide-mediated surfactant-free emulsion copolymerization of methyl methacrylate and styrene using poly (2-(diethyl) aminoethyl methacrylate-co-styrene) as a stimuli-responsive macroalkoxyamine. *Polymer Chemistry* **2014**, *5*, 6163-6170.
43. Huang, J.; Xu, J.; Chen, K.; Wang, T.; Cui, C.; Wei, X.; Zhang, R.; Li, L.; Guo, X. Synthesis of Triblock Copolymers via RAFT Polymerization and Their Application as Surfactants for Crude Oil-in-Water Emulsion. *Industrial & Engineering Chemistry Research* **2015**, *54*, 1564-1575.
44. Wang, F.; Luo, Y.; Li, B.-G.; Zhu, S. Synthesis and Redispersibility of Poly (styrene-block-n-butyl acrylate) Core-Shell Latexes by Emulsion Polymerization with RAFT Agent-Surfactant Design. *Macromolecules* **2015**, *48*, 1313-1319.
45. Perrin, P.; Porcar, I.; Tribet, C. Stimuli-responsive emulsions stabilized by polymeric surfactants. *Polymer International* **2003**, *52*, 465-470.
46. Dupin, D.; Howse, J. R.; Armes, S. P.; Randall, D. P. Preparation of stable foams using sterically stabilized pH-responsive latexes synthesized by emulsion polymerization. *Journal of Materials Chemistry* **2008**, *18*, 545-552.
47. Morse, A. J.; Dupin, D.; Thompson, K. L.; Armes, S.; Ouzineb, K.; Mills, P.; Swart, R. Novel Pickering Emulsifiers based on pH-responsive poly (tert-butylaminoethyl methacrylate) Latexes. *Langmuir* **2012**, *28*, 11733-11744.
48. Yi, C.; Liu, N.; Zheng, J.; Jiang, J.; Liu, X. Dual-responsive poly (styrene-alt-maleic acid)-graft-poly (N-isopropyl acrylamide) micelles as switchable emulsifiers. *Journal of Colloid and Interface Science* **2012**, *380*, 90-98.
49. Amalvy, J.; Unali, G.-F.; Li, Y.; Granger-Bevan, S.; Armes, S.; Binks, B. P.; Rodrigues, J.; Whitby, C. P. Synthesis of sterically stabilized polystyrene latex particles using cationic block copolymers and macromonomers and their application as stimulus-responsive particulate emulsifiers for oil-in-water emulsions. *Langmuir* **2004**, *20*, 4345-4354.
50. Zhao, C.; Tan, J.; Li, W.; Tong, K.; Xu, J.; Sun, D. Ca²⁺ ion responsive pickering emulsions stabilized by PSSMA nanoaggregates. *Langmuir* **2013**, *29*, 14421-14428.
51. Wei, Z.; Wang, C.; Zou, S.; Liu, H.; Tong, Z. Chitosan nanoparticles as particular emulsifier for preparation of novel pH-responsive Pickering emulsions and PLGA microcapsules. *Polymer* **2012**, *53*, 1229-1235.
52. Wei, Z.; Wang, C.; Zou, S.; Liu, H.; Tong, Z. Fe₂O₃ nanoparticles as particulate emulsifier: preparation of magnetic and biocompatible PLGA microcapsules. *Colloids and Surfaces A: Physicochemical and Engineering Aspects* **2011**, *392*, 116-123.
53. McKee, J.; Ladmiral, V.; Niskanen, J.; Tenhu, H.; Armes, S. Synthesis of sterically-stabilized polystyrene latexes using well-defined thermoresponsive poly (N-isopropylacrylamide) macromonomers. *Macromolecules* **2011**, *44*, 7692-7703.
54. Zoppe, J. O.; Venditti, R. A.; Rojas, O. J. Pickering emulsions stabilized by cellulose nanocrystals grafted with thermo-responsive polymer brushes. *Journal of Colloid and Interface Science* **2012**, *369*, 202-209.

55. Jiang, J.; Zhu, Y.; Cui, Z.; Binks, B. P. Switchable Pickering emulsions stabilized by silica nanoparticles hydrophobized in situ with a switchable surfactant. *Angewandte Chemie International Edition* **2013**, *125*, 12599-12602.
56. Zhang, Q.; Yu, G.; Wang, W.-J.; Yuan, H.; Li, B.-G.; Zhu, S. Switchable block copolymer surfactants for preparation of reversibly coagulatable and redispersible poly (methyl methacrylate) latexes. *Macromolecules* **2013**, *46*, 1261-1267.
57. Fischer, V.; Landfester, K.; Muñoz-Espí, R. Molecularly controlled coagulation of carboxyl-functionalized nanoparticles prepared by surfactant-free miniemulsion polymerization. *ACS Macro Letters* **2012**, *1*, 1371-1374.
58. Zhang, Q.; Yu, G.; Wang, W.-J.; Yuan, H.; Li, B.-G.; Zhu, S. Preparation of N₂/CO₂ triggered reversibly coagulatable and redispersible latexes by emulsion polymerization of styrene with a reactive switchable surfactant. *Langmuir* **2012**, *28*, 5940-5946.
59. Ceschia, E.; Harjani, J. R.; Liang, C.; Ghoshouni, Z.; Andrea, T.; Brown, R. S.; Jessop, P. G. Switchable anionic surfactants for the remediation of oil-contaminated sand by soil washing. *RSC Advances* **2014**, *4*, 4638-4645.
60. Scott, L. M.; Robert, T.; Harjani, J. R.; Jessop, P. G. Designing the head group of CO₂-triggered switchable surfactants. *RSC Advances* **2012**, *2*, 4925-4931.
61. Liu, Y.; Jessop, P. G.; Cunningham, M.; Eckert, C. A.; Liotta, C. L. Switchable surfactants. *Science* **2006**, *313*, 958-960.
62. Zhao, Y.; Landfester, K.; Crespy, D. CO₂ responsive reversible aggregation of nanoparticles and formation of nanocapsules with an aqueous core. *Soft Matter* **2012**, *8*, 11687-11696.
63. Pocoví-Martínez, S.; Francés-Soriano, L.; Zaballos-García, E.; Scaiano, J. C.; González-Béjar, M.; Pérez-Prieto, J. CO₂ switchable nanoparticles: reversible water/organic-phase exchange of gold nanoparticles by gas bubbling. *RSC Advances* **2013**, *3*, 4867-4871.
64. Brown, P.; Butts, C. P.; Cheng, J.; Eastoe, J.; Russell, C. A.; Smith, G. N. Magnetic emulsions with responsive surfactants. *Soft Matter* **2012**, *8*, 7545-7546.
65. Kaiser, A.; Liu, T.; Richtering, W.; Schmidt, A. M. Magnetic Capsules and Pickering Emulsions Stabilized by Core-Shell Particles. *Langmuir* **2009**, *25*, 7335-7341.
66. Nuyken, O.; Meindl, K.; Wokaun, A.; Mezger, T. A light-sensitive diazosulfonate surfactant as emulsifier for emulsion polymerization. *Journal of Macromolecular Science, Part A* **1995**, *32*, 447-457.
67. Szafraniec, J.; Janik, M.; Odrobińska, J.; Zapotoczny, S. Nanocapsules templated on liquid cores stabilized by graft amphiphilic polyelectrolytes. *Nanoscale* **2015**, *7*, 5525-5536.
68. Deen, G. R.; Gan, L.; Gan, Y. A new cationic surfactant N, N'-dimethyl-N-acryloyloxyundecyl piperazinium bromide and its pH-sensitive gels by microemulsion polymerisation. *Polymer* **2004**, *45*, 5483-5490.
69. Deen, G. R.; Gan, L. New piperazine-based polymerizable monoquatary cationic surfactants: Synthesis, polymerization, and swelling characteristics of gels. *Journal of Polymer Science Part A: Polymer Chemistry* **2009**, *47*, 2059-2072.
70. Kim, K.; Kim, T. H.; Choi, J. H.; Lee, J. Y.; Hah, S. S.; Yoo, H. O.; Hwang, S. S.; Ryu, K. N.; Kim, H. J.; Kim, J. Synthesis of a pH-Sensitive PEO-Based Block Copolymer and its Application for the Stabilization of Iron Oxide Nanoparticles. *Macromolecular Chemistry and Physics* **2010**, *211*, 1127-1136.
71. Wang, Y.; Zhang, X.; Han, Y.; Cheng, C.; Li, C. pH-and glucose-sensitive glycopolymer nanoparticles based on phenylboronic acid for triggered release of insulin. *Carbohydrate Polymers* **2012**, *89*, 124-131.

References

72. Dan, K.; Pan, R.; Ghosh, S. Aggregation and pH Responsive Disassembly of a New Acid-Labile Surfactant Synthesized by Thiol-Acrylate Michael Addition Reaction. *Langmuir* **2011**, *27*, 612-617.
73. Jones, R. G.; Wilks, E. S.; Metanomski, W. V.; Kahovec, J.; Hess, M.; Stepto, R.; Kitayama, T. *Compendium of Polymer Terminology and Nomenclature: IUPAC Recommendations, 2008*. Royal Society of Chemistry: **2009**.
74. Feng, H.; Verstappen, N. A.; Kuehne, A. J.; Sprakel, J. Well-defined temperature-sensitive surfactants for controlled emulsion coalescence. *Polymer Chemistry* **2013**, *4*, 1842-1847.
75. Kodger, T. E.; Sprakel, J. Thermosensitive molecular, colloidal, and bulk interactions using a simple surfactant. *Advanced Functional Materials* **2013**, *23*, 475-482.
76. Dorresteyn, R.; Billecke, N.; Parekh, S. H.; Klapper, M.; Müllen, K. Polarity reversal of nanoparticle surfaces by the use of light-sensitive polymeric emulsifiers. *Journal of Polymer Science Part A: Polymer Chemistry* **2015**, *53*, 200-205.
77. Warwel, S.; Brüse, F.; Demes, C.; Kunz, M.; Klaas, M. R. G. Polymers and surfactants on the basis of renewable resources. *Chemosphere* **2001**, *43*, 39-48.
78. von Rybinski, W.; Hill, K. Alkyl Polyglycosides- Properties and Applications of a new Class of Surfactants. *Angewandte Chemie International Edition* **1998**, *37*, 1328-1345.
79. Chen, C.-K.; Wang, Q.; Jones, C. H.; Yu, Y.; Zhang, H.; Law, W.-C.; Lai, C. K.; Zeng, Q.; Prasad, P. N.; Pfeifer, B. A.; Cheng, C. Synthesis of pH-Responsive Chitosan Nanocapsules for the Controlled Delivery of Doxorubicin. *Langmuir* **2014**, *30*, 4111-4119.
80. Calejo, M. T.; Cardoso, A. M. S.; Marques, E. F.; Araújo, M. J.; Kjøniksen, A.-L.; Sande, S. A.; de Lima, M. C. P.; Jurado, A. S.; Nyström, B. In vitro cytotoxicity of a thermoresponsive gel system combining ethyl(hydroxyethyl) cellulose and lysine-based surfactants. *Colloids and Surfaces B: Biointerfaces* **2013**, *102*, 682-686.
81. Sauer, R.; Turshatov, A.; Balushev, S.; Landfester, K. One-Pot Production of Fluorescent Surface-Labeled Polymeric Nanoparticles via Miniemulsion Polymerization with Bodipy Surfmers. *Macromolecules* **2012**, *45*, 3787-3796.
82. Sauer, R.; Froimowicz, P.; Schöller, K.; Cramer, J.-M.; Ritz, S.; Mailänder, V.; Landfester, K. Design, Synthesis, and Miniemulsion Polymerization of New Phosphonate Surfmers and Application Studies of the Resulting Nanoparticles as Model Systems for Biomimetic Mineralization and Cellular Uptake. *Chemistry - A European Journal* **2012**, *18*, 5201-5212.
83. Grazon, C.; Rieger, J.; Méallet - Renault, R.; Clavier, G.; Charleux, B. One - Pot Synthesis of Pegylated Fluorescent Nanoparticles by RAFT Miniemulsion Polymerization Using a Phase Inversion Process. *Macromolecular Rapid Communications* **2011**, *32*, 699-705.
84. Tieke, B. *Makromolekulare Chemie: Eine Einführung*. John Wiley & Sons: **2014**.
85. Delgado, J.; El-Aasser, M. S.; Vanderhoff, J. W. Miniemulsion copolymerization of vinyl acetate and butyl acrylate. I. Differences between the miniemulsion copolymerization and the emulsion copolymerization processes. *Journal of Polymer Science Part A: Polymer Chemistry* **1986**, *24*, 861-874.
86. Ugelstad, J.; El-Aasser, M. S.; Vanderhoff, J. W. Emulsion polymerization: Initiation of polymerization in monomer droplets. *Journal of Polymer Science: Polymer Letters Edition* **1973**, *11*, 503-513.
87. Landfester, K.; Bechthold, N.; Förster, S.; Antonietti, M. Evidence for the preservation of the particle identity in miniemulsion polymerization. *Macromolecular Rapid Communications* **1999**, *20*, 81-84.

88. Durbin, D. P.; El-Aasser, M. S.; Poehlein, G. W.; Vanderhoff, J. W. Influence of monomer preemulsification on formation of particles from monomer drops in emulsion polymerization. *Journal of Applied Polymer Science* **1979**, 24, 703-707.
89. Landfester, K. Miniemulsion Polymerization and the Structure of Polymer and Hybrid Nanoparticles. *Angewandte Chemie International Edition* **2009**, 48, 4488-4507.
90. Hofmeister, I.; Landfester, K.; Taden, A. Controlled Formation of Polymer Nanocapsules with High Diffusion-Barrier Properties and Prediction of Encapsulation Efficiency. *Angewandte Chemie International Edition* **2015**, 54, 327-330.
91. Staff, R. H.; Schaeffel, D.; Turshatov, A.; Donadio, D.; Butt, H.-J.; Landfester, K.; Koynov, K.; Crespy, D. Particle Formation in the Emulsion-Solvent Evaporation Process. *Small* **2013**, 9(20), 3541-3522.
92. Crespy, D.; Stark, M.; Hoffmann-Richter, C.; Ziener, U.; Landfester, K. Polymeric Nanoreactors for Hydrophilic Reagents Synthesized by Interfacial Polycondensation on Miniemulsion Droplets. *Macromolecules* **2007**, 40, 3122-3135.
93. Torza, S.; Mason, S. G. Three-phase interactions in shear and electrical fields. *Journal of Colloid and Interface Science* **1970**, 33, 67-83.
94. Sundberg, D. C.; Casassa, A. P.; Pantazopoulos, J.; Muscato, M. R.; Kronberg, B.; Berg, J. Morphology development of polymeric microparticles in aqueous dispersions. I. Thermodynamic considerations. *Journal of Applied Polymer Science* **1990**, 41, 1425-1442.
95. Muscato, M. R.; Sundberg, D. C. A note on the morphology of composite polymer particles. *Journal of Polymer Science Part B: Polymer Physics* **1991**, 29, 1021-1024.
96. Nicholson, J. W. *The chemistry of polymers*. Royal Society of Chemistry: **2012**.
97. Landfester, K.; Tiarks, F.; Hentze, H.-P.; Antonietti, M. Polyaddition in miniemulsions: A new route to polymer dispersions. *Macromolecular Chemistry and Physics* **2000**, 201, 1-5.
98. Qi, D.; Cao, Z.; Ziener, U. Recent advances in the preparation of hybrid nanoparticles in miniemulsions. *Advances in Colloid and Interface Science* **2014**, 211, 47-62.
99. Schork, F. J.; Luo, Y.; Smulders, W.; Russum, J.; Butté, A.; Fontenot, K. Miniemulsion Polymerization. In *Polymer Particles*, Okubo, M. Ed., Springer: **2005**; Vol. 175, 129-255.
100. Guyot, A.; Landfester, K.; Joseph Schork, F.; Wang, C. Hybrid polymer latexes. *Progress in Polymer Science* **2007**, 32, 1439-1461.
101. Elias, H.-G. *Makromoleküle: Band 3: Industrielle Polymere und Synthesen*. John Wiley & Sons: **2009**.
102. Auvergne, R.; Caillol, S.; David, G.; Boutevin, B.; Pascault, J.-P. Biobased Thermosetting Epoxy: Present and Future. *Chemical Reviews* **2013**, 114, 1082-1115.
103. Ratna, D. *Handbook of thermoset resins*. ISmithers Shawbury: **2009**.
104. Schlack, P. IG Farbenindustrie AG, *German Patent* **1934**, DE 676.117.
105. Castan, P. DeTrey Frères Co., *Swiss Patent* **1940**, CH 211116.
106. Pham, H. Q.; Marks, M. J. Epoxy Resins. In *Kirk-Othmer Encyclopedia of Chemical Technology*, John Wiley & Sons: **2000**.
107. Hamerton, I. High performance polymers. *Polymer International* **1996**, 41, 101-102.
108. Mullins, M. J.; Liu, D.; Sue, H. J. 2 - Mechanical properties of thermosets. In *Thermosets*, Guo, Q., Ed. Woodhead Publishing: **2012**, 28-61.
109. Pascault, J. P.; Williams, R. J. J. 1 - Overview of thermosets: structure, properties and processing for advanced applications. In *Thermosets*, Guo, Q., Ed. Woodhead Publishing: **2012**, 3-27.

References

110. Okada, H.; Tokunaga, T.; Xiaohui, L.; Takayanagi, S.; Matsushima, A.; Shimohigashi, Y. Direct Evidence Revealing Structural Elements Essential for the High Binding Ability of Bisphenol A to Human Estrogen-Related Receptor- γ . *Environmental Health Perspectives* **2008**, 116, 32-38.
111. Dotan, A. 15 - Biobased Thermosets. In *Handbook of Thermoset Plastics (Third Edition)*, Dodiuk, H.; Goodman, S. H., Eds. William Andrew Publishing: **2014**, 577-622.
112. Park, S.-J.; Jin, F.-L.; Lee, J.-R. Effect of Biodegradable Epoxidized Castor Oil on Physicochemical and Mechanical Properties of Epoxy Resins. *Macromolecular Chemistry and Physics* **2004**, 205, 2048-2054.
113. Lane, B. S.; Burgess, K. Metal-Catalyzed Epoxidations of Alkenes with Hydrogen Peroxide. *Chemical Reviews* **2003**, 103, 2457-2474.
114. Galià, M.; de Espinosa, L. M.; Ronda, J. C.; Lligadas, G.; Cádiz, V. Vegetable oil-based thermosetting polymers. *European Journal of Lipid Science and Technology* **2010**, 112, 87-96.
115. Weller, C. G.; Siebert, E. J.; Yang, Z.; Agarwal, R. K.; Fristad, W. E.; Bammel, B. D. Autodeposition compositions **2003**, WO 2003026888 A1.
116. Unnikrishnan, K. P.; Thachil, E. T. Synthesis and Characterization of Cardanol-Based Epoxy Systems. *Designed Monomers & Polymers* **2008**, 11, 593-607.
117. Boutevin, B.; Caillol, S.; Burguiere, C.; Rapior, S.; Fulcrand, H.; Nouailhas, H. Novel methods for producing thermosetting epoxy resins **2012**, US 20120165429 A1.
118. Pillai, C. K. S.; Prasad, V. S.; Sudha, J. D.; Bera, S. C.; Menon, A. R. R. Polymeric resins from renewable resources. II. Synthesis and characterization of flame-retardant prepolymers from cardanol. *Journal of Applied Polymer Science* **1990**, 41, 2487-2501.
119. Fache, M.; Viola, A.; Auvergne, R.; Boutevin, B.; Caillol, S. Biobased epoxy thermosets from vanillin-derived oligomers. *European Polymer Journal* **2015**, 68, 526-535.
120. Pan, X.; Sengupta, P.; Webster, D. C. High Biobased Content Epoxy-Anhydride Thermosets from Epoxidized Sucrose Esters of Fatty Acids. *Biomacromolecules* **2011**, 12, 2416-2428.
121. Dark, W. A.; Conrad, E. C.; Crossman, L. W. Liquid chromatographic analysis of epoxy resins. *Journal of Chromatography A* **1974**, 91, 247-260.
122. Barton, J. M. Epoxy resin chemistry II. Edited by R. S. Bauer, ACS symposium series No. 221, American Chemical Society, 1983. *British Polymer Journal* **1984**, 16, 108-109.
123. Tesoro, G. Epoxy resins-chemistry and technology, 2nd Edition, Clayton A. May, Ed., Marcel Dekker, New York, 1988, 1, 288 pp. *Journal of Polymer Science Part C: Polymer Letters* **1988**, 26, 539-539.
124. Hagenbucher, M. Enzymatische Epoxidierung und Untersuchung von Epoxid-Amin-Reaktionen in wässrigen Miniemulsionssystemen. Dissertation, Johannes Gutenberg Universität Mainz, **2012**.
125. Tiarks, F.; Landfester, K.; Antonietti, M. One-step preparation of polyurethane dispersions by miniemulsion polyaddition. *Journal of Polymer Science Part A: Polymer Chemistry* **2001**, 39, 2520-2524.
126. Mischke, P. *Filmbildung in modernen Lacksystemen*. Vincentz Network GmbH & Co KG: **2007**.
127. Keddie, J. L. Film formation of latex. *Materials Science and Engineering: R: Reports* **1997**, 21, 101-170.
128. Soleimani, M.; Haley, J. C.; Majonis, D.; Guerin, G.; Lau, W.; Winnik, M. A. Smart Polymer Nanoparticles Designed for Environmentally Compliant Coatings. *Journal of the American Chemical Society* **2011**, 133, 11299-11307.
129. Brown, G. L. Formation of films from polymer dispersions. *Journal of Polymer science* **1956**, 22, 423-434.

130. Ludwig, I. Drying, film formation and open time of aqueous polymer dispersions : an investigation of different aspects by rheometry and Inverse-Micro-Raman-Spectroscopy (IMRS). Dissertation, KIT Scientific Publishing: **2008**.
131. Winnik, M. A. Latex film formation. *Current Opinion in Colloid & Interface Science* **1997**, 2, 192-199.
132. Tamai, T.; Pinenq, P.; Winnik, M. A. Effect of Cross-Linking on Polymer Diffusion in Poly(butyl methacrylate-co-butyl acrylate) Latex Films. *Macromolecules* **1999**, 32, 6102-6110.
133. Causality. <https://en.wikipedia.org/wiki/Causality> (accessed 02.10.20.15).
134. Thesaurus, T. A. H. R. s. latency. <http://www.thefreedictionary.com/latency> (accessed 02.10.2015).
135. Traut, T. Regulatory allosteric enzymes. Springer: **2008**.
136. Luning, U. Switchable Catalysis. *Angewandte Chemie International Edition* **2012**, 51, 8163-8165.
137. Blanco, V.; Carlone, A.; Hänni, K. D.; Leigh, D. A.; Lewandowski, B. A Rotaxane-Based Switchable Organocatalyst. *Angewandte Chemie International Edition* **2012**, 51, 5166-5169.
138. Stoll, R. S.; Hecht, S. Artificial Light-Gated Catalyst Systems. *Angewandte Chemie International Edition* **2010**, 49, 5054-5075.
139. Piermattei, A.; Karthikeyan, S.; Sijbesma, R. P. Activating catalysts with mechanical force. *Nature Chemistry* **2009**, 1, 133-137.
140. Ben-Asuly, A.; Tzur, E.; Diesendruck, C. E.; Sigalov, M.; Goldberg, I.; Lemcoff, N. G. A Thermally Switchable Latent Ruthenium Olefin Metathesis Catalyst. *Organometallics* **2008**, 27, 811-813.
141. Naumann, S.; Buchmeiser, M. R., Latent and Delayed Action Polymerization Systems. *Macromolecular Rapid Communications* **2014**, 35 (7), 682-701.
142. Wagner, M.; Zöllner, T.; Hiller, W.; Prosenc, M. H.; Jurkschat, K. [4-*t*Bu-2,6-{P(O)(*O*iPr)₂}₂C₆H₂SnL]⁺: An NHC-Stabilized Organotin(II) Cation and Related Derivatives. *Chemistry - A European Journal* **2013**, 19, 9463-9467.
143. Binder, W. H. *Self-healing polymers: from principles to applications*. John Wiley & Sons: **2013**.
144. Herbst, F.; Döhler, D.; Michael, P.; Binder, W. H. Self-Healing Polymers via Supramolecular Forces. *Macromolecular Rapid Communications* **2013**, 34, 203-220.
145. Herbst, F.; Seiffert, S.; Binder, W. H. Dynamic supramolecular poly(isobutylene)s for self-healing materials. *Polymer Chemistry* **2012**, 3, 3084-3092.
146. Toohey, K. S.; Hansen, C. J.; Lewis, J. A.; White, S. R.; Sottos, N. R. Delivery of Two-Part Self-Healing Chemistry via Microvascular Networks. *Advanced Functional Materials* **2009**, 19, 1399-1405.
147. White, S. R.; Sottos, N. R.; Geubelle, P. H.; Moore, J. S.; Kessler, M. R.; Sriram, S. R.; Brown, E. N.; Viswanathan, S. Autonomic healing of polymer composites. *Nature* **2001**, 409, 794-797.
148. Blaiszik, B. J.; Kramer, S. L. B.; Olugebefola, S. C.; Moore, J. S.; Sottos, N. R.; White, S. R. Self-Healing Polymers and Composites. *Annual Review of Materials Research* **2010**, 40, 179-211.
149. Jin, H.; Mangun, C. L.; Stradley, D. S.; Moore, J. S.; Sottos, N. R.; White, S. R. Self-healing thermoset using encapsulated epoxy-amine healing chemistry. *Polymer* **2012**, 53, 581-587.
150. Berne, B. J.; Pecora, R. *Dynamic light scattering: with applications to chemistry, biology, and physics*. Courier Corporation: **2000**.
151. Schärfl, W. *Light scattering from polymer solutions and nanoparticle dispersions*. Springer: **2007**.
152. Goldstein, J. I.; Newbury, D. E.; Echlin, P.; Joy, D. C.; Lyman, C. E.; Lifshin, E.; Sawyer, L.; Michael, J. R. Quantitative X-ray analysis: the basics. In *Scanning Electron Microscopy and X-ray Microanalysis*, Springer: **2003**, 391-451.

References

153. Kohl, H.; Reimer, L. *Transmission Electron Microscopy: Physics of Image Formation*. Springer: **2008**.
154. Grubb, D. Radiation damage and electron microscopy of organic polymers. *Journal of Materials Science* **1974**, 9, 1715-1736.
155. Uhl, A.; Bendig, J.; Leistner, J.; Jagdhold, U.; Bauch, L.; Böttcher, M. Nonstatistical degradation and development characteristics of poly (methylmethacrylate) based resists during electron beam exposure. *Journal of Vacuum Science & Technology B* **1998**, 16, 2968-2973.
156. Kuntsche, J.; Horst, J. C.; Bunjes, H. Cryogenic transmission electron microscopy (cryo-TEM) for studying the morphology of colloidal drug delivery systems. *International Journal of Pharmaceutics* **2011**, 417, 120-137.
157. Hell, S. W.; Wichmann, J. Breaking the diffraction resolution limit by stimulated emission: stimulated-emission-depletion fluorescence microscopy. *Optics Letters* **1994**, 19, 780-782.
158. Hell, S. W. Far-Field Optical Nanoscopy. *Science* **2007**, 316, 1153-1158.
159. Freire, E.; Mayorga, O. L.; Straume, M. Isothermal titration calorimetry. *Analytical Chemistry* **1990**, 62, 950A-959A.
160. Michael J. Blandamer, P. M. C.; Engberts, a. J. B. F. N. Titration microcalorimetry. *J. Chem. Soc., Faraday Trans* **1998**, 94, 2261-2267.
161. Mezger, T. *Das Rheologie Handbuch*. 4th Ed., Vincentz: **2012**.
162. Dahlquist, C. A. *Tack, Adhesion Fundamentals and Practice*. MacLaren and Sons: **1969**, 143-151.
163. Heddleson, S.; Hamann, D.; Lineback, D. The Dahlquist criterion: applicability of a rheological criterion to the loss of pressure-sensitive tack in flour-water dough. *Cereal Chemistry* **1993**.
164. Botella, A.; Dupuy, J.; Roche, A.-A.; Sautereau, H.; Verney, V. Photo-Rheometry/NIR Spectrometry: An in situ Technique for Monitoring Conversion and Viscoelastic Properties during Photopolymerization. *Macromolecular Rapid Communications* **2004**, 25, 1155-1158.
165. Greiner, A.; Wendorff, J. H. Electrospinning: A Fascinating Method for the Preparation of Ultrathin Fibers. *Angewandte Chemie International Edition* **2007**, 46, 5670-5703.
166. Li, D.; Xia, Y. Electrospinning of Nanofibers: Reinventing the Wheel? *Advanced Materials* **2004**, 16, 1151-1170.
167. Huang, C.; Soenen, S. J.; Rejman, J.; Lucas, B.; Braeckmans, K.; Demeester, J.; De Smedt, S. C. Stimuli-responsive electrospun fibers and their applications. *Chemical Society Reviews* **2011**, 40, 2417-2434.
168. Sahay, R.; Kumar, P. S.; Sridhar, R.; Sundaramurthy, J.; Venugopal, J.; Mhaisalkar, S. G.; Ramakrishna, S. Electrospun composite nanofibers and their multifaceted applications. *Journal of Materials Chemistry* **2012**, 22, 12953-12971.
169. Xie, J.; MacEwan, M. R.; Schwartz, A. G.; Xia, Y. Electrospun nanofibers for neural tissue engineering. *Nanoscale* **2010**, 2, 35-44.
170. Teo, W. E.; Ramakrishna, S. A review on electrospinning design and nanofibre assemblies. *Nanotechnology* **2006**, 17, R89.
171. Bhardwaj, N.; Kundu, S. C. Electrospinning: A fascinating fiber fabrication technique. *Biotechnology Advances* **2010**, 28, 325-347.
172. Huang, Z.-M.; Zhang, Y. Z.; Kotaki, M.; Ramakrishna, S. A review on polymer nanofibers by electrospinning and their applications in nanocomposites. *Composites Science and Technology* **2003**, 63, 2223-2253.
173. Crespy, D.; Friedemann, K.; Popa, A.-M. Colloid-Electrospinning: Fabrication of Multicompartment Nanofibers by the Electrospinning of Organic or/and Inorganic Dispersions and Emulsions. *Macromolecular Rapid Communications* **2012**, 33, 1978-1995.

174. Yarin, A. L. Coaxial electrospinning and emulsion electrospinning of core-shell fibers. *Polymers for Advanced Technologies* **2011**, *22*, 310-317.
175. Agarwal, S.; Wendorff, J. H.; Greiner, A. Use of electrospinning technique for biomedical applications. *Polymer* **2008**, *49*, 5603-5621.
176. Gentsch, R.; Pippig, F.; Schmidt, S.; Cernoch, P.; Polleux, J.; Börner, H. G. Single-Step Electrospinning to Bioactive Polymer Nanofibers. *Macromolecules* **2011**, *44*, 453-461.
177. Xia, H.; Song, M. Preparation and characterization of polyurethane-carbon nanotube composites. *Soft Matter* **2005**, *1*, 386-394.
178. Zilg, C.; Thomann, R.; Mülhaupt, R.; Finter, J. Polyurethane Nanocomposites Containing Laminated Anisotropic Nanoparticles Derived from Organophilic Layered Silicates. *Advanced Materials* **1999**, *11*, 49-52.
179. Carroy, A.; Hintermann, T.; Baudin, G.; Bauer, D.; Contich, P.; Dietliker, K.; Faller, M.; Kohli Steck, R.; Lordelot, C.; Misteli, K. Novel latent catalysts for 2K-PUR systems. *Progress in Organic Coatings* **2010**, *68*, 37-41.
180. Tanzi, M. C.; Verderio, P.; Lampugnani, M. G.; Resnati, M.; Dejana, E.; Sturani, E. Cytotoxicity of some catalysts commonly used in the synthesis of copolymers for biomedical use. *Journal of Materials Science: Materials in Medicine* **1994**, *5*, 393-396.
181. Adam, N.; Avar, G.; Blankenheim, H.; Friederichs, W.; Giersig, M.; Weigand, E.; Halfmann, M.; Wittbecker, F.-W.; Larimer, D.-R.; Maier, U.; Meyer-Ahrens, S.; Noble, K.-L.; Wussow, H.-G. Polyurethanes. In *Ullmann's Encyclopedia of Industrial Chemistry*, Wiley-VCH: **2000**.
182. Kirschbaum, S.; Landfester, K.; Taden, A. Unique Curing Properties through Living Polymerization in Cross-linking Materials: Polyurethane Photopolymers from Vinyl Ether Building Blocks. *Angewandte Chemie International Edition* **2015**, *54*, 5789-5792.
183. Chernov, O. V.; Smirnov, A. Y.; Portnyagin, I. A.; Khrustalev, V. N.; Nechaev, M. S. Heteroleptic tin (II) dialkoxides stabilized by intramolecular coordination $\text{Sn}(\text{OCH}_2\text{CH}_2\text{NMe}_2)(\text{OR})$ (R = Me, Et, ⁱPr, ^tBu, Ph). Synthesis, structure and catalytic activity in polyurethane synthesis. *Journal of Organometallic Chemistry* **2009**, *694*, 3184-3189.
184. Zöllner, T.; Iovkova-Berends, L.; Dietz, C.; Berends, T.; Jurkschat, K. On the Reaction of Elemental Tin with Alcohols: A Straightforward Approach to Tin(II) and Tin(IV) Alkoxides and Related Tin-oxo Clusters. *Chemistry - A European Journal* **2011**, *17*, 2361-2364.
185. Bianchini, G.; Scarso, A.; Sorella, G. L.; Strukul, G. Switching the activity of a photoredox catalyst through reversible encapsulation and release. *Chemical Communications* **2012**, *48*, 12082-12084.
186. Ge, Z.; Xie, D.; Chen, D.; Jiang, X.; Zhang, Y.; Liu, H.; Liu, S., Stimuli-Responsive Double Hydrophilic Block Copolymer Micelles with Switchable Catalytic Activity. *Macromolecules* **2007**, *40* (10), 3538-3546.
187. Chen, F.; Yuan, L.; Gu, A.; Lin, C.; Liang, G. Low-temperature cure high-performance cyanate ester resins/microencapsulated catalyst systems. *Polymer Engineering & Science* **2013**, *53*, 1871-1877.
188. Deyrail, Y.; Zydowicz, N.; Cassagnau, P. Polymer cross-linking controlled by release of catalyst encapsulated in polycarbonate micro-spheres. *Polymer* **2004**, *45*, 6123-6131.
189. Yuan, L.; Chen, F.; Gu, A.; Liang, G.; Lin, C.; Huang, S.; Nutt, S.; Chen, G.; Gao, Y. Synthesis of poly(urea-formaldehyde) encapsulated dibutyltin dilaurate through the self-catalysis of core materials. *Polymer Bulletin* **2014**, *71*, 261-273.
190. Fickert, J.; Rupper, P.; Graf, R.; Landfester, K.; Crespy, D. Design and characterization of functionalized silica nanocontainers for self-healing materials. *Journal of Materials Chemistry* **2012**, *22*, 2286-2291.

References

191. Tran, T. H.; Vimalanandan, A.; Genchev, G.; Fickert, J.; Landfester, K.; Crespy, D.; Rohwerder, M. Regenerative Nano-Hybrid Coating Tailored for Autonomous Corrosion Protection. *Advanced Materials* **2015**, *27*, 3820-3830.
192. Brown, E. N.; White, S. R.; Sottos, N. R. Retardation and repair of fatigue cracks in a microcapsule toughened epoxy composite-Part II: In situ self-healing. *Composites Science and Technology* **2005**, *65*, 2474-2480.
193. Cho, S. H.; White, S. R.; Braun, P. V. Self-Healing Polymer Coatings. *Advanced Materials* **2009**, *21*, 645-649.
194. Jonsson, M.; Nordin, O.; Malmström, E.; Hammer, C. Suspension polymerization of thermally expandable core/shell particles. *Polymer* **2006**, *47*, 3315-3324.
195. Kawaguchi, Y.; Ito, D.; Kosaka, Y.; Okudo, M.; Nakachi, T.; Kake, H.; Kim, J. K.; Shikuma, H.; Ohshima, M. Thermally expandable microcapsules for polymer foaming-Relationship between expandability and viscoelasticity. *Polymer Engineering & Science* **2010**, *50*, 835-842.
196. Hansen, C. M., *Hansen solubility parameters: A user's handbook*. Taylor & Francis Group: **2007**.
197. Hofmeister, I.; Landfester, K.; Taden, A. pH-Sensitive Nanocapsules with Barrier Properties: Fragrance Encapsulation and Controlled Release. *Macromolecules* **2014**, *47*, 5768-5773.
198. Palaskar, D. V.; Boyer, A.; Cloutet, E.; Alfos, C.; Cramail, H. Synthesis of Biobased Polyurethane from Oleic and Ricinoleic Acids as the Renewable Resources via the AB-Type Self-Condensation Approach. *Biomacromolecules* **2010**, *11*, 1202-1211.
199. Lu, Y.; Tighzert, L.; Dole, P.; Erre, D. Preparation and properties of starch thermoplastics modified with waterborne polyurethane from renewable resources. *Polymer* **2005**, *46*, 9863-9870.
200. Paul, C. W. Pressure-Sensitive Adhesives (PSAs). In *Handbook of Adhesion Technology*, da Silva, L. M.; Öchsner, A.; Adams, R., Eds. Springer: **2011**, 341-372.
201. Scherzer, T. S., M.W. . In *Simultaneous analysis of the UV curing of acrylate-nanoparticle formulations by combined photorheometry and FT-NIR spectroscopy*, Proceedings RadTech Europe 2009 Conference, Nizza **2009**, 946-954.
202. Dittmar, K.; Siesler, H. W. Near-infrared light-fiber spectroscopic reaction monitoring of the synthesis of diphenylurethane. *Fresenius' Journal of Analytical Chemistry* **1998**, *362*, 109-113.
203. Workman Jr, J.; Weyer, L. *Practical guide and spectral atlas for interpretive near-infrared spectroscopy*. CRC Press: **2012**.
204. Cardolite, C. *Phenalkamines*. <https://www.cardolite.com/phenalkamine> (accessed 08.10.2015).
205. Zhang, Y.; Foos, R.; Landfester, K.; Taden, A. Thermoset-thermoplastic hybrid nanoparticles and composite coatings. *Polymer* **2014**, *55*, 2305-2315.
206. OECD. *Test No. 105: Water Solubility*. OECD Publishing (accessed 19.11.2013).
207. Guyot, A. Advances in reactive surfactants. *Advances in Colloid and Interface Science* **2004**, *108-109*, 3-22.
208. Baier, G.; Friedemann, K.; Leuschner, E.-M.; Musyanovych, A.; Landfester, K. pH Stability of Poly(urethane/urea) Capsules Synthesized from Different Hydrophilic Monomers via Interfacial Polyaddition in the Inverse Miniemulsion Process. *Macromolecular Symposia* **2013**, *331-332*, 71-80.
209. Rosenbauer, E.-M.; Landfester, K.; Musyanovych, A. Surface-Active Monomer as a Stabilizer for Polyurea Nanocapsules Synthesized via Interfacial Polyaddition in Inverse Miniemulsion. *Langmuir* **2009**, *25*, 12084-12091.
210. Liu, T.; Li, Z.; Wu, Q.; Ma, X. Synthesis of nanocolorants with crosslinked shell by miniemulsion polymerization stabilized by waterborne polyurethane. *Polymer Bulletin* **2010**, *64*, 511-521.

211. Naghash, H.; Akhtarian, R.; Iravani, M. Synthesis and properties of polyvinyl acetate emulsion copolymers by three novel non-ionic functional polyurethane surfactants. *Korean Journal of Chemical Engineering* **2014**, *31*, 1281-1287.
212. Dong, Y.; Jin, Y.; Wei, D. Surface activity and solubilization of a novel series of functional polyurethane surfactants. *Polymer International* **2007**, *56*, 14-21.
213. Shim, S. E.; Jung, H.; Lee, K.; Lee, J. M.; Choe, S. Dispersion polymerization of methyl methacrylate with a novel bifunctional polyurethane macromonomer as a reactive stabilizer. *Journal of Colloid and Interface Science* **2004**, *279*, 464-470.
214. Chanamai, R.; McClements, D. J. Isothermal titration calorimetry measurement of enthalpy changes in monodisperse oil-in-water emulsions undergoing depletion flocculation. *Colloids and Surfaces A: Physicochemical and Engineering Aspects* **2001**, *181*, 261-269.
215. Kevelam, J.; van Breemen, J. F. L.; Blokzijl, W.; Engberts, J. B. F. N. Polymer-Surfactant Interactions Studied by Titration Microcalorimetry: Influence of Polymer Hydrophobicity, Electrostatic Forces, and Surfactant Aggregational State. *Langmuir* **1996**, *12*, 4709-4717.
216. Wang, G.; Olofsson, G. Titration Calorimetric Study of the Interaction between Ionic Surfactants and Uncharged Polymers in Aqueous Solution. *The Journal of Physical Chemistry B* **1998**, *102*, 9276-9283.
217. Hamberger, A.; Landfester, K. Influence of size and functionality of polymeric nanoparticles on the adsorption behavior of sodium dodecyl sulfate as detected by isothermal titration calorimetry. *Colloid and Polymer Science* **2011**, *289*, 3-14.
218. Lewis, E.; Murphy, K. Isothermal Titration Calorimetry. In *Protein-Ligand Interactions*, Ulrich Nienhaus, G., Ed. Humana Press: **2005**, Vol. 305, 1-15.
219. Fryd, M. M.; Mason, T. G. Time-Dependent Nanoemulsion Droplet Size Reduction By Evaporative Ripening. *The Journal of Physical Chemistry Letters* **2010**, *1*, 3349-3353.
220. Cipelletti, L.; Ramos, L.; Manley, S.; Pitard, E.; Weitz, D. A.; Pashkovski, E. E.; Johansson, M. Universal non-diffusive slow dynamics in aging soft matter. *Faraday Discussions* **2003**, *123*, 237-251.
221. De Smet, Y.; Deriemaeker, L.; Parloo, E.; Finsy, R. On the Determination of Ostwald Ripening Rates from Dynamic Light Scattering Measurements. *Langmuir* **1999**, *15*, 2327-2332.
222. Eastoe, J.; Young, W. K.; Robinson, B. H.; Steytler, D. C. Scattering studies of microemulsions in low-density alkanes. *Journal of the Chemical Society, Faraday Transactions* **1990**, *86*, 2883-2889.
223. Udenfriend, S.; Stein, S.; Boehlen, P.; Dairman, W.; Leimgruber, W.; Weigele, M. Fluorescamine: a reagent for assay of amino acids, peptides, proteins, and primary amines in the picomole range. *Science* **1972**, *178*, 871-872.
224. Musyanovych, A.; Adler, H.-J. P. Grafting of Amino Functional Monomer onto Initiator-Modified Polystyrene Particles. *Langmuir* **2005**, *21*, 2209-2217.
225. Schaeffel, D.; Staff, R. H.; Butt, H.-J.; Landfester, K.; Crespy, D.; Koynov, K. Fluorescence Correlation Spectroscopy Directly Monitors Coalescence During Nanoparticle Preparation. *Nano Letters* **2012**, *12*, 6012-6017.
226. Horzum, N.; Muñoz-Espí, R.; Glasser, G.; Demir, M. M.; Landfester, K.; Crespy, D. Hierarchically Structured Metal Oxide/Silica Nanofibers by Colloid Electrospinning. *ACS Applied Materials & Interfaces* **2012**, *4*, 6338-6345.
227. Joe, D.; Golling, F. E.; Friedemann, K.; Crespy, D.; Klapper, M.; Müllen, K. Anisotropic Supports in Metallocene-Catalyzed Polymerizations: Templates to Obtain Polyolefin Fibers. *Macromolecular Materials and Engineering* **2014**, *299*, 1155-1162.

References

228. Stoiljkovic, A.; Ishaque, M.; Justus, U.; Hamel, L.; Klimov, E.; Heckmann, W.; Eckhardt, B.; Wendorff, J. H.; Greiner, A. Preparation of water-stable submicron fibers from aqueous latex dispersion of water-insoluble polymers by electrospinning. *Polymer* **2007**, *48*, 3974-3981.
229. Yuan, W.; Zhang, K.-Q. Structural Evolution of Electrospun Composite Fibers from the Blend of Polyvinyl Alcohol and Polymer Nanoparticles. *Langmuir* **2012**, *28*, 15418-15424.
230. Wohnhaas, C.; Friedemann, K.; Busko, D.; Landfester, K.; Balushev, S.; Crespy, D.; Turshatov, A. All Organic Nanofibers As Ultralight Versatile Support for Triplet-Triplet Annihilation Upconversion. *ACS Macro Letters* **2013**, *2*, 446-450.
231. Jo, E.; Lee, S.; Kim, K. T.; Won, Y. S.; Kim, H.-S.; Cho, E. C.; Jeong, U. Core-Sheath Nanofibers Containing Colloidal Arrays in the Core for Programmable Multi-Agent Delivery. *Advanced Materials* **2009**, *21*, 968-972.
232. Billiet, S.; Hillewaere, X. K. D.; Teixeira, R. F. A.; Du Prez, F. E. Chemistry of Cross-linking Processes for Self-Healing Polymers. *Macromolecular Rapid Communications* **2013**, *34*, 290-309.
233. Pratama, P. A.; Sharifi, M.; Peterson, A. M.; Palmese, G. R. Room Temperature Self-Healing Thermoset Based on the Diels-Alder Reaction. *ACS Applied Materials & Interfaces* **2013**, *5*, 12425-12431.
234. Cho, S. H.; White, S. R.; Braun, P. V. Room-Temperature Polydimethylsiloxane-Based Self-Healing Polymers. *Chemistry of Materials* **2012**, *24*, 4209-4214.
235. Park, J.-H.; Braun, P. V. Coaxial Electrospinning of Self-Healing Coatings. *Advanced Materials* **2010**, *22*, 496-499.
236. Hillewaere, X. K. D.; Teixeira, R. F. A.; Nguyen, L.-T. T.; Ramos, J. A.; Rahier, H.; Du Prez, F. E. Autonomous Self-Healing of Epoxy Thermosets with Thiol-Isocyanate Chemistry. *Advanced Functional Materials* **2014**, *24*, 5575-5583.
237. Lee, M. W.; An, S.; Lee, C.; Liou, M.; Yarin, A. L.; Yoon, S. S. Self-healing transparent core-shell nanofiber coatings for anti-corrosive protection. *Journal of Materials Chemistry A* **2014**, *2*, 7045-7053.
238. Guimard, N. K.; Oehlenschlaeger, K. K.; Zhou, J.; Hilf, S.; Schmidt, F. G.; Barner-Kowollik, C. Current Trends in the Field of Self-Healing Materials. *Macromolecular Chemistry and Physics* **2012**, *213*, 131-143.
239. Chen, Y.; Kushner, A. M.; Williams, G. A.; Guan, Z. Multiphase design of autonomic self-healing thermoplastic elastomers. *Nature Chemistry* **2012**, *4*, 467-472.
240. Jin, H.; Mangun, C. L.; Griffin, A. S.; Moore, J. S.; Sottos, N. R.; White, S. R. Thermally Stable Autonomic Healing in Epoxy using a Dual-Microcapsule System. *Advanced Materials* **2014**, *26*, 282-287.
241. McIlroy, D. A.; Blaiszik, B. J.; Caruso, M. M.; White, S. R.; Moore, J. S.; Sottos, N. R. Microencapsulation of a Reactive Liquid-Phase Amine for Self-Healing Epoxy Composites. *Macromolecules* **2010**, *43*, 1855-1859.
242. Fong, H.; Chun, I.; Reneker, D. H. Beaded nanofibers formed during electrospinning. *Polymer* **1999**, *40*, 4585-4592.
243. Friedemann, K.; Turshatov, A.; Landfester, K.; Crespy, D. Characterization via Two-Color STED Microscopy of Nanostructured Materials Synthesized by Colloid Electrospinning. *Langmuir* **2011**, *27*, 7132-7139.
244. Meyer, L.; Wildanger, D.; Medda, R.; Punge, A.; Rizzoli, S. O.; Donnert, G.; Hell, S. W. Dual-Color STED Microscopy at 30-nm Focal-Plane Resolution. *Small* **2008**, *4*, 1095-1100.
245. Busko, D.; Balushev, S.; Crespy, D.; Turshatov, A.; Landfester, K. New possibilities for materials science with STED microscopy. *Micron* **2012**, *43*, 583-588.

246. Hertz, P. Über den gegenseitigen durchschnittlichen Abstand von Punkten, die mit bekannter mittlerer Dichte im Raume angeordnet sind. *Mathematische Annalen* **1909**, 67, 387-398.
247. Herrmann, C.; Turshatov, A.; Crespy, D. Fabrication of Polymer Ellipsoids by the Electrospinning of Swollen Nanoparticles. *ACS Macro Letters* **2012**, 1, 907-909.
248. Beckert, H., Fanghänel, E., Habicher, W. D., Metz, P., Pavel, D., & Schwetlick, K. In *Organikum*, 22nd Ed.; Wiley-VCH: **2004**, 303.
249. P. Schlichting, U. R., K. Müllen. New Synthetic Routes to Alkyl-Substituted and Functionalized Perylenes *Liebigs Ann./Recueil* **1997**, 395-407.
250. Bijlard, A.-C.; Winzen, S.; Itoh, K.; Landfester, K.; Taden, A., Alternative Pathway for the Stabilization of Reactive Emulsions via Cross-Linkable Surfactants. *ACS Macro Letters* **2014**, 3 (11), 1165-1168.
251. Bijlard, A.-C.; Kaltbeitzel, A.; Avlasevich, Y.; Crespy, D.; Hamm, M.; Landfester, K.; Taden, A., Dual-compartment nanofibres: separation of two highly reactive components in close vicinity. *RSC Advances* **2015**, 5 (118), 97477-97484.

9 Appendix

9.1 List of Figures

Figure 1. Mechanism of coalescence (upper part) and Ostwald ripening (lower part).....	4
Figure 2. Potential curve of two approaching, electrostatically (left) and sterically (right) stabilized particles as a function of distance.....	5
Figure 3. Summary of functions which can be added to surfactants.....	9
Figure 4. Schematic principle of miniemulsion polymerization.....	12
Figure 5. Film Formation Principle of a nonreactive latex (left) and reactive 2K dispersions (right).	22
Figure 6. Schematic principle of the P1K-concept.	25
Figure 7. Self-healing principles.	27
Figure 8. Measurement principle for isothermal titration calorimetry.....	31
Figure 9. Measurement principle for oscillatory rheology.....	33
Figure 10. Principle of electrospinning.	35
Figure 11. Schematic presentation of the release profile of an ideal thermolatent catalyst.	38
Figure 12. Morphology of the isooctane nanocapsules.....	41
Figure 13. Morphology of the catalyst nanocapsules.....	42
Figure 14. STEM analysis of the TLCN 3 nanocapsules.	42
Figure 15. Thermal properties of the catalyst nanocapsules.	44
Figure 16. Isothermal rheology measurements of the catalyst nanocapsules at 50 °C.	46
Figure 17. Isothermal rheology measurements of the catalyst nanocapsules at 120 °C.	48
Figure 18. Isothermal rheology, temperature and concentration dependencies, storage stability of the catalyst nanocapsules.....	50
Figure 19. FT-IR spectra comparing the cured PU-film before and after curing.....	52
Figure 20. <i>In-situ</i> NIR-analysis of the curing at 120 °C.	52
Figure 21. Morphology of the PU-composite.	53
Figure 22. Morphology and T_g of the reinforced composite.	54
Figure 23. Preparation and principle of a P1K-system.	57
Figure 24. Educt properties of the P1K raw materials.	61
Figure 25. Curing kinetics and potlife of the different P1K-systems in bulk.	63

Figure 26. Room temperature cure and determination of T_g s in the P1K-systems.	64
Figure 27. Curing enthalpies of the P1K-systems.	65
Figure 28. Principle of the cross-surf concept.	69
Figure 29. Reactivity of the epoxy surfactants.	71
Figure 30. Spectral characterization of the epoxy surfactants.	73
Figure 31. Colloidal stability of the amine emulsions.	75
Figure 32. ITC analysis of the interfacial reaction between amine and epoxy surfactant.	76
Figure 33. Curing of amine emulsions with epoxy dispersions and morphology of the cured film.	78
Figure 34. P1K-concept.	79
Figure 35. Particle sizes of amine and epoxy emulsions versus surfactant concentration.	80
Figure 36. Time-dependent stability of amine and epoxy emulsions.	81
Figure 37. Time-dependent stability of the P1K-dipsersions and references.	87
Figure 39. Morphology of the P1K-system.	91
Figure 40. Turbidity measurements of the P1K-systems.	92
Figure 41. Turbidity measurement P1K-3 and its reference.	93
Figure 42. Absorption and emission spectra for the fluorescamine-NX5454 derivate.	94
Figure 43. Calibration curves for the fluorescamine assay for the different P1K-systems.	95
Figure 44. Relative concentrations of primary amines for the different P1K-systems.	97
Figure 45. Relative concentrations of primary amines for the P1K-3 reference.	97
Figure 46. Schematic presentation of the colloid electrospinning process and the statistical distribution of the epoxy and amine compartments in the nanofibers.	102
Figure 47. External morphology of the nanofibers.	103
Figure 48. Internal morphology of the nanofibers.	104
Figure 49. Resolution of confocal versus STED microscopy.	104
Figure 50. Computation and TEM analysis on the distribution of colloids within the nanofibers.	107
Figure 51. DSC and HPLC analysis to access the reactivity of the nanofibers.	109
Figure 52. Morphology after reaction.	110
Figure 53. Self-healing ability of the PVA-EA nanofibers.	111
Figure 54. Absorption and emission spectra of diphenylperylene in toluene.	132
Figure 55. Absorption and emission spectra of BODIPY in toluene.	132

9.2 List of Tables

Table 1. Summary of common heterophase systems and their composition.	3
Table 2. Applications of surfactants and classification according to their HLB value.	7
Table 3. Composition, colloidal properties and encapsulation efficiencies of the synthesized nanocapsules.	39
Table 4. Comparison of onset-, peak- and glass transition temperatures of the nanocapsules measured with DSC.	44
Table 5. Mechanical properties of the catalyst nanocapsules at different temperatures.	47
Table 6. Nitrogen content and AHEW of the phenalkamines by potentiometric titration.	59
Table 7. Properties of the educts used for the preparation of the different P1K-systems.	61
Table 8. Summary of the curing and thermal properties of the different P1K-systems.	65
Table 9. Composition of the synthesized surfactants.	69
Table 10. Properties of the epoxy surfactant series.	72
Table 11. Particle sizes of A&E before their mixing to form P1K-dispersions.	82
Table 12. Optical evaluation and T_g s of the P1K-systems after film formation.	85
Table 13. SEM images of the P1K-1 films.	88
Table 14. SEM images of the P1K-2 films.	89
Table 15. SEM images of the P1K-3 films.	90
Table 16. Colloidal properties and details regarding the nanofibers.	101
Table 17. Parameters used for the computations.	106
Table 18. Optical evaluation of the salt water corrosion test.	113
Table 19. Preparation of the catalyst nanocapsules.	116
Table 20. Preparation of the P1K-thermosets.	120
Table 21. Preparation of amine and epoxy miniemulsions.	127
Table 22. Preparation of the P1K-dispersions.	128
Table 23. Sample preparation and amine concentrations for the fluorescamine assay.	129
Table 24. Fits for the fluorescamine assay in the P1K-systems.	129
Table 25. Fits for the turbidity measurements in the P1K-systems.	130

9.3 List of Abbreviations

1K	One component
2K	Two component
A&E	Amine and epoxy colloids
AHEW	Amine hydrogen equivalent weight
ASTM	International technical standard
BADGE	Bisphenol-A diglycidylether
BDDMA	1,4-butanediol dimethacrylate
Bis-A	Bisphenol-A
BMA	Butyl methacrylate
BOX	Benzoxazine
CMC	Critical micelle concentration
CTAB	Cetyl trimethylammonium bromide
DBTL	Dibutyltin dilaurate
DC-STED	Dual color stimulated emission depletion
DETA	Diethylenetriamine
DLS	Dynamic light scattering
DLVO	Derjaguin, Landau, Verwey, Overbeek
DMTA	Dynamic mechanical analysis
DSC	Differential scanning calorimetry
ECH	Epichlorohydrine
EDA	Ethylenediamine
EDX	Energy dispersive x-ray analysis
EE	Encapsulation efficiency
EEW	Epoxy equivalent weight
ES	Epoxy surfactant
EtAc	Ethyl acetate
FCCS	Fluorescence cross correlation spectroscopy
Fomrez	Dimethyltin didecanoate
FT-IR	Fourier transformation infrared spectroscopy
FWHM	Full width half maximum

GHS	Globally harmonized system of classification and labelling of chemicals
HD	Hexadecane
HLB	Hydrophilic lipophilic balance
HPLC	High pressure liquid chromatography
IO	Isooctane
IPDI	Isophorone diisocyanate
ITC	Isothermal titration calorimetry
IUPAC	International Union of Pure and Applied Chemistry
KPS	Potassium peroxydisulfate
LCST	Lower critical solution temperature
MAA	Methacrylic acid
MFFT	Minimum film formation temperature
MMA	Methyl methacrylate
MSDS	Material safety datasheet
NC547	Epoxidized cardanol resin
NCO	Isocyanate group
NIR	Near Infrared spectroscopy
NMR	Nuclear magnetic resonance spectroscopy
nrES	Non-reactive Epoxide surfactant
NX5454, NC641	Phenalkamines
o/w	Oil-in-water emulsion
OECD	Guideline for testing of chemicals
P1K	Pseudo one component
PDI	Polydispersity index
PEO	Poly (ethylene oxide)
PMMA	Poly(methylmethacrylate)
PPO	Poly (propylene oxide)
PU	Polyurethane
PVA	Poly(vinyl alcohol)
RT	Room temperature
RTM	Resin transfer molding
SC	Solid content
SCT	Theoretical solid content

Appendix

SDS	Sodium-dodecylsulfate
SEC	Size exclusion chromatography
SEM	Scanning electron microscopy
Surfmer	Surfactant+monomer
TEM	Transmission electron microscopy
T_g	Glass transition temperature
TGA	Thermogravimetric analysis
THF	Tetrahydrofuran
TLCN	Thermolatent-catalyst-nanocapsules
UV	Ultra violet
VOC	Volatile organic compound
w/o	Water-in-oil emulsion
XRF	X-ray fluorescence spectroscopy

9.4 List of Symbols

A_{ij}	Interfacial area between components i, j
c	Concentration
D	Hydrodynamic diameter
d	Diffraction limit
D_s	Diffusion coefficient
F_C	Capillary forces
f_{EA}	Fraction of the components E,A compared to total amount
F_G	Deformation resistance
G	Gibbs free energy
G^*	Complex shear modulus
G'	Storage modulus
G''	Loss modulus
I	Intracavity intensity
I_s	Saturation intensity
k_B	Boltzmann constant
M	Molecular weight
M_n	Number-averaged molecular weight
M_w	Weight-averaged molecular weight
n	General variable
$N_{A,B}$	Number of A or B molecules
$n\sin(\alpha)$	Numerical aperture
p	Conversion
$P_{Laplace}$	Laplace pressure
P_n	Degree of polymerization
R	Universal gas constant
r	Ratio of reactants
r_h	Hydrodynamic radius
S_i	Spreading coefficient of component i
T	Temperature
t	Time
$\tan\delta$	Loss factor
Z_{av}	z-averaged diameter

Appendix

γ	Strain
γ_0	Strain amplitude
γ_{ij}	Interfacial tension between component i,j
δ	Phase angle
η	Dynamic viscosity
η^*	Complex viscosity
λ	Wavelength
$\Pi_{osmotic}$	Osmotic pressure
ρ	Density
τ	Shear stress
ω	Angular frequency
∞	Infinite

9.6 Scientific Contributions

Publications

- Bijlard, A.-C.; Hansen, A.; Lieberwirth, I.; Landfester, K.; Taden, A., A nanocapsule-based approach towards physical thermolatent catalysis, *submitted*.
- Bijlard, A.-C. and Wald, S.; Crespy, D.; Taden, A.; Wurm, F. R.; Landfester, K., Functional Colloid Stabilization, *in preparation*.
- Bijlard, A.-C.; Landfester, K.; Taden, A.; PIK-systems, *in preparation*.
- Bijlard, A.-C.; Kaltbeitzel, A.; Avlasevich, Y.; Crespy, D.; Hamm, M.; Landfester, K.; Taden, A., Dual-compartment nanofibres: separation of two highly reactive components in close vicinity. *RSC Advances* 2015, 5 (118), 97477-97484.
- Taden, A.; Bijlard, A.-C.; Hansen, A.; Landfester, K.; Nanokapseln als thermolatente Polymerisationskatalysatoren oder –initiatoren, EP 15189377.3
- Bijlard, A.-C.; Winzen, S.; Itoh, K.; Landfester, K.; Taden, A., Alternative Pathway for the Stabilization of Reactive Emulsions via Cross-Linkable Surfactants. *ACS Macro Letters* 2014, 3 (11), 1165-1168.

Conferences

- Oral presentation: “Understanding the interactions of epoxides and amines as reactive compartments in aqueous dispersions”, 250th ACS National Meeting & Exposition, Boston, MA, United States, 16.-20.08.2015.
- Poster presentation: „Epoxy/Amine nanofibers for corrosion protection“, European Scientific Advisory Board Meeting, Henkel Adhesive Technologies, Düsseldorf, 23.-24.02.2015.
- Poster presentation: “Autonomic self-healing of electrospun epoxy-amine nanofibers”, European-Winter School on Physical Organic Chemistry (E-WiSPOC) in Bressanone, South Tyrol, 01-06.02.2015. The poster was awarded the poster prize.
- Oral presentation: “Waterbased epoxy/amine systems”, Review Meeting Henkel/MPI Cooperation, Düsseldorf, 30.-31.10.2014.
- Poster presentation: “Interactions between epoxy and amine droplets separated by water and their film formation”, Ostwald Colloquium on Particles@Interfaces, Mainz, 17.-19.09.2014. The poster was awarded the poster prize.
- Poster presentation: “Alternative pathway for the stabilization of reactive emulsions via cross-linkable surfactants”, Frontiers of Polymer Colloids Conference, Prague, 20.-24.07.2014.
- Oral presentation: “Pseudo 1K Systems”, Review Meeting Henkel/MPI Cooperation, Düsseldorf, 17.-18.10.2014.